Exo-S

Starshade Probe-Class

Exoplanet Direct Imaging Mission Concept

FINAL REPORT MARCH 2015

CL #15-1155

National Aeronautics and
Space Administration

Jet Propulsion Laboratory
California Institute of Technology
Pasadena, California

Exo-S: Starshade Probe-Class Exoplanet Direct Imaging Mission Concept

Final Report

ExoPlanet Exploration Program
Astronomy, Physics and Space Technology Directorate
Jet Propulsion Laboratory
for
Astrophysics Division
Science Mission Directorate
NASA

March 2015

Science and Technology Definition Team

Sara Seager, Chair (MIT)
W. Cash (U. Colorado)
S. Domagal-Goldman (NASA-GSFC)
N. J. Kasdin (Princeton U.)
M. Kuchner (NASA-GSFC)
A. Roberge (NASA-GSFC)
S. Shaklan (NASA-JPL)
W. Sparks (STSci)
M. Thomson (NASA-JPL)
M. Turnbull (GSI)

JPL Design Team:
K. Warfield, Lead
D. Lisman
R. Baran
R. Bauman
E. Cady
C. Heneghan
S. Martin
D. Scharf
R. Trabert
D. Webb
P. Zarifian

Acknowledgments

The STDT would like to thank Serge Dubovitsky, Brian Hirsch, Steve Krach, Siu-Chun Lee, Christian Liebe, Martin Lo, Luis Marchen, Zahidul Rahman, Carl Seubert, Chris Stark, and Brian Trease for their contributions to the engineering design and analyses that went into this report: Milana Wood for her help with the cost estimate and CATE discussions; Brian Lim for his help with the technology development plan; Joby Harris for the design of the report cover and fact sheet; Marissa Rubio for her logistical support; and Steve Unwin for his careful review and many suggestions for this final report. For their flexibility in accommodating our evolving design and their independent review, the STDT thanks the Aerospace Corporation's CATE team. The STDT would also like to thank Bob Brown for his contributions to the known giant planet observation sequence and science, Andrew Howard for his completeness estimates of known RV targets, and Karl Stapelfeldt for his contribution on the exoplanet science landscape in 2024. Last, but not least, the STDT would like to thank Samantha Ozyildirim for her many hours spent editing this report.

Disclaimer

The cost information contained in this document is of a budgetary and planning nature and is intended for informational purposes only. It does not constitute a commitment on the part of JPL and Caltech.

Exo-S STARSHADE

Probe-Class Exoplanet Direct Imaging Mission Concept

Direct imaging is a powerful but challenging technique for exoplanet detection and characterization. A space-based telescope above the blurring effects of the Earth's atmosphere is required to detect light from a rocky planet in the glare of its Sun-like host star. The combination of a telescope and a starshade aligned to suppress starlight provides the high contrast and sensitivity needed to image exoplanets in reflected light. Exo-S will detect and measure the spectra of a diverse range of planet types, down to Earth-size planets around the most favorable target stars.

IMPORTANCE TO NASA

"Discover and study planets around other stars, and explore whether they could harbor life" *– NASA 2014 Science Plan*

Exo-S will address this question by:

- Searching for new exoplanets – giant planets down to Earth-size planets in a range of orbits including habitable zones
- Characterizing known giant exoplanets and newly discovered exoplanets with spectroscopy
- Observing circumstellar dust to study planets in context of planetary systems and to quantify exozodiacal dust levels

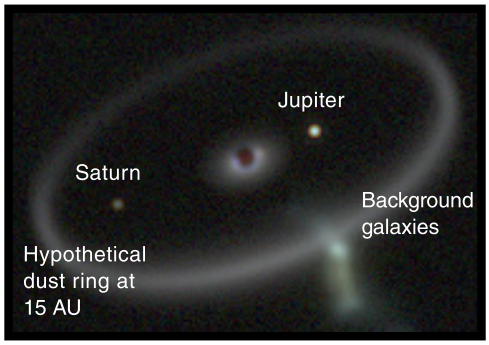

Simulated image considering a 2.4-m telescope and starshade. Image shows nearby G0 V (solar type) star, Beta Canum Venaticorum, if it contained all 8 solar system planets, a cloud of warm dust comparable to 1 zodi, and a dust ring from a Kuiper belt.

BENEFITS AND STRENGTHS

- Inner working angle independent of telescope aperture
- Absence of outer working angle, field of view only limited by detector size
- Nonspecialized commercial space telescope can be used
- Inherently broadband images
- Capability of detecting Earth-size planets in the habitable zone of favorable target stars even with a small aperture

EXPECTED SCIENCE

Exo-S will detect a range of planet types in various orbits around their host star. Modeling efforts have included calculating the probability of imaging an exoplanet and developing an optimized observing sequence to maximize the number and variety of stars observed. Exo-S examined the following three observing scenarios:

Case 1: *Input list favoring stars with accessible habitable zones, Earth twins, 1.1-m telescope, Earth-leading orbit*

Case 2: *Input list focusing on deep observations for maximum spectral return, 1.1 m telescope, Earth–leading orbit*

Case 3: *Same input list as Case 1, mission scenario setup for rendezvous with 2.4 m WFIRST/AFTA telescope, L2 orbit*

Mean Planet Yields

Case	1	2	3
HZ Earth	1.1	0.6	1.7
Earth	0.3	0.4	0.6
Sup. Earth	1.6	1.1	2.7
Sub Nep	3.1	3.0	5.2
Neptune	4.5	4.7	7.1
Jupiter	6.4	7.0	9.4
Known Giant Planets	14.0	14.0	12.0
Total	**31.0**	**30.8**	**38.8**

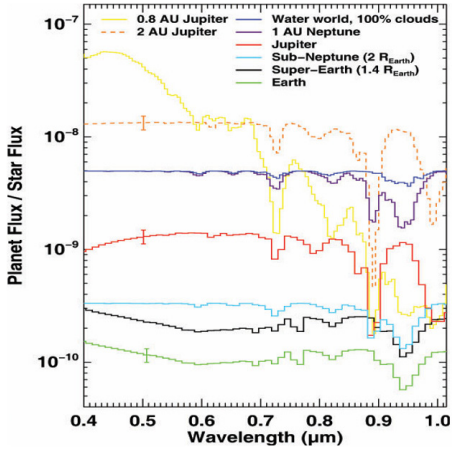

Differences and similarities in brightness and spectral features for a variety of exoplanet types. Optical reflectance spectra of a diverse suite of exoplanets are shown without added noise. Solar system analogs, super Earths, and sub-Neptunes features are readily distinguishable with a R=70 spectrum.

MISSION CONCEPTS

Rendezvous Mission

- A starshade designed to work with an existing telescope
- WFIRST/AFTA 2.4 m is studied in an L2 orbit

Dedicated Mission

- A starshade co-launched with and dedicated to a small space telescope
- A commercial 1.1-m telescope was studied for a mission in a heliocentric, Earth-leading, Earth-drift away orbit

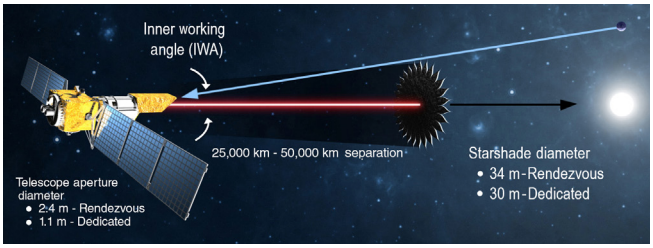

FLIGHT SYSTEM OVERVIEW (DEDICATED MISSION SHOWN)

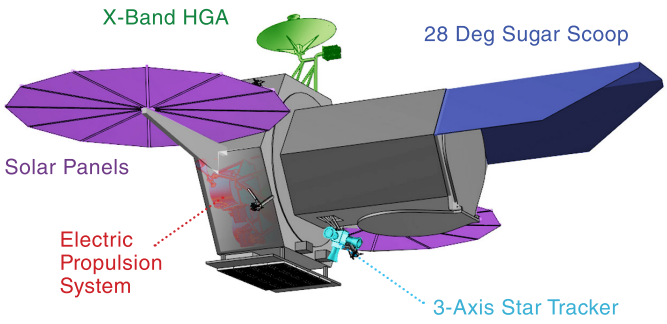

Starshade components:
- *Laser beacon*
- *Patch antennas*
- *Deployment mechanisms*

Chemical propulsion for:
- *Spin control- Dedicated*
- *Spin control and retargeting- Rendezvous*

Inner disk covered with an opaque shield

Shaped petals to control diffraction

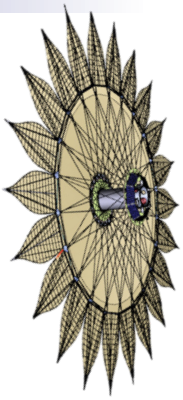

3 bands for imaging:

	Rendezvous		Dedicated	
	IWA	Band	IWA	Band
Blue	71 mas	425-602 nm	80 mas	400-647 nm
Green	100 mas	600-850 nm	102 mas	510-825 nm
Red	118 mas	706-1000 nm	124 mas	618-1000 nm

INSTRUMENT PACKAGE (DEDICATED MISSION SHOWN)

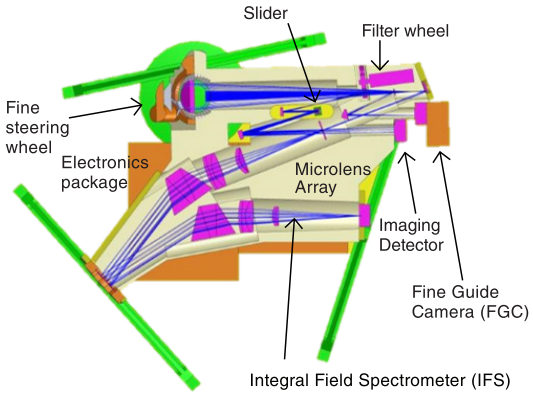

Instrument Package	Function	Field of View (arcsec)	Optical Throughput	Wavelength (nm)
Planet Cam	Imaging	60	51%	400-1000
IFS	Spectra	3	42%	400-1000
FGC	Formation Flying	120	47%	1400-1600

TECHNOLOGY DEVELOPMENT

Resolve key open issues:
- Control edge-scattered sunlight
- Demonstrate contrast and suppression performance and validate optical models
- Demonstrate lateral formation-sensing accuracy
- Demonstrate flight-like petal fabrication and deployment
- Demonstrate inner disk deployment with optical shield

All key open issues are fully funded and planned to demonstrate subsystem performance to TRL-5 by FY 2018.

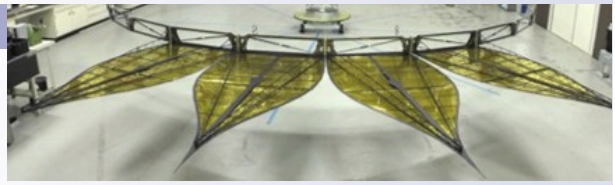

Technology demonstration of half-scale perimeter truss with starshade petals

FIELD TESTS

Dry lake bed open-air test of a 1-m class starshade with a 2-km baseline, designed to characterize the sensitivity to lateral control errors and the benefit of spinning the starshade.

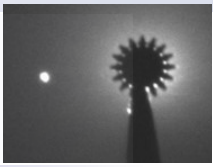

HERITAGE

- Perimeter truss uses industry-standard deployment for communications antennas larger than 10m
- Stowing technique for petals is similar to those used on wrapped rib antennas
- Commercial bus
- Commercial telescope

Dedicated Mission Schedule

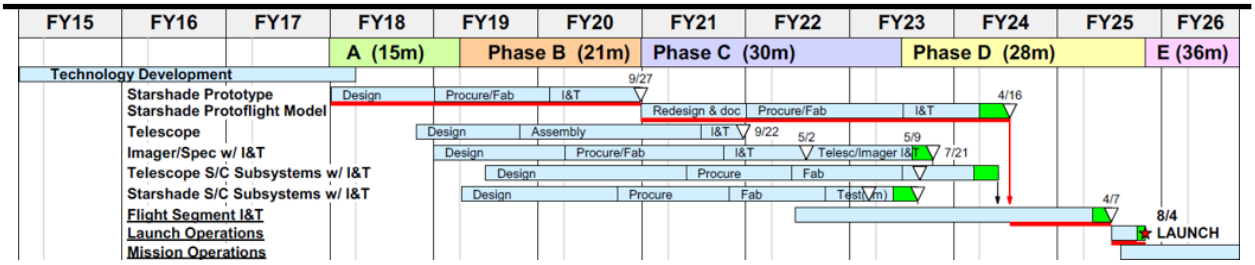

Table of Contents

Executive Summary

Can we find another planet like Earth orbiting a nearby star? To find such a planet would complete the revolution, started by Copernicus nearly 500 years ago, that displaced Earth as the center of the universe…. Astronomers are now ready to embark on the next stage in the quest for life beyond the Solar System—to search for nearby, habitable, rocky or terrestrial planets with liquid water and oxygen…. The observational challenge is great, but armed with new technologies…astronomers are poised to rise to it.
–New Worlds, New Horizons, 2010

For the first time in human history, the technological reach exists to discover and characterize planets like Earth orbiting stars other than the Sun. A space-based direct imaging mission to ultimately find and characterize other Earths is a long-term priority for space astrophysics (NRC 2010).

The Exo-Starshade (Exo-S) Science and Technology Definition Team (STDT) is tasked by NASA to study the starshade-telescope mission concept under the 'probe' class of space missions, with a targeted cost of $1B (FY15 dollars). Per the STDT charter, the mission should be ready for a 'new start' in 2017, with launch in 2024, and science beyond the expected ground capability at the end of the mission. The Exo-S mission concept study began in May 2013 and ran until delivery of the Final Report in March 2015.

Science Goals and Observing Program

Exo-S is a direct imaging space-based mission to discover and characterize exoplanets. With its modest size, Exo-S bridges the gap between census missions like Kepler and a future space-based flagship direct imaging exoplanet mission.

The Exo-S mission has four science goals. The first goal is *to discover new planets from Earth size to giant planets*. Within this goal is the possibility of discovering Earth-size exoplanets in the habitable zones (HZ) of Sun-like stars—arguably one of the most exciting pursuits in exoplanet research (**Figure ES-1**).

Figure ES-1. To the rest of the Universe, Earth appears as an exoplanet. The starshade-telescope mission is capable of imaging exoplanets with the properties of Earth orbiting at least 10 Sun-like stars. Image: Earth as seen from the Voyager I spacecraft at a distance of 4 billion miles. Credit: NASA/JPL.

The second science goal is *to measure spectra of a subset of newly discovered planets*. The Exo-S spectral range is from 400–1,000 nm, with a spectral resolution of up to R=70, which enables detection of key spectral features. Of particular interest are the so-called sub-Neptune exoplanets, planets with no solar system counterparts. Spectral resolution depends on the target brightness.

The third science goal is designed to guarantee outstanding science return: *to characterize known giant planets, by measuring spectra and constraining masses.* The known giant planets are detectable by virtue of extrapolated position in the 2024 timeframe.

The fourth science goal is *to characterize planetary systems, with a specific interest in studying circumstellar dust in the context of known planets*. Observations will shed light on the dust-generating parent bodies (asteroids and comets), as well as assess exozodi levels for future missions.

Direct imaging exoplanet science is a daunting task not afforded justice by a few outlined goals. Several pressing astrophysical questions have come to the forefront, including: how much can be learned about planets with limited spectral and temporal information; how planets can be efficiently distinguished from

background sources; how stray light from binary stars should be handled; and how exozodiacal dust levels higher than the solar system's might impact the science harvest of a direct imaging mission. Answering these concerns requires a large-scale dedicated effort in the coming years.

The science goals are carried out by an observing program, created from balancing the search for new exoplanets with the spectral characterization of known giant planets. A key factor is the time and fuel it takes to align the starshade and telescope system to observe the next target star, and therefore the number of possible retargets available within the mission lifetime.

An input star list is used to design an efficient observing sequence. Each target star is observed once during the first two years of the mission. The list and number of target stars (ranging from 40 to 55 for the two years) and the predicted planet yield, depends on the strategy for types of planets to be harvested and telescope aperture. Three different case studies are presented in this report. Follow-on observations are possible during the third year of the Exo-S mission, for confirmation of potential detections and spectroscopic observations. The actual observing schedule is adaptable to real-time discoveries.

Starshade Description and Unique Advantages

A starshade flies in formation with a telescope and employs a precisely shaped screen, or external occulter, to block starlight, creating a high-contrast shadow that enables direct imaging of planets (**Figure ES-2**). Most designs feature a starshade tens of meters in diameter that is separated from the telescope by tens of thousands of kilometers.

The main strength of a starshade mission is that the starshade itself is nearly completely responsible for starlight suppression. Most significantly, the inner working angle (IWA; the closest angle on the sky at which a planet can be imaged) and the planet-star flux contrast achieved in the telescope image (the reduction in starlight at the planet location) are both independent of the telescope aperture size. This 'decoupling' of the IWA from telescope diameter enables detection of planets down to the size of Earths with a small and relatively simple space telescope.

The starshade mission challenge is the length of time needed to realign the starshade and telescope for each new target star, which can take several days to a couple of weeks. Nevertheless, multiple feasibility studies performed over the last several years demonstrate that a compelling search and characterization program is achievable.

A starshade offers many additional critical advantages including: unlimited outer working angle (OWA) for outer planet observing (field of view limited by detector size), broadband visible to near-infrared wavelength operation, and high throughput for efficient spectroscopy. Additionally, and most importantly, no special optical or wavefront control requirements are imposed on the telescope because the starshade itself performs the starlight suppression.

Mission Designs

The Exo-S STDT studied two viable and compelling starshade-telescope missions for exoplanet direct imaging, targeted to the $1B cost guideline and incorporating cost-driven specific design solutions for several mission aspects.

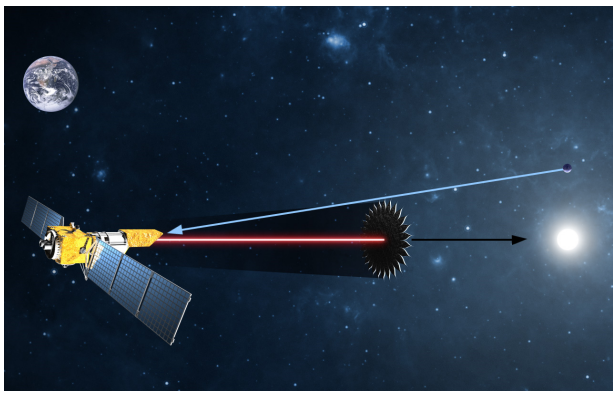

Figure ES-2. A starshade, also called an external occulter, is a precisely shaped screen that flies in formation with a telescope. The starshade blocks starlight to create a high-contrast shadow so that only planet light enters the telescope.

The first Exo-S mission concept is a starshade and telescope system dedicated to each other for the sole purpose of direct imaging for exoplanets (the 'Starshade Dedicated Mission' or 'Dedicated Mission'). The starshade and telescope co-launch, sharing the same launch vehicle, conserving cost. The telescope spacecraft provides the propulsion to retarget and control formation. The starshade is 30 m (16-m-diameter inner disk with 22 7-m petals [**Figure ES-3**]). The Dedicated Mission orbits in a heliocentric, Earth-leading, Earth drift-away orbit.

The Dedicated Mission's telescope, instrument, and spacecraft bus system are kept to low-cost units with extensive flight heritage. The telescope is a 1.1-m-diameter aperture commercially available telescope used for Earth imaging (NextView; with four currently operational), with the predominant modification being the addition of a lightweight sunshade. The telescope has a conventional instrument package that includes the planet camera, an integral field spectrometer (IFS), and a guide camera. The telescope spacecraft bus is based on the Kepler bus. The starshade spacecraft is a simplified version of the Wide-field Infrared Survey Explorer (WISE) bus.

The second Exo-S mission concept is a starshade that launches separately to rendezvous with an existing on orbit space telescope (the 'Starshade Rendezvous Mission' or 'Rendezvous Mission'). A rendezvous mission greatly augments the existing telescope's capability, reduces science down time as the starshade repositions, and lowers the cost and risk of the starshade direct imaging science. With these advantages in mind, the STDT elected to study the Rendezvous Mission.

The existing telescope adopted for the study is the WFIRST/AFTA (Wide-Field Infrared Survey Telescope / Astrophysics Focused Telescope Assets). The WFIRST/AFTA 2.4-m telescope is assumed to have previously launched to a halo orbit about the Earth-Sun L2 point, away from the gravity gradient of Earth orbit, which is unsuitable for formation flying of the starshade and telescope.

A telescope and its spacecraft are made starshade ready by adding or modifying hardware needed for formation flying (a guide camera to receive a laser beacon signal from the distant starshade and a radio transponder to measure inter-spacecraft range), and an appropriate broadband instrument for planet detection and spectral characterization. The impact on WFIRST/AFTA for starshade readiness is minimized; the existing coronagraph instrument performs as the starshade science instrument, formation guidance is handled by the existing coronagraph focal planes with minimal modification, and an added transponder.

For the Rendezvous Mission, the starshade is 34 m (20-m diameter inner disk and 28 7-m petals), and the starshade spacecraft performs the retarget and formation control maneuvers. The starshade spacecraft bus system is a simple single-string design based on the WISE bus.

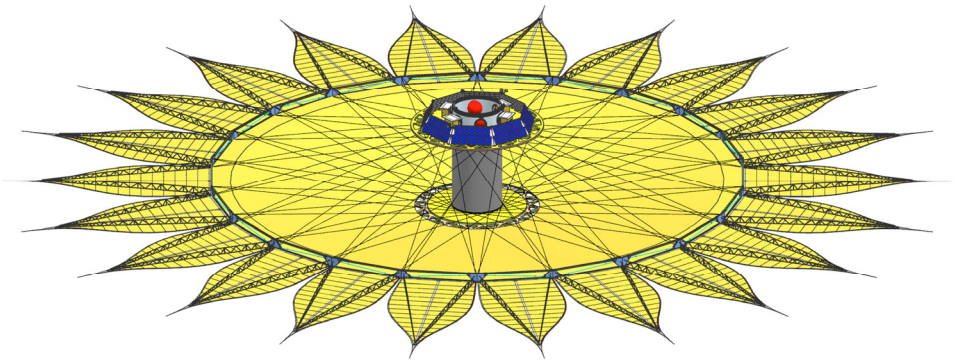

Figure ES-3. Fully deployed starshade configuration.

Both mission options use a low-cost, intermediate-class launch vehicle with a 5-m diameter payload fairing.

Out of the two mission options presented, the larger telescope offers an order of magnitude reduction or better in integration times relative to the baseline mission. This translates into an increase in the number of target stars observed and increases the number of small planets that can be characterized to the full desired level of R=70.

The starshade design, fabrication, deployment, and technology development are provided in this report. While the starshade has not flown before, extensive heritage exists from large deployable antennas**.** A perimeter truss has deployable antenna heritage and forms the starshade inner disk and controls deployed petal positions. The specific shape of the petals is found via an optimization process that creates the possible broadband shadow at the telescope aperture for a given starshade diameter and petal length.

Technology Development

Full-scale, ground-based end-to-end testing is not possible for the full starshade-telescope system; rather, it is replaced by a two-step process. First, subscale testing will demonstrate a dark shadow in broadband light in the lab and validate the optical model to the required levels of a few times 10^{-11} contrast. The dark hole formed by a full-size starshade at its distance of 25,000 to 50,000 km is described by exactly the same diffraction equations as a small-scale starshade in a laboratory facility. To date, laboratory testing of starshades several centimeters in diameter has validated optical propagation models by achieving starlight suppression in monochromatic light to a few parts in 10^{-10}, close to required flight levels.

Second, metrology tests of the full-scale flight starshade will verify that the starshade will have the correct shape on-orbit. A precision-manufactured petal prototype has demonstrated that a starshade petal can be manufactured to the required shape tolerances with flight-like materials. Deployment tests have shown that the petals can be deployed to the required position tolerances (**Figure ES-4**). The testing program gives high confidence that a properly constructed starshade will perform as predicted on-orbit.

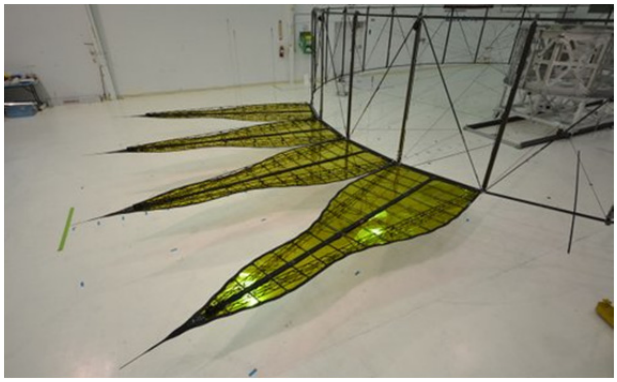

Figure ES-4. Deployment demonstration of a partial starshade prototype from 2013 at Northrop Grumman Corporation facilities.

Beyond optical model validation, precision deployment, and shape control, the remaining starshade engineering challenges (primarily related to long-distance formation flying and stray light control) are well understood and achievable (see Section 9 and Appendix C).

Summary

The starshade-telescope system probe-class mission offers a breakthrough opportunity for space-based exoplanet direct imaging: compelling science can be returned at the same time as the technological and scientific framework is developed for a larger flagship mission. The starshade can reach to the discovery of Earth-size planets in the habitable zones of nearby stars using a relatively small space telescope. This capability is due to the planet-star flux contrast and IWA being nearly independent from the telescope aperture size. The starshade is responsible for blocking the starlight, enabling a non-specialized space telescope. Starshade technology progress is on track for a new start in 2017.

1 INTRODUCTION

1.1 Scientific Introduction: Worlds Innumerable

Humanity stands on a great threshold of space exploration. On one side of this threshold is the knowledge that planets orbiting stars other than the Sun exist and are common. These worlds beyond our solar system are called exoplanets, and astronomers now understand that one or more planets orbit nearly every star in the Milky Way galaxy (Cassan et al. 2012). On the other side of this great threshold is the actual detection of these exoplanets: the robust identification of Earth-like exoplanets ('exo-Earths') with habitable conditions, possibly with signs of life inferred by the detection of 'biosignature gases' in their atmospheres. To cross this threshold of discovery, a space-based telescope with the capability for starlight suppression is needed. Such an observatory must be designed to block out the blinding light of the nearest stars and search for planets orbiting these stars.

The charter of the Exo-Starshade (Exo-S) Science and Technology Definition Team (STDT) is to demonstrate a viable starshade-telescope space mission concept targeted at $1B that has a compelling and impactful direct imaging exoplanet science program. The primary goal of the Exo-S starshade-telescope system is to discover new planets, from Earth size to giant planets. Exo-S will be capable of discovering rocky exoplanets in the habitable zones (HZs) of the most favorable target stars. A second major mission goal is to measure spectra of a subset of newly discovered planets, which will enable a first look at the composition, structure, and diversity of these worlds. A third mission goal is designed to guarantee outstanding science return: to characterize known giant planets, by measuring their spectra and masses. The known giant planets are detectable by virtue of extrapolated position in the 2024 timeframe. A fourth mission goal is to study and reveal how circumstellar dust is distributed in these systems, which will help in the understanding of dust-generating parent bodies (asteroids and comets), as well as possibly point to unseen planets below the mission's direct detection thresholds.

1.1.1 The Diversity and Ubiquity of Exoplanets

The planetary systems in our corner of the galaxy show astonishing diversity, providing astronomers with surprises at every turn. The first planet discoveries revealed many Jupiter-size planets orbiting very close to their stars, a surprising finding that led to substantial revisions in planet formation theory. These initial discoveries raised questions about whether planetary systems with architectures more like ours might be unusual. From a variety of observing techniques, it is now clear that planets exist at all masses, semi-major axes, and orbits—such that there will be a variety of interesting planets to discover in any parameter space (**Figure 1.1-1**). Furthermore, while each planetary system is certainly unique, there is still plenty of room for habitable worlds like our own.

Of most excitement to the public and exoplanet community is the NASA Kepler space telescope findings that small planets are extremely common in our galaxy (**Figure 1.1-1**). Kepler has specifically found that: planets 1.75 to 3 times the size of Earth are nearly 10 times more common than giant planets (Fressin et al. 2013 and Howard 2013; **Figure 1.1-2**); multiple planet systems somewhat reminiscent of our inner solar system are common (Lissauer et al. 2014; Rowe et al. 2014); and approximately 1 in 5 Sun-like stars may have an Earth-size planet in the star's habitable zone (Petigura et al. 2013).

While most of the Kepler results are for planets with orbital periods of 200 days or less, due to observational selection effects, a logical extrapolation is accepted as a solid inference: that small planets in our galaxy are common. Planets under a certain size (about 1.75 Earth

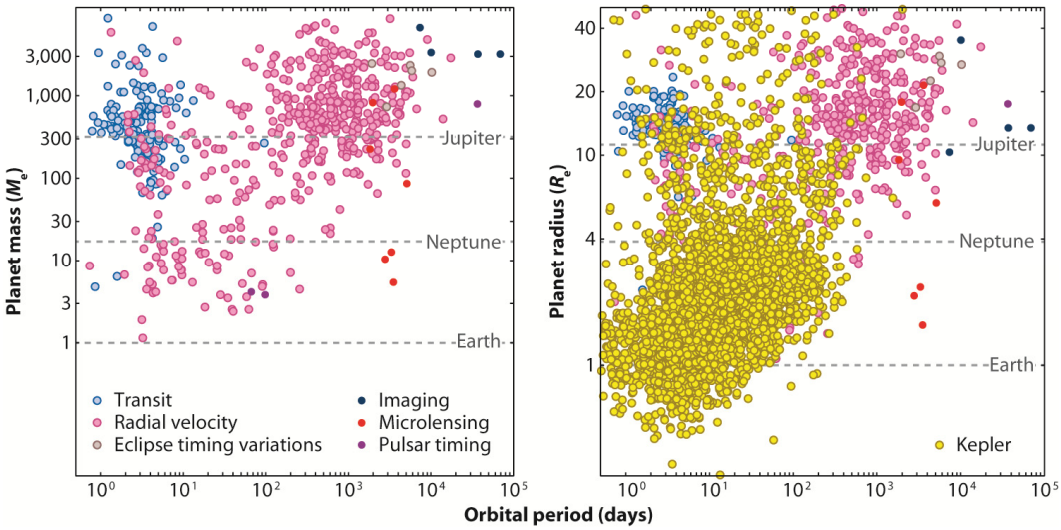

Figure 1.1-1. Exoplanet discovery space as of 2014. Color coded according to the planet discovery technique. Plotted as mass vs. orbital period (left) and not including Kepler discoveries. Plotted as radius vs. orbital period (right, and using a simplified mass-radius relationship to transform planet mass to radius) shows just how many exoplanets have been discovered, most by the Kepler Space Telescope. The paucity of planets of Earth's size or mass and orbit motivates an exo-Earth discovery mission. (Image from Batalha 2014.)

radii) are likely to be rocky (based on the densities of abundant materials in planetary systems). This commonality of small exoplanets strongly motivates a dedicated space mission capable of searching the nearest stars for rocky exoplanets.

The current harvest of small exoplanets includes a completely unexpected finding: the existence of planets with no solar system counterparts, the so-called 'super Earths' and 'sub-Neptunes' loosely defined as between about 1.75 to 3 Earth radii in size. The prevalence of planets in this size range is supported for a variety of orbital separations by the transit technique (Fressin et al. 2013 and Howard 2013), radial velocity (RV) surveys (Howard 2013), and microlensing studies (Sumi et al. 2010). Planets are referred to as sub-Neptunes (or sub-Neptune–size planets) if they have a thick 'gas envelope', and super Earths if they are predominantly rocky with thin atmospheres. The difference is a critical one—planets with gas envelopes will almost certainly be too hot at their surfaces to accommodate life.

Super Earths and sub-Neptunes are a boon for direct imaging searches like Exo-S. Super Earths, being larger than the Earth, are easier to detect than exact Earth twins—yet they still hold the promise of habitability to life if found in their circumstellar habitable zone. Sub-Neptunes, even larger in size than super Earths, will be even easier to detect, and the brightest will offer the potential for spectroscopic atmospheric characterization. Most sub-Neptunes found via transit searches have surprisingly low mean densities. These may be so-called 'water worlds' (with 50% or more water by mass with thick steam atmospheres), or massive rocky planets that have significant H or H/He envelopes, or smaller versions of Neptune that have a water or methane interior with significant H or H/He envelopes (see **Figure 2.2-7**, and Rogers and Seager 2010). By observing the light of the low-density sub-Neptune planets separately from the light of their stars, Exo-S will be able to offer a first glimpse into the true nature of these worlds.

The field of exoplanets has seen many other revolutionary discoveries in the last decade, all supporting the diversity of exoplanets and exoplanetary systems (Winn and Fabrycky 2015). Most of the findings are

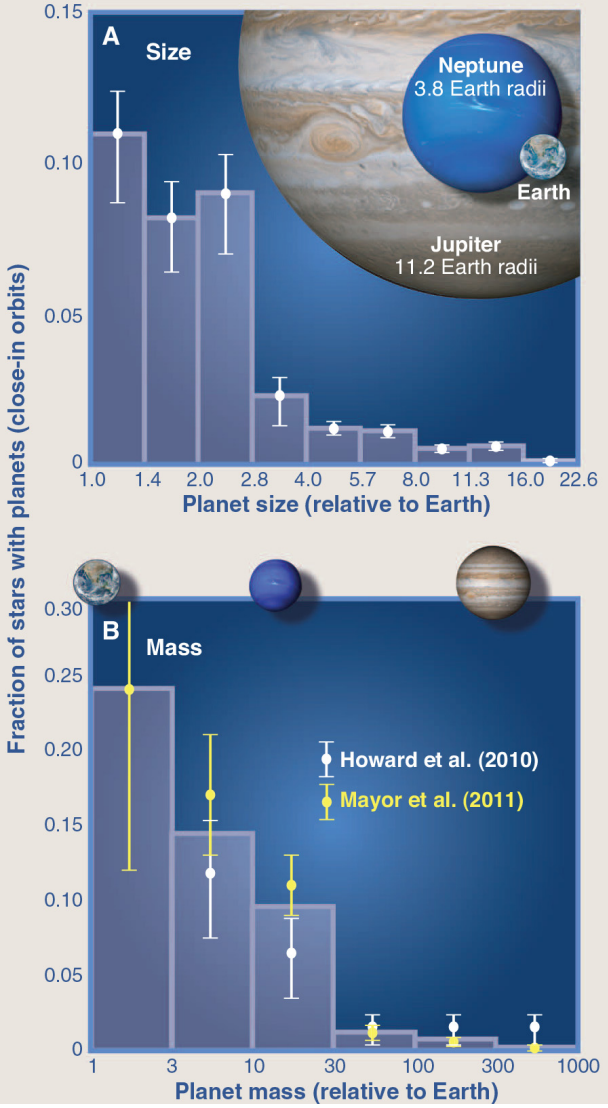

Figure 1.1-2. The (A) size and (B) mass distributions of planets orbiting close to G- and K-type stars.

The distributions rise substantially with decreasing size and mass, indicating that small planets are more common than large ones. Planets smaller than 2.8 R_E or less massive than 30 M_E are found within 0.25 AU of 30 to 50% of Sun-like stars. (A) The size distribution from transiting planets shows occurrence versus planet radius. (B) The minimum mass (M sin i) distributions show the fraction of stars having at least one planet with an orbital period shorter than 50 days (orbiting inside of ~0.25 AU). Both distributions are corrected for survey incompleteness for small/low-mass planets to show the true occurrence of planets in nature. (Image and caption from Howard 2013.)

related to uncovering new populations of exoplanets and defining their characteristics, for example: hot Jupiters (Seager and Deming 2010); hot super Earths (Batalha et al. 2011); circumbinary planets (Doyle et al. 2011); compact multiple planet systems (Lissauer et al. 2014); planets with a suggested high carbon-to-oxygen (C/O) ratio (dubbed 'carbon planets'; Madhusudhan et al. 2011); sub-Neptunes and super Earths (Howard et al. 2013), and others. The vast array of new findings supports the sentiment that the discovery space for exoplanets is large, and that a dedicated, direct imaging mission like Exo-S is the first step in entering this new realm of exoplanetary exploration.

1.1.2 Exoplanet Atmospheres

The diversity of exoplanets is expected to extend to planet atmospheres. Out of dozens of exoplanet atmosphere observations (Seager and Deming 2010; Madhusudhan et al. 2014), a handful of hot transiting exoplanets have detailed atmosphere measurements across a wide wavelength range. The example of the transiting hot sub-Neptune planet GJ 1214b, observed in transmission with space- and ground-based telescopes, is a good one (**Figure 1.1-3**). GJ 1214b is hypothesized to be dominated by clouds (Kreidberg et al. 2014, and references therein), which is unexpected because the atmosphere was previously thought to be too hot for water clouds but too cold for high-temperature condensate clouds thought to be possibly be present on hot Jupiters. The hot transiting planet spectra are enough to gather a glimpse at planets that are similar in size, mass, and parent star type, but have different atmospheres. On the other hand, a number of hot Jupiters observed via transmission spectroscopy at 2 µm do indeed show water vapor absorption (measured by the Hubble Space Telescope [HST] Wide Field Camera 3 [WFP3]; e.g., Deming et al. 2013 and Wakeford et al. 2013).

At present, only a subset of exoplanets are accessible to atmosphere observations. The majority are transiting planets, which can be observed in the combined light of the planet and star without need for spatial separation of the planet and star on the sky. Transiting planets require a fortuitous alignment, and an

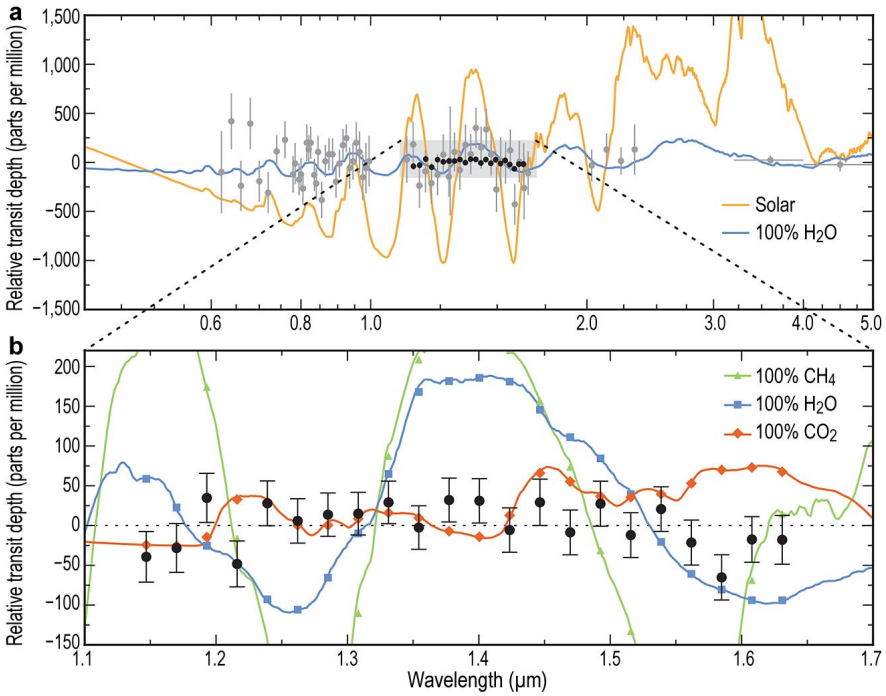

Figure 1.1-3. Transmission spectrum of the hot sub-Neptune exoplanet GJ 1214b. **a)** Measurements from the Wide Field Camera 3 (WFC3) instrument on the Hubble Space Telescope (black points) and other ground- and space-based telescopes (grey points), compared to theoretical models (lines). The colored points correspond to the models binned at the resolution of the observations. The error bars correspond to 1 σ uncertainties. Data rule out a cloud-free solar composition (orange line) and a high-mean-molecular-mass atmosphere (for example, 100% water, blue line). **b)** Detailed view of the GJ 1214b transmission spectrum (black points) compared to high-mean-molecular-mass models (lines). The data are inconsistent with cloud-free high-mean-molecular-mass scenarios. Data are consistent with a featureless spectrum. The featureless spectrum may be caused by high-altitude clouds in the GJ 1214b atmosphere. Figure from Kreidberg et al. 2014. For details and data sources (other than the HST/ACS points) see Kreidberg et al. 2014.

Earth analog around a nearby Sun-like star is unlikely to be transiting. A few planet atmospheres have been observed by a high spectral dispersion cross-correlation technique taking advantage of the planet's orbital motion and a known template of high spectral resolution molecular lines (Snellen et al. 2010); this technique is limited to short-period planets with a high Doppler shift in the planetary spectrum compared to the stellar spectrum. A third subset of planets with observed spectra is giant planets far from the star, via ground-based direct imaging in near-infrared wavelength bands. The most spectacular example of this is for the young star and nearly face-on planetary system, HR 8799 (**Figure 1.1-4**). This system contains four massive planets orbiting between 15–70 AU, and spectra of all four planets have been acquired in the near-infrared (Oppenheimer et al. 2013; Konopacky, Quinn, and Barman 2013). The HR 8799 example shows the power of direct imaging plus spectroscopy to reveal intriguing differences in the compositions of these planets despite their identical age, forming from the same initial materials, and very similar masses (5–7 M_J).

Planets akin to those in our solar system cannot have their atmospheres observed with current technology and techniques. Space-based direct imaging with Exo-S will open up atmospheres of many types of planets to be observed and studied by their reflected light spectrum. The Exo-S accessible planet atmospheres include some solar system analog planets, if they are discovered to exist around nearby stars (Section 2).

1.1.3 An Anticipated Diversity for Planet Habitability and Biosignature Gases

The variety of exoplanets in terms of orbits, masses, and possibly atmospheres, is now established. As a consequence, habitable planets may vary widely and be different from the Earth analog (see **Figure 1.1-5**, and Seager 2013 and references therein). The fundamental reason is that surface temperatures are governed by the atmospheric greenhouse properties and the range of atmospheric composition and mass is not predictable *a priori*. For example, it is possible a 10 Earth mass, 1.75 Earth radii planet with an H_2-dominated atmosphere could be habitable and host biosignature gases (Seager et al. 2013).

Most of the gases in the Earth's atmosphere that exist to the 100 parts per trillion level, with the exception of the noble gases, are produced by life, although most of them also exist due to photochemical or geological processes. Therefore, while oxygen

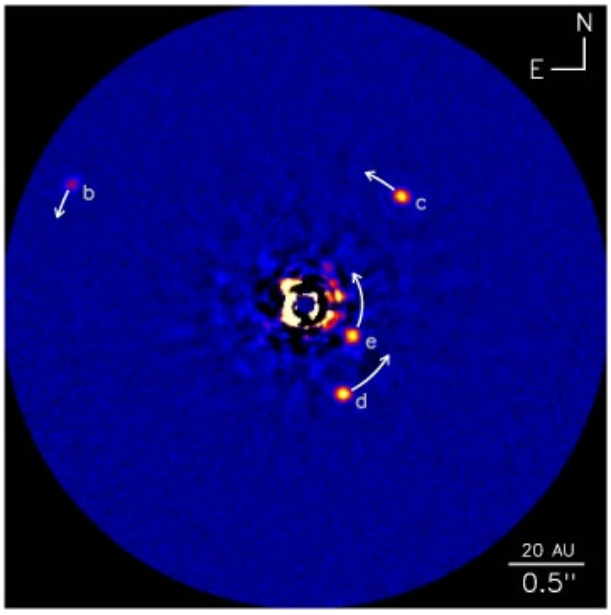

Figure 1.1-4. Direct imaging of young exoplanetary system HR 8799 b, c, d, and e, at infrared wavelengths. All four planets show spectral features hinting at a different balance of atmospheric constituents, including methane, acetylene, carbon dioxide, ammonia, and the possibility of iron and silicate clouds. Credit: W.M. Keck Observatory.

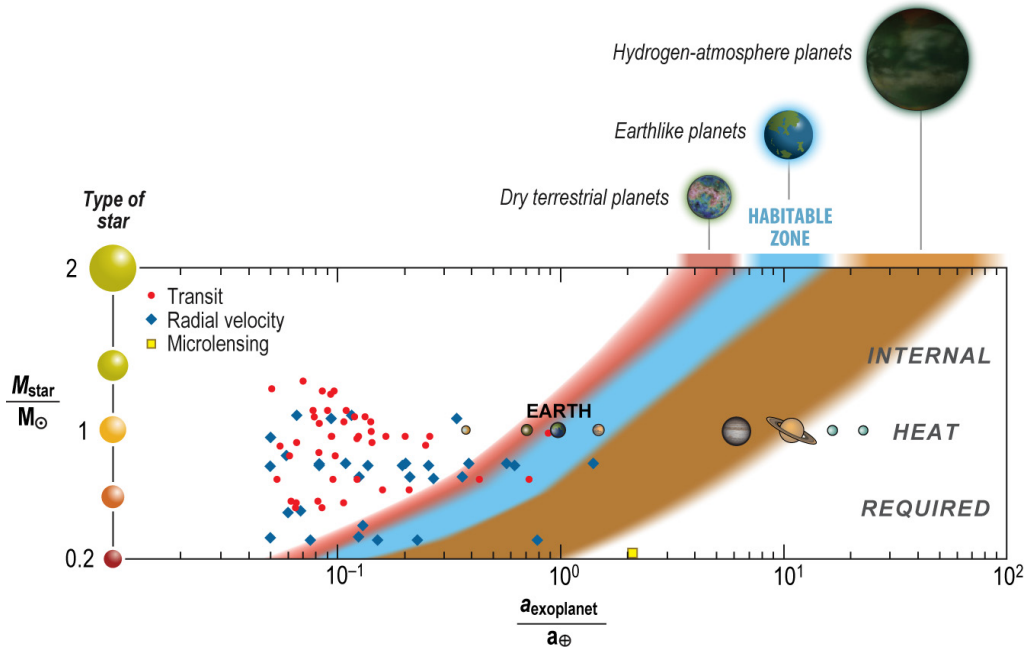

Figure 1.1-5. The extended habitable zone. The light blue region depicts the 'conventional' habitable zone for N_2-CO_2-H_2O atmospheres. The red region shows the habitable zone as extended inward for dry planets, as dry as 1% relative humidity. The outer brown region shows the outer extension of the habitable zone for hydrogen-rich atmospheres and can even extend out to free floating planets with no host star. The solar system planets are shown with images. Known super Earths (here planets with a mass or minimum mass less than 10 Earth masses) taken from Rein 2012. (From Seager 2013.) See Seager 2013 and references therein. For a discussion of the inner edge of the habitable zone, see Zsom et al. 2013 and references therein. For a discussion of the traditional habitable zone, see Kopparapu et al. 2013.

is touted as the most robust biosignature gas, the need for a broad spectral range is essential to detect unexpected gases (as compared to photochemical equilibrium planet atmosphere models) that may attribute to life. (For a review and further details see Seager and Bains [2015].)

While Exo-S will be capable of surveying at least 10 stars for Earth-size exoplanets, the opportunity that planets larger than Earth could be habitable or host life opens a promising avenue for discovery, since the difference between a planet of 1.75 and 1 Earth radii is significant from the standpoint of observational detection and characterization.

1.1.4 Why Space-Based Direct Imaging?

The space-based direct imaging search for Earths is a natural and essential next step in a continuing series of NASA exoplanet missions. Only space-based direct imaging can eventually find a large number of Earth-size planets orbiting Sun-like stars and identify them as Earth-like by spectroscopy.

Many other planet search activities that aim to reach down to habitable zone rocky planets are underway but nearly all are focused on M dwarf host stars. The high-contrast measurements required for rocky planets orbiting K dwarf through Sun-like and larger host stars can only be accomplished from space, above the blurring effects of Earth's atmosphere.

Transiting Planets

Earth-size planets transiting Sun-like stars are unsuitable for atmospheric characterization because the projected atmosphere annulus of such planets onto a Sun-like star area is likely too small to be measured by the transit transmission technique (Kaltenegger and Traub 2009). The numerous Earth-size planets transiting Sun-size stars discovered by NASA's pioneering Kepler Space Telescope were never intended for atmosphere follow-up (see Section 1.3 for future planned transit space discovery missions). Earth-size planets transiting nearby M dwarf star planets will be discovered by the all-sky NASA's Transiting Exoplanet Survey Satellite (TESS; launch 2017; Ricker et al. 2014) with a handful anticipated to be in the star habitable zone with atmospheric characterization enabled by the James Webb Space Telescope (JWST).

Non-Transiting, High Orbital Velocity (i.e., Short-Period) Planets

The large ground-based telescopes of the future may characterize the atmospheres of known small planets orbiting M dwarf stars (as discovered by RV surveys or even by transit surveys) by working with a high spectral dispersion cross-correlation technique taking advantage of the planet's orbital motion and a known template of high spectral resolution molecular lines. While this is limited for habitable zone planets to a handful of the brightest M dwarf stars and planets in short periods, one to a few Sun-like stars might be accessible (Snellen et al. 2013).

Direct Imaging from Ground-Based Telescopes (See Figure 1.3-1)

Habitable planets around bright nearby M dwarf stars can be directly imaged in reflected light at near-IR wavelengths with large ground-based telescopes (20–40-m diameter aperture) optimized for small IWA high contrast imaging. Owing to the small star size and the smaller orbital distance for habitable zones as compared to Sun-like stars, a rocky planet-to-M dwarf star reflected light contrast is 10^{-7} to 10^{-8} (already similar to capabilities of upcoming generation of Extreme-AO [adaptive optics] systems on existing 8-m aperture diameter ground-based telescopes.) While direct imaging of Earth analogs around Sun-like stars requires a detection contrast performance ($\sim 10^{-10}$) that cannot obtained from the ground, habitable planets around M dwarf stars are at $\sim 10^{-7}$ contrast in reflected light at near-IR wavelengths. The habitable zone for nearby M dwarf stars is angularly very small (<40 mas)

and in the near-IR requires a ~30-m diameter telescope. Optimistically, a couple of hundred M dwarf stars are suitable to be surveyed (Guyon and Martinache 2013).

1.1.5 Summary

The Exo-S mission of a starshade-telescope system will impact exoplanet science in a foundational way by finding and characterizing a set of exoplanets only accessible by space-based direct imaging. 'Comparative exoplanetology' by way of atmospheric spectroscopy enables comparison of the sample of hot Jupiters to their colder giant planet counterparts. Spectra of a number of sub-Neptunes have the potential to help us understand the nature of these enigmatic planets. If Earth analogs are common, the Exo-S mission has outstanding potential to detect planets of Earth size in the habitable zones of a couple of dozen nearby Sun-like stars.

1.2 Technical Introduction

1.2.1 Starshade Conceptual Introduction

A starshade (also called an external occulter) is a spacecraft with a carefully shaped screen flown in formation with a telescope (**Figure 1.2-1**). The starshade size and shape, and the starshade-telescope separation, are designed so that the starshade casts a very dark and highly controlled shadow, suppressing the light from the star while leaving the planet's reflected light unaffected. In this way, only the exoplanet light enters the telescope. Most designs feature a starshade tens of meters in diameter that is separated from the telescope by tens of thousands of kilometers.

One might expect, based only on geometric optics, the starshade to be only a bit larger than the diameter of the telescope aperture, circular in shape, and flying in formation close to the telescope. However, diffraction around a circular occulter results in a degraded shadow that is many orders of magnitude brighter than needed for exoplanet imaging. The degraded shadow could be mitigated by employing a much larger and more distant starshade, but the size and distance rapidly becomes prohibitive. Since the early 1960s, it has been known that a circular screen with a radial apodization at large starshade-telescope separations would create a sufficiently dark shadow with a reasonably sized starshade. While such a radial apodization is not manufacturable with sufficient accuracy, it can be approximated using a ring of petals, leading to the special shape of the starshade. Within the family of solutions for the starshade-telescope separation, and the starshade overall size, petal number and shape, the actual solution chosen and its implementation is ultimately driven by engineering design constraints.

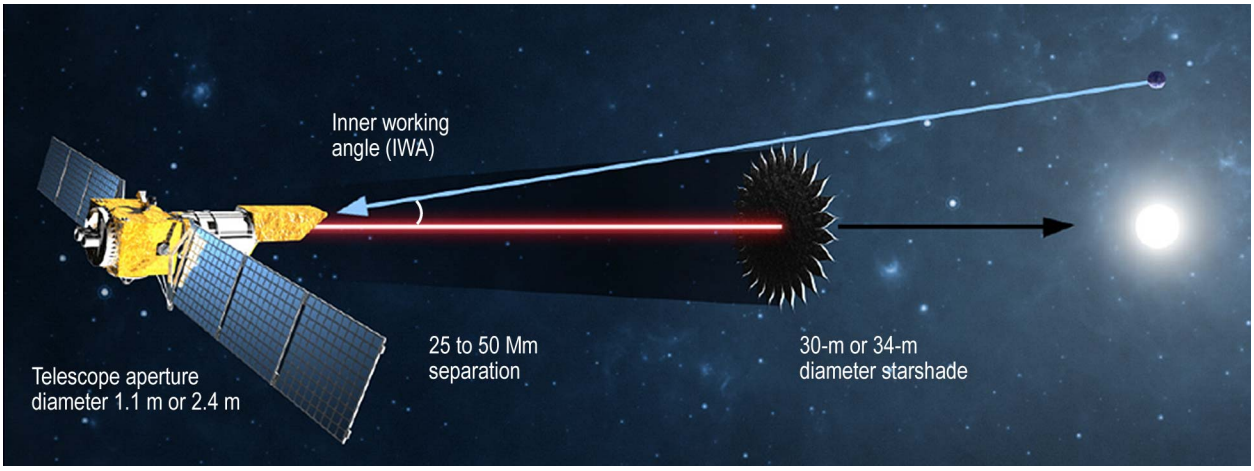

Figure 1.2-1. Schematic of the starshade-telescope system (not to scale). Starshade viewing geometry with IWA independent of telescope size.

1.2.2 History

The idea of using an (apodized) starshade to image planets was first proposed in 1962 by Lyman Spitzer at Princeton (Spitzer 1962). In this landmark paper (in which he also suggested that NASA build and fly what would later became the Hubble Space Telescope and the Chandra Observatory), he proposed that an external occulting disk could be used to block most of the starlight from reaching the telescope, thus enabling the direct imaging of planets around nearby stars. He realized that diffraction from a circular disk would be problematic for imaging an Earth-like planet due to an insufficient level of light suppression across the telescope's pupil. He posited that a different edge shape could be used instead, foreshadowing today's approach. In 1974, the idea was revived by G.R. Woodcock of the Goddard Space Flight Center using apodized starshades. In 1985, Marchal (1985) discussed the use of an opaque disk surrounded shaped petals, but while they were impractically large, they foreshadowed the modern design.

In 1995, the floodgates of exoplanet discovery were opened and interest in occulters grew. Several mission concepts were proposed using apodized starshades. Copi and Starkman in 2000 revisited the apodized starshade and found transmissive solutions defined by polynomials; their proposed mission was called the Big Occulting Steerable Satellite (BOSS). A few years later, Schultz et al. (2003) proposed a similar mission dubbed UMBRAS (Umbral Missions Blocking Radiating Astronomical Sources). However, these suggestions were hampered by the difficulty in manufacturing a transmissive surface within the tight tolerances necessary. In 2004, Simmons (2004 and 2005) again looked at using starshades based on shaped pupil designs and suggested that the star-shaped design (Vanderbei et al. 2003) was promising.

Then, in 2006, Cash (2006) showed that an occulter consisting of an opaque solid inner disk surrounded by petals forming an offset hypergaussian function, tip-to-tip about 60 m in diameter, created a broadband, deep shadow. With a small IWA and reasonable manufacturing tolerances, this design finally allowed for the possibility of an affordable solution.

Designs based on a solid inner disk and shaped petals form the basis of several variations in the apodization function. Vanderbei et al. (2007) developed a non-parametric, numerically generated approach to petal shape design. The resulting numerical designs allow for optimization considering engineering constraints such as petal tip and valley width, petal length, and overall diameter, while preserving desired science performance.

In 2008, two teams were selected under the Astrophysics Strategic Mission Concept Study (ASMCS) to study starshades. Cash et al. (2009) reported on the New Worlds Observer, while Kasdin et al. (2009) described THEIA. Both missions were proposed with a 4-m-diameter telescope coupled with a starshade to achieve the sensitivity required to characterize Earth-like planets in the habitable zones of their parent stars.

1.2.3 Starshade Strengths

There are several strengths that a starshade approach brings to exoplanet imaging and characterization. Most significantly, the IWA and the contrast achieved in the telescope image (the reduction in starlight at the planet location) are separated.

A starshade operates by suppressing the light from a parent star before it enters the telescope where it can scatter and hide the very faint planet. Suppression is defined as that fraction of the parent star's light that is allowed to enter the telescope.

Contrast is the amount of background signal in a single telescope resolution element expressed as a fraction of the central star's brightness. Contrast can be degraded by

scattered and diffracted unsuppressed starlight, exozodiacal light, local zodiacal light, and detector dark noise.

With a starshade, the starlight is almost entirely suppressed, and the IWA limit at which a planet is visible off the limb of the starshade depends only on the size and distance of the starshade. In principle, even a tiny telescope would be adequate for direct imaging of small exoplanets. In practice, the telescope aperture must be sufficiently large to provide adequate signal and low enough noise from the residual limitations on contrast.

Because the starlight never enters the telescope, there is no need for specialized optics to achieve high contrast (which typically reduce throughput), and a relatively simple space telescope is all that is needed. On-axis obstructions or mirror segments do not interfere with starlight cancellation and wavefront correction is not required (which frees the telescope from tight thermo-mechanical requirements).

An additional significant feature of the starshade-telescope system is the absence of an outer working angle (OWA). A 360° suppressed field of view (FOV) with angles from the star limited only by the detector size is obtained with each image. This is particularly useful for imaging debris disks or planets at large orbital separations, thereby studying planetary systems as a whole.

The starshade works over a broad bandpass. Numerically optimized designs balance the desired bandpass with other science drivers and engineering constraints. Hypergaussian designs have no lower limit to their bandpass.

The starshade-telescope system can detect Earth-size planets in the habitable zone of Sun-like stars even with a small telescope (on order of 1- to 2-m aperture diameter). This ambitious statement is allowed by the fact that nearly all of the starlight suppression is done by the starshade. As long as the tolerances for starshade petal precision manufacturing, deployment, and formation flying control are met (see **Table 1.2-1** and Section 6.4), the Exo-S mission will be capable of reaching the 10^{-10} contrast level needed to directly observe Earth analog exoplanets around Sun-like stars. An important related point supporting starshades with small telescopes is that wavefront correction is not required. If high-precision wavefront correction were required, the telescope collecting area would be a limiting factor on the starlight suppression, since wavefront sensing and control relies on collecting enough target starlight to sense the time-dependent optical imperfections that need to be corrected. In the wavefront correction case, small telescopes put Earth-Sun flux contrast levels out of reach.

The starshade's powerful capability for starlight suppression means the challenges of reaching the required IWA all lie with the starshade. The contrast, on the other hand, is limited by the convolution of the telescope response with the unsuppressed light, the internal telescope noise, and the sources of background from the sky. The challenges associated with producing a successful telescope-starshade system can be divided into 'programmatic challenges' and 'technical challenges'.

Table 1.2-1. Summary of technology status and plans.

Key Challenges	Driving Spec	Technology Status
Dynamic stability	Deformations < 15 ppm after 10 s	Verified by analysis with large margins
Thermal stability	Non-uniform deformations ≤ 10 ppm	Verified by analysis with large margins
Manufacturing tolerance	Petal width < 100 μm (4 mil)	Demonstrated per TDEM-09
Deployment tolerance	In-plane petal root position ≤ 0.5 mm	Demonstrated per TDEM-10
Edge-scattered sunlight	Edge radius curvature <1 μm	Demo in progress per TDEM-12
Laboratory contrast demo and model validation	10^{-10} contrast at flight Fresnel Number	Demo in progress per TDEM-12
Formation flying	Sensing for lateral control ±1 m	Requires technology demonstration

1.2.4 Programmatic Challenges

The starshade represents a new kind of system, one that has never been flow before, and therefore presents unique programmatic challenges. First, a full-scale, ground-based end-to-end system test for the starshade-telescope system is impossible because of the large size of the occulting screen (tens of meters), the large separation distances between the telescope and starshade (tens of thousands of kilometers), and the guidance, navigation, and control (GN&C) formation flying requirements. Subscale testing (see Section 6.3), together with computer performance modeling and simulations is the only alternative.

The second programmatic challenge is operational: for a given mission duration, the starshade has a limited number of retarget maneuvers (on the order of 30 per year) due to retarget times (from several days to a couple of weeks) and fuel constraints, meaning that only a limited number of stars can be observed over the mission duration. More than one starshade can lessen, but not remove, the problem of limited number of target stars. For a shared telescope, the retargeting time would be used for general astrophysics observations, allowing about 25% of telescope time for exoplanet direct imaging.

1.2.5 Technical Challenges

The major technical challenges must be considered in light of flight-proven technologies for analogous commercial large deployable antenna systems in addition to highly successful starshade-specific NASA-funded technology demonstrations over the last years. This subsection provides a brief overview of the starshade mission's technical challenges; concept technology readiness is detailed in Section 9.

Key technology challenges, once considered tall-pole issues, but now considered demonstrated are: precision petal manufacturing, precision deployed positioning, and on-orbit stability.

Petals must be precisely manufactured to the specified petal width profile, or optical apodization function (with tolerance ≤ 100 µm). This capability was successfully demonstrated by a Technology Development for Exoplanet Missions (TDEM) activity (see **Figure 1.2-2**).

Petals must be precisely deployed to the specified petal root positions, as controlled by the perimeter truss (in-plane root positions ≤ 500–750 µm). This capability was successfully demonstrated by a TDEM activity (see **Figure 1.2-3**).

Petal width profiles must be precisely maintained on-orbit (non-uniform thermal deformations ≤ 10 ppm). This capability was successfully demonstrated by analysis. Predicted deformations are a small fraction of allocations. Dynamic deformations are also allocated and successfully demonstrated by analysis with large margins, aided by the structural attenuation and damping provided by

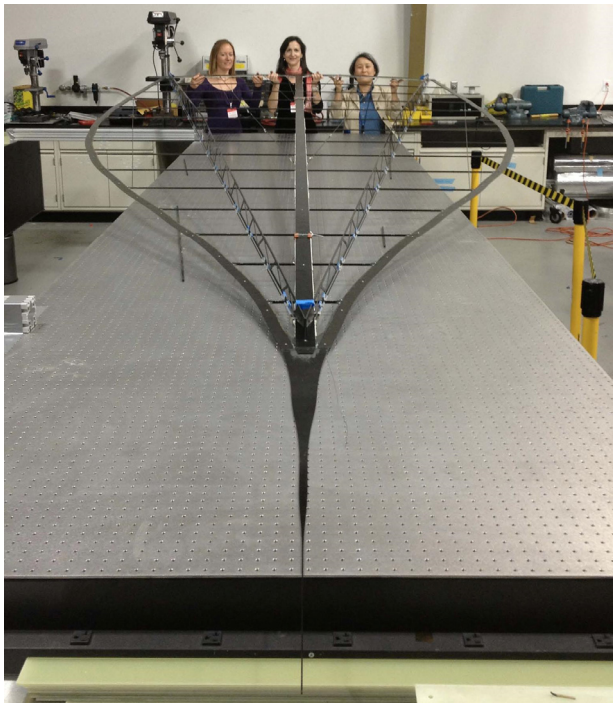

Figure 1.2-2. Flight-like petal. Petal shown in picture is an early prototype used for manufacturing tolerance verification tests.

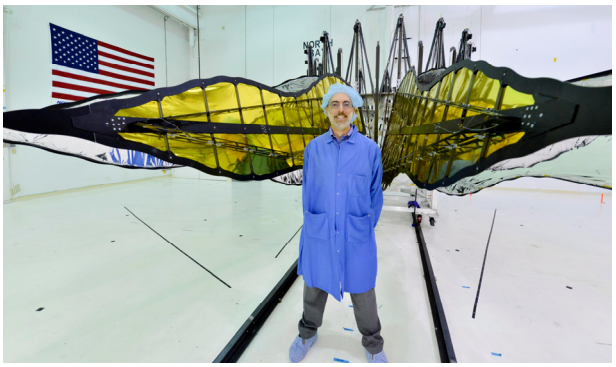

Figure 1.2-3. Starshade stowage and deployment test with four petals and a 1st generation starshade truss. JPL/Princeton/NGC.

the starshade. Dynamic deformations are allocated after some transient period during which larger deformations are acceptable because they are not sensed by the instrument.

Key starshade technology challenges, currently considered tall-pole issues and in work are: optical model validation by subscale contrast performance demonstration, control of edge-scattered sunlight, and development of the starshade optical shield (OS) blanketing system (see Appendix B for OS details). Activities are funded to address these issues prior to 2017.

Formation flying at distances of tens of thousands of kilometers is an issue that has not been previously demonstrated. Formation flying is needed to keep the telescope positioned within the dark shadow created by the starshade to a lateral tolerance of ±1 m. Additionally, the separation distance must be kept within ±250 km for effectiveness of the optical bandpass. Mitigating the driving lateral control challenge are the low disturbance environments of heliocentric Earth-leading, Earth drift-away or L2 orbits. As a result, the formation flying challenge is primarily sensing the relative lateral position of the starshade. The Exo-S mission accomplishes this sensing with a fine guidance camera (FGC) operating with the telescope. Activities to demonstrate sensing and control algorithms and hardware have been recently selected as part of the 2013 NASA ROSES TDEM program.

1.2.6 The Range of Starshade Mission Concepts

The starshade mission concept has a vast range of options. A starshade can be co-launched with a telescope or launched separately for a rendezvous with an existing starshade-ready telescope. A starshade-ready telescope is one that has hardware needed for formation flying (a guide camera to receive a laser beacon signal from the distant starshade and a radio transponder to measure interspacecraft range), and an appropriate broadband instrument for planet detection and spectral characterization. The starshade spacecraft or the telescope spacecraft can be charged with moving to retarget on the next target star. The telescope could be dedicated to work only with the starshade, or the telescope could be shared with a space telescope for general astrophysics.

The starshade and telescope orbit must be away from the high gravity of Earth orbit for long-distance formation flying control. A co-launched starshade and telescope could go to a heliocentric drift-away orbit—either Earth-trailing (e.g., Spitzer, Kepler) or Earth-leading —or the Earth-Sun L2 orbit. A starshade that launches independently for later rendezvous with an existing telescope would have to go to the Earth-Sun L2 orbit. A concept of two or more starshades to work with a single telescope would also be viable and would enable more efficient use of the telescope as one starshade could be used for observations while the other is repositioned to the next observational target (Koleman and Kasdin 2007).

A range of starshade sizes have been discussed from a small starshade on order of 30 m in diameter that would work with a 1.1-m-diameter aperture telescope, through a 70-m starshade that would have gone with the JWST (Soummer et al. 2010), all the way up to a >100-m-diameter starshade that would be paired with a future 10- to 16-m class telescope (Postman et al. 2012; Seager et al., in prep).

Given the cost and schedule constraints of the Exo-S STDT study, only two of the possible mission concepts were studied. Both have starshade sizes with perimeter truss deployment systems that have heritage from large radio communication high-gain antenna systems.

1.2.7 Summary

Starshade technology development has approached a point where successful technology demonstrations and well-defined technology gaps enable a clear path forward with manageable risk (see Appendix C, Technology Plan). An appropriate funding effort for the remaining engineering challenges will enable achievement of technology readiness goals. For more details on the technology gap list and technology development plans, see Section 9 and Appendix C.

1.3 State of the Field at the Time of Probe Launch: The Exoplanet Science Landscape in 2024

Planetary systems consist of a range of planets from giant planets through sub-Neptune–size planets through rocky terrestrial planets and even down to Moon-size planets, and belts of small bodies that generate debris particles. Ongoing research, upcoming developments in ground-based instrumentation, and the launch of new space missions will continue to advance knowledge of exoplanetary system components in the coming decade. Nevertheless, a probe-scale exoplanet direct imaging mission can offer unique capabilities. This subsection sets the likely context for exoplanet science at the time Exo-S would launch.

1.3.1 Indirect Detections Using Stellar Reflex Motion

Radial velocity surveys have detected 583 planets as of late 2014 (http://exoplanets.eu); the median orbital period of these detections is around 1 year. While the median semi-amplitude of these detections is 38 m/sec (http://exoplanets.org; larger than the solar reflex velocity induced by Jupiter), only a dozen planets have measured RV semi-amplitude below 2 m/sec. The best claimed detection to date has a 0.5 m/sec semi-amplitude for the very bright star alpha Centauri B. Today's measurement precision of 50 cm/sec is expected to improve toward 10 cm/sec with the Very Large Telescope (VLT)/ Echelle SPectrograph for Rocky Exoplanet and Stable Spectroscopic Observations (ESPRESSO) and similar instruments on extremely large telescopes (European Extremely Large Telescope [E-ELT], Giant Magellan Telescope [GMT], Thirty Meter Telescope [TMT]). However, stellar RV jitter arising from spots and activity sets a natural noise floor near 2 m/sec (Bastien et al. 2014). Only in the quietest stars—or through careful averaging, filtering, and detrending of the data—will RV detections be achieved for semi-amplitudes below 1 m/sec. Such detections will also be limited to stellar types F8 or later because earlier types lack a sufficient density of narrow absorption features. RV surveys to date have detected most of the Jupiter-mass planets within a few AU of late-type stars, but generally lack sensitivity to Neptune-mass planets outside a few tenths of an AU (Howard and Fulton 2015). A new dedicated RV program with 50 cm/sec precision and focused on direct imaging targets could, by 2024, extend this sensitivity to planets of Saturn-mass and greater with periods up to 20 years, and to 8 $M_{\oplus}$ super-Earths with periods of several years. Complementary measurements of stellar astrometric wobble by the European Space Agency (ESA) Gaia all-sky survey will detect and measure orbit inclinations for planets of Jupiter mass or larger and periods <5 years around unsaturated nearby stars (V>6), and could potentially be extended to stars as bright as V=3 with pipeline software improvements (Martin-Fleitas et al. 2014). The orbital elements for the inner giant planets of nearby late-type stars should be well in-hand by 2024.

1.3.2 Transits

Transit observations with the Kepler (and COnvection ROtation et Transits (CoRoT)) space telescopes have revealed the frequency and radius distribution of short-period (P<1 yr) exoplanets by photometrically monitoring selected fields of solar-type stars. The 2017 TESS mission will identify shorter-period (P ~< several weeks) planets around several hundred thousand bright field stars distributed around the sky. Around M stars, TESS detections will extend down to 1 $R_\oplus$ in the habitable zone. RV follow-up of TESS detections will reveal their mass distribution and the planetary mass-radius relationship. Spectroscopic measurements made during transit and secondary eclipse by the JWST, ELTs, and other facilities will constrain the temperatures and albedos of these planets, and for clear, low-molecular weight atmospheres may detect high-opacity atmospheric species such as Na I, H_2O, and CH_4. The PLATO (PLAnetary Transits and Oscillations of stars) mission will launch in 2024 and identify a new sample of transiting planets. By 2024, transit work should have built a strong statistical picture of the bulk properties of inner planetary systems and collected atmospheric spectral information for many of their larger objects.

Although not limited to transits, there is an exoplanet atmosphere characterization technique worth mentioning: high resolution (R > 100,000) spectroscopic cross-correlation template matching for exoplanets orbiting fast enough so that their atmospheres are Doppler-shifted with respect to the star. This technique robustly identified CO and H_2O on exoplanets, including non-transiting ones (Snellen et al. 2010). This technique may be used with the large 20–40 m ground-based telescopes of the future to characterize the atmospheres of known small planets in the habitable zone of late M dwarf stars (as discovered by radial velocity surveys or even by transit surveys), though the number of favorable M dwarf target stars may be limited (Snellen et al. 2013).

1.3.3 Exoplanet Imaging Detections

Only a handful of exoplanets have been imaged directly in their near-infrared thermal emission (e.g., Marois et al. 2010; http://exoplanets.eu). This is due to the limited contrast capabilities of current instrumentation (Lawson 2013, Figure 1), especially at small angular separations from a star. A new generation of high-contrast imagers based on extreme adaptive optics systems is now being deployed behind large ground-based telescopes. Dozens of exoplanet imaging detections at 10^{-7} contrast and ~0.5″ separation should be achieved by these systems in the near-infrared (Gemini Planet Imager [GPI], VLT Spectro-Polarimetric High-contrast Exoplanet Research [SPHERE], Subaru Coronagraphic Extreme Adaptive Optics [SCExAO]), which would enable detection and spectroscopy of thermal emission from warm (T>500 K; very young or massive) gas giant planets. An appropriately designed extremely large telescope (ELT) in the 30-m class would be capable of such detections at even smaller inner working angles ~0.12″, but with only modestly better contrast. However, the extreme adaptive optical systems needed for such observations are not currently baselined for ELT first-generation instruments, and thus are not expected to be on-sky until the late 2020s.

Ground-based, high-contrast imaging is limited by rapid wavefront changes arising from atmospheric turbulence. For a solar twin at 10 pc distance (H mag 3), a deformable mirror sized to create a ~0.5″ radius dark field cannot suppress the residual speckles to levels fainter than 10^{-7} of the central star brightness. This limit is defined by the available photons per subaperture in a reduced coherence time (Oppenheimer and Hinkley 2009, Table 2) and is nearly independent of telescope aperture size. To detect fainter objects, speckle averaging and subtraction methods must be employed. It is unclear how well this could be done, as the temporal behavior of residual atmospheric speckles at 10^{-7} contrast has never been characterized. Experience at less

challenging contrast levels suggests that detections a factor of 10 below the raw contrast floor should be achievable. 10^{-8} contrast would enable detections of thermal emission from nine massive giant planets around nearby solar-type stars (Stapelfeldt 2006). It has been suggested that ELTs could detect planets in reflected light as small as 1 $R_{\oplus}$ at this contrast level, if they are present in the habitable zones of bright nearby M dwarfs (Guyon and Martinache 2013). Optimistically, up to 200 target stars are available, however, the required stellar properties (V<8 for sufficient guidestar photons, d<22 pc to resolve the habitable zone with an ELT) may limit the number of target stars.

JWST/Near Infrared Camera (NIRCam) coronagraphy should be capable of detecting companions at contrasts of 10^{-6} at separations beyond 1.5 arcsec, capturing objects like our own Jupiter in 4.5 μm thermal emission if they are orbiting the nearest M stars. The uncertain luminosity evolution of young giant planets clouds the picture somewhat (Marley et al. 2007), but it appears that the some of the more massive planets orbiting nearby (d<20 pc), young (age<1 Gyr), low-mass (M<1.0 Msun) stars could be in view by 2024.

1.3.4 Disk Imaging

Imaging of protoplanetary disks is being revolutionized by the Atacama Large Millimeter/submillimeter Array (ALMA), which will be able to resolve dynamical structures driven by protoplanets at angular resolutions approaching 0.01 arcsec. Protoplanetary disks in the nearest star-forming regions (d~150 pc) are ideal ALMA targets, as their high optical depths give them high surface brightness in the submillimeter continuum. Debris disks are found around older main-sequence stars, with many nearby (d~25 pc) examples. They are optically thin with a much lower dust content and much fainter submillimeter continuum emission; it will therefore be a challenge even for ALMA to resolve their detailed structure. ALMA will map a limited number of the brightest debris disks (Ld/Lstar>10^{-4}) at 0.1 arcsec resolution. In addition to their exoplanet imaging capability, new adaptive optics coronagraphs now being deployed to large ground telescopes should image bright debris disks with comparable resolution and with sensitivity a few times better than ALMA but in the near-infrared (Perrin et al. 2015). Similar instruments on ELTs would extend the resolution and IWAs of such studies to 10 and 30 milliarcsec, respectively. With its 0.3 arcsec resolution at 20 μm, JWST will resolve warm dust emission around a sample of nearby A stars. New warm disks identified by the Wide-field Infrared Survey Explorer (WISE) mission will be particularly important targets. A wealth of new data detailing the internal structure of bright circumstellar disks will have emerged by 2024, seeding a new theoretical understanding of disk structure, dynamics, and evolution.

1.3.5 Summary

While the advances described above will be remarkable scientific milestones, they fall well short of the goal of obtaining images and spectra of planetary systems like our own, as shown in **Figure 1.3-1**. The TESS mission will detect inner terrestrial planets transiting nearby cool stars, but their spectroscopic characterization will be restricted to red dwarf stellar hosts and will be challenging even using JWST. High-contrast imaging will detect and characterize warm giant planets, but not cool objects at 10^{-9} contrast, like our own Jupiter and Saturn in their orbits around a solar-type star. Sharp images of dusty debris disks will be obtained, but only those with optical depths several hundred times that of our own asteroid and Kuiper belts. RV and astrometric surveys will have identified the majority of nearby stars hosting giant planets. What is currently missing from the 2024 exoplanetary science toolbox are space observatories that can study photons from cool planets (ranging from giants down to super Earths) and resolve tenuous dust disks around nearby Sun-like stars.

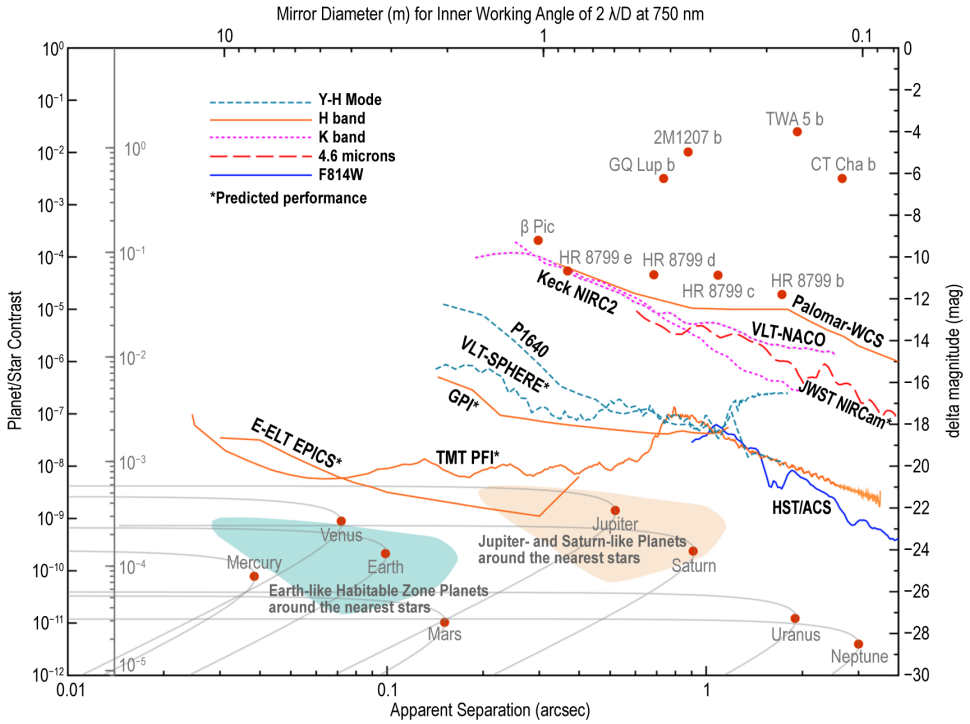

Figure 1.3-1. Direct imaging contrast capabilities of current and future instrumentation. (From Lawson 2013.)

2 SCIENCE GOALS AND OBJECTIVES

2.1 Science Goals

Exo-S mission science goals:

1. *Discover new exoplanets from Earth size to giant planets*
2. *Measure spectra of a subset of newly discovered planets*
3. *Measure spectra and masses of currently known giant planets*
4. *Study planetary systems including circumstellar dust*

The Exo-S mission has four science goals. The first goal is *to discover new planets from Earth size to giant planets*. Within this goal is the possibility of discovering Earth-size exoplanets in the habitable zones (HZ) of at least 10 Sun-like stars—arguably one of the most exciting pursuits in exoplanet research.

The second science goal is *to measure spectra of a subset of newly discovered planets*. The Exo-S spectral range is from 400–1,000 nm, with a spectral resolution of up to R=70, which enables detection of key spectral features. Of particular interest are the so-called sub-Neptunes, planets with no solar system counterparts, loosely defined as 1.75 to 3 times the size of Earth. The sub-Neptune planets have very low densities compared to Earth, yet their actual composition is not known.

The third science goal is designed to guarantee outstanding science return: *to characterize known giant planets, by observing their spectra and measuring or constraining planet mass.* The known giant planets are detectable by virtue of extrapolated position in the 2024 timeframe. Molecular composition and the presence/absence of clouds or hazes will yield information on the diversity of giant planet atmospheres.

The fourth science goal is *to characterize planetary systems, with a specific interest in studying circumstellar dust in the context of known planets*. Observations will shed light on the dust-generating parent bodies (asteroids and comets), and the dynamical history of the system, as well as possibly point to unseen planets below the mission's direct detection thresholds. An assessment of dust levels in the habitable zones of nearby stars is a major unknown affecting mission planning for future flagship mission concepts.

The science yield, in terms of how many planets are discovered and to what spectral resolution small planet atmospheres can be characterized depends both on the observing strategy (how the finite number of starshade retargets are allocated) and the telescope aperture.

2.2 The Imaged Planetary System

To illustrate what data from the Exo-S will look like, a simulated image for the Rendezvous Mission is presented in **Figure 2.2-1**. The image shows a hypothetical planetary system around the nearby (8.44 pc) G0 V star Beta Canum Venaticorum if it contained all eight solar system planets, a cloud of warm dust comparable to the solar zodiacal cloud (1 zodi) and a dust ring from a Kuiper belt located 15 AU from the star. The center of the image is blocked by the starshade.

The brightness of the giant planet Jupiter analog (just to the right of image center) vivifies Exo-S's science goal of characterizing known giant planets; this planet creates the brightest pixel in the image by far.

The Saturn analog (the bright point left of image center) and the terrestrial planet analogs Earth and Venus illustrate the Exo-S mission's capability to discover new planets. The Earth and Venus analogs appear as colored peaks (left and right respectively) on top of the exozodiacal dust.

The exozodiacal dust cloud is the bright ring at the image center. Exozodiacal dust is a challenge for all planet-imaging missions. Although the peak of the exozodiacal signal in this scene is comparable to the brightness of the Venus spot, the image of Earth is about twice as bright as the exozodiacal light background

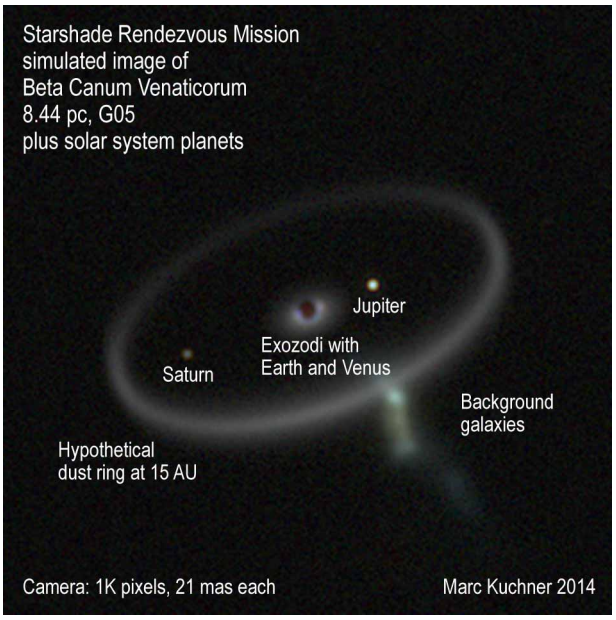

Figure 2.2-1. Simulated image of the Rendezvous Mission's observation of a solar-system–like planetary system orbiting a nearby Sun-like star. The image is a composite of three bands (510, 658, 825 nm), square-root scaled and mapped to blue, green, and red to create a false-color image. The planets in this simulation are all placed at quadrature, with albedos (and colors) taken from Traub (2003) and adopting a Lambertian scattering phase function. The simulation includes photon noise, read noise of 2.8 e-/pixel and dark current of 5.5e-4 e-/pix/sec, assumes a total throughput of 20% and a 2000 second read cadence. For reference, with these assumptions, the Venus twin in this system is detected at a signal to noise ratio of about 12. The model for background galaxies was generated with the Illustris cosmological simulation (Vogelsberger et al. 2014) converted to mock images using stellar population synthesis models (Torrey et al. 2014). (Courtesy of Gregory Snyder at the Space Telescope Science Institute).

in that pixel. Vivid images of a complete dust ring made by the starshade will help constrain the scattering phase function of the dust, which in turn should enable some level of subtraction of the dust signal from the planet light.

Exo-S will observe different components of planetary systems as illustrated by the hypothetical Kuiper belt dust ring at 15 AU from the star. Exo-S will likely discover and make spectacular images of such cold dust rings around some of the target stars. The dust ring in the image is brighter than the Kuiper belt but fainter than prior survey limits (Hillenbrand et al. 2008).

Exo-S will see background objects that are superimposed on the planetary system, as illustrated by the green background galaxies (lower right of the image). With an assumed integration time of 1 day, the sensitivity of this model scene is roughly comparable to that of the original Hubble Deep Field, which contained roughly one galaxy in every 6 square arcseconds, meaning about six galaxies would appear in the Exo-S field of view.

2.3 Exploring the Exoplanet Zoo

An overview for the expected science return for individual planets for different types of observational targets is presented in this section. The planetary systems accessible to Exo-S can be divided into three types: systems in which giant planets are already known to exist; systems in which Earth-size planets in the habitable zone are detectable by Exo-S; and systems in which planets larger than Earth (i.e., super Earths, sub-Neptunes, and other new types of planets not seen in the solar system) are detectable. The exoplanet zoo extends to planets around stars other than Sun-like, which includes different stellar radiation environments at the planet.

Measured spectra of exoplanet atmospheres are at the heart of the Exo-S mission's planetary characterization. From spectra, key molecular constituents in exoplanetary atmospheres may be identified, a fundamental planetary property. From the atmospheric composition, information on the bulk composition of the planet's interior may be inferred, in some cases constraining planet formation and evolution processes. Exo-S will greatly advance the field of exoplanet characterization by accessing many types of planets in the planetary zoo for the first time.

The Exo-S mission has spectral capabilities in the range of 400–1000 nm, in three separate bands. The bands are blue, green, and red, and the actual wavelength ranges for each color are shown in **Table 2.3-1**. The starshade covers the full spectral range in three separate

Table 2.3-1. Starshade parameters.

Mission	Dedicated			Rendezvous		
Starshade Parameters	**IWA**	**km**	**Band (nm)**	**IWA**	**km**	**Band (nm)**
Blue Band	80	38675	400–647	71	49500	425–602
Green Band	102	30330	510–825	100	35065	600–850
Red Band	124	25025	618–1000	118	29805	706–1000

bandpasses. To preserve the optical performance in each bandpass, the starshade must move towards or away from the telescope (the separation distance increases in inverse proportion to wavelength to preserve the same optical performance). The IWA, which is the angular size of the starshade radius as seen by the telescope, also changes accordingly. The bandpasses and starshade-telescope separations and IWAs are captured in **Table 2.3-1**.

A comparison of spectra (observed or modeled) of Earth, other solar system planets, and exoplanets is presented in **Figure 2.3-1**. The comparison highlights the Exo-S science return for each type of target system as well as illustrates the anticipated quality and resolution of exoplanet spectra.

2.3.1 Known Giant Planet Masses and Atmospheres

Giant planets known to exist from ground-based radial velocity (RV) surveys are a priority for Exo-S as a category of planets for guaranteed science return. Based on their size and hence brightness, Exo-S can obtain relatively high-resolution spectra (R=70, SNR=10). The list of currently known giant

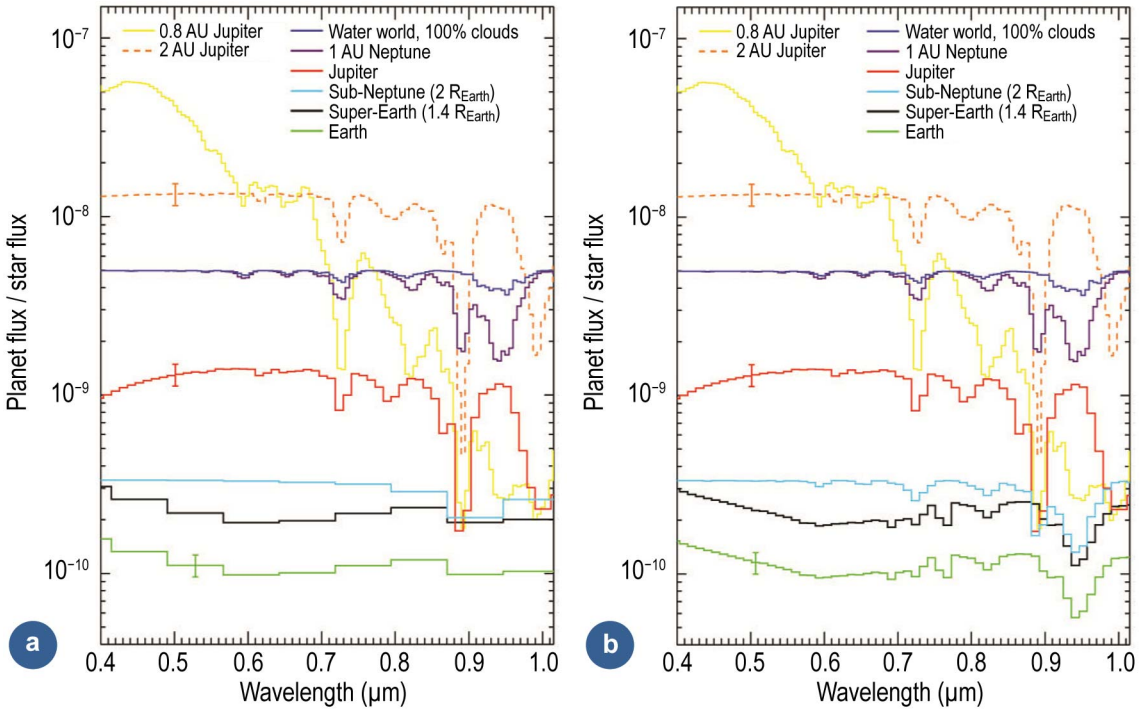

Figure 2.3-1. Differences and similarities in brightness and spectral features for a variety of exoplanet types. Optical reflectance spectra of a diverse suite of exoplanets are shown without added noise. The Jupiter spectrum is based on the observed spectrum in Karkoschka (1994). The other two Jovian planet spectra are models from Cahoy et al. (2010). The Neptunian and water world spectra are models from Renyu Hu (personal communication). The Earth spectrum is a model developed to match Earth observations from the EPOXI mission (Robinson et at. 2011), while the super Earth is that model scaled by $(1.5\ R_\oplus/1\ R_\oplus)^2$. Figure 2.3-1a is for the 1.1-m Dedicated Mission and Figure 2.31b for the 2.4-m Rendezvous Mission. These plots roughly represent the best spectra possible with each mission. In both cases, there are 2 pixels per resolution element (Nyquist sampling). For the Rendezvous Mission plot, all spectra were convolved to a spectral resolution of 70. The fainter planets cannot be observed to this high a resolution with the Dedicated Mission, so the Earth, super Earth, and sub-Neptune spectra were convolved to R=10. Three representative flux error bars are placed at 0.5 μm. The errors are the noise per pixel for spectra with SNR=10 per resolution element. Image credit: A. Roberge.

planets that Exo-S could observe is shown in **Table 2.3-2**.

Prior to launch of Exo-S, most of the orbital properties of the known giant planets will have been determined from RV measurements, with the exception of orbital inclination. A photometric measurement of the known giant planet by Exo-S at the right time would collapse the remaining uncertainty on the planetary orbit, enabling all orbital elements to be known. The planet orbit inclination will enable the upper limit on planetary mass to be converted into a true mass (albeit with measurement uncertainties).

Planet mass is a fundamental property of a planet because it is connected to a planet's internal and atmospheric structure and it affects basic planetary processes such as the cooling of a planet, its plate tectonics, magnetic field generation, outgassing, and atmospheric escape. Therefore, combined with the amount of energy received by the planet at the top of its atmosphere from the host star, a mass measurement and model atmosphere calculations will be well-suited to bring a significant increase in an understanding of a known giant planet. Note that Gaia will measure orbital inclinations for planets with masses larger than Jupiter's mass and with orbital periods less than one year (Section 1.3).

The first image of the planet will not only yield a planet mass determination but also an apparent brightness and separation from the star. The apparent brightness can be converted into a true brightness considering the planet's illumination phase as derived from the orbital information.

The planet radius is also a fundamental planetary property and while it is conceivable to infer a planet size from the planet's true brightness, it is not possible because of the unknown planet albedo. Both planet size and albedo contribute to the planet's true brightness. A few approaches to constrain the planet radius are possible. First, mass-radius relationships of known planets could be used to infer a probability distribution of radii given the known planetary mass. Second, models of the planet might be capable of placing constraints on the planet albedo thereby constraining planet size. Models interpreting low-resolution spectra may constrain a planet surface gravity, together with the planet mass can give constraints on planet radius. An actual determination of either albedo or planet radius, would require follow-up observations that

Table 2.3-2. Known giant planet targets for the Exo-S mission.

HIP	Common	d(pc)	# Planets
7513	Ups And	13.49	4
7978	Q01 Eri	17.43	1
10626	HD 13931 b	44.23	1
16537	epsilon Eridani	3.21	1
22336	HD 30562	26.42	1
22627	GJ 179 b	12.29	1
24205	HD 33636 b	28.36	1
26394	Pi. Men	18.32	1
27253	HD 38529	39.28	2
31592	7 Cma b	19.75	1
33212	HD 50554 b	29.91	1
37826	Pollux	10.36	1
40952	HD 70642 b	28.07	1
43587	Rho Cnc	12.34	5
49699	HD 87883	18.2	1
50473	HD 89307 b	32.36	1
53721	47 UMa	14.06	3
65808	HD 117207 b	33.05	1
71395	HD 128311	16.5	2
74500	23 Lib	26.21	2
79248	14 Her	17.57	1
80337	HR 6094	12.78	1
83043	BD+25 3173	10.34	1
83389	HD 154335	18.59	1
85647	GJ 676 A	16.45	4
86796	Mu Ara	15.51	4
90485	HD 169830 c	36.6	2
95467	HD 181433 d	26.76	3
96901	16 Cyg B	21.21	1
97336	HD 187123 c	48.26	2
98767	HD 190360	15.86	2
99825	HD 192310	8.91	2
106353	HD 204941 b	26.9	1
106440	HD 204961	4.95	1
109388	BD-05 5715	9.1	1
113137	HD 216437	26.74	1
113421	HR 8734	19.86	2
116616	HD 222155 b	49.1	1
116727	Gam Cep	14.1	1

would subsequently map out the illumination phase light curve. This challenging measurement (Seager, Whitney, and Sasselov 2000) is most accessible for planets with low orbital inclinations. The current Design Reference Missions (DRMs) do not plan for such follow-up observations during the prime mission phase of Exo-S.

Exo-S will obtain spectra of up to R=70. The planet's spectrum will provide a wealth of further information over a brightness measurement. The shape of the spectrum would help determine the wavelength-dependent reflectivity of the planet, which is controlled by atmospheric thickness and any cloud and haze layers (**Figures 2.3-2 and 2.3-3**). The overall spectral shape will therefore give an indication of the presence or absence of cloud or haze layers. Absorption features from CH_4, H_2O, NH_3, and CO, and emission features from Na and K are within the wavelength range of anticipated Exo-S observations. The depths and widths of these features would be measured, from which the concentrations of these species could be determined or constrained.

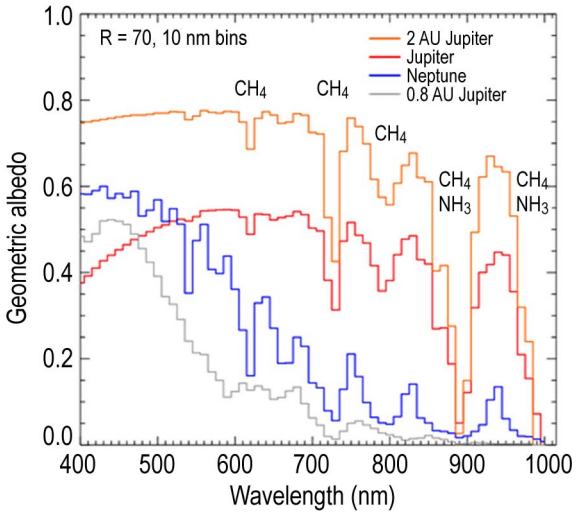

Figure 2.3-2. Giant planet spectra: geometric albedo spectra of real and modeled giant planets. The spectra have been convolved to R=70 spectral resolution and re-binned onto a wavelength grid with 10 nanometer bins. The observed spectra of Jupiter and Neptune from Karkoscha (1999) are shown with red and blue lines, respectively. Two model giant planet spectra from Cahoy et al. (2010) are also plotted. They are warm Jupiter-like plants located 2 AU (orange line) and 0.8 AU (gray line) from a Sun-like star. The 2 AU Jupiter is very bright due to water clouds, while the 0.8 AU Jupiter is cloudless and darker.

It is important to note that not all molecular species can be measured for all planets; for example, only warmer giant planets would exhibit spectral features from H_2O (in colder planets H_2O is trapped as solid or liquid particles in clouds) and only the warmest giant planets will have Na and K in atomic form (in colder planets the alkali metals are in gas phase or solid molecules). Only high abundances of NH_3 and CO will be detectable, because they have relatively weak spectroscopic features.

From spectral features, many things could be inferred, albeit with significant uncertainties. For planets with clouds at an altitude that is favorable (Hu 2014), the C/H/O ratio of the planet's atmosphere could be determined from observing two or more spectral features of the same molecule. For each individual planet, compositional information can be used with models of atmospheric structure to estimate the planet's surface gravity.

The bulk composition of known giant planets is relevant for planetary formation theories, as elemental composition is

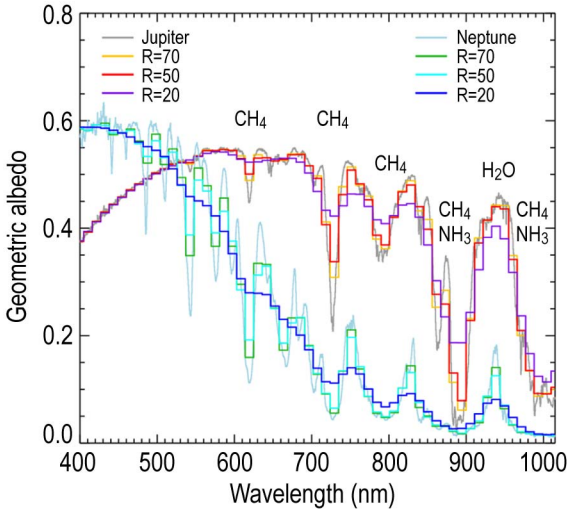

Figure 2.3-3. Jupiter and Neptune spectra (Karkoschska 1994) degraded to spectral resolutions of R=20, 50, and 70. The strongest water vapor band in this spectral wavelength range is seen at 940 nm.

ultimately a function of that formation history. The composition of planets may be related to star type, stellar metallicity, planet orbit (especially with respect to the ice line), migration history, size of the planet, and formation mechanism. While Exo-S will not have a large enough sample of planets to address all these individual factors affecting composition, it will add to a growing data set with which researchers will tackle these issues.

New planets may be discovered in systems with known giant planets, namely planets of too low mass to have been detected by any prior RV surveys. A maximum planet mass could be determined by the upper limits or lack of RV detections. Dynamical stability calculations of systems with multiple planets may also be able to provide constraints on planet mass, given information or assumption about the planetary orbits (e.g., Barnes and Greenberg 2006).

2.3.2 Earths in the Habitable Zone

For a set of extremely valuable targets, the small inner working angle (see **Table 2.3-1**) and optical performance of Exo-S will allow the mission to discover planets in the habitable zones of their stars. The goal is to characterize these planets as best as possible. For Earth-size planets, the Exo-S spectral resolution depends on the telescope aperture and the planet brightness, and in some cases will be limited to imaging detections.

The most interesting targets Exo-S will attempt to observe will also be the most difficult to detect and characterize. Earth-size planets in the habitable zones of their stars are at the edge of detectability for the mission, because their faintness requires long integration times. Detection confirmation is achieved by integrating all the light across the entire observation band. Characterization via spectroscopy is far more difficult than detection (**Figures 2.3-1** and **2.3-4**), because the observation requires a high SNR in each spectral resolution element. The significantly longer integration time for spectroscopy over discovery is prohibitively long in some cases. For many Earth-size planets in the habitable zone, colors instead of spectra will be measured.

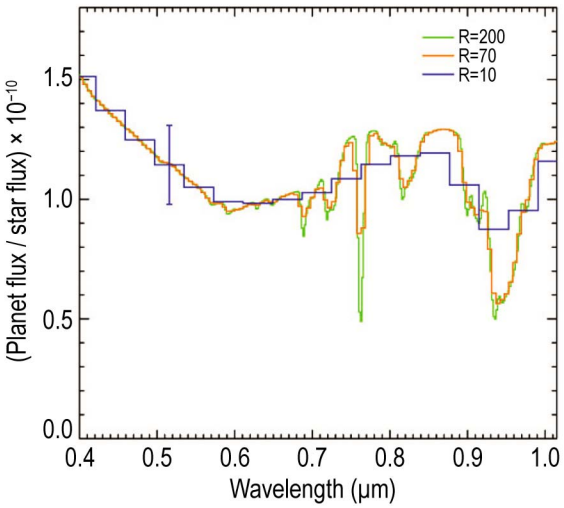

Figure 2.3-4. Simulated reflected light Earth spectrum degraded to spectral resolutions of *R*=200, 70, and 10.

The lack of spectra will complicate confirmation of point sources as planets, because spectral information is useful for discriminating between planets and background sources (see Section 3.1). Without such information, any point sources would effectively be planet candidates until they are confirmed as planets by some other means.

For targets for which spectroscopy is infeasible, confirmation of the light source as a planet will take place in one of two ways. For stars with high proper motion, confirmation would occur by continuing to observe until the star moves at least one point spread function (PSF) width on the detector, to establish common proper motion between the planet candidate and star. For stars with low proper motion, it will take too long for this movement to occur and it would be more efficient to revisit the target at a later epoch. For these purposes, the 'cutoff' between high and low proper motion is the time for a revisit (between two to four weeks). This means that Exo-S would continue to observe targets with proper motion sufficient to move the star one PSF

width in two to four weeks or less; and would leave other targets for confirmation with a follow-up observation, possibly in the third year of the mission, or by other means as described in Section 3.1.

For the best Earth analog targets, the Dedicated Mission will be able to obtain low-resolution (R=10, SNR=10) spectra (**Figure 2.3-1a**). This basic information may allow confirmation or rejection of a planet candidate without a revisit. Additionally, the low resolution spectrum would allow the following determinations: the presence/absence of a thick atmosphere via the effects of Rayleigh scattering; the presence/absence of hazes and clouds via their reflectivity and absorption properties. This will be enough to contribute to a preliminary classification of the planet, but confirmation of it as a rocky body or its habitability would require follow-up observations with a larger-diameter telescope.

Higher-resolution spectra (R=70, SNR=10) are obtainable for the most favorable Earth analog planet candidates with the Rendezvous Mission (**Figure 2.3-1b**). Spectra (especially in the case of a cloud-free atmosphere) can enable immediate confirmation of planet candidates based on spectral feature wavelength and depth. The spectra will also yield identification of atmospheric gases such as water vapor (indicative of liquid water oceans for small planets) and methane (of interest for geological and biological reasons).

The first detections of biosignature gases are of immense interest to the exoplanet community. A spectral resolution of R=70 would enable measurement of the biosignature gas O_2 if it is present in the lower atmospheres of exoplanets. Detecting both O_2 and H_2O is important to rule out some false positive scenarios (Domagal-Goldman et al. 2014). The green (and red) band is suitable for observing the gas O_2 and the red band is most suitable for observing H_2O vapor features.

Regardless of the level of spectroscopy, any Earth-like candidates observed would deliver critical preliminary information on this class of worlds. This would build a bridge to a future exoplanet flagship mission, which would be able to utilize even larger apertures, smaller inner working angles, and larger wavelength ranges to assess planet habitability and any presence of biosignature gases.

2.3.3 Sub-Neptunes, Super Earths, and a Variety of Star Types

Exoplanets are incredibly diverse and not limited to giant planets (Section 2.3.1) or Earth-size planets (Section 2.3.2) but extend to the full range of sizes (and masses and densities) allowed by physics. While there are no solar system planets larger than Earth but smaller than Neptune, such planets appear to be the most common planets in our galaxy (Howard et al. 2010; Buchhave et al. 2012; Burke et al. 2013; Sumi et al. 2010). This leaves the exoplanet community in a situation where little is known about the most common type of exoplanet. Note that super Earths are defined as planets that are predominantly rocky with thin atmospheres whereas sub-Neptune planets are loosely defined as planets with a massive enough gas layer that it forms an ‘envelope’.

Fortunately, because they are larger than Earth, the sub-Neptune planets are favorable for detection and characterization with Exo-S. With measured spectra, headway can be made through the great deal of uncertainty on their possible bulk compositions (see the diversity of anticipated spectra in **Figures 2.3-5** and **2.3-6**.) In particular, the presence or absence of clouds and possibilities for solid surfaces beneath a thin atmosphere may be inferred from the depth of spectral features across a wide wavelength range. The analysis of any photochemical hazes may also lend insights into the chemistry of the planet, and also help infer the bulk chemical processes from which those hazes are derived. Such hazes are known to exist on Venus and Titan, are present in smaller quantities on the solar system giant planets, and have already been proposed to

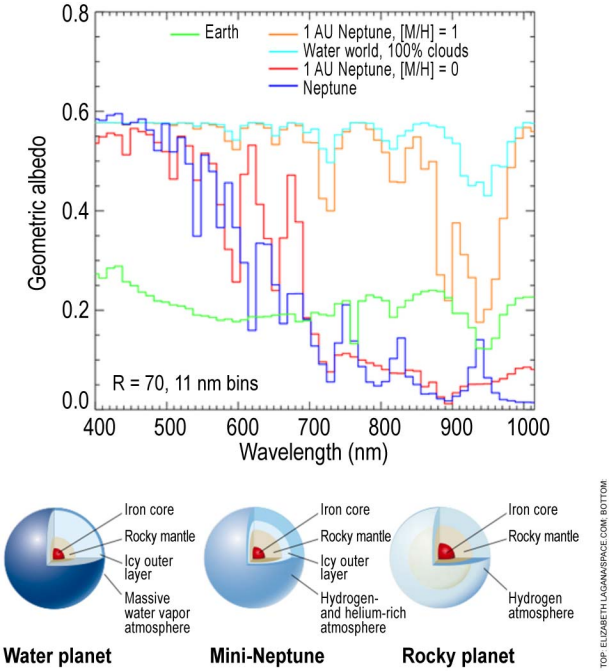

Figure 2.3-5. Geometric albedo spectra of modeled sub-Neptunes (R. Hu, private communication). Neptunes and sub-Neptunes will appear somewhat similar in terms of albedo spectra. The very natures of sub-Neptunes are unknown, and three possibilities are outlined in the cartoon diagram.

explain some ground- and space-based exoplanet transmission spectra observations. Of particular interest is that super Earths or even some low-mass sub-Neptune planets exterior to the traditional habitable zone may have suitable surface temperatures to host life by a strong greenhouse gas atmosphere or envelope composed of H_2 (Pierrehumbert and Gaidos 2011).

The relatively high-resolution *R*=70 spectra of sub-Neptune (or Neptune-size) planets will deliver much of the same information as the *R*=70 spectra of the gas giants (see Section 2.3.1 and for an additional sample spectrum see **Figure 2.3-7**). Specifically, the abundances of H_2O, CH_4, and potentially NH_3 will be measured, as will the presence/absence of clouds and photochemical hazes. From these measurements, elemental ratios (C/O/H/N) may be constrained through modeling.

It is fair to say that atmospheric measurements of sub-Neptune–size exoplanets are critical for making progress in understanding this new class of planet.

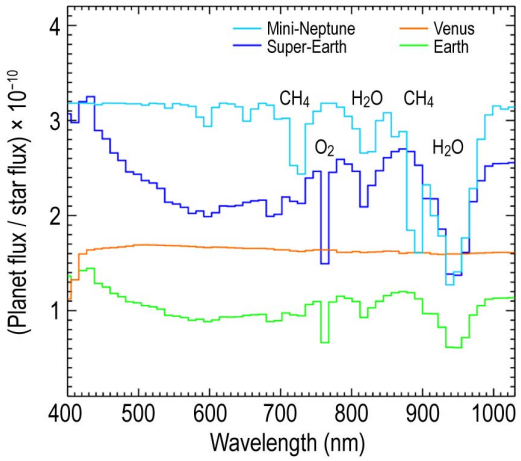

Figure 2.3-6. Simulated spectra of small planets. The Earth, Venus, and super Earth models are from the Virtual Planet Laboratory (VPL; http://depts.washington.edu/naivpl/). The sub-Neptune model is from Renyu Hu (personal communication). The spectra have been convolved to *R*= 70 spectral resolution and re-binned onto a wavelength grid with 11 nanometer bins.

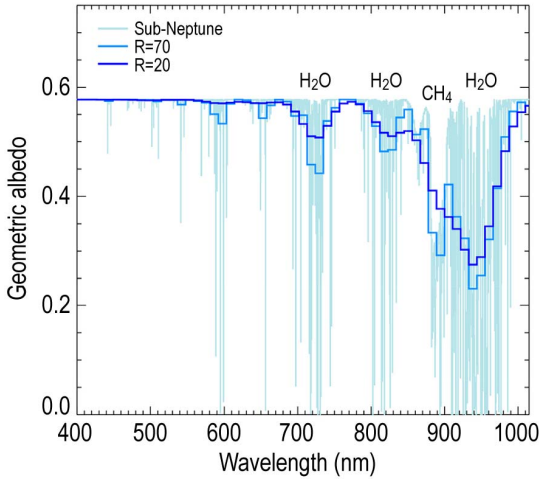

Figure 2.3-7. A theoretical spectrum for a metal-rich Neptune at 2 AU, valid also for smaller planets (i.e., sub-Neptunes) degraded to spectral resolutions of *R* = 20 and 70. The strongest water vapor band in this spectral wavelength range is seen at 940 nm. CH_4 is needed to identify a planet as a sub-Neptune and not a rocky world with a thin atmosphere.

Atmospheric composition may lead to an understanding of the sub-Neptune planet formation pathways, as the elemental compositions may be determined by their formation location and orbital migration within a protoplanetary disk.

2.4 Approach to Target Selection

The approach to target star selection is based on two main factors. First, the total number of

stars that can be observed is set by the number of retargets possible during the mission lifetime; the starshade and telescope have to realign for each new target star and it takes several days to a couple of weeks for the starshade or telescope to move across the sky. Second, the path across the sky determines the order in which stars are observed. This path is optimized based on fuel usage, taking field of regard into account including solar and Earth exclusion angles. Any approach to target star selection for the Exo-S mission must therefore carefully consider the sequence of observations and the priority of target stars within the larger sample of stars for which exoplanets may fall within the detection space.

The Exo-S mission gives priority to stars with known giant planets, because of their guaranteed science return (see Section 2.3). Because of their well-determined orbits, observations can be timed to ensure a high probability of detection (in many cases it is 100%), mass determination, and spectral characterization. As the highest priority category, the known giant planet target stars provide anchors in the sequence of observations (see Section 5 for a detailed description of the DRM). Known giant planet target stars are listed in **Table 2.3-2**. The selection and timing of Exo-S observations of known giant planets is described in Section 5.

Beyond the target stars with known giant planets, Exo-S's next priority is the search for new planets. The number of target stars with discoverable interesting planets is large. Two distinct approaches to target selection have been considered. The first emphasizes a search for Earth twins (1 Earth radius, albedo = 0.2), while the second emphasizes a rich diversity of worlds orbiting a diverse set of stars.

The Earth twin search prioritizes stars whose habitable zones are most accessible, and sets instrument maximum integration times to according to the likely brightness of Earth twins. In contrast, the planet diversity search selects targets from the brightest stars in the sky and observes them to the limiting sensitivity of the instrument. Often this means longer integration times than the Earth twin search, but it affords more opportunities for giant planet discovery and spectral characterization in the same planetary system. The overall discovery rate of the two approaches is about the same, but the diversity and characterizations of discovered planets are significantly different (see Section 5 for quantification).

Juxtaposing the two approaches to target star selection provides a new perspective on the flexibility of the Exo-S mission and its potential for discovering diverse and habitable worlds (Section 2.6).

The master input list of stars is called ExoCat and it includes all known stars with visual magnitude V<8 within 30 pc, along with stellar data and other calculated information relevant to direct imaging of exoplanets (Turnbull 2015, in prep). Target star lists for different approaches are culled from the master list. The target star lists are used as input for the DRM. The DRM process selects stars based on integration time limits, completeness, fuel constraints, and solar and Earth-pointing exclusion angles to provide observation sequences.

The following two subsections provide target selection details for each target star selection approach.

2.4.1 Target Star List for Exploring Habitable Zones

Given the overwhelming significance of an Earth-like planet discovery, and given the starshade's small IWA and deep sensitivity, a naturally desirable approach to target star selection is one that maximizes the number of detectable Earth-size planets in the habitable zones of nearby Sun-like stars. Observations of lower priority targets are considered if they are favorably located on the sky. The first approach to target selection for this study (hereafter, 'maximum HZ' approach) includes three tiers of targets:

- **Tier 1.** The list of stars with known giant planets that fall within the detection space and have short characterization times (described in Section 2.3.1),
- **Tier 2.** Target stars with observable habitable zones and favorable planet-to-star contrast ratios for Earth twins, and
- **Tier 3.** Stars that are good candidates for new sub-Neptune or giant planet detection.

There are two primary considerations for selecting high priority stars to search for Earth twin candidates (the Tier 2 sample). First, for each target, a significant portion of the habitable zone must fall within the Exo-S detection space. Second, the integration time to detect an Earth-twin planet must be reasonably short.

The 'completeness' is a useful quantitative metric that gives the probability of detecting a particular planet type in a single observation if that planet is present around the star (see Brown 2005 for a full explanation). The completeness is calculated by simulating a suite of test planets with the appropriate characteristics (e.g., size, albedo, and a desired range of semi-major axes) and all possible orbits (e.g., inclination and eccentricity), then calculating what fraction are detectable (i.e., both outside the IWA and bright enough to be detected) in a single observation. Choosing targets stars with the highest completeness therefore maximizes the chances of detecting planets of interest during the mission lifetime.

To identify high priority Tier 2 targets for the maximum HZ approach, an IWA of 102 mas (for the Dedicated Mission) or 100 mas (for the Rendezvous Mission) in the green band and contrast floor of 4×10^{-11} is assumed. (A few stars for the Dedicated Mission require the lower IWA [80 mas] of the Dedicated Mission's blue band.) The habitable zone completeness is then calculated for each star assuming Earth-twin planets orbiting within the circumstellar HZ boundaries (0.75 to 1.77 AU scaled by the square root of the bolometric stellar luminosity; Kopparapu et al. 2013). These planet properties are summarized in **Table 2.4-1**.

Table 2.4-1. Planet characteristics assumed for completeness calculations.

	Earth	Sub-Neptune	Jupiter
Radius	1	2.5	11
Geometric Albedo	0.2	0.41	0.52
Inner Zone (AU)	0.75 (scaled)	0.75	0.75
Outer Zone (AU)	1.77 (scaled)	5	10

The second criterion for selecting stars to maximize the number of Earth-twin candidates that can be detected is that the planets must be detectable within about a 15-day integration. Longer integrations force the starshade to 'rush' to the next target to avoid solar and Earth-pointing constraints, wasting fuel and limiting the number of observable targets. The integration time calculations are described in detail in Section 5. In sum, the times are set to reach different planet-to-star flux ratios for different type stars, just long enough to detect Earth-twin planets in the HZ.

To arrive at the list of high priority targets for Earth twin detection, a lower limit is applied to the habitable zone completeness, and an upper limit is applied to integration time for detection (summarized in **Table 2.4-2**). The resulting list of most favorable Tier 2 targets consists of solar-type main sequence stars (F5V to K9V) within ~11 parsecs. Less luminous, later-type stars (i.e., M dwarfs) have HZs hidden completely within the mission's IWA, even for the nearest stars. For stars earlier than F6/7V (~2.9 L_{sun}), habitable zones are larger but the planet-to-star flux ratios dip below the instrument's 4×10^{-11} systematic contrast floor. A more complete discussion of this selection effect appears in Turnbull et al. (2010).

In addition to the two selection criteria on HZ completeness and exposure time, stars with known 'tight and bright' stellar companions are excluded, as stray light from the companion will increase the background flux, leading to longer integration times and limiting the achieved contrast. The excluded multiple

stars are listed in Appendix A: in **Table A.1-2** for the Dedicated Mission and in **Table A.1-4** for the Rendezvous Mission. Stars with known bright circumstellar dust disks are also excluded as they would increase the background flux and hence the exposure times needed to detect planets.

The stars in this Tier 2 list also allow for sub-Neptune–, Neptune-, and Jupiter-size planet detection outside the IWA. For the Exo-S contrast limit of 4×10^{-11}, sub-Neptunes (2.5 Earth radii) can be detected out to ~3 AU separation from all target stars, while Neptunes and Jupiters (3.9 and 11 Earth radii, respectively) are detectable out to 5 AU and 12 AU, respectively. This maximum physical separation for detectability is the same for all targets regardless of stellar type.

Table 2.4-2. Maximum HZ observational criteria.

Criterion	Value	Comment
HZ Completeness	>25%	Retargeting overhead
Integration Time	≲15 days	Number of targets

With this input star list, there are still times when there are large gaps on the sky between target stars, forcing the starshade to make large, fuel-wasting translations. At these times, it is sensible to observe other stars along the path, even if Earth-twin planets cannot be observed around them. A set of stars (Tier 3) was therefore selected for which sub-Neptune planets can be observed with the same observational criteria described above (completeness >25% and integration time less than about 15 days). These larger, brighter planets are easier to detect than Earth-size planets, and the host stars cover spectral types from A0V to M1V.

After the stars for which sub-Neptune planet discovery is possible, any remaining gaps in the starshade path across the sky are filled with stars having completeness >25% for Jupiter-size planets and for which R=70 spectra of those planets can be obtained in less than four days. These stars are also considered part of Tier 3. For the sub-Neptune and Jupiter calculations, the assumed planet parameters are given in **Table 2.4-1**.

The input target star lists for the maximum HZ approach are given in **Table A.1-2** for the Dedicated Mission and in **Table A.1-4** for the Rendezvous Mission. There are more stars (414 total) for the Rendezvous Mission than for the Dedicated Mission (237 stars) because of the consideration of integration time for the final input target lists.

2.4.2 Target Star List for Maximizing Planet Diversity

The second approach to target selection does not concentrate solely on the habitable zone but instead focuses on exploring a wide range of planets around a wider variety of star types. This approach, the 'maximum diversity' approach, utilizes the full sensitivity of Exo-S on every blind search target, 'going deep' on every star to detect all the planets that can be seen. The small IWA (100 mas in the green band) and low contrast floor (4×10^{-11}) of Exo-S permit this approach to yield a rich diversity of small to large planets with hot, warm, and cold temperatures. (Note that hot, warm, and cold are used as a proxy for the planets interior to the habitable zone, in the habitable zone, and exterior to the habitable zone respectively. The stellar energy flux received by the planet is the known parameter, not the actual planet temperature which is controlled by atmospheric properties.)

Many of the types of planets that could be discovered via the maximum diversity approach are not accessible to other detection techniques (e.g., RV or transits). For example, bright early-type stars (i.e., A/F-type) are not typically targeted by RV searches due to their lack of strong visible-wavelength photospheric absorption lines. With thousands of possible target stars, mission lifetime is the limiting factor on the total planet harvest, not the IWA or contrast floor.

The maximum diversity approach to Exo-S target selection includes three tiers of targets:

- **Tier 1.** The list of stars with known giant planets that fall within the detection space and have short characterization times (described in Section 2.3.1),
- **Tier 2.** A short list of six prime science targets, with five targets having high habitable zone completeness (>20%) and short exo-Earth detection times (less than about 10 days), and
- **Tier 3.** An input list of stars having short detection times for all types of planets, from hot, Earth-size objects to cold Jupiter-size planets

The six Tier 2 prime science targets consist of the very best stars for searching for Earth-twin candidates in the HZ: those having large angular HZ sizes, high planet-to-star flux ratios, short integration times, and no close companions. These six prime science targets are very nearby solar-type stars, listed in **Table 2.4-3.** By virtue of their short times to exo-Earth detection, these very nearby stars offer the greatest opportunities for return visits and follow-up observations of candidate exo-Earths. Every effort should be made to observe these stars in the first year of the mission. Note that although one of the six prime science target stars (HIP 2021) in fact has a low completeness for Earth twins (close to 10%), the star is still kept on the list.

To construct the rest of the input star list, the observational criteria utilized is given in **Table 2.4-4**. To begin with, the planet-to-star flux ratios of Earths (R = 1 R_{Earth}) and super Earths (R = 1.4 R_{Earth}) located at the Exo-S IWA, assuming quadrature illumination, were calculated for every star in the master target list. Stars were eliminated for which the planets had ratios fainter than the systematic contrast floor (4×10^{-11}). Stars for which the planets were fainter than V=30 were also eliminated, which limits their detection times to less than about 15 days. For these stars, planets larger than Earths and super Earths (sub-Neptunes, Neptunes, and Jupiters) can also be detected at the IWA, assuming their albedos are not extremely low.

Table 2.4-4. Max planet diversity observational criteria.

Criterion	Value	Comment
limΔmag	26	4×10^{-11} sensitivity limit
Faintest Planet	V<30	Mitigate confusion
Integration Time	$\lesssim$15 days	Consequence of V<30

The resulting target list includes stars that could host Earth-, super Earth–, sub-Neptune–, Neptune-, and Jupiter-size planets detectable in less than ~15 days of exposure time per star. An additional 45 stars could host super Earth–, sub-Neptune–, Neptune-, and Jupiter-size planets detectable to Exo-S in less than ~15 days of exposure time (Earths require longer integrations). (Note that alpha Cen A and B are not included as Exo-S targets because of their large angular diameters and concerns about scattered light from the unobstructed bright companion.)

Removing the systems with known small-separation binaries, the input target star list for new planet discoveries has 63 stars. This list contains a wide range of spectral types (44 A

Table 2.4-3. Exo-S required input targets for exo-Earth discovery and spectroscopy.

HIP	Common Name	Spec Type	C_{HZ}	t_{det} (days)	Glat	[Fe/H]	Notes
2021	beta Hyi	G2IV	8.5%	2.8	-40	0.07	Very high proper motion, near south celestial pole, long term RV trend (>20 yr)
8102	tau Ceti	G9V	49%	7.4	-73	0.52	Highest completeness star in the sky, after alpha Cen B, very high proper motion
17378	delta Eri	K0IV	23%	7.7	-46	0.16	'Rana'. Subgiant, appears to be non-variable despite listing in NSV
22449	Tabit	F6V	28%	4.6	-23	0.03	Single star, erroneously listed as spectroscopic binary in WDS
27072	gam Lep A	F7V	32%	8.6	-24	-0.12	GL 216 A, bright K star companion GL 216 B at 96 (missing from HIP)
99240	delta Pav	G8IV	48%	7.8	-32	0.33	Very high proper motion, near south celestial pole, older, high metallicity star

through late F-type stars, 19 G- to early K-type stars), including 10 giant stars, and 3 subgiant stars.) . As expected, there are far more early-type stars present than in the HZ-focused lists. Combined with the target stars with known giant planets, the input target star list for the maximum diversity approach for the Dedicated Mission includes 99 total stars (see **Table A.1-3** in Appendix A).

2.4.3 Target Star List as Input to the DRM

The target star lists are used as input to the three different DRM cases studied (described in detail in Section 5). The target star list for exploring habitable zones is used in two cases: Case 1 for the Dedicated Mission (1.1-m aperture) and Case 3 for the Rendezvous Mission (2.4-m aperture). The target star list for maximizing planet harvest by emphasizing overall planet diversity is used in Case 2 for the Dedicated Mission. The maximum diversity list with the Rendezvous Mission was not studied, because with limited time and resources the Exo-S team took the point of view that the capability of characterizing Earth twins with the larger aperture is more scientifically compelling than the gain in planet diversity. The scientific return for the three cases is presented in Section 2.6.1.

2.5 The Observational Approach

This section summarizes the high-level characteristics of the planned observations for each type of target. Full details of the observation parameters and observing sequence strategy appear in Section 5. It is important to note that not every star in each input target list is observed in a particular DRM realization. This is a function of the starting point and date, and the distribution of stars on the sky.

Some level of onboard automation is required to assess the system's observed mean exozodiacal background light level. If the level is too high to detect any planets in a reasonable amount of time, the instrument will automatically take a wide-field image of the dust structure, then move on to the next target. Determination of the threshold dust levels, and development of algorithms to handle the decision-making process, will be the subject of future study.

One important change affecting the observational approach is the change-out of the Interim Report's slit spectrometer for an integral field spectrometer (IFS). The IFS captures spatially resolved spectra through the use of a lenslet array followed by dispersive elements and then a detector. A trade study shows both options have similar mass and cost (the IFS was slightly higher in cost due to its lower technical maturity). The slit spectrometer also has slightly better throughput than the IFS. But the observational method is far simpler with the IFS since it collects spectral and spatial information of the entire FOV in one observation. The slit spectrometer requires the use of the imager to establish the spatial location of the planets before the slit can be placed. Multiple planets systems further complicate the observation method since each planet needs to be located before the slit can be placed. With the IFS, all planet spectra can be collected in the same observation.

2.5.1 Spectroscopy of Known Giant Planets

For the giant planets already known from RV surveys, all orbital parameters of the planets (except possibly the inclinations) will be measured in advance of the mission. Therefore, it will be possible to plan to observe them in optimal time windows. If the planet inclinations and therefore masses are known in advance (from Gaia, for example), then the window is larger. If a measurement of planet inclination is needed from the Exo-S mission observations, then the time window is more constrained.

Spectra in the green observing band will be obtained, covering 515–825 nm for the Dedicated (1.1-m) Mission and 600–850 nm for the Rendezvous (2.4-m) Mission. The spectrum will have resolution R=70 and

continuum S/N=10 per resolution element, providing valuable good quality spectra for planets with known masses and orbital parameters. No return visits will be planned for the known giant planet targets during the prime mission lifetime.

2.5.2 Reconnaissance of Planet Discovery Targets

For planet discovery targets, previously unknown planets will be searched for, ranging from cold Jupiter-size planets to hot Earth-size planets. For each star in Case 1 (maximum HZ target list for the Dedicated Mission), the initial survey observation done in the first two years of the mission is a low-resolution spectrum. This spectrum will be obtained in the green band (510–825 nm, IWA=102 mas), except for three Earth-candidate targets that will be observed with the blue band (400–647 nm, IWA=80 mas) to maximize habitable zone coverage.

The exposure times will be set to reach some limiting delta magnitude relative to the star (limΔmag). For stars with L<1.6, limΔmag = 25.5 + 2.5logL. For higher luminosity stars, limΔmag = 26 (a contrast ratio of 4×10^{-11}, the instrument's systematic contrast limit). These variable depth observations will provide continuum S/N=4 per *R*=7 resolution element for Earth-twin planets in the habitable zone. This translates to S/N=7 in the integrated broad observing band, giving a missed detection probability <0.1% for Earth-twins. Higher spectral resolution and/or S/N can be obtained on any brighter planets detected.

For Case 2 (maximum diversity target list for the Dedicated Mission), the initial survey observation is again a low-resolution spectrum in the green band. Here, the exposure times were set to achieve the best possible contrast (limΔmag = 26) on every star, giving S/N=4 per *R*=7 resolution element on the faintest planet detectable. Again, higher spectral resolution and/or S/N can be obtained on any brighter planets detected, up to *R*=70.

Case 3 (maximum HZ for the Rendezvous Mission) uses the same basic strategy for the input target star lists as Case 1. The bandpasses are slightly different (green band covers 600–850 nm, blue band covers 470–670 nm). The larger aperture permits continuum S/N=4 per *R*=9 resolution element for Earth-twin planets in the habitable zone.

2.5.3 Third Year Follow-up

The third year of the Exo-S mission is dedicated for return to any promising planet candidates for follow-up observations. These observations could be relatively quick images to confirm common proper motion or parallax with the host stars. They could also be deeper spectra with higher resolution and/or S/N or spectra in different bands (blue, green, or red), providing access to different spectral features.

The flexibility of the Exo-S mission means the observing strategy can be altered in real time as needed.

2.6 The Science Return

2.6.1 Assessing the Exoplanet Harvest

A subset of the stars on the input target lists are selected for the actual observing sequences for the first two mission years by the DRM process described in Section 5. For Case 1, 14 known giant planet host stars and 28 additional blind search targets are observed. For Case 2, 14 known giant planet host stars and 24 additional blind search targets are observed. For Case 3, 12 known giant planet host stars and 43 blind search targets are observed.

To estimate the expected yields of observed planets from the three DRM cases, for each list of observed stars, the IWA and limiting contrast reached were used in each survey observation to calculate the completeness achieved for a range of different planets. The planets considered were Earths, super Earths, sub-Neptunes, Neptunes, and Jupiters. The assumed parameters of each planet type appear in **Table 2.6-1**. The planets were furthermore put into three temperature classes based on the energy received from the

host star. For a Sun-twin star, the 'hot' class has semi-major axes between 0.01–0.75 AU, 'warm' between 0.75–1.77 AU (the traditional HZ), and 'cold' between 1.77–10 AU. The distance ranges were scaled by the square root of the stellar luminosity for other spectral types.

Table 2.6-1. Planet characteristics for yield calculations

Planet	Radius (R_{Earth})	Geo. Albedo
Earths	1	0.2
Super Earths	1.4	0.2
Hot Sub-Neptunes	2.0	0.2
Warm Sub-Neptunes	2.0	0.5
Cold Sub-Neptunes	2.0	0.4
Hot Neptunes	3.9	0.2
Warm Neptunes	3.9	0.5
Cold Neptunes	3.9	0.4
Hot Jupiters	11	0.2
Warm & Cold Jupiters	11	0.5

The completenesses for every planet size and stellar flux combination were calculated for each observed star, with the further assumptions that all the test planets are on circular orbits and are uniformly distributed in Log(period). Details on the methodology may be found in Stark et al. (2014). The final cumulative completenesses for each case, summed over all observed stars, appear in **Table 5.4-1** in Section 5.

To turn cumulative completenesses into expected planet yields, the completenesses must be multiplied by the occurrence rates for each type of planet. For Earth-size planets in the habitable zones, a 16% occurrence rate is adopted, a value calculated from the Kepler planet occurrence relations extrapolated to our adopted HZ orbital radii boundaries (Petigura et al. 2013, Stark et al. 2014). For all other planet types, the occurrence rate is assumed to be 10%. Refining these rates based on results from Kepler and ground-based RV surveys will be the focus of future study.

The total numbers of stars searched for planets (and hence the expected total number of planet discoveries) are shown for Cases 1, 2, and 3 in **Figures 2.6-1**, **2.6-2**, and **2.6-3**, respectively. In Cases 1 and 2, the results are very similar. However, as compared to Case 1 the Case 2 observing program finds a larger number of bright planets that can be spectrally characterized, while Case 1 has a higher yield of 'warm' Earth and super-Earth planets orbiting within the habitable zone.

In Case 1, the best spectrum achievable on any Earth twin in the HZ, no matter how much mission time is devoted, has R=10 and SNR=10; even this is only possible for five stars. For Case 3, 22 stars (four with less than a 32-day integration) with Earth twins in the HZ could have planet spectra obtained with R=70 and SNR=10. Case 3 discovers more planets and immediately provides better quality spectra on the planets in the initial survey observation.

2.6.2 Circumstellar Disk Science

Debris dust from the destruction of asteroids and comets is a ubiquitous feature of planetary systems, including our own. Little is known

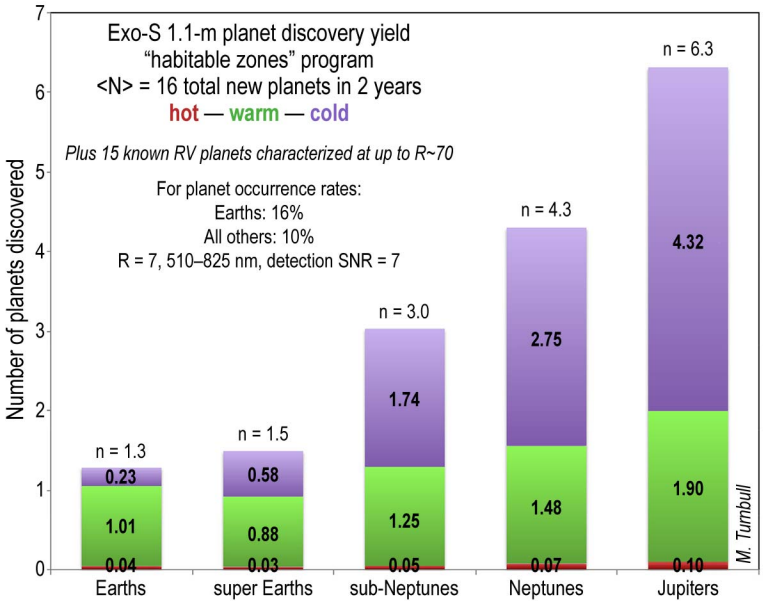

Figure 2.6-1. The predicted Exo-S 1.1-m planet discovery yield in the first two years of operations, for the Case 1 target selection scenario designed to maximize the number of habitable zone Earths discovered.

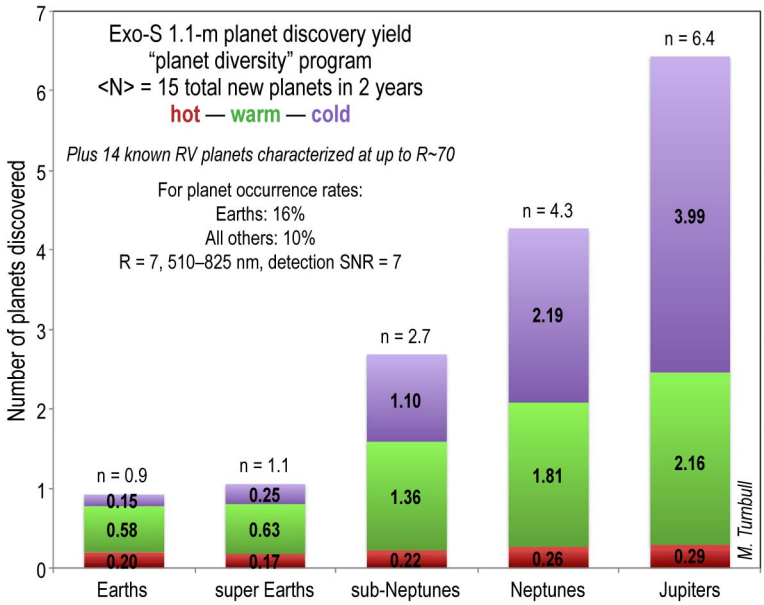

Figure 2.6-2. The predicted Exo-S 1.1-m planet discovery yield in the first two years of operations, for the Case 2 target selection scenario designed to maximize the diversity of planets discovered.

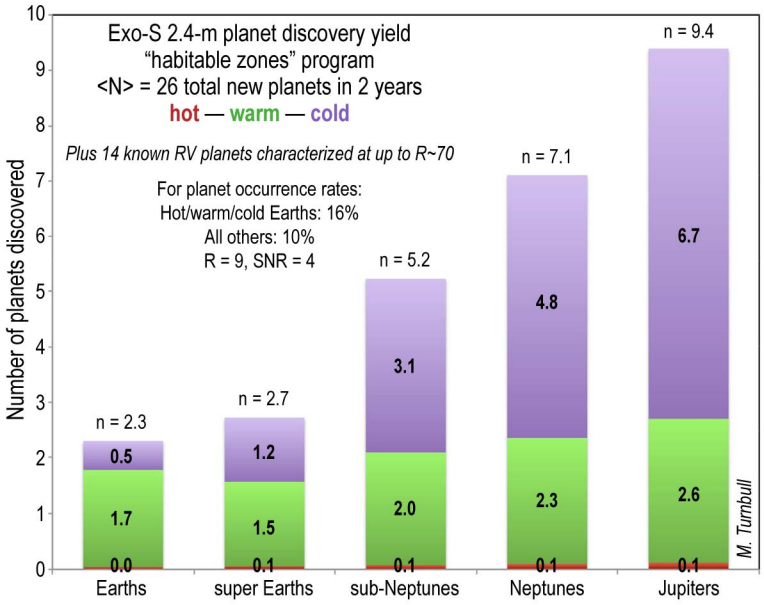

Figure 2.6-3. The predicted Exo-S 2.4-m planet discovery yield in the first two years of operations, for the Case 3 target selection scenario designed in part to maximize the discovery of habitable zone Earths.

about warm dust in the inner reaches of systems where habitable planets are expected to reside. In the solar system, the warm dust interior to the asteroid belt (the zodiacal dust) appears to come largely from the evaporation of comets (Nesvorny et al. 2010).

For every star observed with Exo-S, a multicolor image of light scattered from exozodiacal dust will be obtained. This information can be used with disk models to constrain the grain properties (size, composition, shape). The range of dust properties will shed light on the characteristics of the dust source bodies, remnants of the planet formation process.

Furthermore, debris disk morphologies reflect the gravitational perturbations of the planets they contain (e.g., Dawson et al. 2011); observing structures in debris disks offers a potentially powerful indirect tool for finding planets and constraining their masses and orbital parameters. For example, Neptunes and super Earths orbiting at semi-major axes beyond roughly 15 AU have orbits too long to permit detection via RV, transit, or astrometric techniques within a human lifetime. They are also too faint ($\sim 10^{-12}$ in planet-star flux contrast) to detect directly with any known technique. The only way to detect true Neptune analogs may be to study the structures they imprint on debris disks.

Observations of τ Ceti and ε Eridani with the Exo-S probe will be well suited to this task. Imaging of ε Eridani with Spitzer suggests a complex system with five possible dust components, including belts at 3 AU and 20 AU, which the Exo-S mission will easily resolve (Backman et al. 2009). The τ Ceti system apparently exhibits both a hot dust component (di Folco et al. 2007) and a cold dust component (Greaves et al. 2004), both of which are also accessible to the Exo-S mission. This complex structure

hints that there may be planets sculpting the belts, which may be imaged with Exo-S.

Models suggest that in massive debris disks like those around τ Ceti and ε Eridani, Neptune-mass planets can sculpt the disk into eccentric rings. Observing these rings can constrain the planet's mass and orbital eccentricity (e.g., Chiang et al. 2009).

Observations of new habitable zone dust clouds by Exo-S will provide further opportunities to harness planet-disk interactions in aid of planet detection. Models suggest that a 2 Earth-mass planet can produce a detectable resonant structure in an exozodiacal cloud similar to the solar zodiacal cloud at 1 AU, whose morphology can constrain the planet's mass and eccentricity (**Figure 2.2-1**; Stark and Kuchner 2008). The signatures get stronger further from the star, and in dust clouds dominated by larger grains or generated by dynamically cooler sources. In some circumstances, a Mars-mass planet may even yield a detectable signature, a dust ring with a gap at the planet's current location.

2.7 Science Traceability Matrix and Requirement Flow Down

The Exo-S science goals align directly with specific NASA and National Research Council (NRC) strategic goals (**Table 2.7-1**) expressed in the *NASA Strategic Plan 2014* and the NRC's most recent Decadal Survey report, *New Worlds, New Horizons in Astronomy and Astrophysics* released in 2010. The Exo-S science program laid out in this report—detection and spectral characterization of dozens of new and known exoplanets, along with the imaging and characterization of their local planetary systems—directly addresses NASA's strategic objective 1.6:

> *Discover how the universe works, explore how it began and evolved, and search for life on planets around other stars*.

Furthermore, Exo-S's ability to discover and characterize rocky planets in the habitable zones of a favorable subset of target stars includes the spectral range for the biosignature gas oxygen and methane, and for the habitability indicator water vapor. Exo-S therefore offers the groundbreaking opportunity to finally begin perhaps the most

Table 2.7-1. Exo-S observational and measurement requirements.

Strategic Goals	Science Objectives	Observational Requirements	Measurement Requirements
NASA Strategic Plan 2014 • Objective 1.6: Discover how the universe works, explore how it began and evolved, and search for life on planets around other stars. New Worlds, New Horizons (2010 Decadal Survey) • Do habitable worlds exist around other stars, and can we identify the telltale signs of life on an exoplanet? • How diverse are planetary systems? • How do circumstellar disks evolve and form planetary systems?	Discover new exoplanets ranging in size from Earth-like to giant planets	Survey at least 10 Sun-like stars with ≥ 25% probability of detecting an Earth-twin in HZ	Planet contrast sensitivity ≤ 4E-11 (limΔmag ≥ 26)
			Planet detection SNR > 6
	Characterize newly discovered planets	Collect spectra of all newly discovered planets, including spectral features of methane, water, ammonia, carbon monoxide, carbon dioxide, sodium, potassium, ozone	Spectral resolution (Earths or larger) ≥ R10 Spectral resolution (sub-Neptunes or larger): ≥ R50 Planet characterization SNR: ≥ 10
			Total bandpass = 400–1,000 nm
	Characterize known giant planets, including: atmosphere and mass	Collect spectra of at least 10 known giant planets, including spectral features of methane, water, ammonia, carbon monoxide, carbon dioxide, sodium, potassium, ozone	IWA ≥ 100 mas
			Spectral resolution (giants): ≥ R70 Planet characterization SNR: ≥ 10
			Planet cross-track position ≤ 0.01 AU
	Characterize planetary systems	Measure circumstellar dust in the context of detected planets	FOV > 10 AU at 10 pc
		Characterize background sources	Measure polarization

challenging aspect of this objective: "to search for life on planets around other stars."

The Exo-S science also addresses several key strategic questions posed in the 2010 Decadal Survey. The characterization of biosignature gases key to NASA's objective also work toward answering the Decadal Survey question: "do habitable worlds exist around other stars, and can we identify the telltale signs of life on an exoplanet?" Disk and planetary system characterization measurements will address the NRC's question on how circumstellar disks form planetary systems. The total collection of Exo-S science will expand the knowledge of the diversity of planetary systems.

Observational requirements and science objectives are mostly in a one-to-one mapping. The objective to discover new planets resulted in the observational requirement to survey a minimum number of stars. The characterization of known, newly discovered planets, and planet-forming disks all require spectral measurements. The need to characterize background sources was also connected to the planetary system characterization since this objective requires the widest FOV and will observe the most background objects. The STDT determined targeted counts of a minimum survey of 10 stars with 25% completeness for Earth-twins in the habitable zone, and the characterization of 10 known RVs, are large enough samples to permit some comparative planetology.

Several observational requirements drive important design requirements and greatly affect the characteristics of the resulting mission's design. The ability to detect and characterize down to HZ rocky planets drives the contrast requirement. The targeted atmospheric constituent gasses and expected planet type set spectral resolutions and SNRs. The 100 mas IWA is needed to both access the HZ and to reach the planned number of known giant planets. Finally, the need to capture entire planetary systems and dust disks determines the minimum field of view.

3 DETECTING AND CONFIRMING EXOPLANET CANDIDATES

This section provides an overview of the properties of background sources that may appear in Exo-S images and discusses strategies for confirming or rejecting candidate detections. Also provided is a list of precursor science activities essential for maximizing Exo-S's scientific yield.

3.1 Challenges for Planet Discovery

Deep imaging in close proximity to nearby stars will reveal not only planetary companions, but a plethora of background sources and exozodiacal light with unresolved structure. How can these astrophysical contaminants be efficiently distinguished from planets?

3.1.1 Exozodiacal Dust

The inner regions of the solar system are awash with small dust grains coming from comets and asteroids, i.e., zodiacal dust. Similar dust is seen around other nearby stars and complicates direct imaging of exoplanets in two ways: (1) as a source of photon noise and (2) as a source of confusion due to unresolved structures that could masquerade as planets (Roberge et al. 2012). Background flux from exozodiacal dust (exozodi) will likely dominate the signal of an Earth-analog exoplanet in direct images and spectra, even if exozodi levels are no greater than the solar system's zodiacal dust level. Exozodi levels around nearby stars may be as important to the success of efforts to characterize Earth-like exoplanets as the fraction of stars with potentially habitable planets ($\eta_\oplus$).

Currently, little is known about the dust surrounding most Exo-S targets. This situation will be improved within the next few years by a new ground-based survey for exozodi around nearby stars (called HOSTS) using the Large Binocular Telescope Interferometer (LBTI) (Hinz 2013). The HOSTS survey will measure the integrated 10-μm thermal emission from warm dust down to about 10 times the solar system zodiacal dust level at 1 AU scales.

The LBTI HOSTS survey, however, will not address two additional aspects of the exozodiacal dust problem for a future exo-Earth imager. First is the issue of how to convert the observed 10-μm dust emission to an optical surface brightness: a value for the dust albedo must be adopted in order to predict the exozodi background that Exo-S will encounter. Secondly, the HOSTS survey data, integrated over the fringe pattern of a nulling interferometer, will provide little information on the spatial distribution of the exozodiacal dust. While the HOSTS survey will certainly aid mission planning for Exo-S in helping to constrain overall dust levels, the Exo-S probe itself will be sensitive to disks as faint as 0.1 times as bright as the solar zodiacal cloud. As an exceptionally powerful probe of this astrophysical noise source, Exo-S will provide information that will help guide planet-imaging missions for decades to come.

High levels of exozodiacal dust emission lengthen the exposure times required to detect planets. Precursor knowledge from LBTI of prohibitively high dust levels around particular stars will be used to exclude targets before the mission commences. For stars with unexpectedly high dust levels, Exo-S will briefly observe the system to characterize the dust, then move on to other targets.

3.1.2 Background Sources—Extragalactic

Away from the galactic plane, the Exo-S probe will essentially see a Hubble Ultra Deep Field (HUDF) for every imaged target star. The primary concern is a veritable ocean of (1) brighter (V<28) extended galaxies and (2) ultra-faint unresolved galaxies (mostly V>28) displaying a wide range of colors ($-2 < B–V < 2$) and tending toward the extreme blue at the faintest magnitudes (Coe et al. 2006; Pirzkal et al. 2005). In cases where an unresolved background galaxy falls within the expected multicolor range for planets, proper motion

discrepancies and spectroscopic follow-up will be able to disambiguate these sources upon the second visit to the target star, as described in Section 2.3.6.

Figure 3.1-1 shows a 1 arcmin^2 field-of-view (FOV) at high galactic latitude, extracted from the Hubble Extreme Deep Field (XDF, Illingworth et al. 2013). The deepest part of the XDF has a limiting magnitude near V~31, and contains 7,121 galaxies above the 5-sigma significance level in ~4.7 arcmin^2. This corresponds to ~1,500 galaxies in the 1 arcmin^2 FOV of the Exo-S imaging camera. Galaxy counts from other surveys (Windhorst et al. 2011) indicate a few dozen galaxies per FOV at V<25 should be expected, and these brighter, extended, non-uniform sources could make planet detection difficult wherever they dominate the FOV. Meanwhile, examination of the XDF reveals significant image crowding at V~30, where 45% of the pixels contain galaxy light (Koekemoer et al. 2013).

Multicolor photometry of faint sources is available through a variety of deep sky surveys undertaken by the Hubble Space Telescope. The Cosmic Assembly Near-infrared Deep Extragalactic Legacy Survey (CANDELS) is a large HST 'multi-cycle treasury' program to unify data previously acquired on five major deep-fields. "Covering approximately 800 arcmin^2, CANDELS will image over 250,000 distant galaxies within five popular sky regions which possess rich existing data from multiple telescopes and instruments: GOODS-S, GOODS-N, UDS, EGS, and COSMOS" (Guo et al. 2013).

Figure 3.1-1. A one arcmin^2 FOV (corresponding to the planet detection field for the Exo-S imaging camera), extracted from XDF (Illingworth et al. 2013). About 1,500 extragalactic sources down to V~31 are present in this image.

Source catalogs presenting ultraviolet (UV) to the mid-infrared (IR) photometry are currently available for the Great Observatories Origins Deep Survey southern field (GOODS-S) field as observed in CANDELS: http://candels.ucolick.org/data_access/GOODS-S.html. This particular mosaic reaches a 5 σ limiting depth of 27.4, 28.2, and 29.7 AB for CANDELS wide, deep, and Hubble Ultra Deep Field HUDF regions. The catalog contains 34,930 sources in an area of 173 arcmin^2, 30,547 of which have complete ACS photometry in the B to I range (F435W, F606W, F775W, F814W corresponding approximately to B, V, R, I). Each pointing has an individual limiting magnitude; hence, the faint magnitude cutoff spans a range depending on its location within the survey field. The source density to the average limiting magnitude is about 200 sources per armin^2, consistent with estimates above, and representing a lower limit to the extragalactic contamination rate. The XDF, going about 2 magnitudes deeper, finds about 7× higher source density. If the source density is indeed 1,500 arcmin^{-2}, the probability of encountering an object within a 1 arcsec^2 FOV (comparable to the FOV of the Exo-S IFU) is ~40% for magnitude ~31. Not only that, the color distribution for these faint objects (**Figure 3.1-2**) is very broad and encompasses the range of expected planet colors. Thus, for faint planet candidates, the faint galaxy population is likely to be a significant confusion issue. Our knowledge will improve as the data catalog releases from the XDF proceed, removing the

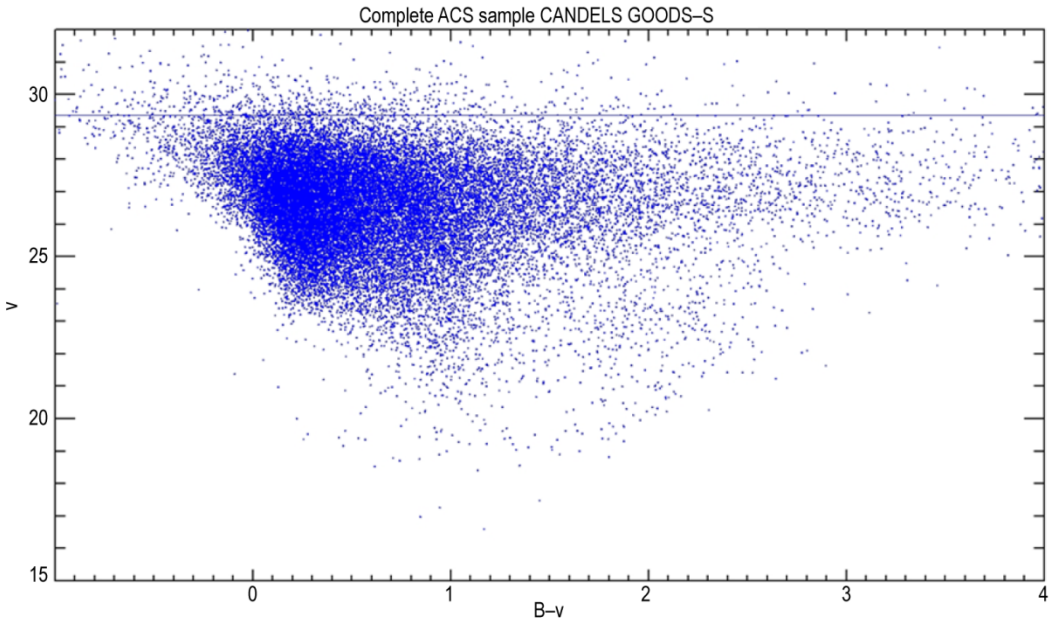

Figure 3.1-2. Color-magnitude diagram for faint extragalactic sources, derived from CANDELS GOODS-S catalogs covering 173 arcmin^2. The horizontal blue line indicates the approximate catalog completeness limit.

necessity for extrapolation to magnitudes fainter than the cutoff, e.g., in the CANDELS data.

3.1.3 Background Sources—Galactic

At low galactic latitudes, background stars will be present in the Exo-S planet search field. As the starshade acquires its target, previously unseen 'bright' background stars (V = 10–20 mag) will emerge within the Exo-S FOV and potentially overwhelm portions of the detector for planetary companions. Meanwhile, fainter background stars may masquerade as planet candidates. Star counts are expected to be near 100,000 stars per square degree for $10 < V < 20$ mag (or about 25 bright stars in every 1 arcmin^2 planet camera field), and 500,000 stars per square degree for the range $20 < V < 25$ (i.e., as many as 100 faint stars in each 1 arcmin^2 planet camera field; Binney and Merrifield 1998). At V>25, the star counts must eventually decline due to the finite size of the galaxy, but variability in galactic extinction make this somewhat unpredictable for any given field of view.

Figure 3.1-3 shows a $5' \times 5'$ field of background stars near η Cas A (HIP 3821) down to a limiting magnitude near V~22 (from the Space Telescope Science Institute [STScI] Digitized Sky Survey, POSS2/UKST [Second Palomar Sky Survey/UK Schmidt Telescope] blue image). This target is currently part of the

Figure 3.1-3. A 5' × 5' field of background stars near η Cas A (HIP 3821) to a limiting magnitude near V ~ 22 (from the STScI Digitized Sky Survey, POSS blue image), illustrating the number of 'bright' background stars likely to appear in planet search images. The Exo-S FOV is 1'× 1'. This target star is currently part of the Exo-S DRM for the exo-Earth search.

Exo-S Design Reference Mission (DRM) for the exo-Earth search. To reduce contamination from brighter background stars, it may be necessary to co-add short exposures, or to commence observations with relatively short exposures and increase exposure times if no bright background stars are present. Another approach is simply to design a mission program that avoids targets in regions of known or suspected high stellar background density. Finally, many Exo-S targets are high proper motion stars, and mission programming would be aided by deep imaging with the Hubble Space Telescope (HST) or James Webb Space Telescope (JWST), several years in advance of the direct imaging mission. In this case, the exact distribution of background sources could be characterized and the observing protocol adapted accordingly.

Fainter background stars (V>25) will be significantly reddened, and therefore it may be possible upon the first visit to distinguish them from planet candidates through broadband color data. However, it is clear that in broadband measurements, planets shining in reflected starlight will display a wide range of colors, just as stars do.

To quantitatively estimate the likely background contamination and colors of galactic stars, we utilize the Besançon stellar population synthesis model available at http://model.obs-besancon.fr/, described by Robin et al. (2003). The model utilizes a self-consistent galactic gravitational potential in agreement with Hipparcos results and measurements of the galactic rotation curve. The model is tuned to produce reliable statistics from U through K bands, and is based on the star formation history of the thin disc, thick disc, spheroid, and bulge of the galaxy.

Figure 3.1-4 shows typical color-magnitude figures for galactic longitude zero. To derive these representative plots, simulations were generated using Besançon model defaults, and a solid angle of 0.01 square degrees (36 arcmin^2) subsequently

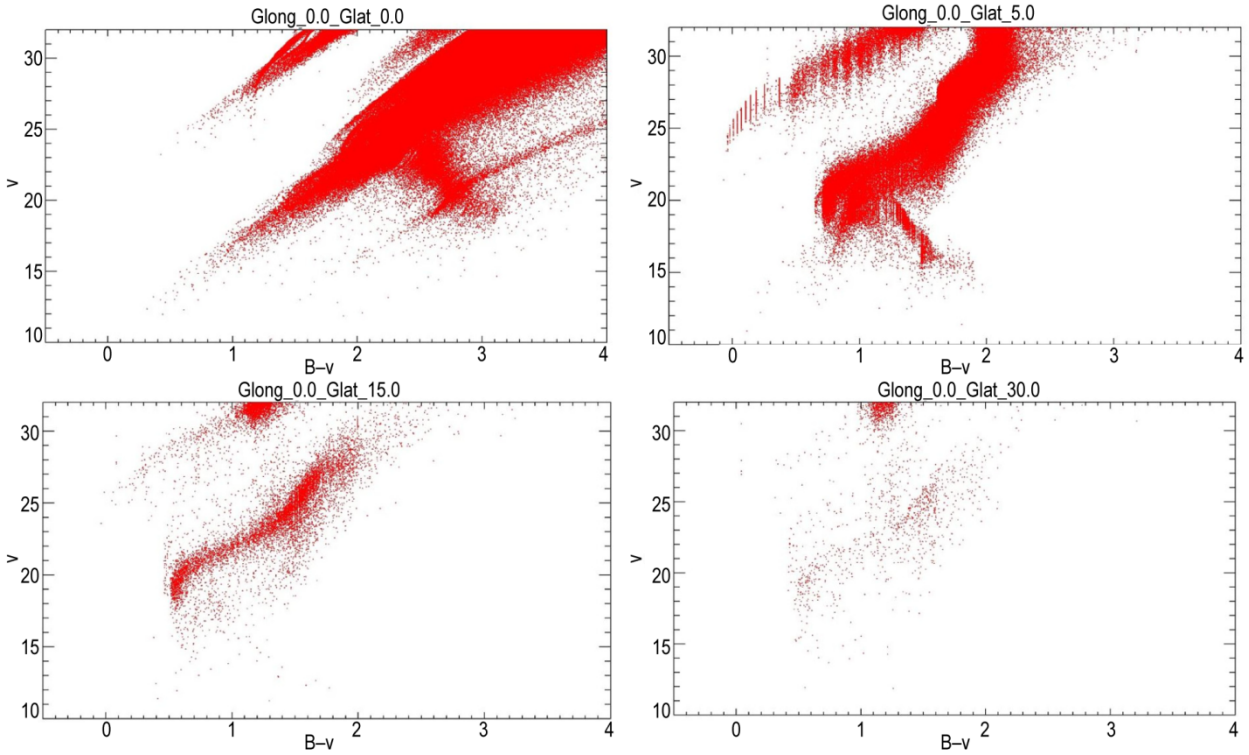

Figure 3.1-4. Color-magnitude figures from the Besançon model of the galaxy, shown for galactic longitude 0° and latitudes 0°, 5°, 15° and 30°. Above *b*~30°, the probability of finding a galactic star in an area of 1 arcsec^2 falls below 1%.

normalized to derived densities per square arcsec. In principle, analyses can be carried out for all targets individually, to assess the probability of galactic star contamination as a function of anticipated planet magnitudes. Here, general trends are identified. **Figure 3.1-4** shows that the colors of galactic stars span a wide range. However, the majority of faint stars are also heavily reddened, reflected in the star colors. Hence, discrimination of planets on the basis of colors may be feasible in such regions of the color-magnitude diagrams.

If the local density of stars is n stars/area, then the probability of finding no stars within the unit area is $p=e^{-n}$; therefore, the probability of finding at least one star within an arcsecond is $1-p=1-e^{-n}$. **Figure 3.1-5** shows the derived probability of finding at least one star within one square arcsec of the target (r=0.56 arcsec) for a range of galactic latitudes. The results are recast in **Figure 3.1-6** as the probability of finding at least one galactic star brighter than V=30 and 25, as a function of galactic latitude for galactic longitude zero. The results are insensitive to the value of V magnitude for V~25 or fainter. In conclusion, for galactic latitudes above 30° (or below -30°) the probability of a contamination by a galactic star is less than 1%. However, at all galactic latitudes, the probability remains greater than 10^{-3}. Almost one third, 26/96, of the target sample is within 10° of the galactic plane (|b|<10).

3.1.4 Light from Companion Stars

Many stars of highest interest have known stellar companions, and their presence will inevitably introduce scattered light into the image plane. Assuming that this represents a smooth background, a longer exposure time is required to reach the desired signal to noise for detecting Earth or Jupiter analogs. This will *not* rule out all binary stars, but targets with bright companion stars at small separations may be severely compromised.

In work done prior to the Exo-S study for a 4-m class mission, the relative increase in exposure time to detect an Earth-like planet in the habitable zone was calculated for stars that have separation and magnitude data for companions in the Washington Double Star catalog (priv. comm. C. Noecker). Calculations on the impact of multiplicity may also be carried out using Spyak and Wolfe (1992) and

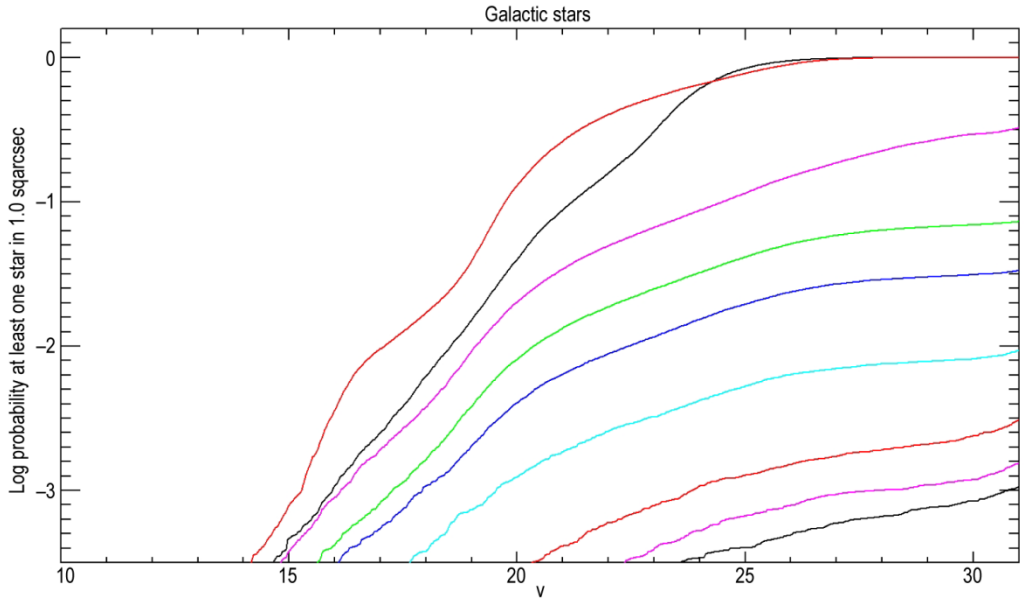

Figure 3.1-5. Log_{10} probability of finding at least one galactic star within 1 arcsec as a function of galactic star V magnitude. The lines are for b=0°, 5°, 10°, 15°, 20°, 30°,45°,60° and 90°, top to bottom (the upper black line deficient in the brighter stars, is the heavily reddened b=0°).

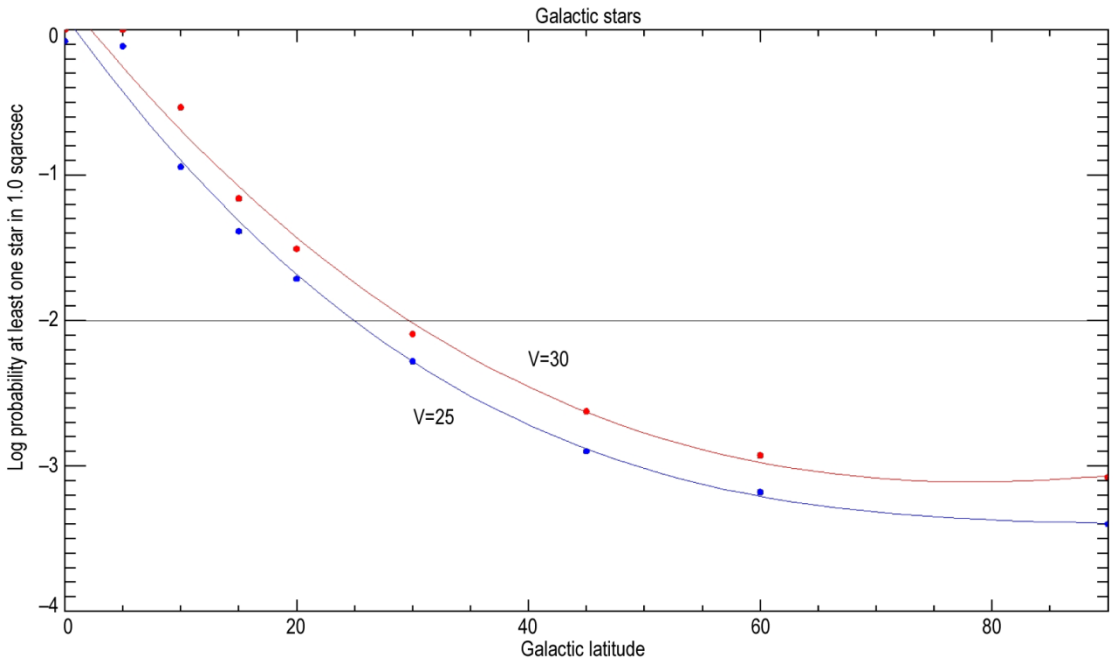

Figure 3.1-6. Symbols show the derived probability of finding at least one galactic star of magnitude V=30 or brighter (red) and V=25 or brighter (blue) with 1 arcsec^2. The probability is insensitive to star magnitude. The horizontal line shows where the probability falls below 1%, at |b|~30°.

Kuhn and Hawley (1999) stray light model predictions.

The key qualitative findings from these calculations are:

1. According to these model predictions, the presence of a companion has little or no effect on integration time for angular separation more than ~40 arcsec. Systems such as α Cen A and B are potentially quite problematic due to the combination of small angular separation and similar brightness of the two components.
2. At smaller separations, stray light from companion stars must be modeled in detail. Many binary star systems with separations less than 40 arcsec will still remain viable targets (e.g., η Cas A) if they are very nearby and/or the magnitude difference of the two components is large.

As elements of preparatory science, stray light calculations will be carried out to assess how exposure times will be affected for all candidate targets that have stellar companions. These calculations will consider the ever-changing separations of the two components, the effects of additional stars in systems with three or more components, and whether both components of very tight (spectroscopic) binaries can be effectively suppressed simultaneously.

The current Exo-S DRM avoids targets where stellar companions are likely to introduce high levels of stray light (see also Section 3.4.1).

3.2 Strategies for Candidate Confirmation

Exo-S will detect many planet candidates, a fraction of which will turn out not to be exoplanets. Described below is a set of strategies for eliminating astrophysical false positives and for confirming bone-fide exoplanets.

Table 3.2-1 summarizes the many distinct methods available for discriminating between exoplanets and background sources. Rigorous identification of a candidate as a planet will require precursor observations, and in some cases repeat observations. It is important to take full advantage of simple photometric discriminants as they are identified. In the

Table 3.2-1. Strategies to distinguish between planets and contaminants. Red text is used to identify strategies that can give immediate confidence that target candidates are planets' italics highlight "Applies to all".

Strategy	Applies to	Comments
Known position	RV planets	
Color/color/magnitude analysis	***All***	Imperfect due to color overlap with confusing objects
Spectrum analysis	Brighter planets	Requires investment of significant amount of observing time
Common proper motion within a month	High proper motion stars—includes many high priority targets	Requires investment of significant amount of observing time
Common proper motion after a revisit	*All*	Requires revisit, potential to 'lose' candidates
Common parallax	Nearest stars	Requires investment of significant amount of observing time
Orbital motion of planet	Close-in planets	Likely to require significant amount of observing time
Polarization properties	Brighter planets within a planetary system	Provides immediate confirmation for brighter planets
Time-dependent photometry—is there a periodic signal, variability?	*Rotating, structured planets—likely to be ~all*	Requires sensitive time series of substantial duration
Stellar variability light echo	Variable stars	Requires sensitive time series of substantial duration
Precursor observations	Best studied stars (archival)	Provides (limited) information on astrophysical context

event that background contamination is deemed too problematic, the target can simply be excluded from the sample.

3.2.1 Known Giant Planets

For the known giant planets, median magnitudes are all brighter than V=30; 8 of 14 are brighter than V=29, and 7 of 14 are brighter than V=28. The magnitude range is calculated assuming a Jupiter-radius and Jupiter-albedo planet, given the known orbital parameters, the date of observation, and all possible inclinations. Of those fainter than V=29, all but one have galactic latitude >30 deg so galactic star contamination is unlikely. An inspection of the data in the HST extreme deep field (XDF; Illingworth et al. 2013) provides estimates of about a 5% probability of encountering an extragalactic source brighter than V=30, and only about 2–3% for V<29, within approximately 0.25 arcsec^2, the approximate width of the allowed annulus on the sky for the giant planets to appear at the date of observation. Therefore, the background contamination by extragalactic sources is unlikely to be significant for these planets.

3.2.2 Photometric Analysis

Discrimination between a planet and a potential background astrophysical object based solely on standard magnitude and color systems is extremely challenging (**Figures 3.2-1** and **3.2-2**).

Figure 3.2-1 shows a color-magnitude diagram for combined galactic and extragalactic background sources for galactic latitude b=10° (described in Section 3.1.3). Solar system planets around neighboring stars would lie in the region of the diagram dominated by extragalactic background sources, with V in the range approximately, 25–30 and B-V roughly 0–2. The color-color diagram in **Figure 3.2-2** shows the distribution of the galactic and extragalactic samples in B-V/V-R. The positions of the solar system planets and moons are indicated. For Earth, the colors change due to diurnal rotation coupled with changing surface and cloud patterns, and phase variations as the Earth's aspect relative to the Sun changes.

Specially crafted bandpasses have the potential to provide much better discrimination targeted at specific planetary features, providing a physical basis for distinguishing between planets and stars. For example, a large water band absorption feature would not be present in a typical stellar atmosphere. An extreme example of a filter designed to select oxygen bearing planets is to focus on the 255 nm Hartley band of ozone. On Earth, that

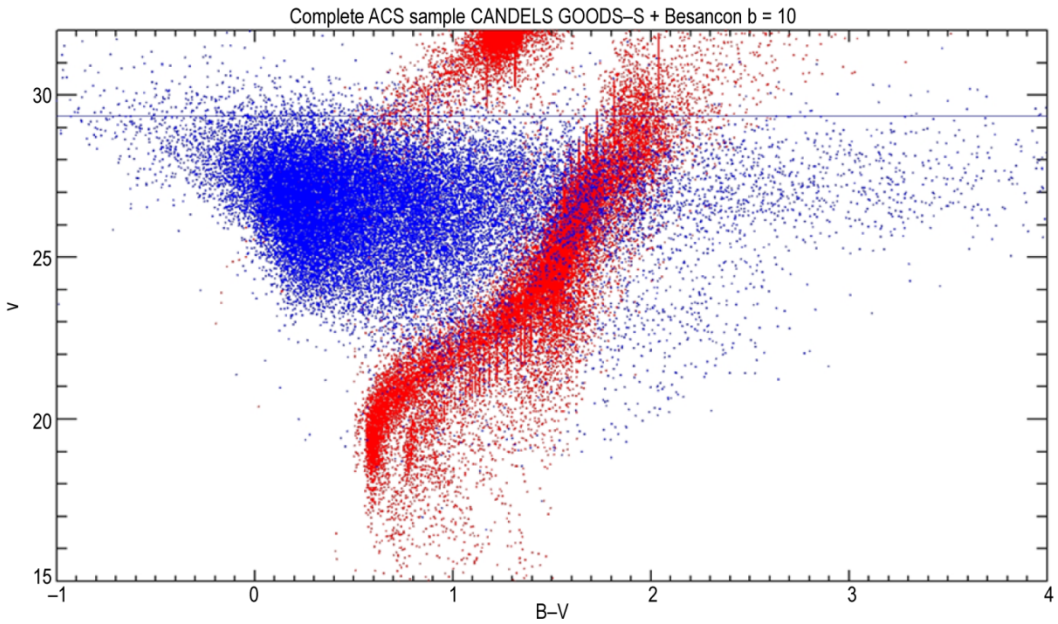

Figure 3.2-1. Color-magnitude diagram showing faint extragalactic sources (blue) together with galactic stars (red) for *b*=10°. The horizontal blue line indicates the approximate completeness limit for the extragalactic source catalog. The theoretical statistical model of the galaxy does not exhibit incompleteness.

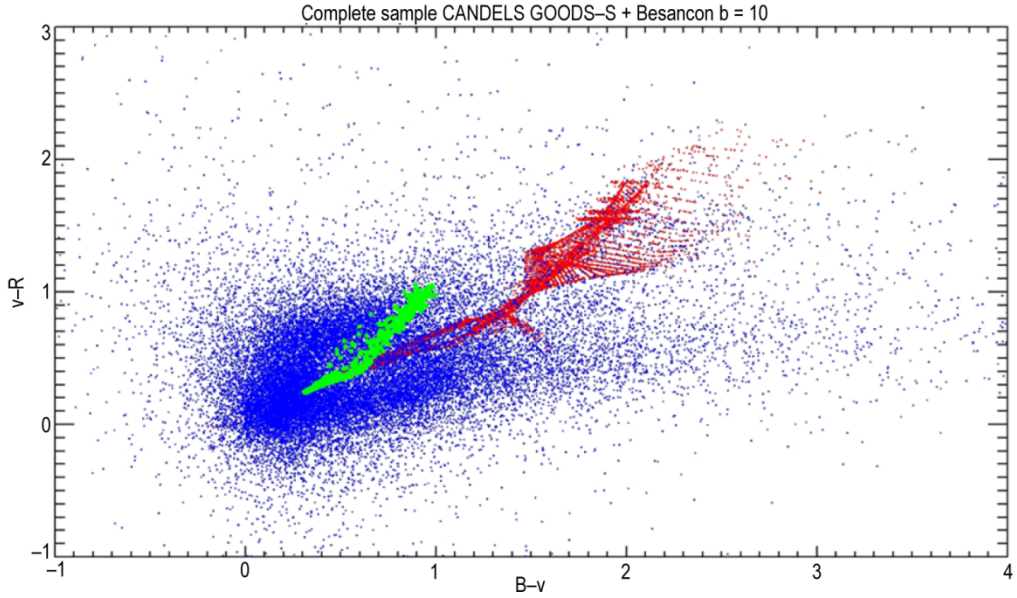

Figure 3.2-2. B-V versus V-R for model galactic stars (red) and extragalactic sources (blue). Also included (green) the track of the Earth, showing diurnal and phase variations (Schwieterman et al., in prep).

feature represents a change in the Earth's flux by several orders of magnitude, a strong feature not present in stellar photospheric spectra (Robinson et al. 2014). The near-UV (NUV) is not, however, accessible to Exo-S, but could be relevant to other mission designs. With an observing strategy that utilizes the IFU to always obtain spectra, there is an opportunity to construct post facto a selection of photometric bandpasses specifically designed to distinguish planets and stars.

The power of using customized bandpasses can be demonstrated by showing its effectiveness with solar system planets (for which, of course, the spectra are known). As a 'proof of concept', **Figure 3.2-3** shows object

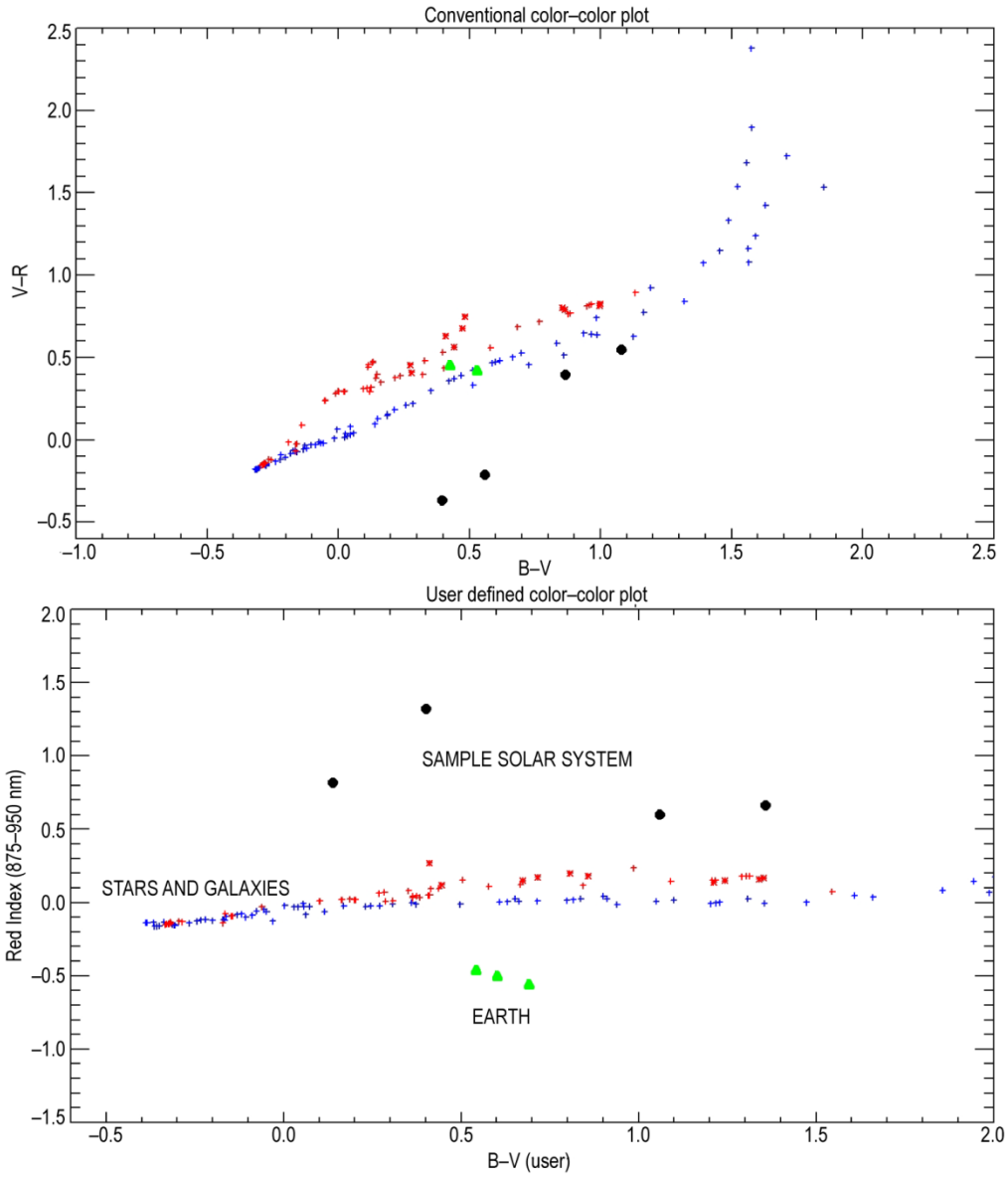

Figure 3.2-3. Red and blue points are galaxy models, black points are solar system targets (Jupiter, Saturn, Uranus and Titan) and green points are derived from spectra of the Earth. Upper panel shows conventional two-color diagram, while lower panel recasts the plot using specially defined bandpasses. Note that exoplanet simulated spectra may have colors different from the planets shown here.

colors calculated from a set of model spectra derived from catalogs in the HST Calibration Database (http://www.stsci.edu/hst/observatory/crds/astronomical_catalogs.html). The top panel shows the distribution of points in standard BVR space, while the bottom panel shows colors in an example set of user-defined bands. The red points are galaxy models from the Kinney-Calzetti atlas, and Bruzual-Charlot evolutionary models, and the blue points are from the Bruzual stellar atlas. Black points are solar system targets (Jupiter, Saturn, Uranus and Titan) and green points are derived from three spectra of the Earth. The user-defined bandpasses are rectangular centered at 450, 625, 875, 950 nm, with widths of 100, 50, 50, 75 nm respectively. In the bottom panel, the horizontal axis, B-V (user), is the user-defined (450–625) index expressed in magnitudes, and the y-axis is the user-defined red (875–950)

index in magnitudes, sensitive to strong molecular absorption in the planet spectra. Other similar bands may also be defined to focus on different spectral features.

The discrimination between planets and background sources using the custom bands is an effective technique, but is dependent on the ability to process the integral field spectrograph (IFS) spectra post facto, or to design a customized set of imaging filters in the event that a detection camera is utilized.

3.2.3 Spectrum Analysis

Planets and background sources have fundamentally different spectra, as the former are likely to have molecular atmospheres while the latter will generally have distinctive spectra that are well understood from a wealth of other observations (the exception might be bare rock Mercury-like planets). Therefore, one obvious way of discriminating between planets with atmospheres and background sources is with spectroscopy. If spectra with sufficiently high S/N and spectral resolution can be acquired, then this means will automatically distinguish the planets through the detection of molecular absorption features. The S/N and resolution necessary to do this for different types of planets and background sources is the subject of future study. It is likely that spectra of sufficient quality to robustly distinguish between planets and background sources can be obtained for most of the giant planets (Jupiters and Neptunes) observed with Exo-S but probably not the faintest planets (sub-Neptune-size to Earth-size planets.).

3.2.4 Proper Motion, Parallax, and Orbital Motion

Many of the targets in the Exo-S sample are high proper motion stars, and some of the most promising candidates are amongst the highest. If the stellar motion against the backdrop of galactic and extragalactic sources is sufficiently high, and the candidate is physically associated with the star, they will move together. Similarly, as the target stars are amongst the nearest, common parallax may provide a means to determine if a candidate is close to the target in distance. The degree to which common proper motion and parallax may be identified depends on the accuracy to which the planet's position can be measured relative to the star and hence to their background.

To exclude a planet as a candidate, it is necessary to measure its motion relative to the host star and known direction of proper motion of the star, which is assumed to be perfectly centered behind the starshade. It is also assumed that the PSF has diffraction limited to full width at half maximum (FWHM) at 760 nm of 0.146 arcsec and 0.067 arcsec, corresponding to telescopes of aperture diameter 1.1-m and 2.4-m, respectively. The standard deviation is $\sigma = \mathrm{FWHM}/2\sqrt{(2\ln 2)}$, and for a measurement with signal-to-noise ratio (SNR), the uncertainty in a position measurement (in *x, y*, or radius *r*) is σ/SNR. The DRM observing strategy is crafted such that in search mode, an Earth in the habitable zone of the host star would yield an SNR=6. Hence, the uncertainty with which the positions of Earth-like planets can be measured is ~0.01 and 0.005 arcsec for the 1.1-m and 2.4-m telescopes, respectively. For a 5σ detection of motion, the distance moved needs to be 0.05 arcsec or 0.024 arcsec, respectively. It is assumed that post-processing methods allow retrieval of this accuracy from a slowly moving target, even though strictly speaking it applies to the final integrated summed PSF. [Note: Due to errors in x and y combining in quadrature, measurement of radius r is positive definite and distributed according to the Rice distribution. A small correction for the positive bias to r needs to be applied. Uncertainty distributions will be well characterized and standard correction techniques will apply.]

The proper motions and parallaxes for all targets are known. The horizontal and vertical lines in **Figure 3.2-4** indicate the detection limits for proper motion and parallax within a single month of observing. Orbital motion will also be an ingredient of the apparent

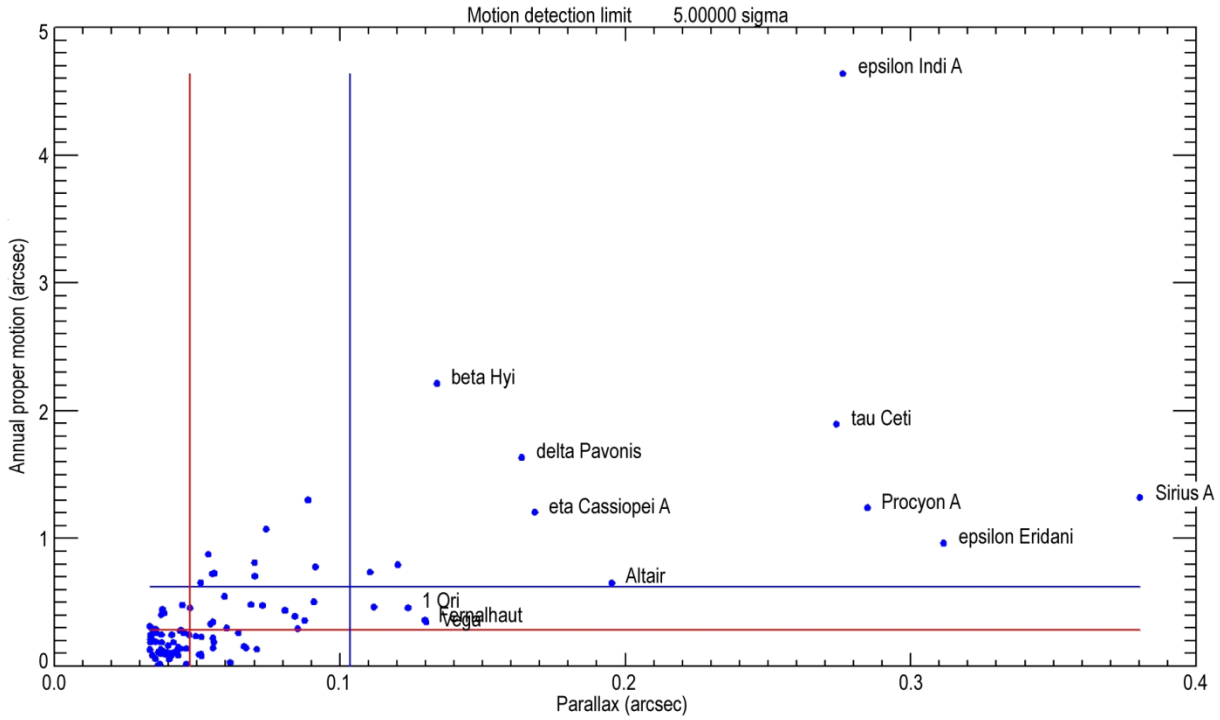

Figure 3.2-4. Exo-S targets' distribution of parallax and proper motion, with lines indicating motion detection sensitivity for the Dedicated Mission 1.1-m (blue) and Rendezvous Mission 2.4-m (red) telescopes over 1 month.

movement of a planet, and will need to be inferred as a residual from known proper motion and parallax.

There are several confirmation strategies that are reliant on time dependence in the Exo-S images, which are described in the following subsections:

Common Proper Motion within One Month

Common proper motion is a powerful discriminant for confirming exoplanet candidates, but the observing impact on the DRM is substantial. Orbit evolution may carry the planet too close to the star for detection upon a first revisit. However, essentially all targets lend themselves to proper motion measurement after a year. The highest proper motion targets in this sample can be detected in only a month of observing (see **Figure 3.2-4**).

Common Proper Motion after a Revisit (One Year)

If revisits are required to establish whether a source is a planet, then the impact on the DRM is substantial. Further, if the object of interest that triggered the revisit was in fact a planet, the planet's orbit may have moved it too close to the star for observation in later visits. Nevertheless, essentially all targets lend themselves to proper motion measurement after a year.

Common Parallax

The amount of motion induced by the target's parallax depends on the Exo-S orbit and time of observation. Parallax motion is maximized over a 6-month baseline, with the target direction orthogonal to the line joining the two observations. Exo-S cannot be optimized for parallax measurement due to solar avoidance constraints; therefore, low emphasis is placed on this strategy. Nevertheless, in one month, the telescope will move ~0.5 AU. In favorable cases, this yields motion of ~0.5ϖ where ϖ arcsec is the parallax of the star. This is the underlying assumption for **Figure 3.2-4** and **Table 3.2-2**.

Planet Orbital Motion

In one month, the Earth moves 30° around its orbit. If S is the angular separation of an Earth-like planet from its host star, the orbital motion will be ~0.52 S, if the orbit is viewed pole-on.

Table3.2-2. Number of targets from a sample size of 96 that have sufficiently large motion to allow measurement.

	Dedicated Mission 1.1-m	Rendezvous Mission 2.4-m
Proper motion in 1 month	20	43
Proper motion in 1 year	92	93
Parallax in 1 month	15	49

For a 1.1-m telescope, the limit in motion is 0.05 arcsec, hence S~0.1 arcsec, corresponding to a distance of 10 pc for an Earth twin. For the 2.4-m, the accuracy is twice as high, and hence orbital motion can potentially be seen to 20 pc. The orbital motion parameter can be calculated individually for any given star or planet, though unlike proper motion and parallax, the direction is unknown, as is the orbital inclination. For higher inclination orbits, the amount of motion is reduced, and minimized at planetary elongation where planet visibility is maximized.

In conclusions:

- For essentially all targets, proper motion can discriminate between planets and background objects after a year.
- For the majority of the highest priority targets, confirmation of a planet candidate can be done after a month or less using either proper motion, parallax, or both.
- A significant, but unknown, number of planets are likely to exhibit detectable orbital motion within a month.

3.2.5 Polarization Properties

Planets shining by light scattered from their host star are expected to exhibit polarization at a level of a few percent up to many tens of percent. If polarization is detected, the position angle of the polarization electric vector is a discriminator. If it is orthogonal to the line joining the candidate to the star, then this is a strong indicator that the candidate is a planet—seen in reflected light that is polarized via scattering in its atmosphere or from its surface. The density of background polarized sources is not known, but is certainly much lower than the density of all background sources, and if a further discriminant is applied, which is that the electric vector position angle be within, say, 5° of the tangent vector, a further reduction would be obtained in the probability that the source is background. Exozodi disks are also likely to be polarized, and polarized flux images (as opposed to polarization degree) are analogous to direct images in which separate identification of planet and disk must be done. As in non-polarized direct imaging observations, an exozodi clump could masquerade as a planet, although they may differ in their degree of polarization.

The uncertainty on polarization scales with the SNR per image, while the uncertainty on polarization position angle scales with the product of polarization and SNR (Miller, Robinson, and Goodrich 1987). For a position angle uncertainty of 10°, a 3 σ detection of polarization degree is necessary, which requires an SNR of 4–8× that of the faintest detection in the field (assuming a 5 σ detection limit). Thus, polarimetry candidate identification can be applied to planets that are modestly brighter than the faintest detectable planets. Note that for polarimetric determination, unlike photometric characterization, the entire spectrum can be used; therefore, some reduction in this SNR factor will be possible, by about a factor 2 in favorable circumstances.

As well as serving as a discriminator for exoplanet candidates, polarimetry offers a variety of diagnostics that will enhance the scientific yield of the mission, including information on the geometry and properties of exozodi dust, and possible sensitivity to planetary clouds, hazes, and oceans.

3.2.6 Time-Dependent Photometric Properties

The amplitude of diurnal variations of reflected planetary light can be significant, up to tens of percent, and has the potential to offer a circumstantial discriminant against background sources (Ford, Seager, and Turner 2001). A model of the Earth as viewed from the Moon shows substantial color (and magnitude changes (Schwieterman et al., in

prep). The color (and magnitude) changes are substantial. While any individual exposure, of order an hour or less, will have insufficient signal to track the photometric light curve of the candidate accurately, a classical time series analysis of the complete observation has the potential to reveal weak periodic signals within the noisy time series. Without doubt, specialized software tools can be developed, optimized for the particular circumstance of the Exo-S mission (Pallé et al. 2008).

3.3 Preparatory Science Recommendations

The most effective use of Exo-S observing time, as well as the most complete scientific understanding of its results, requires an up-front investment in preparatory science: supporting observations, database research, modeling, and theory. Some of the key activities are described in this section.

3.3.1 Precursor Imaging Observations

Precursor observations of Exo-S target stars have the potential to reveal any major problems with individual targets. These can include bright nearby stars, bright background galaxies, and nebulosity. However, even in the presence of large proper motion, nearby stars will not move beyond the scattered light halo of the target star (see **Figure 3.3-1**). Therefore, extremely deep HST images are not feasible, even without consideration of the large amount of time that might be required. Future space based precursor observations with JWST of WFIRST/AFTA could potentially provide a better view of the background vicinity, if their coronagraphs are employed.

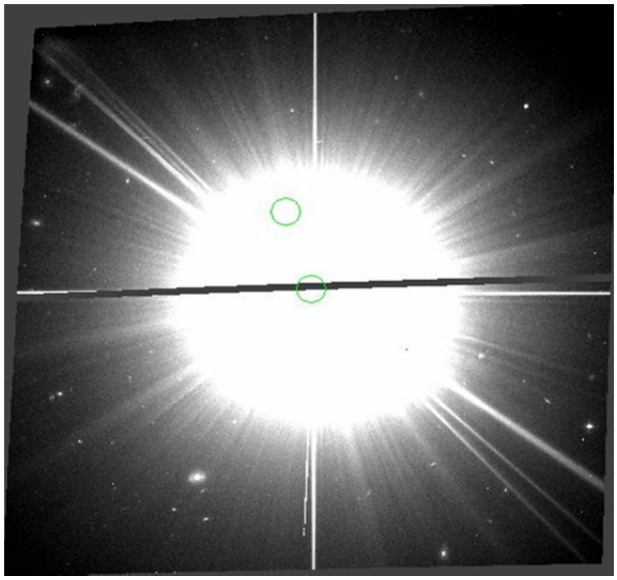

Figure 3.3-1. HST ACS image of Epsilon Eri, 200 arcsec on a side. The circles are 5 arcsec radius, separated by 30 arcsec equivalent to proper motion of 3 arcsec/yr for 10 years.

Nevertheless, since the Exo-S target stars are amongst the nearest and most well-studied stars in the sky, there is a considerable body of archival HST imaging data already available. **Table 3.3-1** gives a representative view of the Mikulski Archive for Space Telescopes (MAST) contents for those observations ingested into the Common Archive

Table 3.3-1. Target star entries currently in MAST.

Star ID	MAST CAOM entries	Star ID	MAST CAOM entries
Fomalhaut-HIP113368	406	HIP57632	10
HIP27321	375	HIP77622	10
epsilonEridani-HIP16537	157	HIP65109	8
Vega-HIP91262	156	HIP109427	6
ProcyonA-HIP37279	122	HIP27288	6
SiriusA-HIP32349	86	HIP78072	6
tauCeti-HIP8102	43	Regulus-HIP49669	4
Altair-HIP97649	40	HIP114996	3
HIP32607	22	HIP746	3
HIP3419	16	etaCassiopeiA-HIP3821	2
HIP17378	14	HIP27072	2
HIP53910	13	HIP93747	2
HIP76267	11	1Ori-HIP22449	1
alphaAnd-HIP677	10	HIP116584	1
HIP116727	10	HIP94376	1

Observation Model (CAOM). **Table 3.3-1** lists the number of images derived from a search of the primary HST imaging cameras, ACS, WFC3, STIS-CCD, and WFPC2. Inspection of these images certainly will be worthwhile, and could be a potential subject for an HST archival proposal. If other resources are available to enable the analysis, the data are publically available.

3.3.2 Theory and Modeling

There is a great deal of theoretical and modeling work that needs to be done in advance of the launch of Exo-S or any space-based direct imaging planet discovery mission.

Exozodi will have asymmetries and other features caused by planets. Dynamical simulations of the effects of planets on exozodi have the potential to improve the observation strategy of Exo-S by way of exozodi subtraction for planet detection. Such simulations would also help understand the potential for exozodi observations to deliver additional information on the planets themselves

Research on planet spectral features and their retrieval from R=70 or lower resolution spectra will improve the science return from the mission. This will require synthesis of expertise from planetary scientists that have a rich history in obtaining and interpreting solar system spectra, astronomers with expertise on transit spectra of exoplanets, and Earth scientists that continually advance our techniques for interpreting remote sensing spectral information. Specific challenges include, but are not limited to, the effects of clouds and aerosols on spectra, the uncertainties associated with measurements of specific spectroscopic features, and the degeneracies that exist in the identification of a particular feature or set of features.

Finally, advances in our understanding of 'exoplanet systems science' in the spirit of 'Earth systems science' is required. Earth scientists understand that our home planet's atmospheric properties are a part of complex relationships with other system components in the planet. Interactions with the biosphere, hydrosphere, cryosphere, and planet interior all have profound effects on the atmosphere; in turn, the atmosphere affects these other systems. As a result of these interactions, a complete understanding of any measurement of the atmosphere requires an integrated, interdisciplinary approach. While direct measurements of exoplanet surfaces and interiors will not be possible for Exo-S targets, this interdisciplinary approach will enable maximum scientific return from observations of these worlds. Ideally, this would mean having generalized models that can rapidly simulate planets with a wide range of surface and subsurface system properties. Additionally, it would benefit greatly from having a generalized global climate model, well-validated against current Earth and solar system observations and flexible enough to simulate planets much larger than Earth.

The science return from Exo-S would be optimized if the exoplanet research community received the benefits of a sustained and significant intermodal comparison effort.

3.3.3 Limits on Undiscovered Planets

Most of what is currently known about nearby planetary systems comes from radial velocity (Doppler) monitoring surveys (http://exoplanet.eu/). For Exo-S and other direct imaging missions, Doppler surveys provide two essential precursor science products: (1) Neptune- to Jupiter-mass targets of opportunity for spectroscopic follow-up, as included in the DRMs described in Section 5, and (2) constraints on planets are *not* present in those systems. For some nearby stars, the Doppler technique has completely surveyed for giant planets within several AU orbits, but many Exo-S targets have not been probed with Doppler spectroscopy. Much remains to be learned in the near term from a dedicated monitoring effort.

As a key part of preparing for a direct imaging mission in the next decade, Exo-S targets for both Case 1 and Case 2 mission programs should be included in a high precision, high cadence monitoring campaign, such as that now planned for the WIYN observatory.

In support of the present study, Howard and Fulton (2014; hereafter 'HF14') examined Exo-S target stars with historical Doppler measurements in the California Planet Survey (CPS) in order to place upper limits on the masses of any potential planets not detected in each system, and to identify targets where gains can still be made by continued Doppler monitoring. Among 127 high priority targets for the Exo-S Case 1 'habitable zone maximization' approach, HF14 found 57 stars with radial velocity measurements. Of the remaining 70 Exo-S target stars, 24 are too far south to be observed by the California program, which was carried out at the Lick and Keck Observatories. Other targets missing from the Doppler lists have early spectral types (<F4V, 19 targets), are evolved beyond the main sequence (3 targets), or are binaries (22 targets). These types of targets are typically excluded from Doppler surveys because photospheric jitter, fewer spectral lines, higher average rotation rates, surface oscillations, and/or modeling difficulties (in the case of binaries) all cause decreased precision in detecting planet mass companions. HF14 did not examine the full input list for the Exo-S Case 2 'maximum planet diversity' approach, which was developed late in the Exo-S study. However, given the larger number of early type stars included in the Case 2 observing program (e.g., Sirius, Procyon, Fomalhaut), it appears unlikely that many additional Exo-S targets would be found among the CPS lists.

For targets in the Exo-S survey, the existing Doppler measurements are typically sensitive to Saturn-mass planets inside of 1 AU and Jupiter-mass planets inside of ~3 AU. In the best cases, the measurements are sensitive down to approximately Neptune-mass planets within 3 AU orbits. However, there is great potential to improve upon this within the next decade by a dedicated Doppler monitoring program. Key recommendations resulting from the HF14 study, and supported by the Exo-S STDT, are as follows:

1. For main sequence G and K dwarfs, a 10-year survey could be complete to super Earths (M_p sin i = 10 $M_\oplus$) in few AU orbits. All target G and K dwarf Exo-S targets should be observed at least 10 times per year with as high a precision as possible (≤2 m s−1) to detect or place limits on super Earths and Neptune-mass planets in few AU orbits.
2. For evolved stars, Doppler detection of giant planets in few AU orbits is feasible. As part of the recommended precursor Doppler campaign, all Exo-S giant stars targets should have their RV jitter measured by current Doppler instruments. For the large fraction of giant stars with jitter small enough to permit the detection of giant planets in few AU orbits, each target should be observed 10 times per year per star for at least 10 years, at a precision no worse than the jitter.
3. Stars with spectral types earlier than F6V are typically less amenable to Doppler surveys because of their rapidly increasing jitter and decreasing density of spectral lines. However, all Exo-S early-type stars should have their jitter measured by current Doppler instruments. For stars showing low enough jitter to enable giant planet detection in few AU orbits, at least 10 Doppler measurements per year, with a short-term observing cadence designed to average over photospheric jitter, should be carried out in the next decade.
4. Close binary star systems (sky separation < 2″) may remain poor Doppler targets. However, techniques developed by Konacki et al. (2009) show promise for detecting ~M_J planets for close-in orbits

and several M_J planets for ~AU orbits. However, these targets may not be viable for direct imaging searches and should be examined for deletion from the Exo-S target list due to stray light and dynamical stability, as described in Section 3.3.4.

The Exo-S STDT recommends that NASA invest in a high-precision, high-cadence Doppler campaign to search for low-mass (super Earth to sub-Neptune) planets around every Exo-S direct imaging target for both the Case 1 habitable zone maximization and Case 2 maximum planet diversity approaches. Such a campaign should measure the photospheric jitter of every target, followed by high cadence Doppler measurements for the next 10 years for those targets showing low enough jitter to enable detection of planets within ~few AU orbits.

3.3.4 Stellar Multiplicity

Most of the stars in the solar neighborhood are members of a binary or multiple system (Abt 1983; Duquennoy and Mayor 1991; Raghavan et al. 2010), including many of the most favorable stars for imaging exoplanets. Given the large investment of mission lifetime in each target, it is important to consider (1) the likelihood that planetary orbits of interest will be dynamically stable, and (2) the extent to which stray light from an unsuppressed second star will interfere with detecting and characterizing such planets. One extreme solution to this problem is simply to eliminate binary stars from direct imaging target lists. However, there are at least three reasons not to rule out all binaries. First, it is clear that planets can and do form in stable orbits within binary systems (Mathieu 1994), and these systems represent important laboratories in which to study planetary dynamics and evolution. Second, multiplicity is so common among nearby stars that excluding all binaries may necessitate a much higher performance mission (in terms of IWA and contrast limit) in order to achieve a satisfactory yield of exoplanet discoveries. Finally, the added complication of scattered light from bright off-axis companions may only be prohibitive in certain cases.

3.3.4.1 Stray Light from Adjacent Stars

Off-axis starlight that is scattered by non-uniformities in the primary and secondary mirror surfaces will not be fully blocked by a field stop and will therefore illuminate the planet detection pixels. As a result, targets that are either optically or physically associated with another bright star will require longer exposure times to detect and characterize exoplanets. This effect will be more pronounced for brighter companions at smaller separations from the target. Nevertheless, for the very nearby Exo-S targets, exposure times may not be prohibitive. **Table 2.4-8** listed 16 high completeness binary systems from the Exo-S target list that may be problematic for direct imaging planet searches due to stray light contamination and were not included in the DRMs. These stars have small separations (less than 10 arcseconds) and relatively bright companions (V_2 - V_1 < 5). A preliminary analysis using two models (Spyak and Wolfe 1992; Kuhn and Hawley 1999) to calculate scattering off the primary and secondary mirror surfaces found that exposure times could be increased dramatically for these cases (C. Noecker, priv. comm.). To date, no complete analysis has been done to address whether stray light will be a concern for Exo-S. Exposure times for targets in binary systems will depend on (1) distance to the target, (2) separation between the target and companion star, and (3) relative brightness of the companion star as compared to the target. Future near-term studies should quantify as a function of mirror roughness the impact of stellar multiplicity on target selection for direct imaging missions, and strategies to mitigate stray light should be developed accordingly.

3.3.4.2 Dynamical Stability of Planetary Orbits

Exoplanets have now been discovered in both circumbinary and circumstellar orbits in binary

systems (e.g., Dumusque et al. 2012; Doyle et al. 2011; Haghighipour 2010 and references therein). Holman & Wiegert (1999) provided an empirical approximation for assessing the stability of planetary orbits in low eccentricity binaries, and various studies have used this approach to consider whether other systems could host as-of-yet undiscovered planets (e.g., Cuntz 2014; Eggl et al. 2013). More recently, Jaime et al. (2014) have employed an approach that allows mapping of zones of stability in more eccentric binaries and examines the influence of non-periodic flux variations on the habitability of such systems. To date, however, no comprehensive study has been carried out for assessing planetary orbit stability within the multiple star systems on the Exo-S target list. Near-future work should specifically consider the orbit and masses of stellar components of each Exo-S binary in order to assess whether there are likely to be zones of stability within the Exo-S planet-finding field of view.

4 STARSHADE MISSION ARCHITECTURE TRADES

There is a wide range of possible starshade missions but the programmatic constraints of the Exo-S study are challenging for a two-spacecraft architecture. Specifically, the construction of an end-to-end mission concept targeted at $1B limits the possible mission implementation choices to co-launched architectures, due to the current cost of launch vehicles and the best orbits for starshade direct imaging. A more cost-effective starshade mission architecture is one where the starshade is added to an already orbiting astrophysics telescope mission. This scenario greatly augments the existing telescope's capability, reduces science down time as the starshade repositions, and lowers the cost and risk of the starshade direct imaging science. With these advantages in mind, the STDT elected to include this follow-on approach as part of the Exo-S study.

4.1 Mission Options Overview

The design points used to characterize the starshade architecture tradespace are captured in **Table 4.1-1**. The field bifurcates into a two-spacecraft Starshade Dedicated Mission along with two variations, and a single-spacecraft Starshade Rendezvous Mission, including three related variations. The Dedicated and Rendezvous mission case studies (1A and 2C, respectively) are shown in bold.

The Dedicated Mission architecture is co-launched (due largely to the need to keep costs down), which adds significant mass and volume considerations to the telescope and starshade spacecraft designs. The Dedicated Mission design is targeted at meeting all study guidelines. By using a starshade, a low-cost commercial, 1-m class telescope can detect Earth-size planets in the habitable zone (HZ) for a favorable subset of stars. In the Dedicated Mission case, a 1.1-m aperture diameter telescope similar to those used on the GeoEye and WorldView missions, is baselined. Characterization of detected Earth-size planets, however, is limited by aperture-driven observing time constraints. The telescope spacecraft requires less fuel to reposition than the starshade, so the telescope spacecraft is tasked with retargeting and executing formation control maneuvers.

The Rendezvous Mission leverages a separately funded space telescope to provide excellent science at a low cost. The starshade launches separately to *rendezvous* with the telescope, after telescope primary objectives are met. Consequently, the telescope must be in an orbit that enables the later rendezvous of the starshade. The telescope spacecraft must also

Table 4.1-1. Starshade mission options, including two case study missions (1A & 2C) detailed in this report.

Mission					Telescope/Starshade			Instrumentation		
Orbit	#	Case Name	Mission Class/ Duration	Cost ($M FY15)	Tele-scope	Retarget Prop. Responsibility/ Technology	Starshade	Implementation	FOV	Optical Thru-put
Earth Leading	**1A**	**Dedicated Case Study**	**B 3 years**	**~1100**	1.1-m NextView	Telescope SEP	16-m disk 22 7-m petals	Dedicated IFS Dedicated Imager	30 arcsec 60 arcsec	42% 51%
	1B	Dedicated Downgrade	C 3 years	~950						
	1C	Dedicated Tech Demo	D 1 year	~750	0.6-m QuickBird	Telescope Small Biprop	16-m disk 22 6-m petals			
Earth-Sun L2	2A	Rendezvous Hi Performance	B 5 years	~800	2.4-m WFIRST/ AFTA	Starshade SEP*	20-m disk 22 9-m petals	Dedicated IFS Dedicated Imager	30 arcsec 60 arcsec	42% 51%
	2B	Rendezvous Upgrade	C 3 years	~640		Starshade Large Biprop	20-m disk 28 7-m petals			
	2C	**Rendezvous Case Study**	**C 3 years**	**~630**				Coronagraph IFS Coronagraph Imager	2 arcsec 10 arcsec	22% 28%
	2D	Rendezvous Tech Demo	D 1 year	~400		Starshade Small Biprop				

carry some specific hardware needed for formation flying. A formation guidance channel (FGC)—optics and a detector capable of sensing a laser beacon on the starshade—is essential and can be either a modification of an existing science instrument or included in a stand-alone starshade instrument. In addition to the FGC, an interspacecraft radio link is needed for spacecraft-to-spacecraft communications and as a formation flying ranging sensor. A science camera and spectrometer can be either purpose-built for starshade direct imaging or, if similar capabilities exist in the telescope spacecraft's payload, the instruments may be modified if necessary and repurposed for starshade science. Compliance with these requirements constitutes a 'starshade ready' telescope.

WFIRST/AFTA has been adopted as the Rendezvous Mission's telescope reference design for the Exo-S study. Since WFIRST/AFTA is currently in development, design details and a mission study team are available to support discussions regarding payload accommodations. The Rendezvous Mission design looks to minimize the impact on WFIRST/AFTA; no stringent requirements are imposed on the telescope spacecraft. The existing coronagraph instrument performs both science and formation guidance functions without adding focal planes.

All mission options use a low-cost, intermediate-class launch vehicle with a 5-m diameter payload fairing.

4.2 Starshade Overview

Starshades are designed to control starlight diffraction to create a dark shadow around a companion telescope (**Figure 4.2-1**). The shadow is larger than the telescope aperture (by 2 meters) to allow lateral drift (deadband motion of the telescope within the starshade's shadow during formation flying). The inner working angle (IWA) is defined by geometric projection to the starshade tips.

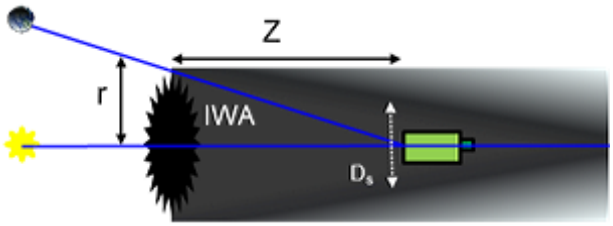

Figure 4.2-1. Definition of outer working angle and shadow diameter. Angle to edge of starshade IWA = r/Z. Shadow diameter $D_S = D_{Telescope} + 2$ m.

Several starshade attributes enable compelling low-cost exoplanet missions with available, non-specialized telescopes:

- The starshade controls the contrast and IWA at which planets can be detected so that the telescope size is not a limiting factor for small planet detection.
- Starlight is suppressed before entering the telescope so that complex wavefront control with extreme telescope stability is not needed.

Starshade mechanical architecture trades are discussed in Section 6.2.1. The JPL-developed perimeter truss starshade architecture is adopted for this study due to its ability to support a co-launched mission architecture. Originally developed in 2010 for the <$1B Occulting Ozone Observatory (O_3) concept study, the design's technology can be at Technology Readiness Level (TRL) 5 by 2017. Other starshade architectures, such as the NGAS-developed concept for the New Worlds Study (Cash et al. 2009), can also be considered for missions with separate starshade and telescope spacecraft launches, and that allow for later technology readiness.

4.3 Science Measurement Requirements

A brief summary of the requirements constraining the Exo-S architecture trades is presented in **Figure 4.3-1**. The measurement requirements stem from science observation requirements (see **Table 2.7-1**), the physical properties of the stars and planets, and constraints imposed by the use of commercially available telescopes.

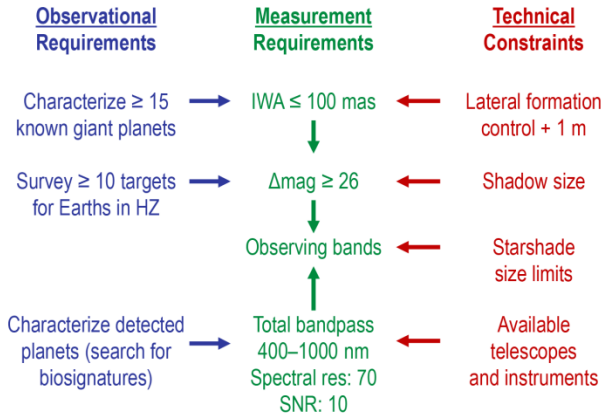

Figure 4.3-1. Science measurement requirement flow down.

The requirement to observe known giant planets loosely sets the maximum IWA at about 100 mas. This relationship is shown in **Figure 4.3-2** with known giant planets, accessible at maximum elongation, to the left of the lines. Observations are limited to planets that are highly likely to be detected based on their planet star separations; i.e., they will be at separations > IWA independent of the unknown inclination. DRM studies show that to schedule 15 observations of individual target stars with known giant planets in a 2-year timeframe requires access to a pool of ~50 planets whose maximum elongation exceeds the IWA at some point in their orbits. As seen from **Figure 4.3-2**, an IWA of 100 mas or less is required to achieve this goal. Known giant planets do not drive planet contrast sensitivity requirements.

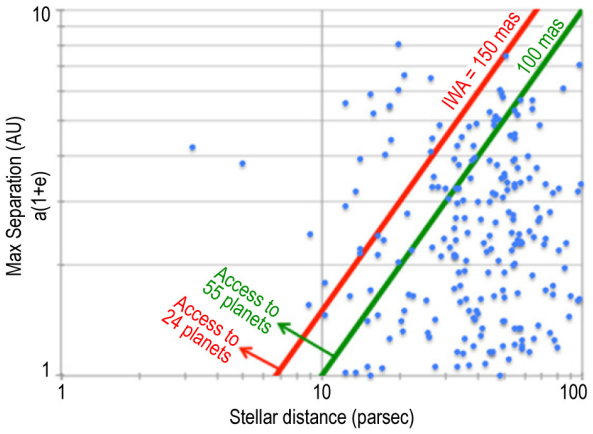

Figure 4.3-2. Access to sufficient known giant planet candidates, to left of IWA contours, requires 100 mas IWA.

The requirement to survey sufficient Earth-twins sets the minimum planet sensitivity (limΔmag) at 26 stellar magnitudes, or 4×10^{-11} contrast. Potential observations are restricted to stars with a greater than 25% planet detection probability (also called 'search completeness'). **Figure 4.3-3** shows candidate stars meeting the search completeness as points beneath the contour lines of limiting magnitude sensitivity. As before, DRM studies show that to schedule ~15 observations, enough to ensure 10 successful characterizations, in a 2-year timeframe requires access to about 50 target stars. From the figure, to achieve this number of candidates with a limΔmag of 26 is needed, with IWA=75 mas for some fraction of the stars. IWA=75 is achieved at lower wavelengths, as detailed below.

The requirement to characterize planets orbiting Sun-like stars sets the observing wavelengths to where Sun-like stars are brightest—at visible and NIR bands. The use of high TRL telescopes and detectors constrains the bandpass to 400–1,000 nm. Silicon detector efficiency plummets at longer wavelengths and both detector efficiency and mirror reflectance degrade at shorter wavelengths.

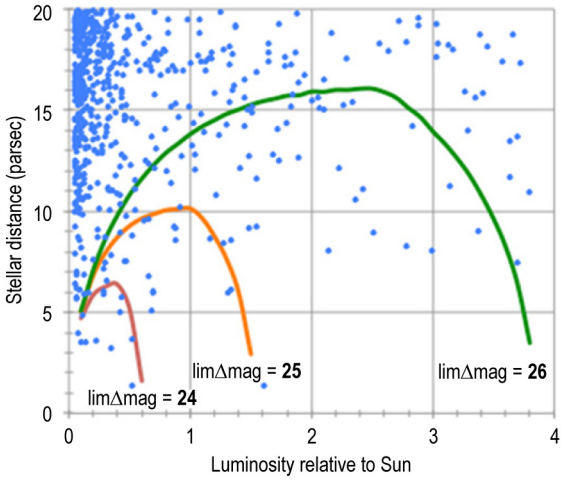

Figure 4.3-3. Access to 50 Earth candidate stars requires limΔmag=26 and IWA=75 mas. Candidates are below contours of ≥ 25% search completeness at varying Δmag.

4.4 Starshade Size and Bandpass

The size of the starshade is a key consideration in the assessment of the mission architecture tradespace. While generally offering better performance, larger starshades weigh more, cost more, are slower to reposition, require more fuel to reposition, and—for those much greater than about 35-m minimum diameter—have a weaker heritage case when compared to flight-proven deployable antennas. This section discusses some of the constraints and considerations used to identify the size and key characteristics of the starshades for the Exo-S study's concepts.

4.4.1 Full Bandpass Size

For a starshade design that meets the previously established requirements of an IWA of 100 mas, and a minimum planet sensitivity at limΔmag = 26, there are two choices to address the required spectral coverage: design a large ~40-m starshade (e.g., 20-m central disk with 9.2-m-long petals) capable of covering the full 400–1,000 nm range (**Figure 4.4-1)** from a single separation distance, or design a more compact starshade that covers a portion of the range, and then change the spacecraft separation distance to move this partial bandpass over the full, required spectral range.

Large starshades add to mass and packaging issues. Additionally, large designs depart from the to-date technology work. This departure would likely require repeating a great deal of already-completed design and validation work, making the study guideline of TRL 5 by 2017 unreachable. Finally, an early Cost and Technical Evaluation (CATE) risk assessment strongly recommended that the starshade size be kept as small as possible to maintain heritage with low-cost deployable communications antennas. Larger starshade designs were viewed as having greater cost risk. With all these issues considered, the architecture trades were constrained to smaller, partial bandpass starshade designs. This will be discussed further in Section 4.4.3.

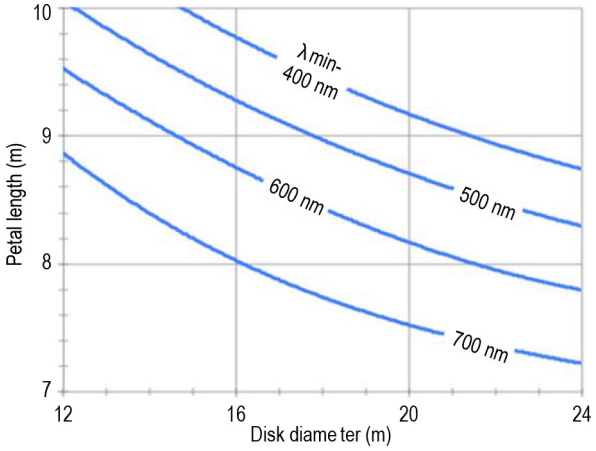

Figure 4.4-1. Starshade dimensions vs. bandpass lower limits. The starshade has: an upper bandpass limit of 1,000 nm, 100 mas IWA, limΔmag =26, 3.1-m shadow. Large starshades are required to cover the full (400–1000 nm) bandpass.

Note that **Figure 4.4-1** shows *optical* dimensions that differ from *mechanical* dimensions by 25 cm. Petals are mechanically longer by 25 cm. The width of this additional 25 cm is sized so that there is no gap between petals at their bases when deployed. The petal optical apodization function does not start until after this initial 25 cm transition. Since there is no gap for the first 25 cm of mechanical petal length, the petals optically appear as being 25 cm shorter, while the radius of the inner disk optically appears as being 25 cm larger. This extension of the inner disk prevents sunlight from scattering off of equipment on the telescope-facing side of the starshade.

4.4.2 Size Limits

The starshade sizing trade requires balancing performance against a series of mechanical constraints. There are three important mechanical factors: a physical limit on the petal length/width aspect ratio, a requirement on petal stiffness, and a limit on the overall length of the starshade petal.

This first factor, the length-to-base-width aspect ratio, L/W, directly affects the petal's manufactured shape stability and its sag under Earth's gravity during ground testing. Gravity sag control with gravity compensation fixtures of manageable complexity sets a limit on required petal stiffness, which is, in turn,

sensitive to the aspect ratio. The aspect ratio also directly affects the in-plane shear, and accordingly, the petal's shape stability. Early prototyping showed that an aspect ratio of 3.2 worked but with little margin (**Figure 4.4-2**). A lower aspect ratio of L/W = π was adopted as a design requirement to add design margin and as a mathematical convenience.

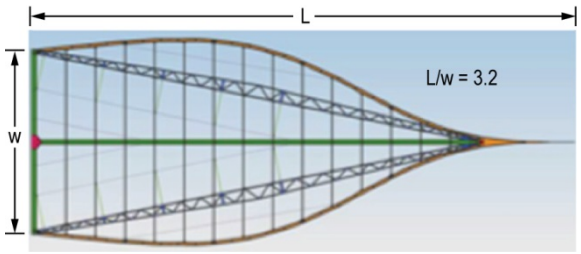

Figure 4.4-2. Petal aspect ratio (length:base width) is preserved with scaling, to satisfy stiffness and shear strength criteria.

For a starshade with n petals, the width of each petal is $W=\pi D/n$, and the petal length is then $L=\pi^2 D/n$. **Figures 4.4-3** and **4.4-4** show this constraint in the diagonal lines for values of n between 20 and 28. For a given diameter truss, and given number of petals (n), only petal lengths below the diagonal lines are allowed.

The third mechanical factor constraining starshade size is limits on the petal length. The both mission petal lengths are limited by launch furling and restraint. When stowed, the starshade petals are wrapped around a 3-m diameter hub (**Figure 4.4-5**). Recent design maturation establishes extra payload envelope clearance margin compared to the design shown in the Exo-S Interim Report. Petal pitch is reduced and the launch restraint system now resides inboard of the petal stack. Petal length can now grow close to the hub circumference. Petal lengths necessary to cover the full bandpass (up to 9 m) are in fact achievable with the baseline architecture. However, the baseline mechanical petal length of 7.25 m is consistent with achieving TRL 5 in 2017, as required by the design study. Petals must fit on available optical benches for assembly and not exceed the length of available metrology systems for shape verification. These facility constraints are certainly surmountable in the future, but do apply here to satisfy the technology readiness guidelines. In addition, the Dedicated Mission petal length is indirectly constrained by a limit

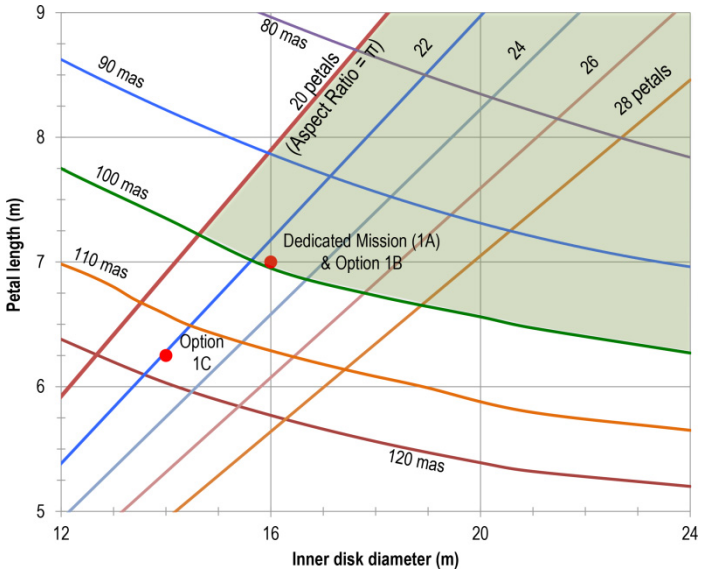

Figure 4.4-3. Dedicated Mission starshade size tradespace for bandpass = 510–825 nm, shadow = 3.1 m, limΔmag = 26.

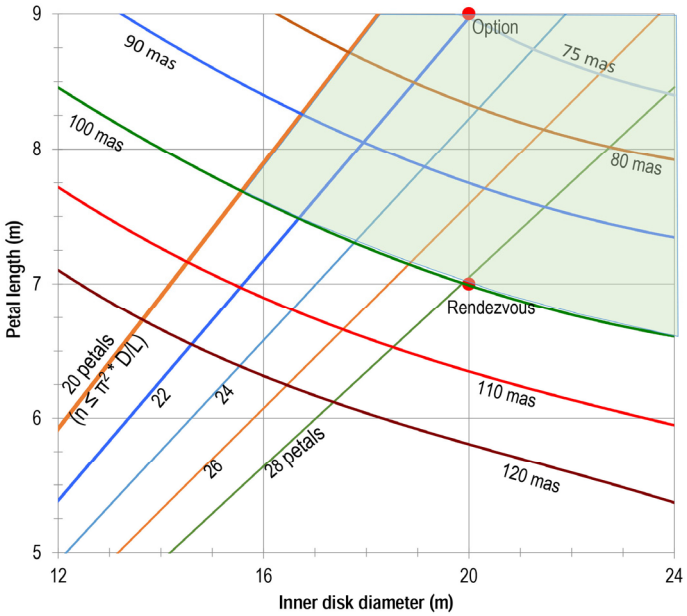

Figure 4.4-4. Available starshade size tradespace for the Rendezvous Mission case study: bandpass = 600–850 nm, 4.4-m shadow, limΔmag =26.

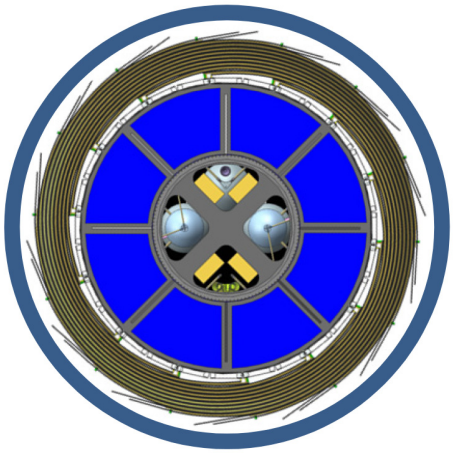

Figure 4.4-5. Stowed starshade with 28 7-m petals fits in payload fairing with margin. Room exists for 22 9-m petals.

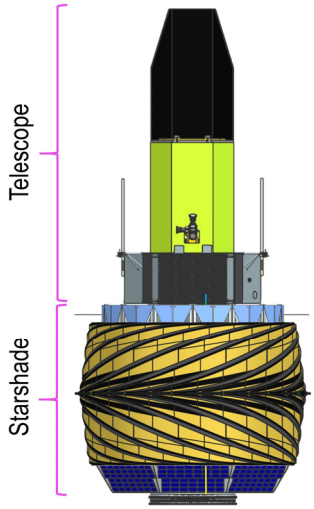

Figure 4.4-6. Dedicated spacecraft in launch configuration.

on the petal width and the aspect ratio. Due to the cost-driven co-launch configuration, the Dedicated Mission spacecraft are stacked, with the telescope spacecraft on top of the starshade spacecraft. The width of the petal accounts for most of the stowed height of the starshade spacecraft (**Figure 4.4-6**). This stacked configuration has an unusually high center-of-gravity (CG) and the current Dedicated Mission design is just in compliance with the launch vehicle's payload CG requirement. Petals longer than the current 7 m could be launched but would cause a significant redesign of the two, largely off-the-shelf spacecraft and the commercial telescope to preserve the current CG. This rework would raise the cost of the mission.

4.4.3 Dedicated Mission Starshade Size and Bandpass

The Dedicated Mission starshade is designed to produce a 3.1-m-diameter shadow (±1 m around a 1.1-m aperture) for planet sensitivity at 26 magnitudes, IWA of 102 mas, and a primary bandpass of 510–825 nm. This is called the 'green band' and is selected to provide access to a large subset of prominent spectral features, as shown in **Figure 4.4-7**. The green band is used for the majority of observations.

The starshade can be moved toward or away from the telescope to change the useful bandpass and IWA. Three distance/wavelength pairs are shown in **Table 4.4-1**.

Separation distance increases in inverse proportion to wavelength to preserve the same optical performance. By moving the starshade out from a nominal distance of 35 Mm to 50 Mm, the IWA is reduced to 75 mas making the 'blue band' useful to explore closer to the

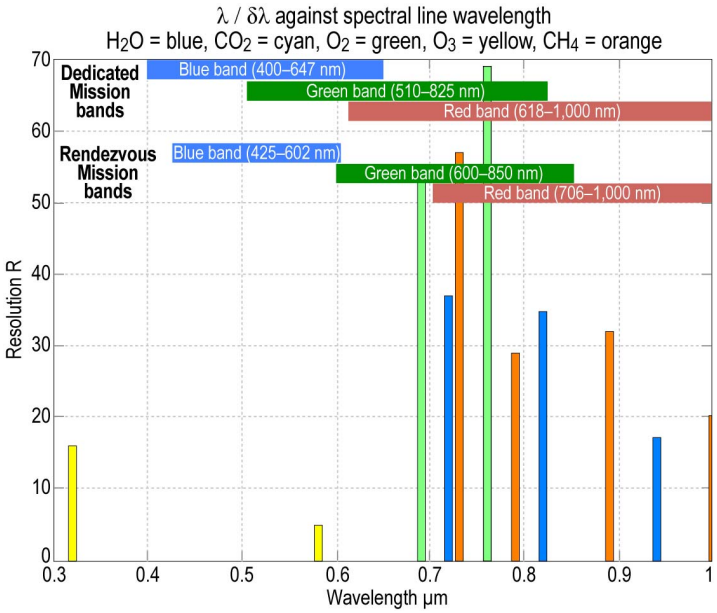

Figure 4.4-7. Primary bandpass (green) covers a subset of prominent spectral features indicative of biologic activity.

Table 4.4-1. Summary of case study parameters.

Case Study	Parameters	Observing Bands		
		Blue	Green	Red
Rendezvous Mission	Bandpass (nm)	425–602	600–850	706–1000
20-m inner disk	IWA (mas)	71	100	118
28 7-m petals	Separation (Mm)	50	35	30
Dedicated Mission	Bandpass (nm)	400–647	510–825	618–1000
16-m inner disk	IWA (mas)	80	102	124
22 7-m petals	Separation (Mm)	39	30	25

star and increase the number of candidate targets for the Earth-twin survey. It may also be used to more fully characterize a planetary system after detecting a planet further from the star.

Moving the starshade closer, to a distance of 30 Mm, provides access to the 'red band' from 618–1000 nm with access to additional important spectral features, but carries a corresponding increase of IWA to 118 mas. This limits red band use to planets that are known to be observable at that IWA. The continuum of distance/wavelengths pairs is discretized by the number of bandpass filters in the camera.

Light from outside the useful bandpass is used for formation guidance, as described in Section 6.3.

4.4.4 Rendezvous Mission Starshade Size and Bandpass

The Rendezvous Mission starshade is designed to produce a 4.4-m-diameter shadow (±1 m around a 2.4-m aperture) for planet sensitivity at 26 magnitudes and IWA of 100 mas. Petal optical length remains 7 m, but the inner disk diameter grows to 20 m to produce the larger shadow. The number of petals grows to 28 to preserve the petal aspect ratio (per $nL/D = \pi^2$). **Figure 4.4-4** shows the allowable starshade dimensions.

The bandpass is slightly restricted and shifted relative to the Dedicated Mission to minimize the impact to WFIRST/AFTA. The coronagraph camera (with coronagraph masks removed from the optical train) performs all starshade instrument functions, without adding focal planes. This requires simultaneous use of the existing direct imager camera and integral field spectrograph (IFS). One performs the starshade science function while the other performs the formation guidance function, using out of band starlight and a laser beacon.

Dichroic filters are added to an existing coronagraph filter wheel to select three science bands and pass the out-of-band light to the active guidance sensor. When observing in the green band, the out-of-band starlight flux is not sufficient to support the formation control loop. The solution adopted here is to shift the green band higher to 600–850 nm. The corresponding red and blue bands are 706–1,000 nm and 425–602 nm, respectively.

4.4.5 Selected Starshade Sizes

With the starshade sizing tradespace established by performance and mechanical limitations (**Figure 4.4-3** for the Dedicated Mission and **Figure 4.4-4** for the Rendezvous Mission) the specific starshade design points must be determined. Since the Dedicated Mission design is attempting to develop a two-spacecraft co-launched system targeted at $1B, cost and mass are high priority design considerations. Consequently, the Dedicated Mission starshade is as small as possible while still meeting the 100 mas IWA performance requirement. The design point selected for the Dedicated Mission case study (option 1A) is a 16-m inner disk and 22 7-m-long petals.

Due to the larger telescope used on the Rendezvous Mission design (2.4 m instead of the Dedicated Mission's 1.1 m), a larger shadow is needed. Accordingly, a larger starshade is necessary to continue to meet the IWA and contrast requirements as in the Dedicated Mission design. To simplify starshade design work, the same petal structural design was used on both the Dedicated and the Rendezvous mission concepts; resizing was addressed by changing the number of petals, and in so doing, changing

the diameter of the inner disk. For the Rendezvous Mission case (option 2C) the starshade has a 20-m inner disk and 28 7-m petals.

4.5 Starshade Dedicated Mission Case Study and Variations

The Dedicated Mission concept and its variations are essentially different looks at the low cost, end-to-end starshade direct imaging mission prescribed by the study charter, with differing degrees of reliability and risk, and corresponding differences in cost, mission duration, and science value.

All three share the same heliocentric Earth-leading, Earth drift-away orbit; repositioning telescope spacecraft; and purpose-built imaging system. For low-disturbance orbits capable of supporting multiday spacecraft alignment on a fixed target, the choices are Earth drift-away or L2. Earth drift-away was the better choice because it has lower gravity disturbances. Limited mission life and low data volumes make the drift-away's inferior communications link a non-issue. Repositioning the telescope spacecraft is the lower propellant choice. And as 'dedicated' missions serving only starshade direct imaging objectives, the instruments for all three options are designed specifically for starshade science.

In all three cases, the launch vehicle first deploys the telescope spacecraft in its operational orbit, then maneuvers to the nominal separation distance, spins up, deploys the starshade, and finally maneuvers away. The starshade spacecraft acquires a safe Sun-pointed attitude. The starshade deployment is ground commanded.

4.5.1 Dedicated Mission Case Study—Option 1A

The Dedicated Mission case is a Class B mission with a 3-year baseline mission duration (the spacecraft carries fuel for 5 years). **Figure 4.4-6** shows the launch configuration.

The reference telescope design is based on the 1.1-m NextView telescope developed for commercial Earth imaging. Several of these telescopes are operational and the telescope is considered a current product line. The as-built telescope is highly compatible with starshade requirements and only limited modification is necessary. The most significant modification is the addition of a sunshade to allow pointing near the Sun without sunlight entering the barrel.

The telescope spacecraft bus is based on the Kepler bus. The telescope spacecraft provides the propulsion to retarget and control formation. The existing hydrazine propulsion system is used for formation control, with a change to slightly larger propellant tanks and the addition of more thrusters. Retarget maneuvers use the XIPS-25 ion engine and xenon propellant. This electric propulsion system is needed due to the limited mass available for retargeting propellant stemming from the cost-driven shared launch configuration, and is an addition to the Kepler-based design.

The starshade spacecraft is a simplified version of the WISE bus. It is spin-stabilized so no reaction wheels are needed. Power is generated via fixed body-mounted solar panels. There is no science data handling. direct-to-Earth communications are limited to engineering functions only. A small hydrazine propulsion system provides pointing and spin-control. The bus structure is ESPA (EELV [evolved expendable launch vehicle] secondary payload adapter) ring-based and provides the separation interface to the starshade.

Details on the Dedicated Mission design can be found in Section 7.

4.5.2 Dedicated Mission Variant Option 1B

Option 1B varies from the case study only in regard to the bus systems. For option 1B, both busses are based upon PROBA-3 (PRoject for On-Board Autonomy) and are procured from a European vendor. The same vendor provides

the ion propulsion system for the telescope spacecraft. The ion engine is an in-house product and all solar electric propulsion (SEP) components are used in the much larger Bepi-Colombo mission to Mercury that is currently in development by this same vendor.

This option was the baseline at the time of the STDT's Interim Report and is expected to cost less than option 1A, but was later deemed too risky in terms of the foreign vendor procurement. As in the Interim Report, option 1B is Class C and has a 3-year mission duration (but carries propellant for up to 5 years).

4.5.3 Dedicated Mission Variant Option 1C

The final Dedicated Mission variant (option 1C) is a technology demonstration mission and is provided as a reference point for the lowest cost dedicated telescope mission. It is a 1-year, Class D mission. The objectives are to characterize a handful of known giant planets, and in so doing, prove out the end-to-end starshade mission technologies.

The telescope is down-sized to 0.6-m-diameter aperture and is based on the QuickBird-1 telescope. The telescope bus is a single string version of the option 1A telescope bus. Reductions in the telescope spacecraft mass and mission duration allow the use of a lower-cost biprop system for retargeting.

The starshade is reduced to a 14-m diameter inner disk with 22 6-m-long petals. The smaller telescope and starshade will deliver a 118 mas IWA—sufficient to reach a number of known giant planets. The starshade bus is a single-string version of the option 1A starshade bus.

4.6 Starshade Rendezvous Mission Case Study and Variations

The Rendezvous Mission family of concepts is centered on leveraging an existing on-orbit telescope asset. Ideally, the starshade would join the telescope around the completion of the telescope's primary science objectives as a follow-on science investigation.

The need to 'rendezvous' with an already on-orbit telescope in a low disturbance environment suitable for multiday spacecraft alignment with a fixed target, narrows the possible orbits to those at L2. To minimize the impact on the telescope spacecraft, retargeting with the starshade is the baseline repositioning approach. This choice also helps minimize the impact on the telescope design.

In addition to the L2 orbital requirement follow-on starshade operations also require the inclusion of a Starshade Ready Package (SRP). The SRP consists of: a science instrument capable of supporting starshade direct imaging, formation guidance sensing capability, and a proximity radio for interspacecraft communications and range measurement.

4.6.1 Rendezvous Mission Case Study—Option 2C

The Rendezvous Mission case is a Class C mission with a 3-year on-orbit mission duration.

The telescope reference design is WFIRST/AFTA. It is assumed, for the purpose of this study, that WFIRST/AFTA conducts its primary mission at Earth-Sun L2. The starshade is not launched unless the telescope is operational.

The current Rendezvous Mission design allowable Sun off-point angles do not completely overlap with those of WFIRST/AFTA. Starshade observations are constrained to within 83° of Sun, to keep sunlight off any telescope facing starshade surface, and greater than 40° from Sun, to keep sunlight out of the telescope barrel. By comparison, the baseline WFIRST/AFTA Sun pointing constraint is 126° to 54°, based upon sizing of the fixed solar array for a geosynchronous orbit mission. It is assumed that a redesign for an Earth-Sun L2 mission affords the opportunity to increase the WFIRST/AFTA solar array and sunshade size consistent with the starshade goal.

Looking to keep the mass, power, and testing impacts to a minimum, the Rendezvous Mission case study adopted a no-new-optical-channel rule when modifying the current WFIRST/AFTA design to support starshade science. Modest changes were needed in the coronagraph's IFS (**Figure 4.6-1**); the details are discussed in Section 8.4.1.

The starshade spacecraft performs the retarget and formation control maneuvers with a conventional bipropellant propulsion system. Propellant and pressurant tanks are installed inside the starshade central cylinder. **Figure 4.6-2** shows the starshade spacecraft configuration.

The spacecraft bus system is a simple single-string design based on the WISE bus. It is spin-stabilized without reaction wheels, generates power via small body fixed solar panels and handles no science data. Direct-to-Earth telecommunications capability is present but is for engineering purposes only since the starshade produces no science data. A proximity radio provides interspacecraft communications and telescope-starshade range measurement via a 2-way ranging code.

The starshade guidance channel (sensed on the telescope using a repurposed coronagraph detector) measures the bearing angle between the telescope boresight and starshade center, and relays this information to the starshade via the proximity radio. The starshade bus system combines the bearing angle with the measured range, computes the lateral formation error and feeds this to the formation control algorithm.

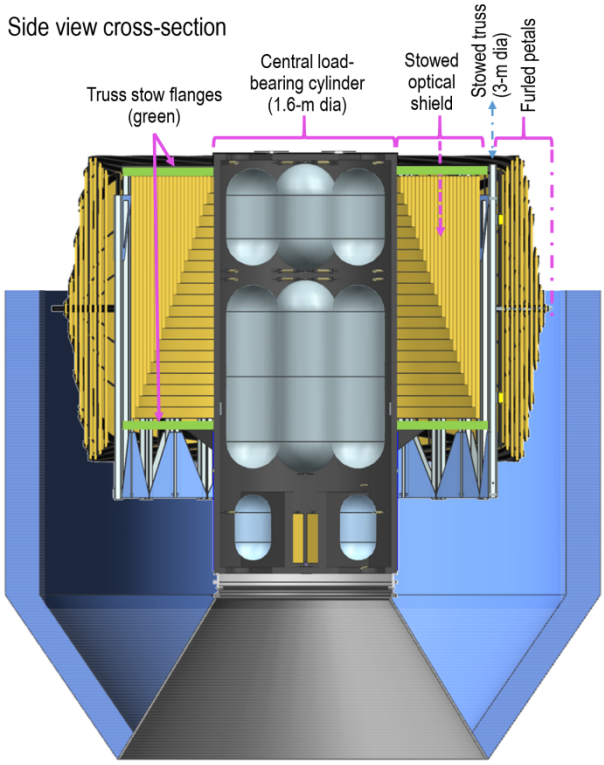

Figure 4.6-2. Rendezvous starshade spacecraft configuration.

Details on the Rendezvous Mission concept design are discussed in Section 8.

4.6.2 Rendezvous Mission Variant Option 2B

Option 2B varies from option 2C only with regards to science instrumentation. Specific starshade channels (field camera, IFU, and FGC) are added to the coronagraph instrument with light picked off near the front end of the coronagraph. The added channels are physically small and are easily packaged within the existing coronagraph envelope. This approach allows for better optimization for starshade science (**Table 4.1-1**).

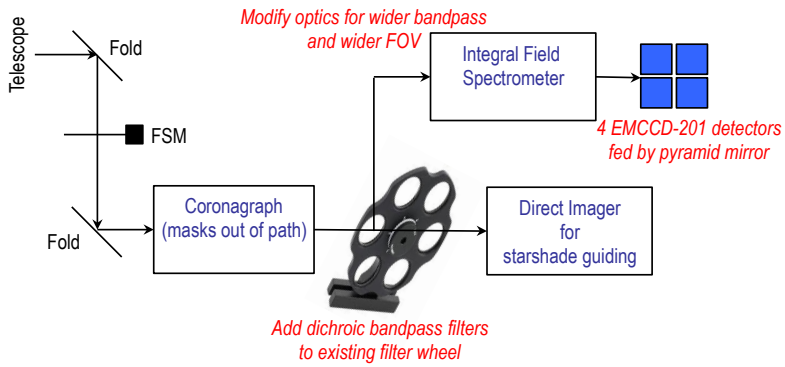

Figure 4.6-1. Block diagram of WFIRST/AFTA coronagraph modified to perform starshade science and guidance functions. (Modifications described in red text.) Shown in IFS mode with Direct Imager used for formation guidance. Other filters use Direct Imager for science and IFS for formation guidance.

The camera and IFU detectors are conventional 4K×4K CCD's (CCD-273). The larger format resolves a FOV constraint inherent with the existing coronagraph. Throughput is greatly increased due to the reduced number of optics. A dedicated guidance camera simplifies the formation control approach. Details of this instrument modification are also discussed in Section 8.4.1.

4.6.3 Rendezvous Mission Variant Option 2A

Mission option 2A is a forward-looking option that delivers greatly enhanced science at higher mission cost and later technology readiness. It is not compliant with study guidelines for technology readiness.

Starshade size is increased (see **Figure 4.4-4**). Inner disk diameter is held at 20 m, but petal length is increased to 9 m and the number of petals is reduced to 22. The objective is to improve IWA, although it is also possible to increase bandpass. The green band IWA is about 75 mas and this provides a dramatic improvement in the number of candidate stars for the Earth-twin survey.

The starshade propulsion system used to retarget is upgraded to a SEP system with ion thrusters. This greatly improves the ΔV capacity, extending the overall mission life to 5 years and increasing the number of observations by >50%. It also introduces a technology challenge to generate the required power without introducing a thermal deformation problem with large solar arrays that cast shadows onto the starshade. The adopted solution is to use thin silicon solar cells that are embedded into the optical shield of the inner disk. This application is still an emerging technology. With so much area available for power generation, this application relaxes the need to optimize for power generation efficiency.

Mission option 2A is Class B with 5-year on-orbit duration. The spacecraft bus is the same as in 2C but upgraded to dual string and uses higher grade parts.

4.6.4 Rendezvous Mission Variant Option 2D

At the low cost end of the tradespace examined in the Exo-S study is mission option 2D, a technology demonstration mission. Mission option 2D produces limited science to demonstrate the starshade technologies on orbit.

The mission uses an upgraded version of the prototype starshade payload rather than building a completely new protoflight starshade. The starshade is the same design used in case study option 2C (34 m, 28 petals). The camera and IFS are also the same repurposed coronagraph detectors used in option 2C.

The mission is class D, consistent with a technology demonstration. Mission life is shortened to 1 year, which is sufficient to demonstrate direct imaging and spectral measurements on a number of known giant planets. The starshade biprop propulsion system is significantly smaller than the case study since the mission duration is only 1 year. The spacecraft bus is single string.

5 DESIGN REFERENCE MISSION

This section presents the Design Reference Mission (DRM) for both the Dedicated (30-m starshade, 1.1-m aperture diameter telescope) and Rendezvous (34-m starshade, 2.4-m aperture diameter telescope) missions. The DRM describes the sequence of observations to be performed and estimates the numbers of planets that will be detected and characterized. It is executed with a Matlab-based tool developed for the Exo-S study.

At least four precedent starshade DRM tools have been reported in the literature, all of them focused on detection and/or characterization of Earth twins (here Earth twin is defined as an Earth-sized planet with Earth's geometric albedo of 0.2) in the habitable zone. Lindler (2007) compared the performance of 5-year missions based on 2.4-m and 4-m telescopes, with starshade inner working angles (IWAs) of 98 and 75 mas respectively, using manually generated DRMs. Hunyadi, Lo, and Shaklan (2007) considered a two-occulter approach with a small, agile starshade used for detection and a larger, more distant one providing a smaller IWA used for characterization. Their automated approach optimized the integration time per target to maximize total mission observational completeness. Savransky, Kasdin, and Cady (2010) developed an algorithm to fully automate the detection, characterization, and follow up observations. They performed statistical analysis of science return in a 5-year mission exploring a thousand simulated 'universes' populated with Earth-twin planets. Glassman et al. (2011) likewise developed algorithms to maximize exo-Earth science return while minimizing spacecraft resource use, for the 5-year New Worlds Observer mission, a 62-m-diameter starshade with a 4-m telescope.

In contrast, the Exo-S study has explored the total planet harvest including, known giant planets from radial velocity (RV) surveys, Earth-sized planets in the habitable zone (HZ) and elsewhere, super Earths, sub-Neptunes, Neptunes, and Jupiters (see **Table 2.6-1** for a definition of planet sizes). The DRM employs a hierarchical approach: an observation schedule of known giant planets, whose availabilities for observation are known from their orbital parameters, forms a 'framework' of observations that have a high probability of success. In between observations of known giant planet, the next set of highest priority stars are scheduled. These stars are selected in one of two programs that focus on either Earth twins in the HZ, or a set of high-priority, high-completeness stars (described in Section 2.4). Observations of lower priority targets are assigned in this way until all the time is accounted for in single-visit scenarios of two and three years.

The DRM strategy and the method for selecting the observational sequence is discussed in Section 5.1. Model assumptions and details are provided in Section 5.2. Section 5.3 describes the three case studies: the Dedicated Mission emphasizing the search for Earth twins in the HZ (Case 1); the Dedicated Mission emphasizing overall planet diversity (Case 2); and the Rendezvous Mission emphasizing the search for Earth twins in the HZ (Case 3). A fourth case using the Rendezvous Mission with emphasis on planet diversity was not considered because the Rendezvous Mission is capable of characterizing Earth twins. This scientifically trumps the gain in known giant planet characterization when diversity is emphasized. DRM results comparing the number and types of planets characterized are presented in Section 5.4. Appendix A contains the detailed observing schedules for the three cases.

5.1 DRM Strategy

The Exo-S DRM is anchored by a set of known giant planet characterization observations that have a high-probability of success. These observations form about 1/3 of the DRM. Their timing is predetermined by the

known orbital parameters. In many cases, there are large gaps in time between the observations and these are populated with observations of either target stars suitable for Earth-twin candidates or other high priority targets. With remaining time, lower priority targets, e.g., stars with high completeness for super Earths or sub-Neptunes, are scheduled.

A recent paper by Brown (2015) shows that astrometry of known giant planets via direct imaging at a single epoch can be used to determine true planet masses to a few percent. The required astrometric precision is ~2 mas for 20% mass determination, and typical exposure times are smaller than the times required to characterize the planets to spectral resolution R=70. Brown has provided the Exo-S study tables of planet detectability including observational completeness and required integration times for the dates January 1, 2024 to December 31, 2028, for all known giant planets that can be resolved with the Exo-S 100 mas IWA (see **Figure 4.3-2**).

For many of the planets, assuming they have diameter and albedo no smaller than Jupiter's, observational completeness on a given day is C=100%; that is, the planet is guaranteed to be at separation >100 mas and to be no more than 22.5 mag fainter than the parent star. For almost all of the known giant planets, there are a sufficient number of days when C > 90% to allow for a viable observing sequence. The criterion C>90% was used when scheduling known RV observations.

Figure 5.1-1 shows how the observation strategy works. An initial target star with a known giant planet is picked based on the date of observation, observational completeness, and solar and Earth-pointing exclusion angles. Different starting dates between January 1 and

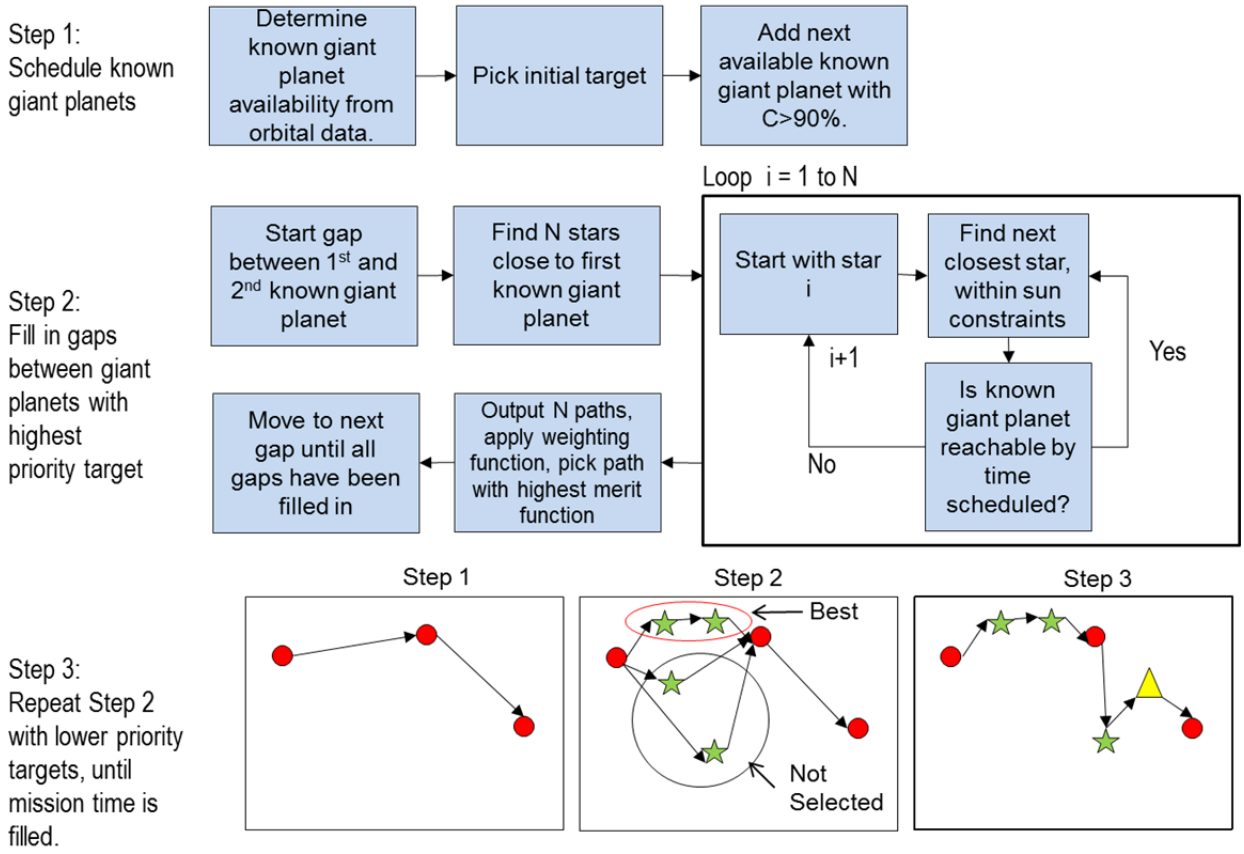

Figure 5.1-1. DRM tool. A hierarchy of observations is used to fill up the allocated time, starting with a known giant planet framework.

December 31, 2024, are considered to permute the observation sequence and study DRM stability. These scenarios result in a sequence of ~10–15 known giant planets observed over a two-year period.

Observations of the next tier of targets are then scheduled as shown in the middle layer of **Figure 5.1-1**. Paths to the N closest unscheduled targets (typically N=3–10 is used) in this tier are calculated as well as a path from the Nth star to the next giant planet. A weighting function to determine the most desired path based on completeness, detection time and slew time is applied, where the weight per path segment is the time derivative of completeness, given by

$$W = \frac{C}{(TDet + TSlew)}$$

for observational completeness C, detection integration time *TDet*, and starshade slew time *TSlew*. The path with the highest weighting function is selected.

Tslew is chosen to make efficient use of propellant. Targets are observable over a window that begins up to 83° from the Sun and extends to as small as 28° (Dedicated) or 40° (Rendezvous) from the Sun. *Tslew* and propellant are computed every 0.1° over the window of opportunity of a given target. It is found empirically that waiting to reach the target ~0.5°, or about a half-day, after it enters the observing window is below the knee in the propellant curve of the rocket equation, saving significant fuel with a just few percent increase in slew time over the minimum.

This strategy is then applied to the next tier of targets, with the higher ranking targets serving as the fixed path end-points for each observation segment. The process stops when all of the available time is used. It is also subject to propellant constraints.

This approach is nearly optimal for each observational tier. Future advances to the DRM will be required to globally optimize the full program.

Table 5.2-1. Instrument and mission parameters.

Parameter	Dedicated			Rendezvous		
Telescope Diameter (m)	1.1			2.4		
Detector Read Time (s)	2000			2000		
Design Contrast	5.E-10			1.E-10		
limΔmag	26			26		
Sharpness	0.08			0.08		
Surface Brightness of Local Zodi (mag/sq. as)	23			23		
Total Dust Surface Brightness (zodis)	7			7		
Solar Glint from a M_v=28 Point Source (zodis)	0.158			0.76		
Detection						
Wavelength (nm)	550			550		
SNR	4			4		
SR	7			9		
Characterization						
Wavelength (nm)	760			760		
SNR	10			10		
SR	70			70		
Mission Inputs						
Orbit	Earth-leading			L2		
ISP (s)	3273			307		
Thrust (N)	0.109			44		
Downlink (hrs)	8			0		
Uplink (hrs)	8			0		
Mass (kg)	1835			3700		
Sun Constraint (deg)	28–83			40–83		
Earth Constraint	Yes			No		
Starshade Parameters	**IWA**	**km**	**Band (nm)**	**IWA**	**km**	**Band (nm)**
Blue Band	80	38675	400–647	71	49500	425–602
Green Band	102	30330	510–825	100	35065	600–850
Red Band	124	25025	618–1000	118	29805	706–1000

5.2 Model Parameters and Assumptions

Table 5.2-1 lists the key parameters that define the instrument and mission models in the DRM. Detector parameters not defined here can be found in **Tables 7.3-2** (Dedicated) and **8.4-2** (Rendezvous).

Starting from the top of the **Table 5.2-1**, the telescope aperture diameters for each mission are 1.1 and 2.4 m, respectively. The full apertures are assumed to be used without a downstream pupil stop. The central obscurations are included in the throughput calculations.

Detector read time is assumed to be 2000 s. This is a compromise between read noise and cosmic ray pollution. Further study is required to determine the optimal setting.

Design contrast is the scatter at the IWA due to imperfections in the starshade and formation flying offsets. For the Dedicated Mission, the contrast is 5×10^{-10}, driven largely by petal placement requirements in the error budget (see Section 6.4). The superior resolution of the Rendezvous telescope contributes to a reduced sensitivity to petal positioning and contrast is set at 10^{-10}. In both cases, the total signal from the instrument is well below the assumed exozodiacal contribution. The design contrast term scatters uniformly around the starshade, contributing to the photometric background but it is not a systematic limiting factor at the limiting instrument sensitivity limΔmag=26. This defines the systematic noise floor below which planets are not detectable.

The 'sharpness' criterion for imaging is based on Nyquist sampling of a diffraction limited Airy pattern, leading to sharpness = 0.08 and an effective number of Nyquist pixels N_{pix} = 1/sharpness = 13 (Burrows et al. 2006). This also determines the area over which background is integrated.

The local zodiacal background is assumed to be uniform over all pixels, with a value of 23 mag/sq. arcsec. The exozodiacal background is assumed to be six times brighter for a total uniform zodiacal light contribution of 20.9 mag/sq. arcsec. For the DRMs discussed below, almost all observations are made at solar angles > 45^{o}, so the zodiacal light level is conservative on the whole.

Sunlight reflects and diffracts from the edge of the starshade resulting in glints as shown in **Figure 9.1-1**. These glints contribute a flux equivalent to 0.16 zodi for the Dedicated Mission, and, by virtue of the larger collecting area, 0.76 zodi for the Rendezvous Mission.

Detection observations with the imaging camera of the Dedicated Mission are made simultaneously in 3 sub-bands spanning 510–825 nm, with each band having R~7. Integration times are chosen to reach SNR=4 per band, with the net SNR=6.9 across the full band. From Kasdin and Braems (2006), this results in both a false alarm probability and a probability of missed detection < 0.001.

The Rendezvous Mission uses the integral field spectrometer (IFS) for direct imaging. All data is collected at R=70 to enable characterization of any detected planets. For detection, spectra are binned off-chip into three sub-bands with R=9 spanning 600–850 nm. Again, integration times are set to achieve SNR=4 per band for detection at the desired limiting magnitude of the observation. The read noise penalty for postdetection binning is incurred but is small compared to on-chip binning for the Rendezvous Mission observations.

Characterization observations require higher SNR because spectral features may be weak. SNR=10 is used for the continuum in characterization observations. For bright gas giants, the instrument spectral resolution is R=70.

The Dedicated Mission lacks a steerable antenna. The DRM includes 16 hours of downlink/uplink per observation during which the high gain antenna is pointed at the Earth. No such overhead is included in the Rendezvous Mission.

Finally, the solar avoidance angles for the two missions are listed. The Dedicated Mission has a 'sugar-scoop' baffle that allows pointing within 28^{o} of the Sun, though this is rarely used in the DRM. The Rendezvous Mission with its faster propulsion system has a solar avoidance

angle of 40°. Both missions have starshades with a shallow conical taper over the central disk. This accounts for the maximum solar avoidance angle of 83°, which places the starshade nearly edge on to the Sun, with a 6° allowance for the taper and a 1° allowance for axial misalignment.

5.3 Case Studies

Three case studies have been performed: the first uses the Dedicated Mission and emphasizes detection of HZ Earth twins by prioritizing these targets and employing a luminosity-dependent limiting magnitude to optimize yield. The second again uses the Dedicated Mission but prioritizes a diverse target list for which the observational completeness is high when the instrument is pushed to its limit, limΔmag=26. The third uses the Rendezvous Mission with its 2.4-m aperture, 34-m starshade, and powerful propulsion system to again emphasize HZ Earth twins.

5.3.1 Case 1: Dedicated Mission, Earth Twins in HZ

A two-year observing sequence for the 41 stars of Case 1 is shown in **Figure 5.3-1**. The input target list is given in **Table A.1-2** in Appendix A and includes known giant planet target stars.

All observations are made using either the 510–825 nm band or, in the case for three Earth candidates, the 400–645 nm 'blue' band with its 80 mas IWA. The blue band was chosen solely to improve obscurational completeness on these targets. A disadvantage of this band is that it places the starshade farther from the telescope, which increases slew time. For Case 1, the limiting contrast ratio expressed in magnitudes is limΔmag = 25.5 + 2.5logL, for L<1.6, and limΔmag = 26 (a contrast ratio of 4×10^{-11}, the instrument's sensitivity limit) for higher luminosity stars. This graduated limiting magnitude reduces observation time on low luminosity stars where high contrast is not required to see planets in the HZ. The detailed observing sequence is tabulated in Appendix A. The third year has been left unscheduled and is available for follow up spectroscopy, background object disambiguation, and orbit determination.

Note that four of the six high priority stars listed in **Table 2.4-3** are also scheduled in this DRM. The two stars that are not observed in the first two years are Beta Hyi and Delta Pav. Different observation sequence permutations could allow all six of the high-priority stars to be observed at the expense of known giant planets or HZ Earth-twin candidates.

5.3.2 Case 2: Dedicated Mission, Planet Harvest

Case 2 draws its high-priority targets from the input target star list given in **Table A.1-3**. All

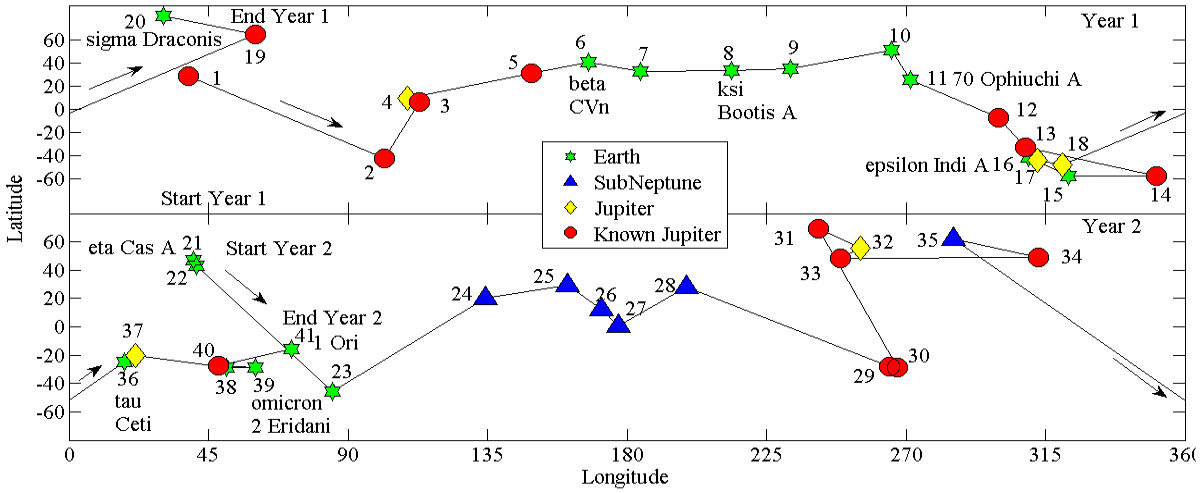

Figure 5.3-1. Observing sequence for Case 1, Dedicated Mission, Earth twins in HZ. Coordinates are ecliptic longitude and latitude.

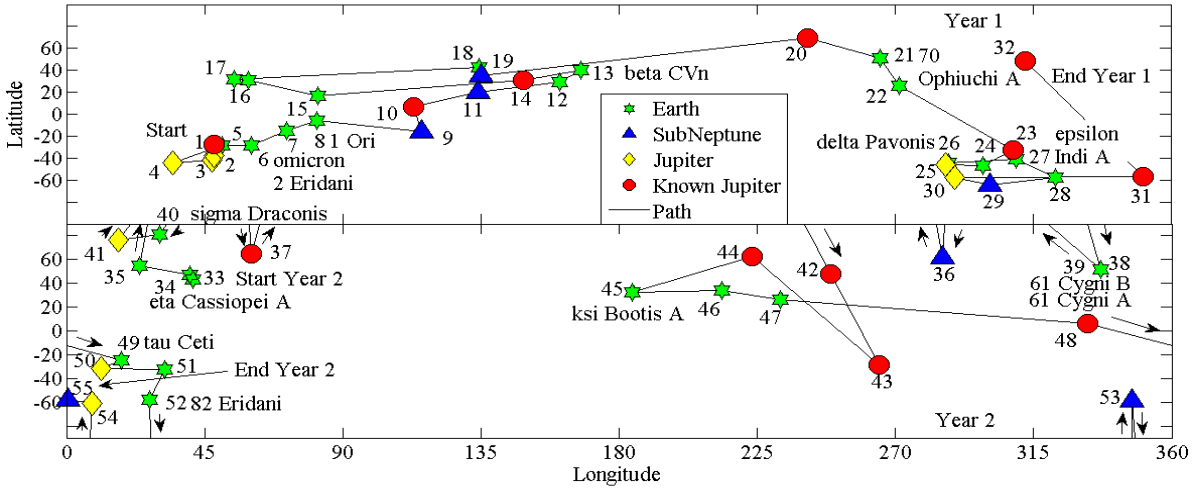

Figure 5.3-2. Observing sequence for Case 3, Rendezvous Mission, Earth twins in HZ. Coordinates are ecliptic longitude and latitude.

non–known giant planet stars are observed to limΔmag=26 using the IFS, in the 510–825 nm band. The DRM includes 38 stars. Because the IFS is always employed, a spectrum is automatically obtained, up to R=70, for sufficiently bright planets. Since observing down to limΔmag takes significant time, some of the stars have high enough common proper motion to differentiate a planet from a background galaxy or star in a single visit (described in Sections 3.1.2 and 3.1.3). This mitigates the need for revisits.

Of the six high-priority targets, all but delta Pav have been scheduled (see Appendix A, Case 2, priority 0 stars).

5.3.3 Case 3: Rendezvous Mission, Earth Twins in HZ

The Case 3 input target star list is provided in **Table A.1-4**. An observing sequence for the Rendezvous Mission is shown in **Figure 5.3-2** for the first two years of the mission, with a total of 55 targets visited. Case 3 employs the same luminosity-based limiting magnitude as Case 1, and uses the IWA=80 mas blue band for 12 HZ Earth-twin candidates to improve completeness. Since this case is based on a starshade used with the WFIRST/AFTA mission, no overhead is placed on the setup time because the observatory has a steerable antenna.

The observation bands are narrower than in Cases 1 and 2, with the green band spanning 600–850 nm and the blue band spanning 470–670 nm. In direct imaging mode, the sub-bands have R=9, compared to R=7 in the Dedicated Mission.

5.4 Results

Target statistics, observational completeness, characterization potential, and anticipated planet yields for the three cases are shown in **Figures 5.4-1** and **5.4-2**, and **Tables 5.4-1** and **5.4-2**.

Table 5.4-1 shows the cumulative observational completeness for the three cases. **Figure 5.4-1** further categorizes the completeness relative to the luminosity-adjusted habitable zone. Hot planets (red) orbit up to 0.75 AU. Warm planets (green) are in the HZ, from 0.75–1.77 AU, and cold planets (blue) exist between 1.77 and 10 AU. Planets

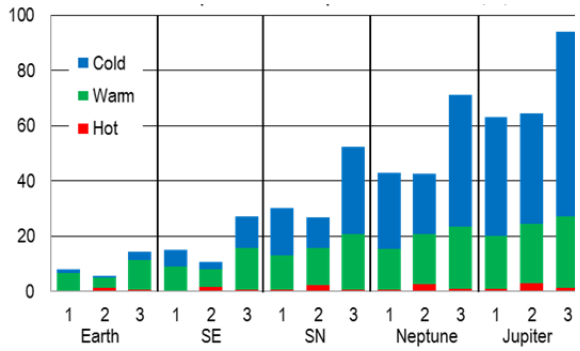

Figure 5.4-1. Observational completeness for the Case 1, 2, and 3 observation scenarios.

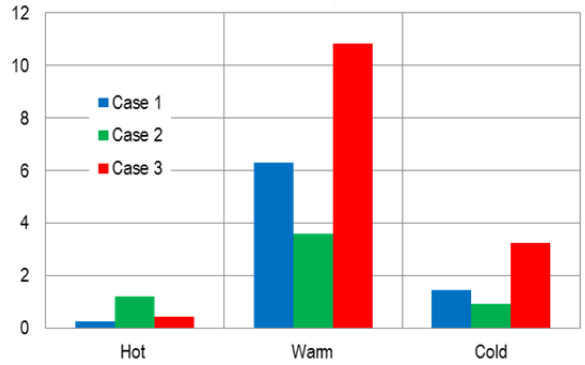

Figure 5.4-2. Observation completeness for Earth-size planets with geometric albedo 0.2 for the three observation scenarios.

beyond 10 AU are not included in the study. The temperature zone boundaries are adjusted by the square root of the bolometric luminosity of each star.

Table 5.4-1 and **Figure 5.4-1** show that observational completeness, which is the combined photometric completeness (limited by limΔmag) and obscurational completeness (limited by IWA), is dominated by giant planets, which are relatively easy to detect in the warm and cold temperature zones. Completeness is reduced for smaller, cold planets because at large separations from the star they become fainter than limΔmag.

Figure 5.4-2 shows that Case 2, which emphasizes planet diversity and peers deeply at a smaller number of targets than Cases 1 and 3, has ~60% of the HZ Earth twin completeness relative to Case 1. In its search for HZ Earth twins, the Rendezvous Mission combines shorter integration times, reduced observational overhead, and faster slew times to observe 28 Earth-twin targets. It achieves an observational completeness of nearly 11 HZs.

On the other hand, the additional diversity in Case 2 gained by observing each target to limΔmag=26 affords a significantly greater likelihood that spectra can be obtained on giant and sub-Neptune planets. By utilizing the IFS at its full spectral resolution for all observations, spectra of Jupiter and other planets are automatically collected should they be present in the image. In Case 2, integration times are sufficiently long enough on

Table 5.4-1. Planet completeness and yield.

	Completeness		
	Case 1	**Case 2**	**Case 3**
HZ Earth	6.3	3.6	10.9
Earth	1.7	2.1	3.7
Super Earth	14.9	10.6	27.3
Sub-Neptune	30.3	26.8	52.3
Neptune	43.0	42.7	71.1
Jupiter	63.2	64.4	93.9
Total	159.5	150.2	259.2
	Mean Planet Yields		
	Case 1	**Case 2**	**Case 3**
HZ Earth	1.0	0.6	1.7
Earth	0.3	0.3	0.6
Super Earth	1.5	1.1	2.7
Sub-Neptune	3.0	2.7	5.2
Neptune	4.3	4.3	7.1
Jupiter	6.3	6.4	9.4
Known Jupiters	14	14	12
Total	**30.4**	**29.4**	**38.8**

Table 5.4-2. Characterization potential.

Number of Targets		Case 1	Case 2	Case 3
Jupiter	R > 20	13	25	29
	R = 70	10	24	19
Sub-Neptune	R > 20	0	24	13
	R = 70	0	0	1

24 targets to obtain R=70 spectra on Jupiters and R > 20 spectra on sub-Neptunes, exclusive of known giant planets, which are also characterized. In Case 3, with the minimum integration time set to one day (this is longer than required for many HZ Earth twin detections), R=70 can be achieved on 19 Jupiters. In Case 1, only half as many observations reach R=70.

In summary, Cases 1 and 3 achieve their goal of high HZ Earth-twin completeness. Case 2 likewise achieves its goal of observing a more diverse set of stars and providing more opportunities for planet characterization.

The expected planet yields are given in the bottom half of **Table 5.4-1**. Mean yields are the observational completeness multiplied by the probability, η_{planet}, that a planet exists. Here it is assumed that η=0.16 for Earths in the HZ, while all other planets have η=0.1 integrated over all three zones. Cases 1 and 2 have nearly identical yields, about 16 non–known giant planets, half of them Jupiters, in addition to the 14 known giant planets whose masses and spectra will be determined. Case 3 has an

expected yield of ~27 planets in addition to 12 known giant planets.

5.5 Final Remarks

The results presented here are for representative two-year-long preordained DRMs. The missions are designed with at least three-year fuel capacity and thus will return additional science in the third year including additional giant planets, characterizations of discovered planets, planet confirmation observations, and potentially orbit-determination observations. A full DRM to model these observations is under development.

6 THE STARSHADE DESIGN AND FORMATION FLYING

The starshade, and its ability to fly in formation with the telescope spacecraft are enabling elements not routine for space missions. This section describes the optical and mechanical design of the starshade, as well as the formation flying system and its operation. An error budget inclusive of both the starshade and formation flying designs is also presented.

6.1 Starshade Optical Design

The starshade's purpose is to create a deep shadow at the aperture of a space telescope by blocking starlight and limiting starlight diffracting into the shadow region. The direct blockage of starlight with a simple, circular, opaque disk (such as that used in the upcoming PROBA-3 (PRoject for OnBoard Autonomy) formation-flying, solar-occulting mission) is insufficient due to starlight diffraction around the disk edge. A transition (or 'apodization') region, starting at the edge of the disk and extending radially outward, is required to mitigate diffraction. Ideally, the apodization region is a continuous gray-scale, but for the sake of a practical implementation, it is approximated as a binary function (all or none of the light passes at any point—an opaque mask). This yields the complex, yet distinctive starshade shape of a central disk with flower-like petals extending radially from the disk perimeter.

There is an infinite family of flower-like starshade shapes that produce a dark shadow suitable for planet hunting given a large enough starshade. To find these shapes, designers began by writing down analytic functions with a few parameters (e.g., Copi & Starkman 2000, Cash 2006). Later, Vanderbei, Cady, and Kasdin (2007) introduced more complex shapes with hundreds of parameters defining the edge shapes, and used linear optimization to choose the parameter values. Further design requirements beyond starlight suppression were set by other scientific and engineering considerations (e.g., disk diameter and petal length limitations, minimum feature sizes, bandpasses) constraining the many degrees of freedom in this optimization.

A three-step optical design process is employed in iterative fashion to find an optimal solution. First, parametric studies are conducted based on a large number of approximate solutions and curve fitting to illustrate trends. Second, some tens of potential designs are run through the optimization scheme to identify candidates with high suppression and consistency with all imposed constraints. Finally, select designs are rigorously verified to provide the requisite starlight suppression at all points in the focal plane. Parameters are adjusted until the design is fully compliant with requirements imposed by scientific and engineering constraints.

Solutions for starshade designs are generated using the linear optimization tool described above, which finds the apodization petal shape—that minimizes the modeled diffracted light over the full shadow region and wavelength range, subject to a predetermined maximum allowable light intensity within the shadow.

There is a small amount of freedom in selecting the number of petals used. The total number of petals is only bounded weakly by optical considerations—too few petals and terms ignored in the approximation slowly begin to become important. Conversely, an increased number of petals makes for smaller petal tips and smaller gaps between petals, as well as simply more hardware to manufacture, test, and deploy. Additional constraints include a minimum petal tip width and inter-petal gap of 1 mm, maximum petal lengths and widths that can be packaged for launch, and upper and lower bounds on the bandpass of operation. Inner working angle (IWA) (i.e., the angular extent of the starshade tip) was allowed to vary when generating families of designs for Exo-S, with the smallest-IWA design with sufficient contrast being selected for the baseline.

Specific point designs are further evaluated for science performance based on the combination of parameters. Planet yield is evaluated for a target list constrained by a candidate starshade's estimated IWA and contrast.

For the Dedicated Mission, available launch packaging volume (considering the starshade is co-launched with the telescope) sets limits on starshade size (7-m petal length, 16-m inner disk diameter) and petal number (22). These limits can be relaxed somewhat for a starshade that is launched independently. In the Rendezvous Mission, the truss is permitted to increase to 20 m, and the petal number is increased to 28 to maintain a similar petal aspect ratio between the two designs. **Figure 6.1-1** shows the baseline petal and starshade shapes. **Figure 6.1-2** shows the same for the Rendezvous Mission.

The Dedicated Mission design is set for observation of Earth twins at wavelengths between 510–825 nm (the 'green' band) at 102 mas IWA and a separation distance of 30,300 km. Additional bands (blue: 400–645 nm and red: 615–1000 nm) are available at inversely proportional separation distances and corresponding IWAs. Each band provides identical suppression at the telescope aperture at the designated separation distance and IWA. The green band is chosen as the baseline because it covers key biomarkers while maintaining an acceptable IWA and a mid-range separation. Conversely, the blue band includes very few biomarkers, while the red band covers the most favorable biomarkers but

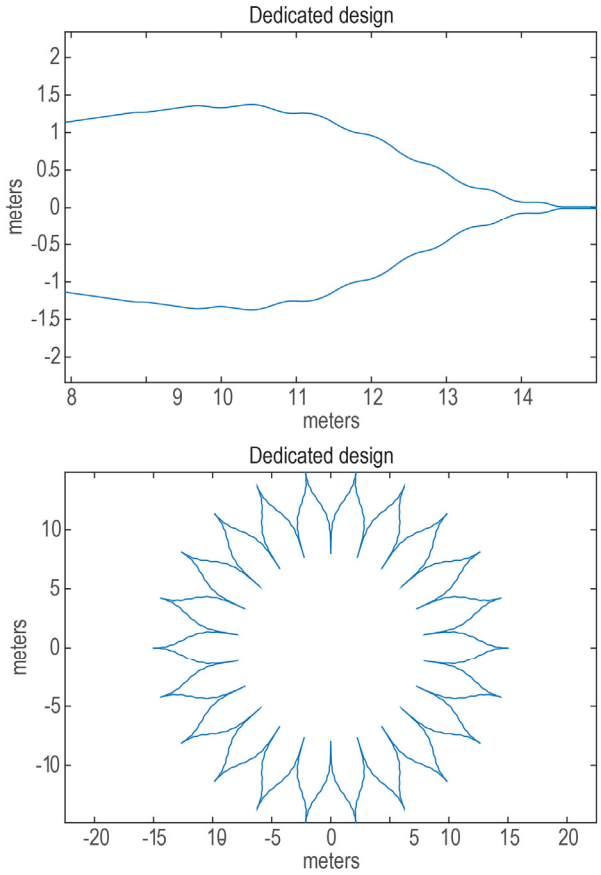

Figure 6.1-1. *Top:* The shape of an individual petal for the Dedicated Mission; the ripples on the petal edges are optimized to provide suppression over a wide band with a small starshade. *Bottom:* The shape of the entire starshade.

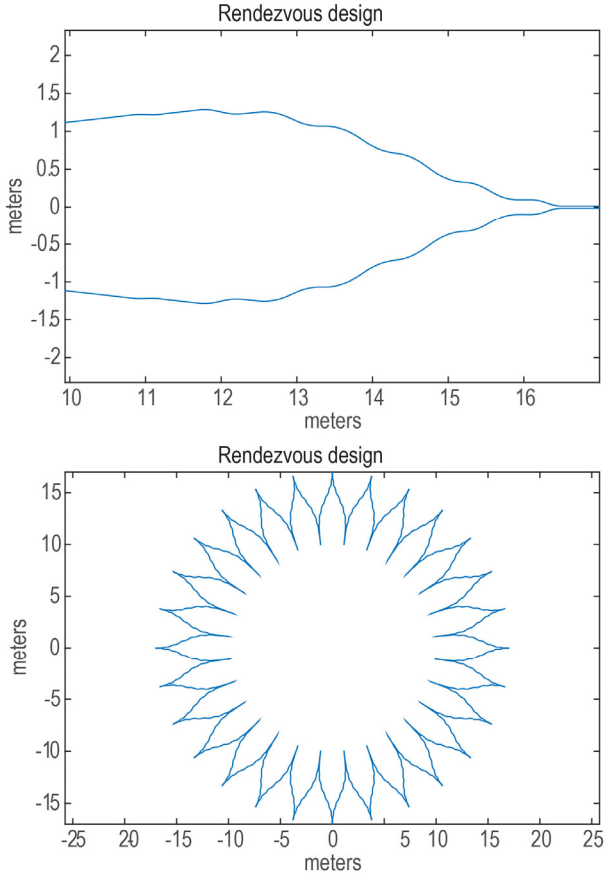

Figure 6.1-2. *Top:* The shape of an individual petal for the Rendezvous Mission. *Bottom:* The shape of the entire starshade.

with significantly reduced observational completeness due to its 18% larger IWA.

The procedure for designing a starshade compatible with an existing telescope (as in the Rendezvous Mission) does not differ appreciably from the procedure for the Dedicated Mission. The optimization is revised to incorporate the appropriate telescope diameter, and point designs are tested for the Rendezvous Mission telescope aperture. For the 2.4-m WFIRST/AFTA telescope, the optimization results in a starshade design with an IWA of 100 mas in a 600–850 nm band tuned to the design of the existing coronagraphic instrument.

6.2 Starshade Mechanical Design

From a mechanical point of view, the starshade is a deployable structure that, upon expansion, creates the requisite optical shape needed to cast a deep shadow on the observing telescope. The starshade is composed of three main elements: the circular inner disk structure (IDS), the petals mounted to the circumference of the IDS, and the opaque optical shield (OS) which covers nearly all of the structure. An example starshade is shown in **Figure 6.2-1** and a deployment sequence shown in **Figure 6.2-2**. This section explains the architectural trades and describes the designs and analyses performed to date that have resulted in the starshades used in the Dedicated and Rendezvous mission concepts.

6.2.1 Mechanical Architecture Approach

The starshade's mechanical architecture is constrained in a number of ways. The structure must fit within a 5-m fairing (along with its enabling spacecraft and a second, telescope-carrying spacecraft) then deploy into a 30-m optical mask once on orbit (**Figure 6.2-3**). It must meet the tight manufacturing and environmental performance tolerances identified in the overall system error budget (Section 6.4). Finally, the architecture must meet challenging cost and schedule programmatic constraints. All of these requirements have limited the starshade architectural tradespace and have shaped the starshade designs used in the Exo-S study.

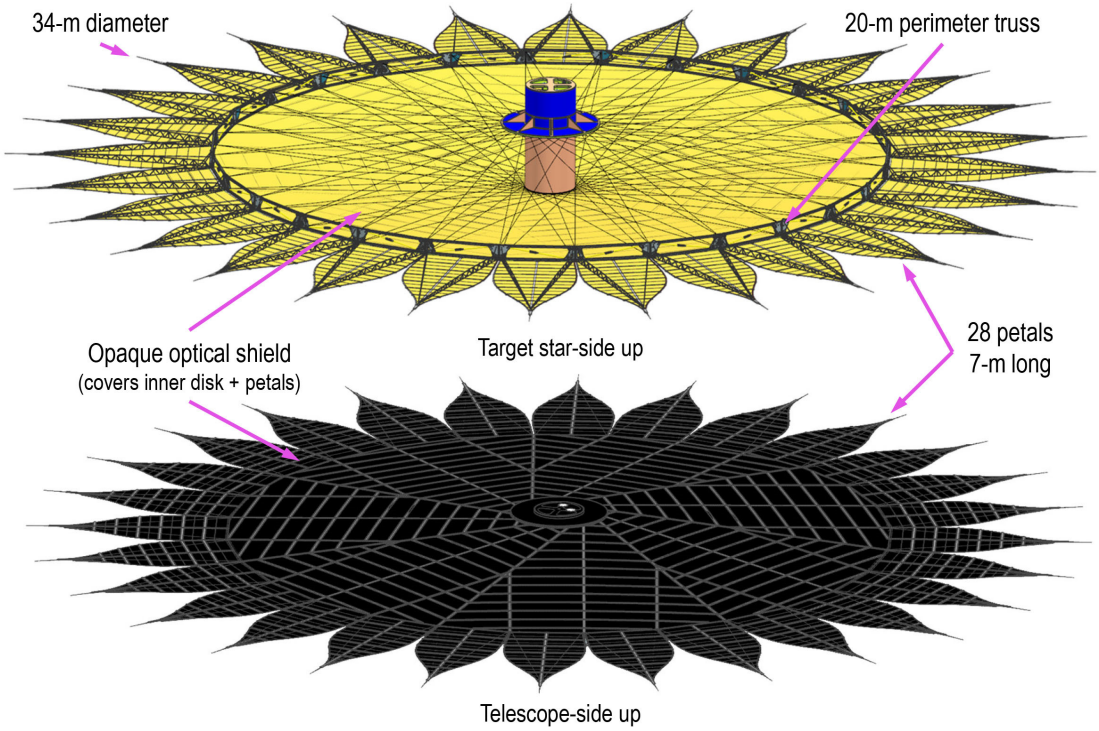

Figure 6.2-1. Fully deployed starshade configuration and major system elements. Rendezvous Mission configuration shown.

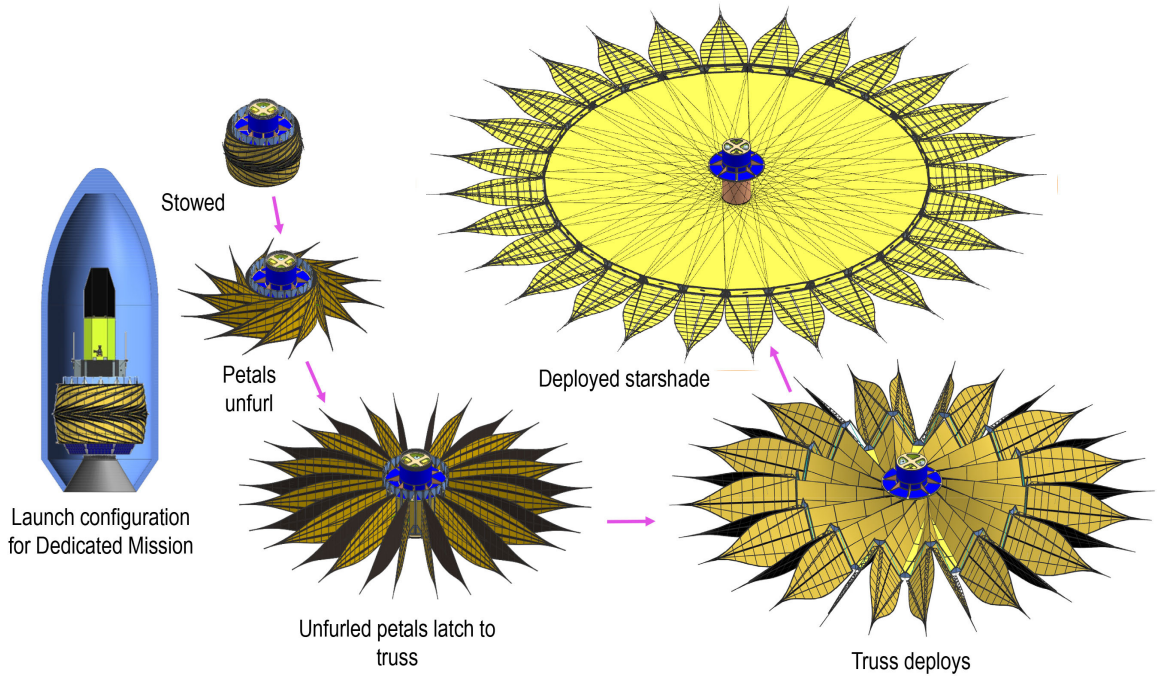

Figure 6.2-2. Starshade deployment sequence.

Only a limited number of large deployable structure architectures were considered as part of this study due to the cost-driven, time-driven need for heritage from a prior space application; a completely new structural architecture would not meet the Probe Study charter requirement of reaching TRL 5 by 2017. Possible architectures were largely drawn from industrial experience with large deployable antenna structures. Additionally, the deployable boom architecture (used on the James Webb Space Telescope's thermal shield) was also considered but was dropped due to fairing packaging difficulties in the Dedicated Mission's co-launched configuration. This architecture may be workable for a differently constrained situation and is currently in use for starshade concepts under development by Northrup Grumman.

Historically, deployable mechanical antenna structures come in two designs: radial rib and perimeter truss. Elements of both can be found in the starshade design. The inner disk structure is fundamentally a perimeter truss structure used successfully in deployable space antennas of approximately the same size. Battens have been reduced in length since space to hold the parabolic antenna surface is no longer a design consideration, and spokes have been added to help provide the required deployed stiffness. The end result is a deployed configuration similar in appearance to a bicycle wheel. The petal stowing method draws from flight-proven radial wrapped-rib antennas that stow about a central cylinder. The result is a compactly stowed design in which the starshade IDS and petals stow concentrically around a central, load-bearing cylinder (hub) as seen in **Figure 6.2-3.**

A further consideration in the starshade architecture is the length-to-width aspect ratio of the petals. Lower ratios make for stiffer petals and better enable the starshade to meet the mechanical performance requirements identified in the error budget (Section 6.4). Ratios above a certain threshold are avoided in the design for this same reason. This has the effect of loosely coupling the inner disk diameter to the number of petals (for a specified petal length); consequently, the number of petals and inner disk diameter must

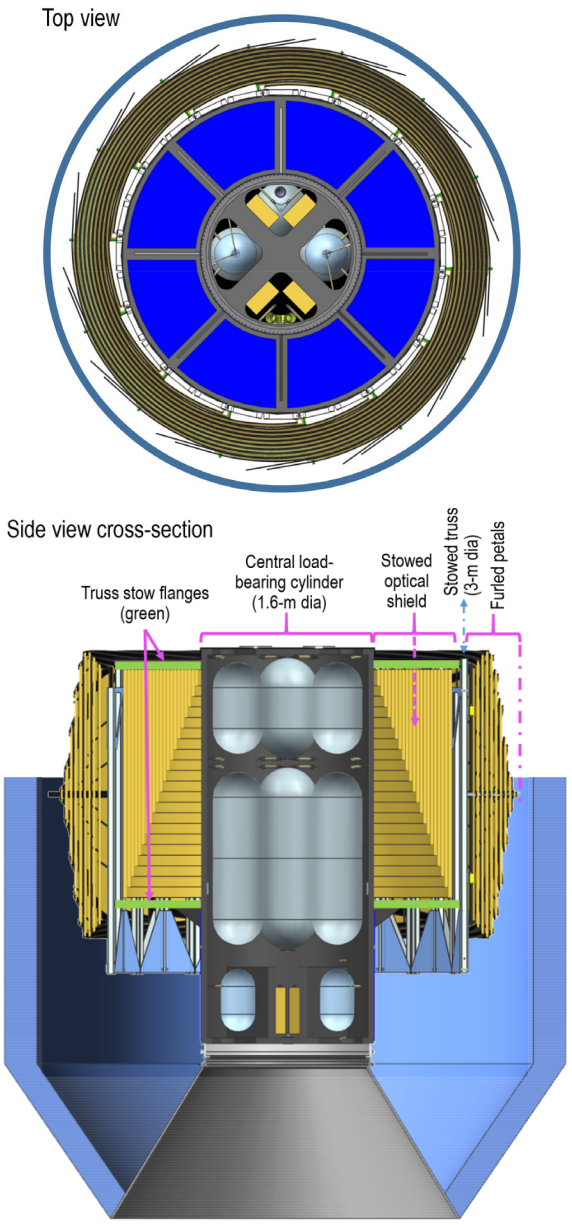

Figure 6.2-3. Stowed starshade (Rendezvous Mission) top-view and cross-section.

be determined jointly through both optical and mechanical analyses.

Finally, with the perimeter truss architecture, petal length is limited by a storage and deployment constraint requiring that the petals not overlap themselves when in the stowed configuration. In the case of the Dedicated Mission design, the petal length is also constrained by the launch stack center of gravity, which is highly dependent on the petal width since it sets the starshade hub height. This width constraint results in a length constraint due to the aspect ratio. For the Dedicated Mission, the current launch center of gravity (CG) is close to the launch vehicle requirement; longer petals than the current design are possible but would require complicated design trades to preserve the current CG.

6.2.2 Dedicated vs. Rendezvous Starshade Designs

The starshade mechanical designs are largely the same. All materials are identical in the equivalent components of each design. Petal structural designs and dimensions are identical. Both rely on the same spoke-supported perimeter-truss inner disk structural architecture. The sole significant difference between the two designs is the smaller inner disk diameter (and by extension the overall tip-to-tip diameter) on the Dedicated Mission design. This change was motivated by the need to conserve mass on the Dedicated Mission due to the required co-launch configuration. The reduction was achieved with minimal design impact by reducing the number of petals and the corresponding bays (polygonal edges) in the perimeter truss.

The two starshade concepts are shown in **Figure 6.2-4**.

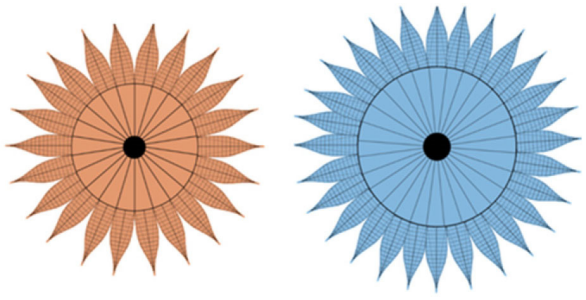

Figure 6.2-4. Starshades for the two mission concepts.

6.2.3 Heritage of the Starshade Mechanical Design

As stated earlier, a large deployment to tight tolerances is the primary structural challenge faced in the starshade's mechanical design. But space-based precision deployments, even to the tolerances required for starshade direct imaging, are not without precedents. The two principal deployable elements of the starshade—the inner disk structure and the petals—draw on two distinct deployable antenna architectures, leveraging the extensive industrial experience with precision deployments.

First launched in 2000, the perimeter truss has become one of two standard structural architectures in use for communication antennas above 10 m in diameter. The perimeter truss has proven to be a mass efficient, reliable, and stiff deployable structure on eight missions to date. The design stows compactly, and has been demonstrated to reliably deploy to Exo-S required positional tolerances in early testing (see Section 9 for details of early perimeter truss deployment testing for starshade applications). The perimeter truss' geometry has the added advantage in that starshade petals attached to the truss' longerons are carried from a vertical stowed-truss position to the deployed, horizontal position by the movement of the deploying truss alone (**Figure 6.2-5**).

Starshade petal designs use stowing techniques similar to those used on many wrapped rib antennas. Primarily flown in the 1980s, wrapped rib antenna designs have been successfully used on over 100 space missions. When deployed, the antenna utilizes a number of radially oriented ribs to hold an RF reflective mesh in a parabolic shape. These ribs are dimensionally deep in the direction perpendicular to the surface of the antenna aperture, creating the necessary stiffness to support the antenna mesh shape. Parallel to the antenna surface, the ribs are thin and flexible, allowing the ribs to wrap around a central cylinder for stowing and launch (**Figure 6.2-6C**). The strain energy from wrapping the ribs about the cylinder is used on-orbit to passively deploy the ribs and antenna.

This same passive deployment technique is used with the starshade petals. With the perimeter truss in its stowed position, the petals are near vertical and pointed radially outward similar to the deployed ribs in the wrapped rib antenna (**Figure 6.2-6A)**. Like the wrapped ribs, the petals have flexibility when wrapped around the hub and stowed truss but retain strain energy once fully wrapped into stowed configuration. As with the wrapped rib design, this energy is later used to passively deploy the petals into radial position prior to the perimeter truss deployment.

Further detail and optimizations to the petal designs the inner disk perimeter truss are described in the sections that follow.

6.2.4 Petal Design

The primary requirements for the mechanical design of the starshade petals are:

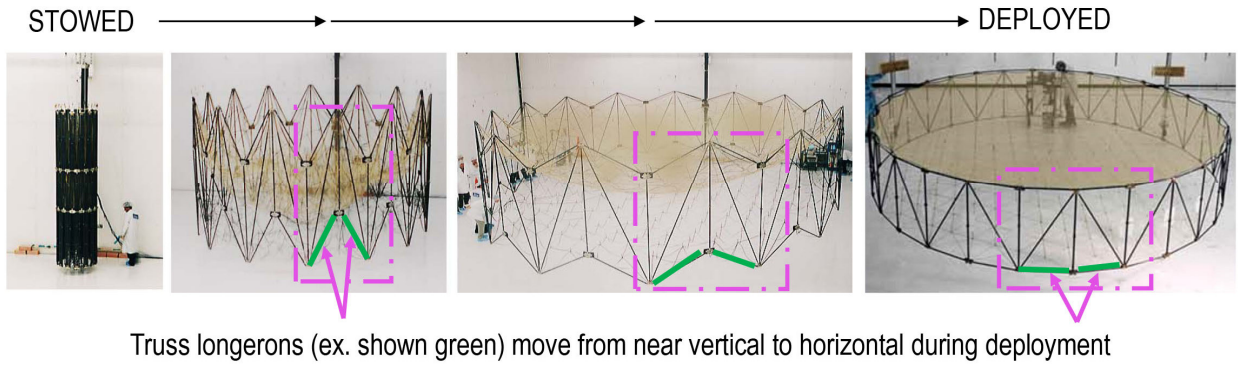

Figure 6.2-5. Antenna perimeter truss deployment sequence. (Astromesh antenna. Photo courtesy of Northrop Grumman Corporation.)

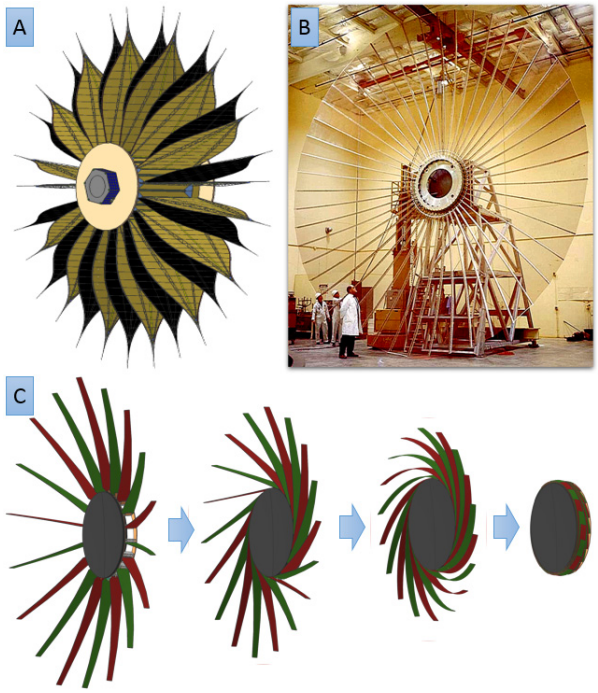

Figure 6.2-6. Wrapped radial rib technology application to starshade petal stowing.

1. The design must permit the stowing of the petals within a 5-m launch fairing along with all other required flight hardware systems for the mission;
2. The petals must deploy to and maintain the required optical starshade shape throughout the duration of the mission; and
3. The petals must be lightweight.

The product of these requirements is the petal design shown in **Figure 6.2-7**.

A starshade petal is a lattice of graphite composite members—called battens and longerons—that intersect a longitudinal central spine. The battens support the structural edge and are critical in the starshade holding its optical shape. Made from carbon composite tubes with a near-zero CTE (coefficient of thermal expansion), the battens enable the petal to meet dimensional stability requirements during on-orbit operations. Longerons provide in-plane shear stiffness for the optical edges. The longerons are also a carbon composite, with a circular cross-sectional shape. This shape allows the longerons to serve as the hinge pins for the petal stiffening ribs. The combined result of these elements is a lightweight lattice stiff enough to maintain the petal shape on-orbit as well as during integration.

Along the petal periphery are the structural edges. The structural edge provides a substrate onto which the precision optical edge segments are attached. The optical edges are produced in nominally 1-m-long segments and are aligned and bonded onto the starshade petals to form a continuous outline, minimizing gaps and offsets between segments.

While the optical edges must form the proper outline to maintain deep suppression of the target star, they must also be designed to minimize stray light. Sunlight glint off of the optical edges could raise the image contrast floor and wash out potential target exoplanets. Minimization of the sunlight glint involves using sufficiently sharp edges with low reflectivity.

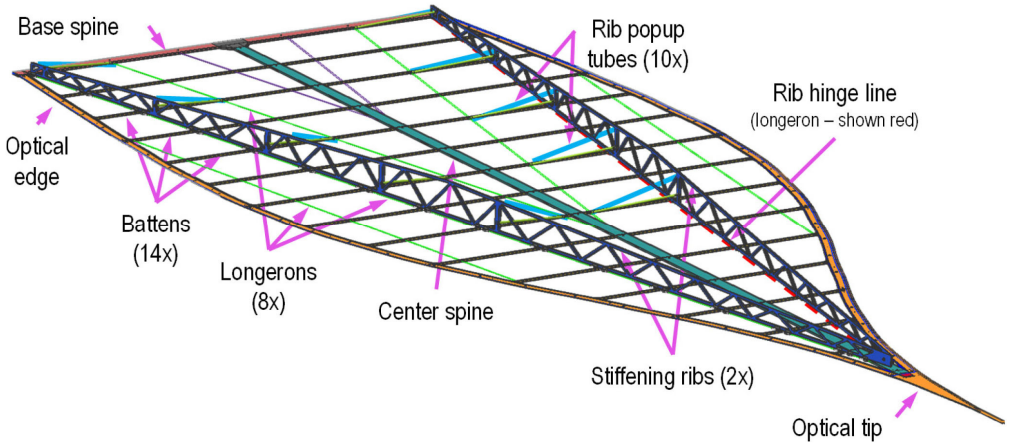

Figure 6.2-7. Petal construction. (Optical shield not shown)

Thermal compatibility between the optical edges and the structural edges is also a factor in the petal mechanical design. Mismatches in thermal expansion between the carbon fiber mechanical edge, and the sharpened optical edge material should be carefully regulated to prevent failure of the optical edge material, or warping of the petal structure due to imposed thermal stresses.

The root of the petal is formed by the base-spine, which is attached to both the center-spine and structural edges and serves as the member to which the truss attaches. The base spine assembly includes two hinge points for the unfurling portion of deployment and two precise latches that then lock the petal into the deployed position. Deployed out-of-plane petal stiffness is achieved via the two base-spine hinge latches and the deployable ribs that latch to the inner disk truss to create a deep, and consequently stiff, beam connection of the petal to the truss.

The petal ribs are oriented along the length of the longest longeron and utilize this longeron as a hinge pin. The ribs fold down against the petal for stowing, bending with the petal as it furls about the cylindrically stowed truss. During petal deployment, the ribs passively deploy once the rib and petal have completed unfurling. The passive rib deployment is initiated by contraction of a pre-stretched tension spring housed inside the rib pop-up-tubes.

The center and base spines are fabricated out of a composite construction with carbon fiber facesheets separated by a foam core. The foam core provides structure for the necessary launch and petal unfurling hardware, while also adding flexibility so that the petal can wrap around the stowed truss for launch. The foam also provides the stowed strain energy used to passively unfurl the petal during deployment.

In the stowed position, the petals are furled about the cylindrically shaped stowed truss, overlapping their adjacent petals. To connect and restrain the petals for launch, the petal center-spines carry cup-cone interfaces on the front and back of the center-spines. When furled, these cup-cone interfaces of adjacent petals align, providing a pseudo-kinematic and structural joint between stowed petals. The stack of cup-cone interfaces are then preloaded by a tensioned cable that passes through stacked petals. The tensioned cable is then cut post launch, releasing the petals.

6.2.5 *Inner Disk Structure*

Like the starshade petals, the inner disk structure shares the same three principal mechanical design requirements: the IDS must stow within a 5-m launch fairing; must deploy to and hold an accurate shape; and must be lightweight. The 'hold-an-accurate-shape' requirement is in part driven by the need for accurate petal placement within the overall starshade structure. The main components of the IDS are the perimeter truss, spokes, and central hub. The IDS functions much like a bicycle wheel, with the perimeter truss operating as the rim, and the spokes tensioning the truss back to the central hub to make the perimeter truss stiff and the IDS optical shape precise.

Also like the petals, the IDS design must minimize sunlight scattering back into the telescope. This requirement sets a constraint on the deployed geometry. Due to worst-case Sun angles, all starshade spacecraft hardware on the telescope side of the starshade must be within a right circular cone defined by a 168° aperture and a base equal to the deployed IDS. The cone ensures that all potentially scattering telescope-facing hardware is always in shadow during observations (**Figure 6.2-8**).

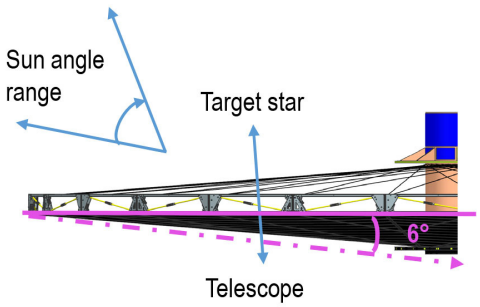

Figure 6.2-8. Geometry for avoiding scattered sunlight.

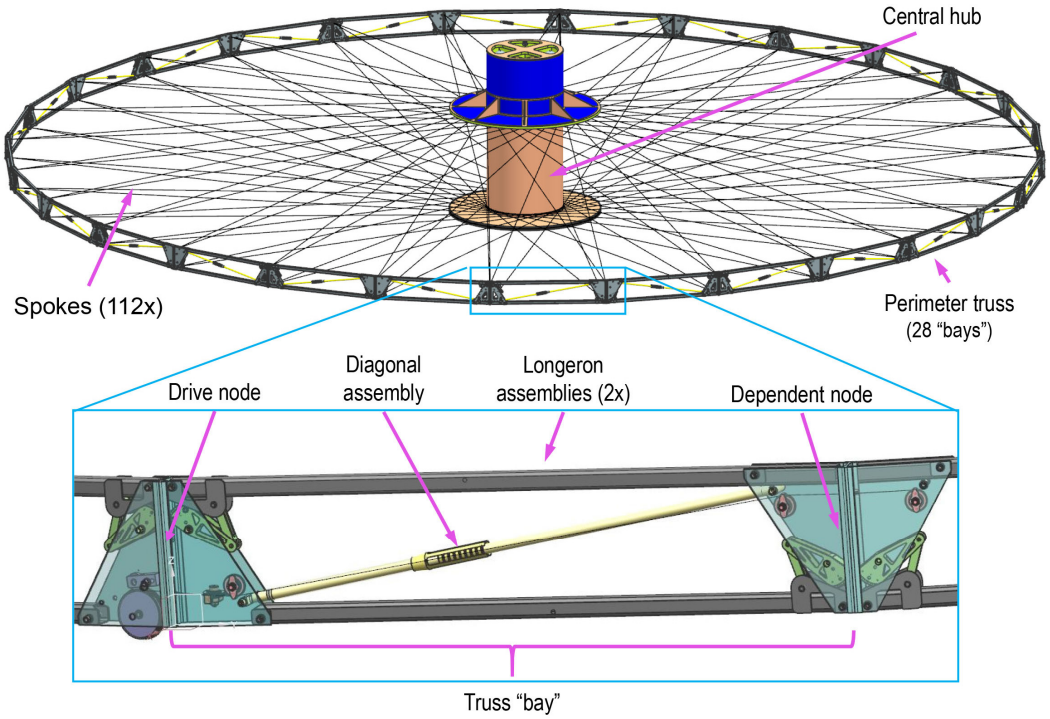

Figure 6.2-9. Truss bay structural detail.

6.2.5.1 Perimeter Truss Geometry & Deployment

The perimeter truss consists of repeated rectangular bays that form a ring-shaped truss (**Figure 6.2-9**). Each bay is a rectangle, formed by horizontal longerons, to which the petals attach, and vertical battens. The diagonal member splits the truss bay into triangles, resisting shearing of the rectangular bay and providing a defined shape to each truss bay. Each of the truss members are pinned to each other at the joints, therefore, there are no moments carried by the truss members.

If the diagonal member is removed, the rectangular truss bay is a four-bar linkage, having no member to resist shearing, and would therefore 'parallelogram'. This is used as an advantage for stowing the large deployed truss into a compact volume; these stow/deploy geometry kinematics are shown in **Figure 6.2-10**. Geometry shows that the chosen diagonal of the truss bay has a shorter length in the deployed versus stowed condition. Because the diagonal members are needed in the deployed state of the truss to create a determinate and shear carrying structure, the diagonal is constructed of a telescoping tube, with the inner tube bottoming out at a designed location inside the outer tube upon final truss deployment.

The truss deployment is controlled by a motor that spools in a braided steel cable,

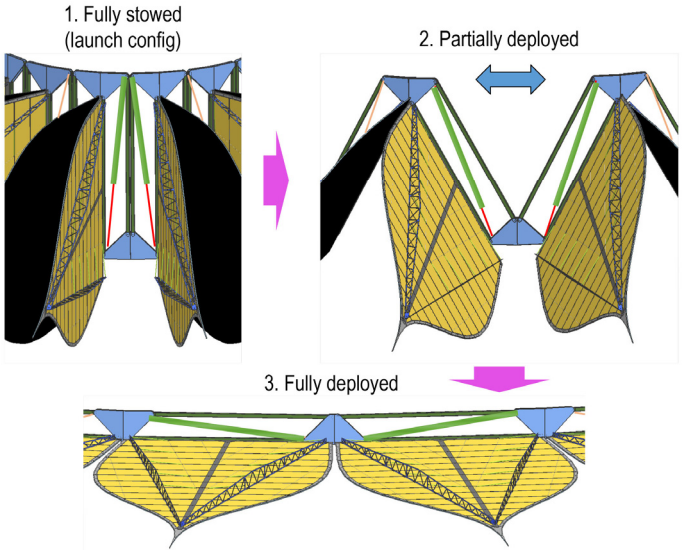

Figure 6.2-10. Truss deployment geometry and sequence.

which winds through the truss, following the path of the diagonal members. Because deployment geometrically shortens the diagonals, the reeling in of the cable inherently forces the bay toward the deployed state. The truss finishes deployment when the inner telescoping tube member bottoms out on the previously mentioned stop at the end of the outer tube. Synchronized deployment of the truss bays is controlled by synchronizer gears at the intersection of each of the bay.

6.2.5.2 Adaptation of the Deployable Antenna Design to a Starshade

The starshade perimeter truss design varies from that of a deployable perimeter truss antenna in only three distinguishable details. **Figure 6.2-11** shows a deployable and measured half-scale proof of concept and testbed of the adapted antenna design for the starshade.

The antenna and the starshade perimeter trusses both use gears in each bay to synchronize the deployment of all bays. With deployable antennas, these gears usually attach at the ends of each longeron with the gears protruding above the plane of the deployed truss. Because the starshade cannot allow protrusions beyond the 6-degree exclusion angle from the shape plane in the direction of the telescope, the gears have been moved internal to the truss and are connected to the longeron rotation via a pinned strut, functioning as a 4-bar linkage.

Another variance is the adjustment of the bay height. A deployable antenna requires a tall truss to create the parabolic antenna shape. This height is not required by the starshade. Furthermore, the starshade benefits from a much reduced truss height geometry in that it greatly shortens the overall stowed truss height, easing the packaging problem with the co-launch starshade configuration. More importantly, shortening the truss bay geometry permits latching the petal rib directly the top of the truss, making for a simpler way to meet petal stiffness requirements.

The last significant variance is related to the stowed diameter and geometry of the perimeter truss. Antenna perimeter trusses are designed as appendages to the spacecraft and

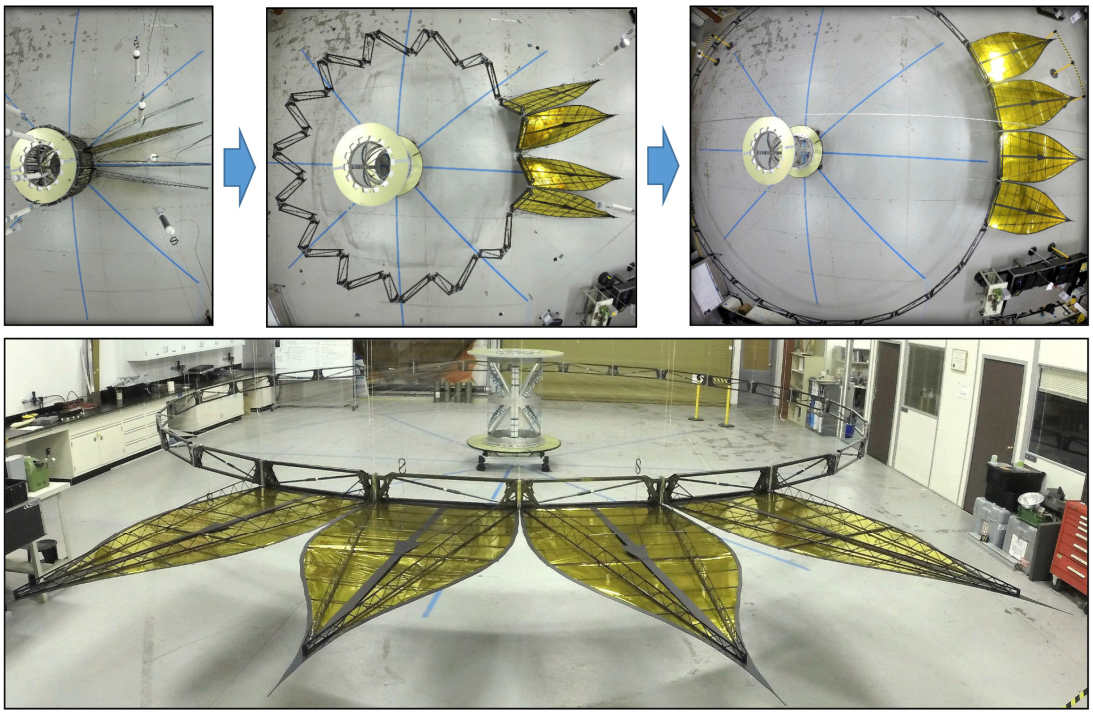

Figure 6.2-11. Half-scale starshade deployment testbed.

are consequently designed to stow as compactly as possible. The starshade truss must stow at a larger diameter than the antenna truss because the petals need a minimum stow diameter to not overstrain their components in the launch configuration. Additionally, in order to wrap the petals concentrically and compactly, the petals need to be vertical before wrapping. For a typical perimeter truss antenna, the petal-mounting longerons would not be vertical if the truss were stowed at a 3-m diameter. To achieve a truss geometry in which the longerons are vertical while stowed, the starshade longeron connection points are moved outward from the batten.

6.2.5.3 Spokes

The starshade spokes are critical in the stiffening of the truss, and therefore the petal root positions. The spokes are composed of very high modulus of elasticity, and near-zero CTE continuous carbon fiber tow surrounded in an over-braid for durability. Because the spokes are such high modulus, the spokes stretch very little upon full truss deployment, ensuring accurate placement of the truss and consequently the petals. Importantly, although stiff in tension, the spokes are flexible like rope, and are thus easily wrapped for launch and managed during deployment. The spoke lacing pattern was determined by optical stiffness of the IDS for carrying and maintaining the position of the petals. The end result of the analysis are spokes that run tangentially off the central cylinder to the longeron intersection points of the truss, resulting in a zero-moment structure.

6.2.5.4 Hub

The central hub comprises a load-bearing cylinder and two flanges (**Figure 6.2-9**), all made of carbon fiber facesheet honeycomb composite for stiffness, strength, thermal expansion, and mass efficiency. The central cylinder carries interfaces for the hub-side of the spokes and acts as a direct interface to the launch vehicle and the co-launched telescope-spacecraft for the Dedicated Mission. The hub's two flanges are the structure about which the perimeter truss stows. The central cylinder houses the optical shield (OS), which is stowed about the cylinder and nested between the flanges.

6.2.6 Optical Shield

While the starshade shape is responsible for casting the appropriate shadow on the telescope, the actual starlight blockage is carried out by the OS. Aside from the primary optical requirements (e.g., starlight transmission, reflectivity, etc.), the OS has a number of important mechanical design requirements. The OS must store compactly, it must minimize starlight passing through micrometeoroid punctures into the telescope, and it must be light weight.

The OS is composed of flexible panels comprising two thin layers of a low-reflectivity, black Kapton film sandwiching a 1.6-cm thick layer of ultra-low density foam. A single layer of black Kapton is sufficiently opaque to suppress the starlight; however, the second layer of Kapton, separated by foam, mitigates the impact of micrometeoroids punctures by reducing the probability that punctures through both layers will align with the star and telescope, and allow starlight to pass through the starshade to the imaging system. Portions of the OS are made more flexible by eliminating the foam, allowing for the OS to be foldable for stowage and deployment. The result is a low aerial density, optically opaque, flexible material that can be applied to both the IDS and petals.

The portion of the optical shield that covers the IDS is rigidly attached to the starshade central hub and is designed to induce negligible loads into IDS. The OS IDS panels are sized and shaped to stow in a 'flasher' origami folding pattern (**Figure 6.2-12**). This pattern folds and unfolds without imparting significant deployment loads into the truss.

The petal OS is pseudo-kinematically mounted, allowing for thermal deformation of

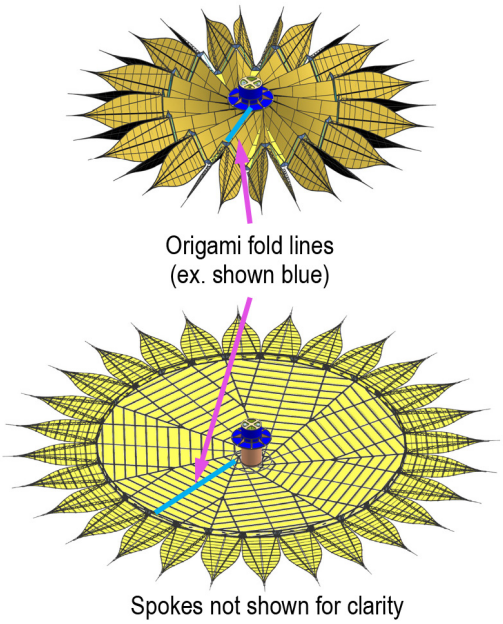

Figure 6.2-12. Origami 'flasher' folding pattern for blanket.

the OS panels with no noticeable distortion to the petal in-plane shape. When applied to the petal structure, the semi-rigid OS panels are flexible enough to furl along with the petal structure. When stowed, the panelized nature allows the panels to move with respect to each other, reducing the amount of motion of any given panel for both furling and thermal expansion on-orbit. Compression is minimized by sizing the stowed furling pitch of the petals to match the OS thickness, so as to only compress the OS along the petal battens and longerons. Detailed information on the OS is provided in Appendix B.

6.2.7 Starshade Mechanical and Thermal Analyses

To ensure that the spacecraft meets static and dynamic launch requirements, and that the starshade's on-orbit dynamic performance meets the concept's error budget requirements, initial static load calculations and Finite Element modal analyses were used to estimate the dimensions and select materials for critical starshade structural elements. Both the Dedicated and Rendezvous mission designs were examined under applicable worst-case conditions. In addition, on-orbit thermal analyses were carried out to verify the starshade's ability to meet dimensional stability requirements needed to achieve the required contrast performance.

6.2.7.1 Launch Structural Analysis

Starshade launch load sizing is largely driven by the required payload axial and lateral stiffness performance. The Dedicated Mission's co-launch configuration necessitates a stiff central load-bearing cylinder to limit lateral deflection (**Figure 6.2-13**). **Figure 6.2-14** captures the deflection and strain energy of the starshade hub's cylinder. Meeting the launch vehicle's payload requirement of a lateral first resonant mode above 10 Hz led to a central cylinder design using a carbon fiber facesheet honeycomb composite tube. The tube has a 1.6-m diameter to directly transfer the load of the top-mounted telescope through the starshade and into the launch vehicle, creating a mass-efficient structure. The tube design was subsequently verified for stress and buckling.

The Rendezvous Mission starshade structural sizing was set by the axial stiffness requirement. The larger, more massive, Rendezvous starshade transfers petal and IDS launch loads into the central hub's radial flanges. These flanges are sized largely due to

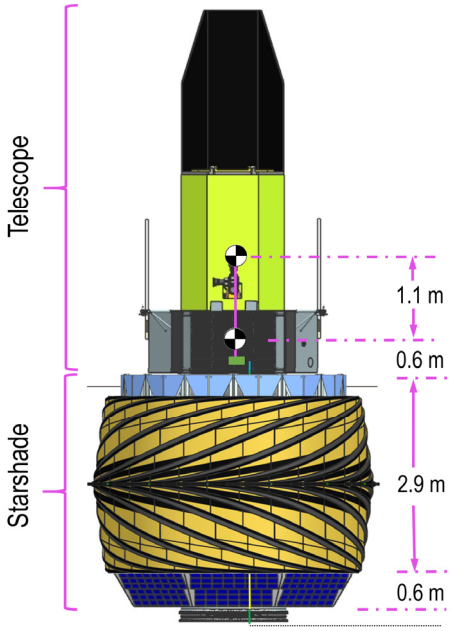

Figure 6.2-13. Launch configuration for the Dedicated Mission.

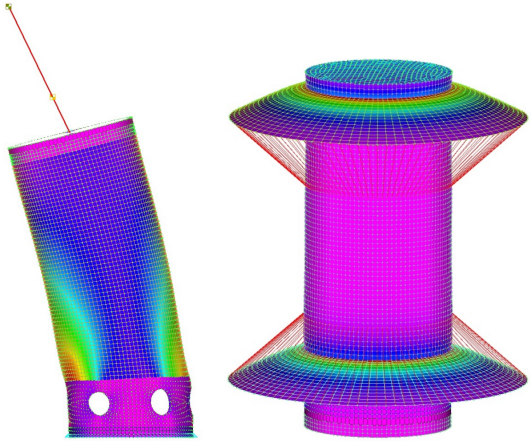

Figure 6.2-14. *Left*: First mode shape of Dedicated Mission at 11.4 Hz with element strain energy density contoured. *Right*: Axial mode shape for Rendezvous Mission at 25 Hz with element strain energy density, truss launch flanges deflected.

the axial excitation of this petal/IDS load during launch. The launch vehicle specifies a first axial mode above 25 Hz. Carbon fiber facesheets with a tall honeycomb core provide the necessary stiffness for these flanges, while also meeting the strength requirements where the flanges connect back to the central cylinder. The axial mode shape for this case is shown in **Figure 6.2-14**, right image. Since the Rendezvous Mission has the heavier petal/IDS load and since both mission designs use the same flange design, the flanges are more than adequate for the Dedicated Mission.

6.2.7.2 On-Orbit Structural Analysis

The starshade on-orbit analysis centers on creating a stiff and sufficiently damped on-orbit structure to ensure that the starshade maintains its optical shape throughout observations. Deployed truss stiffness is highly sensitive to designed spoke stiffness, which can be used to separate petal modes from the overall system mode to limit mass participation of the petals in the system modes. A spoke-stiffness analysis was used to create a sufficiently stiff perimeter truss to which the petals attach. Highlights of this analysis are provided in this section.

Petal vibrational modes were as expected; exhibiting a cantilever mode at 1.43 Hz, followed by a second mode at 3.83 Hz (**Figure 6.2-15**). Neither causes deformation in the critical petal shape plane.

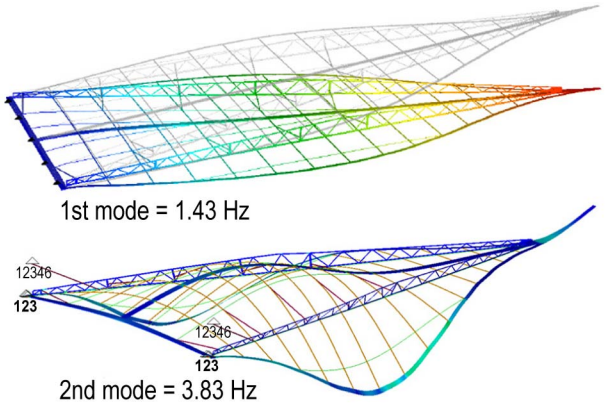

Figure 6.2-15. First and second modes of petal positions.

The system modes start at 1.29 Hz with a 6-lobed deformation of the petals and is followed with three more 'lobed modes' before reaching a 'petal piston mode' at 1.37 Hz, followed by several more 'out-of-plane' modes. An in-plane petal translation occurs at the 146th and 227th modes at 5.8 and 6.78 Hz, respectively (**Figure 6.2-16**). No modes directly contribute to deformation of the key starshade in-plane shape until modes 146 and 227.

Starshade thruster control system firing contribution to the in-plane shape deformation was analyzed to verify that the reaction control system would not significantly affect the iteration time for star observation. Four cases were analyzed to determine the deflection of the petal tip as a result of thruster firing, characterize the system's vibrational damping behavior, and compare this thruster-driven motion to the petal positional requirements specified in the error budget (Section 6.4). The requirement of 50 µm radians of clocking, 50 µm radial, 50 µm tangential, 1 mm out of plane after 10 seconds was easily met.

6.2.7.3 Thermal Design and Analysis

The nominal starshade shape is referenced to a uniform temperature of 293K. Deviations from this reference temperature result in some form of thermal deformation. Uniform or average temperature varies with the target to Sun angle

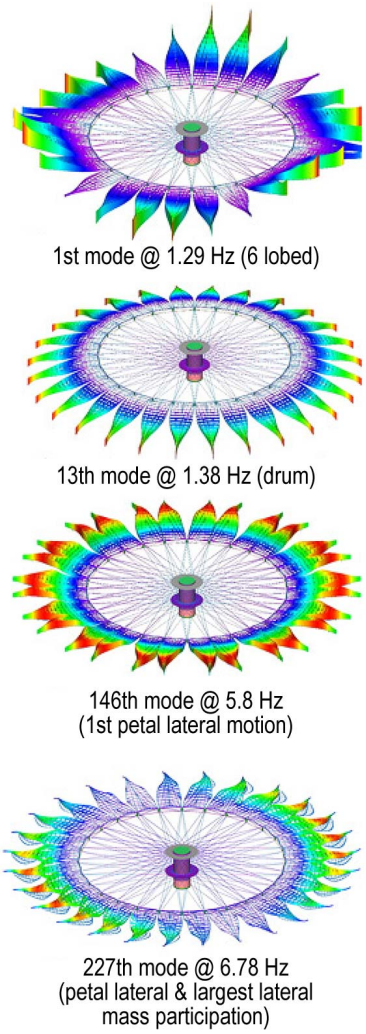

Figure 6.2-16. Relevant system modes.

that is the same as the solar inclination angle as measured from petal surface normal. Non-uniform temperature deviations result from shadowing effects that are limited by the spinning starshade. This section presents the key requirements, thermal design, and analysis results. Compliance with the key requirements is demonstrated with margin.

Optical performance is insensitive to uniform shape changes that affect both petal width and disk radius in equal proportion. Uniform petal/disk changes have the same effect as changing the separation distance between the starshade and telescope. The most critical thermal requirement, in terms of the contribution to instrument contrast, applies to the differential between uniform petal width change and uniform disk radius change. The allocation is ±20 ppm for the Dedicated Mission and ±40 ppm for the Rendezvous Mission (see **Table 6.4-3**). The other significant thermal contributor to instrument contrast is non-uniform petal deformation. The allocation is ±10 ppm for the Dedicated Mission and ±30 ppm for the Rendezvous Mission. The corresponding contributions to contrast are 1×10^{-11} and 2×10^{-12}, respectively.

The starshade mechanical architecture is optimized to limit thermal deformations. All shape critical structures are of graphite construction with low CTE. The optical shield has thermo-optical properties that closely match graphite.

The baseline batten material is commercially available with a measured CTE with magnitude less than -0.2 ppm/K. With high-strain, intermediate modulus graphite, a CTE can be achieved that is more consistent and closer to zero throughout the temperature range than any other commercially available structural material, including quasi-isotropic M-55J and Invar.

Longerons have a targeted CTE of -0.5 ppm/K. This CTE is selected in inverse proportion to uniform temperature changes, as detailed below.

The optical shield's fractional open area can be adjusted to control heat rejection (i.e., effective emittance, ε*) from the anti-Sun side of the starshade. Technology efforts in 2015 include the characterization of optical shield thermal performance. The preliminary ε* estimate is 0.5. Optical performance is insensitive to this parameter as the primary effect is to shift uniform temperatures and not the critical differential temperatures.

A preliminary deployed thermal math model (TMM) of the starshade was constructed in TMG software, as shown in **Figure 6.2-17**. This model is based on an earlier IDS design with different perimeter truss geometry. Thermal results are considered closely representative of the new design and this model is used to

demonstrate compliance with sufficient margin to cover the additional model uncertainty. The model is sufficiently detailed to support transient spatial temperature predictions of all key starshade structural elements at various Sun angles while rotating at 0.33 RPM.

A thermal model of the new inner disk design, with a squatter perimeter truss, is shown in **Figure 6.2-18**. This model does not yet include petals also developed. This new model demonstrates that deviations in spoke temperature have negligible (<1 ppm) effect on disk radius. A second-generation petal TMM will be added to this IDS model in 2015 to complete the baseline TMM and proceed to further design optimization.

Figure 6.2-19 shows transient petal temperature predictions for a petal over a full spin period. Shown in the upper figure are snapshots of the same petal at 7.5 s intervals. The maximum variation of any petal node over a spin period is less than 3 °C. The lower figure shows the corresponding structural deformations for the petal temperatures at a single point in time mapped into the Nastran Finite Element Method (FEM). The maximum in-plane deformation is 45 ppm, but this is dominated by a change in length, which does not directly relate to the allocation. This petal shape was mapped into the optical performance model and yielded an instrument contrast of 9×10^{-12} for the Dedicated Mission and 3×10^{-13} for the Rendezvous Mission. This demonstrates compliance with the allocated contrasts in the corresponding mission error budgets (Section 6.4).

Average truss longeron and petal batten temperatures as a function of Sun angle are shown in **Figure 6.2-20**. The temperature ranges over the span of solar incidence angles are reasonably close to being centered around the 20°C reference temperature (293K). Also, the reference temperature corresponds roughly to the time- average of solar incidence, per DRM studies.

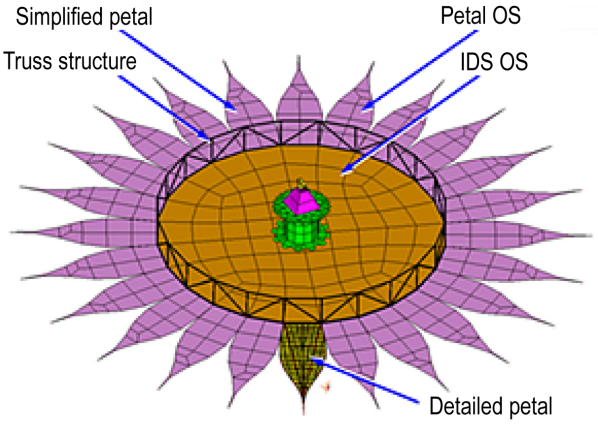

Figure 6.2-17. Starshade system thermal model in TMG.

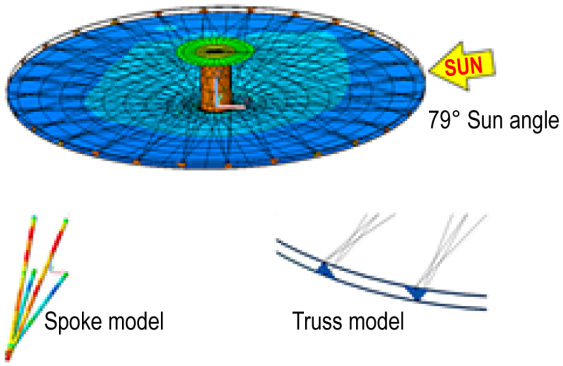

Figure 6.2-18. Updated IDS thermal model in TMG.

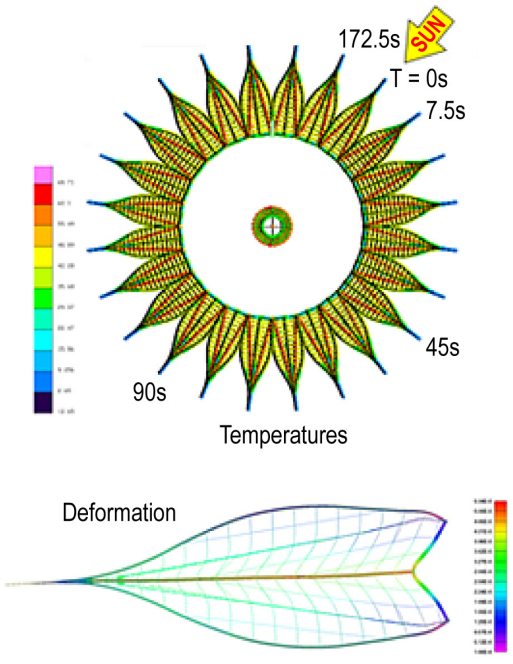

Figure 6.2-19. Petal thermal transient snapshots every 7.5 sec rotating at 0.33 RPM for 79° Sun angle (top). Temperatures mapped into Nastran FEM to yield deformations (bottom).

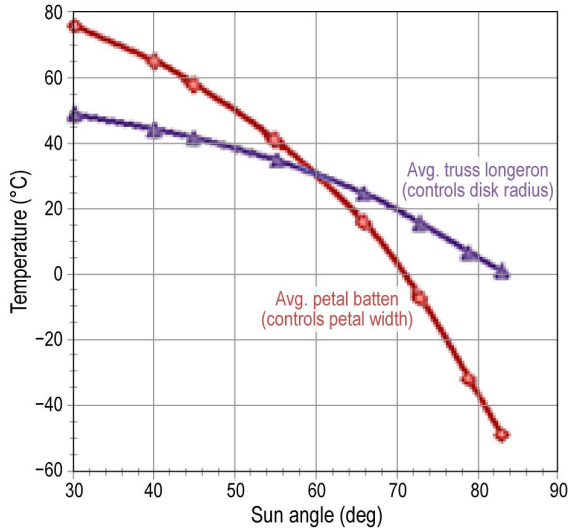

Figure 6.2-20. Temperature predicts for truss longerons and petal battens over full range of operating Sun angles. The maximum 83°Sun angle corresponds to 7° from petal plane.

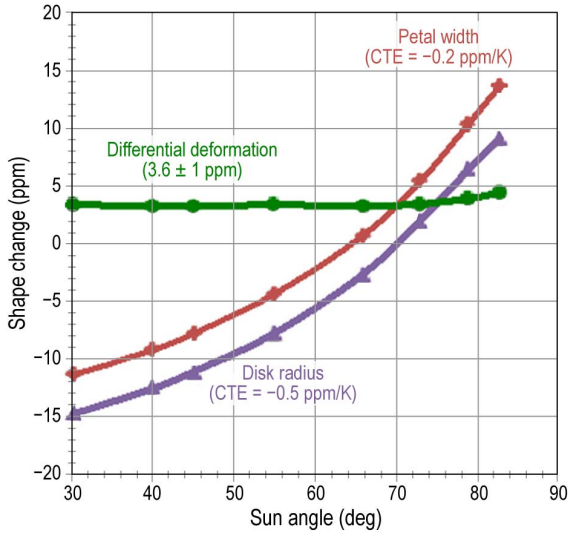

Figure 6.2-21. Uniform thermal deformations to petal width, disk radius and the differential between the two. A bias of 3.6 ppm is indicated.

Petal and disk proportional shape deformations, computed as the product of the deviation from the reference temperature and the CTE, are given in **Figure 6.2-21**. Differential deformation between petal width and disk radius are also shown. Note the bias term of 3.6 ppm. The bias term will be removed with an adjustment to disk radius. This final adjustment will be late in the test program after the characterization of material CTEs and the validation of thermal models. This final adjustment is made with adjusting shims (adding or removing) at the petal mounting interfaces, in the same fashion that the bias in deployed position is removed.

Figure 6.2-22 shows the residual scatter about the mean differential in uniform bias between petal width and disk radius. The maximum differential deformation is 1 ppm. By comparison the allocation is ±20 ppm for the Dedicated Mission and ±40 ppm for the Rendezvous Mission. Additional curves show effect of adding conservative uncertainties to both temperature and CTE. A ±10°C temperature uncertainty is applied to the truss longerons, but this actually represents uncertainty in the temperature differential with petal battens. A CTE uncertainty of ±0.1 ppm/K is applied to both petal battens and truss longerons. The result is a maximum deformation of less than ±15 ppm. This demonstrates large margin relative to the error budget allocated tolerances. The margin is sufficient to cover the uncertainty of imperfect analytical models. Considerable design flexibility exists to create additional margin, if necessary.

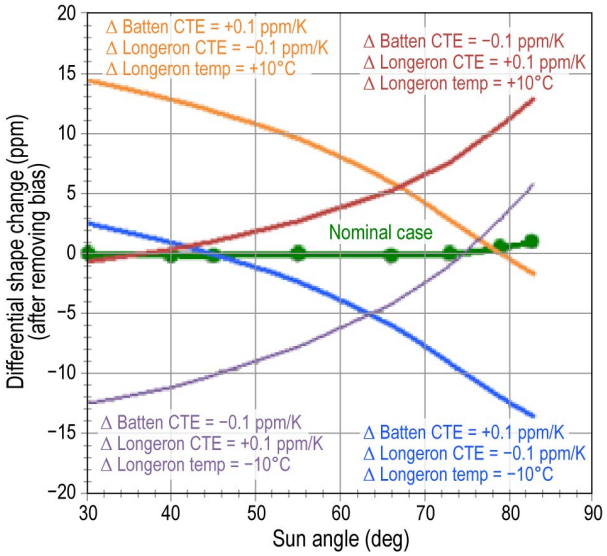

Figure 6.2-22. Residual differential deformation after removing the bias term, for nominal CTE and temperatures plus combinations of longeron CTE and temperature error.

6.3 Formation Flying

Formation flying (FF) is an essential capability to the Exo-S mission. Two-spacecraft formation flying itself is not new: autonomous rendezvous and docking is routinely performed at the International Space Station (ISS) and several technology demonstration missions have used formation flying, such as Orbital Express and PRISMA. The ESA PROBA-3 mission, scheduled to launch in 2018, has a configuration similar to a starshade mission with two-spacecraft axially aligned. While not a new concept in space mission design, it is being used for a new purpose—the synthesis of an occulting observatory able to directly image exoplanets by suppressing the host star's light. This section describes the high-level FF operational requirements and modes, and the Exo-S FF architecture. Details of the Exo-S FF design are restricted under United States export control laws and cannot be included in the publicly released version of this report. They have been included in Appendix D for the purpose of supporting the Cost and Technical Evaluation (CATE) assessment but this appendix will not appear in the public version.

6.3.1 Formation Modes and Requirements

The Exo-S formation flying operational design utilizes three distinct modes: *Transition, Acquisition*, and *Science*. The formation modes and translational control requirements are shown in **Figure 6.3-1**. Transition mode covers the activities needed to move the observatory between target stars. Acquisition mode covers the establishment of co-alignment of the starshade spacecraft and the telescope spacecraft on the new target star. Science mode addresses the maintenance of that alignment during science observations.

At a high-level, formation flying requires interspacecraft range and bearing sensing to the necessary precision levels. All modes measure interspacecraft range using the RF link. For bearing measurements, Transition mode–which has a significantly lower precision requirement than either the Acquisition or Science modes–uses an LED (light-emitting diode) array on the starshade and a star tracker on the telescope. This bearing knowledge is used to autonomously navigate between target stars. Bearing measurements in Science mode use a laser beacon on the starshade that is observed by the formation guidance channel (FGC) within the imaging instrument of the telescope (Note: the FGC function is carried out by the coronagraph imaging camera in the Rendezvous concept). The FGC and laser beacon are collectively referred to as the fine bearing sensor system (FBS). Starlight outside of the band of observation diffracts around the starshade and is collected by the telescope and

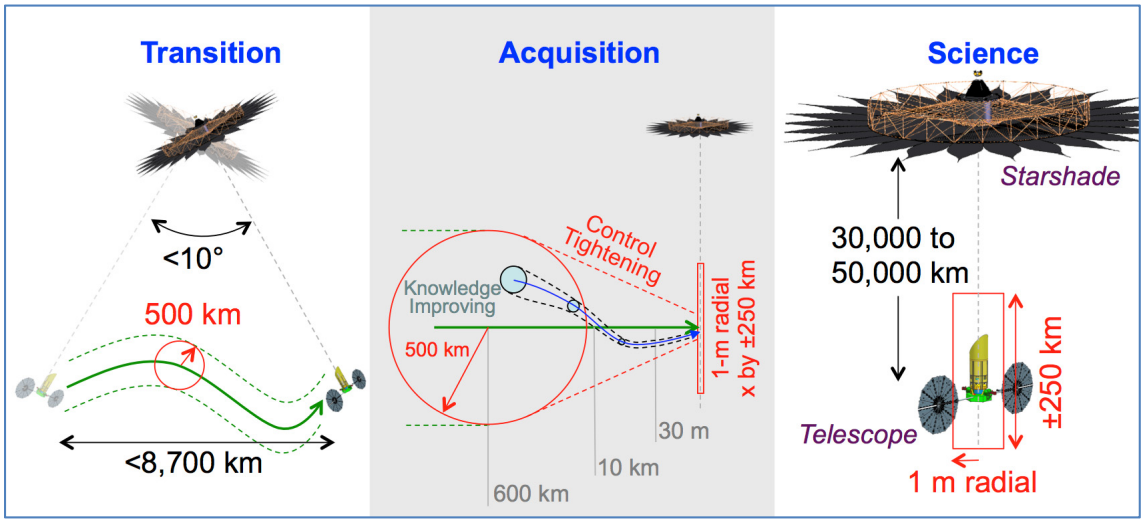

Figure 6.3-1. Formation flying modes and requirements.

detected by the FGC. By sensing both this out-of-band starlight and the starshade's laser beacon, the Science mode adjusts the lateral position of one of the spacecraft to align the two light sources, thus keeping the two spacecraft in formational alignment with the target star. Acquisition mode controls the handoff between the LED/star tracker system used to sense bearing in the Transition mode, and the FBS used to measure bearing in the Science mode.

The driving requirements for formation flying are to laterally align the telescope to within 1 meter of the starshade-star line at spacecraft separations of 30–50 Mm and to longitudinally align to ±250 km. This latter offset is measured using the FBS and the S-band RF link.

Controlling relative spacecraft positions to 1 m for Science mode is not a technological challenge; docking at the ISS requires control to better than 30 cm. The disturbing gravity gradients for a starshade mission are comparable to those experienced during ISS docking through the gravity gradient in low Earth orbit (LEO) at 1 m of separation just prior to docking.

Sensing is another matter: typically, positions must be sensed to 3 to 5 times more finely than the control requirement. Sensing to a factor of three finer than control implies that the lateral offset of the starshade must be sensed to 30 cm at 50 Mm. This offset corresponds to a bearing measurement precision of 6 nrad (1.25 mas).

Three factors help with the 6 nrad precision bearing sensing requirement. One, the large telescope aperture collects a large number of photons (10k to 100k per second) both from the beacon and from the stellar leakage; bearing knowledge improves with the square root of the number of photons. Two, the large aperture has an intrinsically high angular resolving power, and three, apparent starshade offset is magnified by a geometrical effect. A demonstration of the precision-bearing sensor is part of the objectives of TDEM-13 (Kasdin), now starting.

6.3.2 Formation Flying Architecture

Like the previously mentioned formation flying missions, a Leader/Follower (also known as Target/Chase) formation architecture is baselined for Exo-S. The Leader/Follower architecture is one in which a Follower spacecraft controls its position with respect to a Leader spacecraft. The Leader can perform open-loop translational maneuvers if desired. This architecture ensures that the formation is stable if the control law used by the Follower is stable. Importantly, the role of Leader and Follower can be easily swapped. Hence, the starshade or the telescope can perform the thrusting needed to maintain this type of formation architecture.

The formation sensor, guidance, and control techniques are summarized by mode in **Figure 6.3-2**. In all modes, an extended Kalman filter (EKF) is used to combine interspacecraft range and bearing measurements into a Cartesian relative state estimate that is then used for guidance and control.

Also in all modes, RF-ranging is used to determine the interspacecraft distance. Analysis has shown that the Gravity Recovery and Interior Laboratory (GRAIL) S-band Time Transfer System (TTS) can be reasonably scaled to a range of 50 Mm. The TTS uses dual one-way ranging with a pseudo-random code to determine range to ~10 m.

The RF-ranging system also provides low-bandwidth communication for formation coordination and, if the starshade is the Follower, relays bearing measurements made on the telescope spacecraft to the starshade spacecraft.

6.4 Starshade Error Budget

The starshade error budget determines the manufacturing and deployment tolerances, the allowed thermal fluctuations and dynamic motions, formation flying alignment

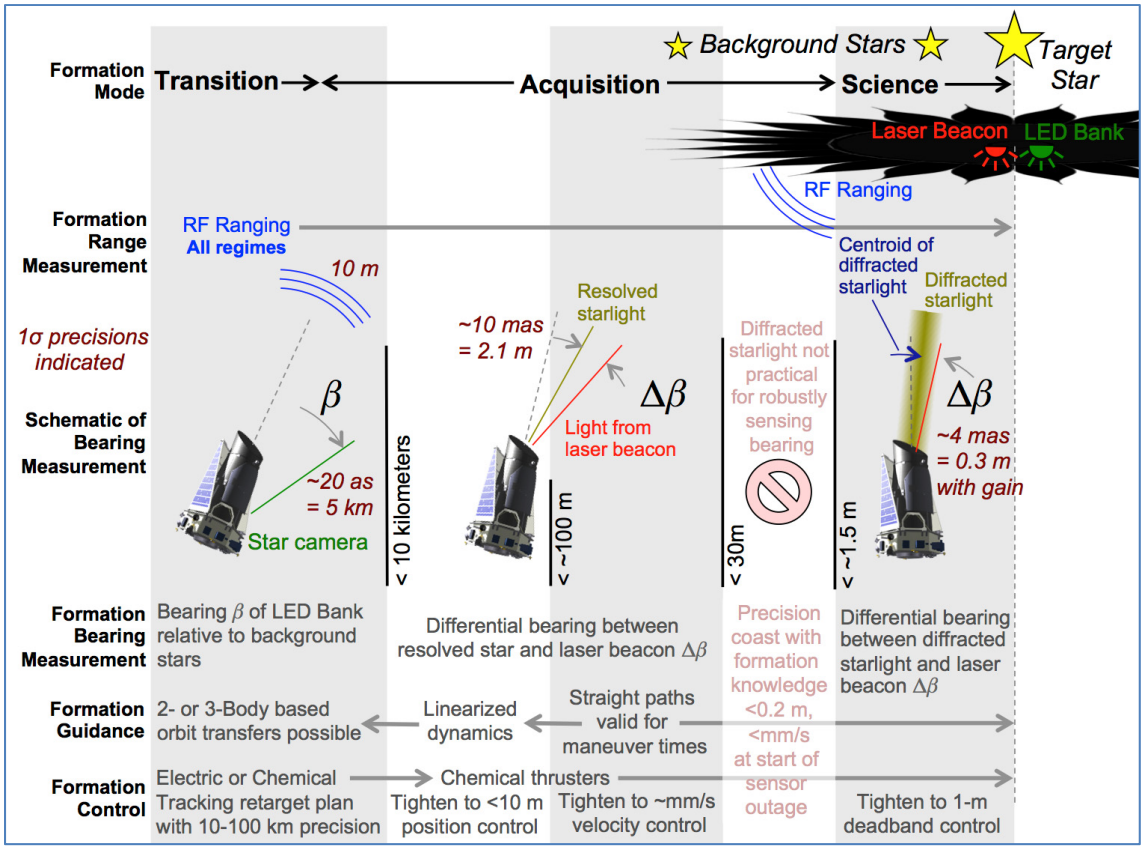

Figure 6.3-2. Formation sensing, guidance, and control by formation mode.

requirements, surface and edge reflectivity requirements, and the allowed transmission due to micrometeoroid damage. The budget is created through electric field propagation modeling of a variety of perturbations to the starshade design under consideration. This section presents error budgets for both the Dedicated and the Rendezvous missions.

6.4.1 Modeling Scatter in the Image Plane

Despite starshades falling in the middle of the Fresnel regime, modeling of propagation from starshades turns out to be challenging due to the range of size scales. Edge shapes have tolerances of tens of microns, while the starshade itself is tens of meters across, and the resulting grid sizes required to capture the grid shape details—$10^6 \times 10^6$ or larger—are difficult to propagate with standard Fourier techniques.

Two approaches have emerged to simplify the propagation calculations by reducing the dimensionality of the problem. The first class (Vanderbei et al. 2007) takes advantage of the radial symmetry of the starshade to break the 2D propagation integral into a series of 1D integrals, and the second class (Dubra and Ferrari 1999, Cady 2012) uses line integrals directly around the edge of the starshade to compute the downstream field. Since the second class of algorithms are particularly amenable to modeling changes of edge shape, an implementation of the boundary diffraction wave approach (Cady 2012) is used to perform the optical modeling for the Exo-S designs.

Analysis is performed with electric fields at the focal plane of the appropriate telescope. Perturbations of the starshade orientation or shape are introduced appropriately to capture each error budget term, and the field is computed at the telescope aperture using a line-integral propagator and then at the telescope focal plane using a standard Fourier propagator. A nominal unperturbed field is computed as well. This is repeated for seven

wavelengths across the starshade's usable band, and the entire set of images is fed to the next stage of sensitivity analysis code.

The images are then processed to determine the mean and standard deviation of the radial and azimuthal components of the energy in a circular swath centered at the petal tips. The swath width is determined by ideal telescope point spread function at each wavelength. Sensitivities are computed for local perturbations and are also applied equally to all petals to determine the sensitivity for global perturbations. These sensitivities are imported to a spreadsheet with worksheets set up to track manufacture, deployment, dynamic, thermal, and formation flying error terms.

6.4.2 Modeled Starshade Perturbations

The modeled perturbations mirror the starshade architecture: a spinning central disk supports petals, each of which is made of a lattice truss supporting high-precision 1-m long edge segments and a tip section. **Table 6.4-1** lists the corresponding perturbations. Broadly speaking, the error budget addresses: petal placement and petal shape inaccuracies; departures of the starshade from its nominal location; and secondary source (besides the target star) scattering effects. These error contributors are a function of manufacturing tolerances, deployment tolerances, dynamics, thermal behavior, formation flying limitations, and starshade edges and surface features. The error budget presented here includes allocations for each of these groups. This work builds upon previous tolerancing (Shaklan et al. SPIE 2010 and 2011, Glassman et al. SPIE 2010), TDEM results (Kasdin et al. 2011 and 2012), and new Exo-S modeling done for this report. **Figure 6.4-1** illustrates one term in the error budget, segment displacement normal to the petal axis, and the corresponding change in image plane contrast.

The perturbations fall into seven distinct categories:

Table 6.4-1. Modeled starshade error budget terms.

Manufacture/ Deployment	Description
Petal Position	Radial, lateral, in-plane clocking, rotation about spine
Segment Shape	0.5, 1, 2, 3, 4, cycle sine and cosine
Segment Placement	Tangential, normal, in-plane clocking
Tip Segment Placement	Radial, azimuthal, in-plane clocking
Truss Ellipticity	In-plane elliptical deformation
Petal Shape + Tip Clip	In-plane and out-of-plane bending, broken tip
Thermal	**Description**
Uniform Petal Expansion	Petal multiplicative shape change
Uniform Truss Expansion	Radially displaces petals
Radial Gradient	Petal base to tip gradient (length and width)
Harmonic Gradient	1, 2, 3, 4, 5 cycles/petal (width only)
Formation Flying	**Description**
Lateral Displacement	Decentration of telescope from center of shadow
Longitudinal Displacement	Position of telescope along line-of-sight to starshade
Other	**Description**
Solar Glint	Sunlight glinting off of petal edges
Surface Scatter	Earthshine, etc. scattering from telescope-facing surface
Holes	Starlight leakage from micrometeoroids

- **Random (local) perturbations** are unique to a petal or a location on a petal, e.g., radial displacement of a petal, or a cyclical shape error on one of the petal segments. It is assumed that uncorrelated random perturbations exist over the whole starshade. Image plane intensity increases as the square of the perturbation amplitude, and intensities from independent perturbations add linearly.
- **Bias (global) perturbations** are common to all petals or petal structures (e.g., radial displacement of all petals by the same amount, or a common cyclical shape error that appears on segment number 3 of all petals). These types of errors may arise from biases in metrology during assembly, systematic machining errors during manufacture, and a number of other causes such as systematic differences between the

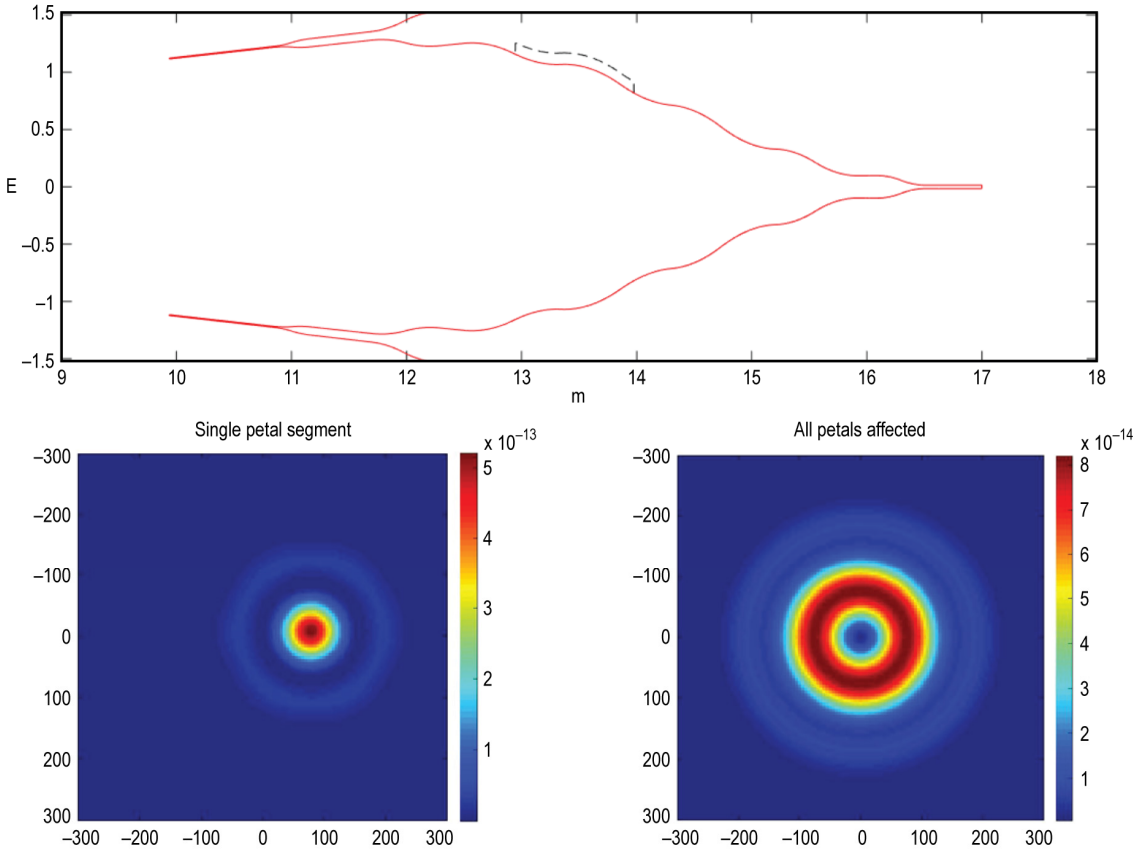

Figure 6.4-1. Example of a local petal perturbation; a 1-m long petal segment is displaced normal to the petal axis. The perturbation is shown enlarged 1000× relative to the displacement in the tolerancing analysis. Axes in the image plane are milliarcseconds. Colors are image plane contrast. Note that the perturbation in a single petal appears off-axis, compared to the on-axis appearance of random amplitude errors distributed amongst the petals

assembled structure on the ground and its post-deployment shape in space.

- **Truss perturbations** are related to defects in the truss and are analyzed with a set of circular harmonics (e.g., elliptical deformation) and truss dynamic modes. Analysis of harmonics higher than the elliptical mode is incomplete at this time.
- **Residual thermal perturbations** are the imprint of shadowing on the rotating starshade; petals cool down as they pass through the shadow of the spacecraft, then warm up as the reappear in the sunlight. The petal thermal response function leaves a warming circular footprint around the starshade.
- **Formation flying and starshade attitude perturbations** lead to scatter in the image plane from both lateral and longitudinal formation flying errors, and starshade orientation.
- **Holes** in the starshade allow starlight to leak directly to the telescope. Some of this light will be coherent with the other perturbations, while multiply-scattered light will add incoherently.
- **Glint and reflection** scatter light from the Sun or other astronomical bodies (e.g., the Earth, Jupiter, the Milky Way) into the telescope.

The first six categories are linked directly to the target star and contributions are expressed in terms of contrast (the ratio of scatter to the peak of the image of the star when it is not blocked by the starshade). The last category, glint and reflection, contributes to the background but is independent of the brightness of the target star. Thus, the contrast

contribution is a function of the star's brightness relative to the scatter source.

It is important to keep in mind that the starshade is spinning at 1/3 rpm and that this is much shorter than the integration time to observe planets. Local perturbations are smeared into full circular arcs and, like global perturbations, they do not contribute to background 'speckles'. The arcs contribute photometric (Poisson) noise, but do not present a systematic noise floor. Likewise, scatter from holes and from random formation flying errors does not lead to a systematic noise floor as these are averaged by spinning and by time, respectively.

However, the starshade is not immune to systematic speckles. Residual thermal perturbations are present and cause an asymmetry linked to the spacecraft shadow. Biases in formation flying also lead to asymmetric scatter. Finally solar glint leaves a distinct two-lobe pattern in the direction toward the Sun, while the conical cover of the central disk leads to a non-symmetric scatter component from bright astronomical bodies.

6.4.3 Allocations

6.4.3.1 Photometric Requirements

Error budget tolerances are allocated to meet a top-level contrast requirement while remaining consistent with tolerances achieved in the starshade technology development program. The contrast requirement has two parts: photometric and systematic. The photometric requirement ensures that the instrument scatter level is below the scatter due to zodiacal and exozodiacal light. The DRM work of Section 5 assumes a total zodiacal flux that is seven times the nominal 23 mag/sq arcsec of the local zodi. With this background, an instrument contrast of 1×10^{-10} with the Rendezvous Mission increases the background counts and the integration time by ~15% for a V=5 star and 37% for a V=4 star. For brighter stars, the instrument background is still more important, but integration times become so short that overall impact on the DRM is minimal.

The Dedicated Mission collects roughly 1/5 as much target light as the Rendezvous Mission, and the same amount of zodiacal light (per pixel). Thus, an instrument contrast of 5×10^{-10} has the same impact on integration time as 1×10^{-10} does for the Rendezvous Mission and is adopted as the photometric floor for the Dedicated Mission.

6.4.3.2 Systematic Requirements

The systematic requirement is much more stringent than the photometric floor. The DRM observes exoplanets as deep as 4×10^{-11} times fainter than the target star (Δmag =26). The systematic requirement adopted here is to keep the local speckle contrast at this level. Exoplanet detection then requires calibration of the systematic background to a level equal to the SNR (e.g., for SNR =10, calibration of the systematic background to 10% is required).

Top level requirements are summarized in **Table 6.4-2**.

Table 6.4-2. Starshade contrast requirements.

Requirement	Dedicated 1.1 m	Rendezvous 2.4 m
Photometric Floor	5×10^{-10}	1×10^{-10}
Systematic Floor	4×10^{-11}	4×10^{-11}

6.4.3.3 Key Tolerances

The contrast requirements are met by allocating key tolerances in accordance with the results of the starshade technology program, briefly summarized here. More technology details are provided in Section 9. A full-scale petal that met the shape requirements for exo-Earth detection was developed in TDEM-09. High-precision (but not razor-blade sharp) optical edges were attached with a precision of 15 µm rms (about ±45 µm tolerance). The segment shapes were measured to be within 30–45 µm tolerance in low spatial frequencies, and 15 µm tolerance in high spatial frequencies. The overall petal shape was accurate to ±100 µm.

A representative inner disk structure, 12 m in diameter, was tested for petal deployment precision in TDEM-10. Petals were attached with a global tolerance within ±100 µm of their ideal design point. Multiple deployments showed that the petal positions repeated to a tolerance of ±200 µm.

In addition to these technology results, dynamics modeling of the disk structure and thermal modeling of petal transients show that these terms will not be significant contributors to the error budget. Thruster firings for station keeping will induce several microns of petal motion and these will damp out to a negligible one micron level after about 10 s. Petals spend about 5 seconds passing through the shadow of the spacecraft as the starshade rotates at 1/3 rpm. Thermal modeling shows that petal width changes are below 1 µm and can be neglected.

Table 6.4-3 lists the key tolerances that drive the photometric and systematic floors. The single most critical parameter in both the Dedicated and Rendezvous mission designs is the global radial placement of the petals. This term is especially significant in the Dedicated Mission design and is allocated the bulk of the pre-launch error budget as shown in **Figure 6.4-2**. The allocation for petal radial position is 150 µm in the Dedicated Mission design and 200 µm for the Rendezvous Mission design—a relaxation compared to the 100 µm achieved in TDEM-10. Additionally, 100 µm (Dedicated) and 250 µm (Rendezvous) is allocated for petal radial post-launch position changes that were not captured in the TDEM tests.

The overall temperature of the starshade, and the difference in temperature between the central disk and petals, are also critical. The allowed strain difference between the truss and petals is 20 ppm (Dedicated Mission) and 40 ppm (Rendezvous Mission). Thermal models discussed in Section 6.2.7.3 show that these strain differences are achieved over a range of incident solar angles from 30–83 deg from the starshade normal.

The other driving terms in the error budget are the segment shape and segment placement tolerances. The segment shape tolerance (±71 µm) is ~50% larger than the tolerance achieved in TDEM-09. Margin was added to account for potential difficulties in manufacturing a sharp edge with the correct

Table 6.4-3. Key requirements for the error budget. Values are 3-sigma tolerances.

	Dedicated 1.1 m	Contrast × 10^{-11}	Rendezvous 2.4 m	Contrast × 10^{-11}
Manufacture				
Petal Segment Shape (Bias)	14 µm	1.4	22 µm	0.37
Petal Segment Shape (Random)	71 µm	0.5	71 µm	0.26
Petal Segment Placement (Bias)	4 µm	0.7	7 µm	0.07
Petal Segment Placement (Random)	45 µm	0.6	53 µm	0.47
Pre-Launch Deployment				
Petal Radial Position (Bias)	150 µm	6.0	200 µm	0.15
Petal Radial Position (Random)	450 µm	0.6	450 µm	0.1
Post-Launch Deployment				
Petal Radial Position (Bias)	100 µm	2.7	250 µm	0.23
Petal Radial Position (Random)	350 µm	0.4	375 µm	0.06
Thermal				
Disk-Petal Differential Strain (Bias)	20 ppm	6.0	40 ppm	0.6
1–5 Cycle/Petal Width (Bias)	10 ppm	1.0	30 ppm	0.2
Formation Flying				
Lateral Displacement	1 m	2.9	1 m	1.1
Longitudinal Displacement	250 km	2.5	250 km	0.43

shape over a 1-m segment. The segment placement requirement of 45 µm (for the Dedicated Mission) was achieved in TDEM-09. The Rendezvous Mission design allows a 50% relaxation of the segment placement requirement. **Table 6.4-4** compares TDEM achievements with Exo-S requirements.

Table 6.4-4. Comparison of TDEM results with Exo-S requirements.

Key Technology	Demonstration	Achieved Tolerance	Required Tolerance
Petal Segment Shape (Random)	TDEM-09	±45 µm	±68 µm
Petal Segment Position (Random)	TDEM-09	±45 µm	±45 µm
Radial Petal Position (Bias)	TDEM-10	±100 µm	±150 µm

The longest wavelength of the bandpass is most sensitive to perturbations, and the Dedicated Mission design is more sensitive than the Rendezvous Mission design. **Figure 6.4-2** shows the manufacturing error budgets for the shortest and longest bands of both the Dedicated and Rendezvous missions. The contrast values for the allocated manufacturing tolerances are listed above the pie charts. The larger value for the Dedicated Mission design shows that it almost 6 times more sensitive to perturbations at the long wavelength limit than the Rendezvous Mission design. This is mainly due to the lower spatial resolution of the telescope spreading scatter out to the IWA and beyond.

6.4.3.4 Overall Performance and Performance Reserve

The high-level starshade photometric error budgets, exclusive of holes, edge glint, and surface reflectivity, are shown in **Figure 6.4-3**. These are 90% confidence error budgets. The manufacturing budgets, constituting about 20% of the total, have already been discussed. The thermal budgets constitute ~25% of the total. For the Dedicated Mission design, this is driven by differential strain between the petals and the truss over a range of solar angles. Formation flying accounts for 11% and 16% of the photometric budgets in the Dedicated and Rendezvous mission systems, respectively. The 'nominal' term in the error budget pie charts refers to the limiting performance of the ideal starshade.

The systematic noise floor is driven by lateral formation flying bias. A bias of 0.4 m contributes to an rms level of 1.7×10^{-11} (Dedicated) and 5×10^{-12} (Rendezvous). The starlight leaking around the starshade is not circularly symmetric in the image plane and can masquerade as a planet. This level of systematic error will require a modest calibration factor of 3–4 for SNR=10 detection of Δmag=26 exoplanets for the Dedicated Mission design, and is acceptable without calibration for the Rendezvous Mission design.

As noted earlier, dynamics models show that a few seconds after a thruster firing (which happens every few hundred seconds), vibrations dampen to a micron level, at which petal motions can be neglected. The dynamics requirements for in plane petal motion are 50 µm and 50 microradians, and out-of-plane rotations are even less restricted. Thus, dynamics is expected to be an insignificant contributor to starshade performance.

The error budgets in this pre-phase A study do not include model uncertainty factors. However, both designs carry 50% performance reserve (equivalent to 33% of the total error budget). This reserve posture is reasonable because:

1. The largest contributors to the error budget have already been demonstrated on hardware with flight-like materials and structures;
2. Dynamics and thermal gradient models show a large performance margin;
3. Performance degradation with loss of contrast is gradual;
4. Only a moderate level of calibration is needed; and
5. The systematic error related to formation flying is a function of three parameters (lateral offset, azimuth of the offset, and longitudinal offset) making its calibration relatively simple.

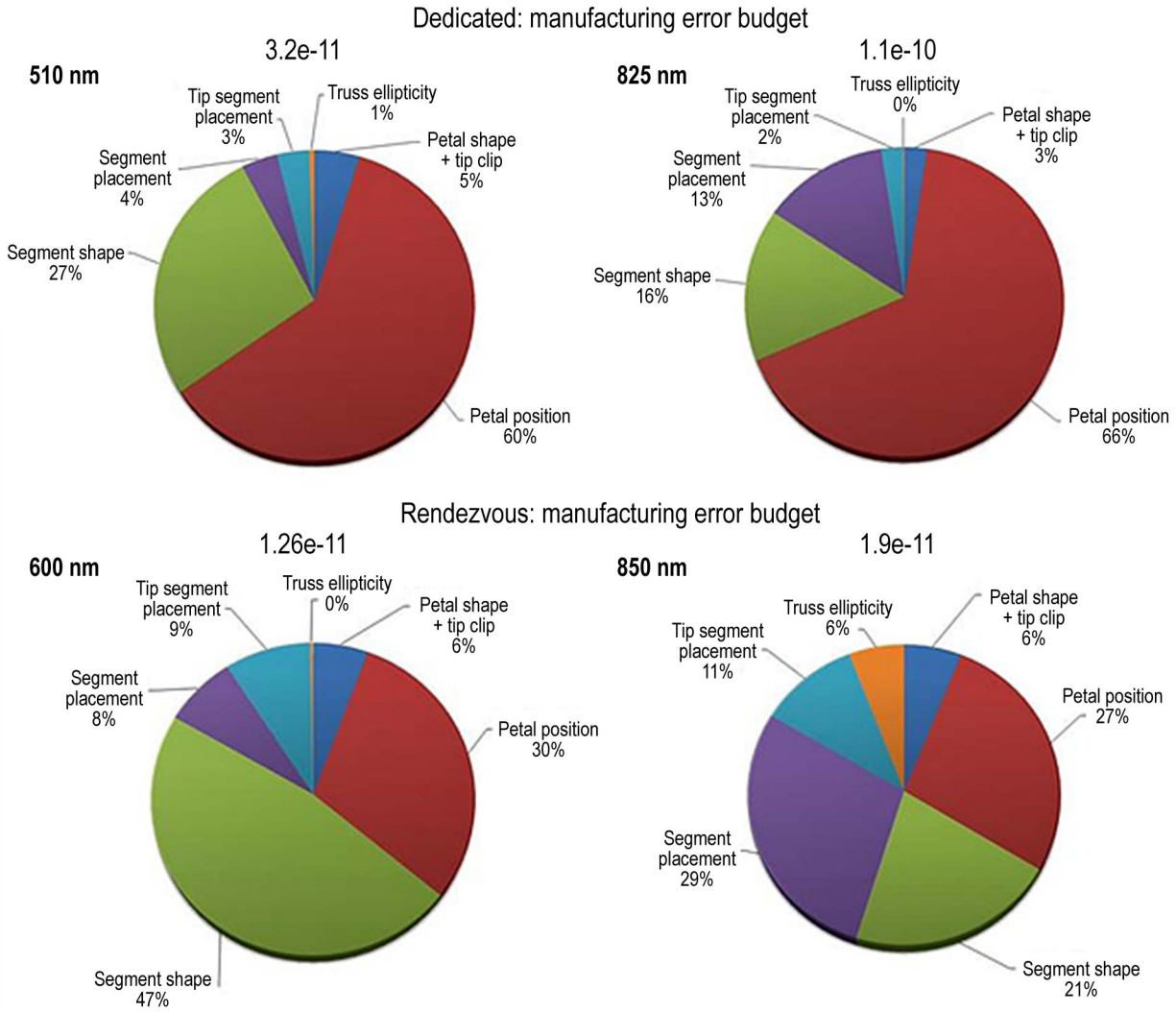

Figure 6.4-2. Allocation of errors to the manufacturing error budget. *Top*: Starshade for the Dedication Mission. *Bottom*: Starshade for the Rendezvous Mission. *Left*: Shortest wavelength of the mid-range bandpass. *Right*: Longest wavelength of the bandpass. Values above the pie charts indicate total contrast for these manufacturing terms.

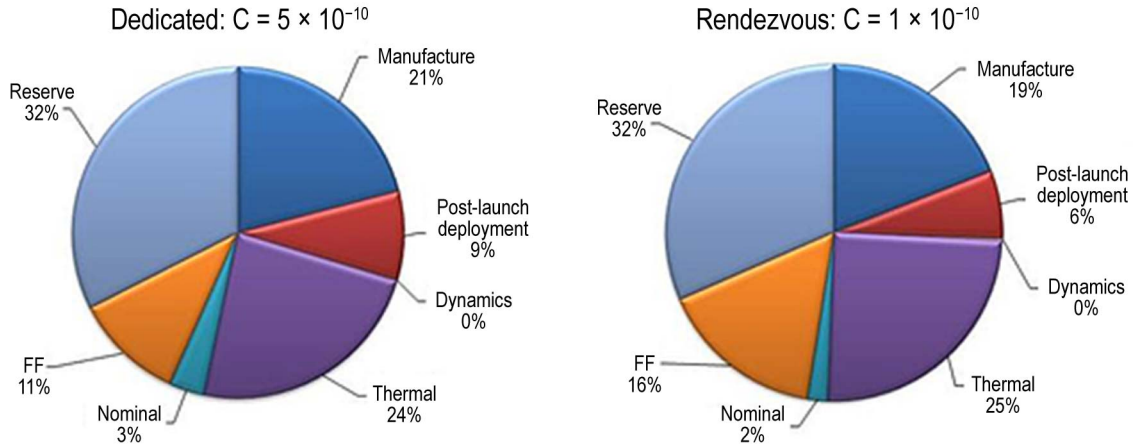

Figure 6.4-3. Overall photometric error budget for the Dedicated and Rendezvous missions.

6.4.4 Holes and Opacity

A cumulative pinhole area of 1 cm^2 is allocated for holes created by micrometeoroids and the associated contrast allocation is 1×10^{-12}. By comparison, a single 1-cm^2 hole leads to 3×10^{-12} contrast (Shaklan et al. 2010). This analysis assumed each pinhole is like an ideal aperture in a single-layer thin screen. However, the starshade uses two layers with cm-scale spacing between layers. If a micrometeoroid were to puncture all layers, the result would be a series of pinholes illuminated by other pinholes. Even if all the holes were aligned toward the telescope, the multiple scatter reduces the transmitted field strength at each layer, and also scrambles the phase of the final transmitted field. This cancels the leakage fields at the telescope more effectively than direct transmission distributed across the starshade. Thus, the tolerances outlined above are conservative, and can probably be relaxed after further analysis. Modeling of the integrated micrometeoroid flux shows that even for a single layer blanket, the ≤1 cm^2 hole area allocation is satisfied (Arenberg et al. 2007). However, this does not account for seasonal micrometeoroid showers when the flux increases by up to two orders of magnitude. A couple of times a year it will be necessary to turn the starshade edge-on to the shower for a period of 1 or 2 weeks.

6.4.5 Optical Edge Scatter

Starshade optical edges will scatter and diffract a small fraction of sunlight. Section 9.1.1 details the modeling of this 'edge-scattered sunlight' and the validation of that model. Fundamentally, the scatter is limited by diffraction even when the edge is infinitely sharp. The diffraction term is equivalent to a source of magnitude V = 27–28 (depending on the solar angle to the starshade surface) near the end of the petal. The allocated post-calibration contrast is 1×10^{-11} and this translates to the following edge engineering specification:

- Product of edge radius of curvature (μm) × reflectivity (%) ≤ 12

This edge engineering specification ensures that light scattered by reflection is well below the level of diffraction. The diffracted light in turn is below the assumed level of exozodiacal and zodiacal light (V = 21 per sq arcsec). Calibration of edge scatter is straightforward because the scatter is a function of a single parameter (solar angle), the starshade spins so that only the average edge shape matters, and the scatter level will be nearly constant during the mission.

In addition to the edge radius requirement, the optical edge must accommodate bending strain, associated with petal stowing, and thermal strain, associated with any mismatch in material CTE relative to the petal structure.

None of these requirements are individually difficult to achieve. In combination, however, they present a moderate material design challenge. For example, the TDEM-09 petal included graphite optical edges (same material as substrate structure) that satisfy all requirements, except for radius of curvature (RoC). Subsequent radius of curvature testing of many different types of graphite revealed that graphite was not a viable material.

The optical edge mechanical design is included on the list of current tall-pole design issues and is addressed further in Section 9.1.3.

6.4.6 Reflectivity of the Starshade

Regehr et al. (2014) have prepared a memo detailing reflection of light from the telescope-facing side of the starshade. This side is covered in black, rip-stop Kapton, installed so that the grid of reinforcing rip-stop threads faces away from the telescope. The material has a relatively, but not perfectly, matte finish and a surface texture with waves resulting from the presence of the fibers on the reverse side of the material.

The starshade has two flat portions, a central disk, and a number of petals around the perimeter of the starshade. The two flat

surfaces are offset relative to each other and joined by an intermediate portion in the shape of a truncated cone, with the normal to the surface of the cone 6° from the axis of the starshade at all points on the cone.

When a point on the starshade is illuminated by a source of light, such as Jupiter, the amount of light reflected from a region around the point into the telescope depends on the angle between the incident light and the local normal to the surface of the starshade, and the angle between the local normal and the direction to the telescope. The Kapton surface of the starshade is modeled using a combination of measurement and interpolation, and the reflectivity of the starshade is calculated using numerical integration over the flat and conical areas of the starshade.

6.4.6.1 The BRDF Model

The bidirectional reflectance distribution function (BRDF) of the Kapton was measured by Surface Optics Corporation of San Diego, California, for five incident zenith angles: 0°, 20°, 40°, 60°, and 80°. For each incident zenith angle, the BRDF was measured for various reflected zenith and azimuth angles, with finer spacing near the specular direction for the non-zero zenith angle.

A net reflectivity curve is computed (**Figure 6.4-4**) after integrating the BRDF numerically over the conical portion of the surface of the starshade, and adding the contribution from the flat portions of the starshade. The y-axis of the figure is expressed in visual magnitudes. For example, with light incident at 40° from the starshade normal, the reflectivity is about 1%, a reduction of 5 magnitudes of the incident light level.

Figure 6.4-5 shows the appearance of the starshade when illuminated by a light source 12° from normal. Most of the reflected energy appears to come from the region of the cone, and is removed by >1 petal length (7 m, or 40 mas) from the IWA defined by the petal tips. The scattered light affects only a portion of the image plane, and only partially overlaps the innermost planets to be observed.

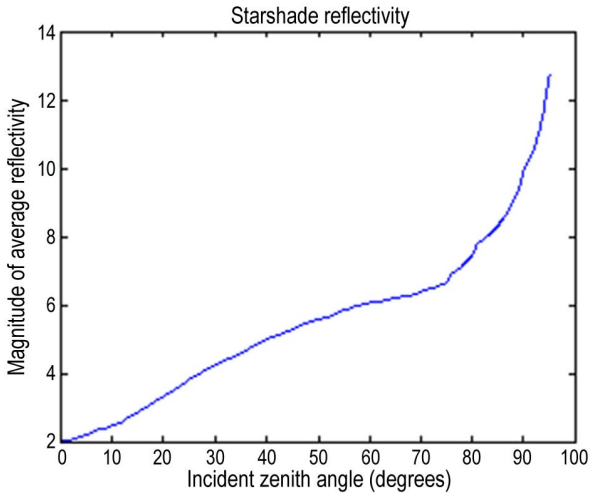

Figure 6.4-4. Average reflectivity of the starshade for a range of incident angles relative to the starshade normal.

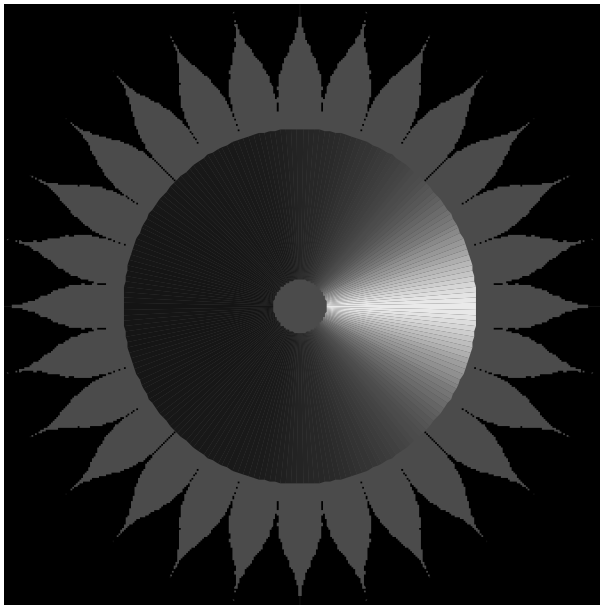

Figure 6.4-5. Starshade illumination from a point source 12° off axis.

6.4.6.2 Illumination by Astronomical Bodies

Table 6.4-5 shows the results of the worst-case illumination by the brightest astronomical sources: Venus, Jupiter, and Mars; and the central region of the Milky Way. Illumination by Venus is less of an issue than Jupiter or Mars because solar pointing restrictions ensure that Venus at its brightest is no closer than 53° from the starshade normal.

Table 6.4-5. Apparent magnitude of the telescope-facing side of the starshade when illuminated by astronomical objects.

Source	Worst-Case Apparent Magnitude of Starshade
Jupiter	29.7
Mars	29.7
Venus	31.3
Milky Way	29.6

6.4.6.3 Illumination by Earthshine

The minimum allowed illumination for Earthshine is computed for both heliocentric Earth-leading, Earth drift-away and L2 orbits. Using the Pallé et al. (2003) model of the Earth's albedo, it is determined that to keep the starshade apparent magnitude fainter than 30, at a distance of 0.1 AU the Earth should be no closer than 81^{o} from starshade normal, while at 0.2 AU it should be no less than 60^{o} from normal. For a wide L2 Lissajous orbit, the non-Lambertian component of the albedo brightens the limb of the Earth and restricts all Earthshine from the front of the starshade, which will place a seasonal pointing restriction on the starshade in its periodic L2 orbit.

These Earthshine illumination results apply to the baseline black Kapton material. An alternative approach is to select a highly specular material and design the cover to minimize slopes due to ripples. This makes the system practically immune to illumination by off-axis sources, effectively removing Earth-pointing restrictions. However, the specular surface would be susceptible to bright glints from sources behind the telescope. This alternative approach is currently under study.

7 STARSHADE DEDICATED MISSION

This section presents a cost-driven design that is aimed at meeting the STDT charter guideline of developing an end-to-end starshade direct imaging concept that could be implemented for a target of $1B. Except for the starshade, all flight hardware elements are either flight proven, or space qualified and scheduled to fly by 2017. The observational performance detailed in Section 5 is fully supported by this design.

7.1 Concept Overview and Key Performance Requirements

The Exo-S Dedicated Mission is a Class B mission with a 3-year prime mission duration and consumables for 5 years. It launches from Cape Canaveral on an intermediate class expendable launch vehicle with a 5-m fairing and operates in a heliocentric Earth-leading, Earth drift-away orbit. Telecommunications and tracking are via the Deep Space Network (DSN), using 34-m-diameter radio antennas. **Figure 7.1-1** shows the mission elements, interfaces, and nomenclature.

The Dedicated Mission is highly constrained by the $1B cost target. This has led to the decision to co-launch the telescope and starshade spacecraft. The use of commercial spacecraft and telescope are also necessary to hold down the total mission cost. As such, the Dedicated Mission uses a Kepler-like spacecraft bus for the telescope, a WISE-based bus for the starshade, and a NextView-based telescope. Cost considerations have also factored into decisions on the overall mission life and on limiting mission science to starshade exoplanet direct imaging.

From the measurement requirements identified in Section 2.7, come the science-driven mission requirements. For the Dedicated Mission, this relationship is captured in **Table 7.1-1**. The mission's key performance requirements are organized into three main design elements: the starshade, the imaging instrument, and the spacecraft/mission. The spacecraft/mission element includes formation flying requirements. The table shows the relationship between the measurement requirements and the design requirements for each of the elements; it does not capture any element-to-element requirement dependencies. Discussions on the basis for the Dedicated Mission requirements are included throughout the report with specific report sections identified in the table.

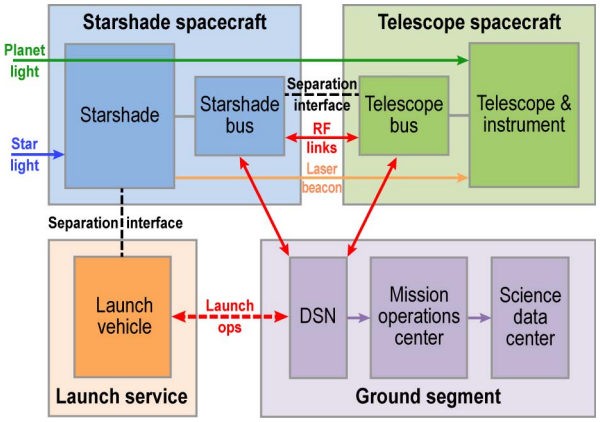

Figure 7.1-1. Exo-S mission interfaces with two spacecraft.

7.2 Mission Design

As noted earlier, the Exo-S Dedicated Mission is co-launched from Cape Canaveral and operates in a heliocentric Earth-leading, Earth drift-away orbit. The launch vehicle deploys the two connected spacecraft (**Figure 7.2-1**) on a direct trajectory to a heliocentric Earth-leading, Earth drift-away orbit. The telescope spacecraft deploys its solar arrays and acquires a safe Sun-pointed state as the master spacecraft. Separation occurs after initial health checks and push-off springs provide a safe separation distance. The starshade spacecraft spins up, deploys the starshade, and acquires a safe, Sun-pointed state. The telescope spacecraft moves approximately 40,000 km from the starshade and lines up on the first test target star; performance verification begins. Commissioning is complete within 30 days after launch and the prime mission begins.

Table 7.1-1. Dedicated Mission design requirements

<table>
<tr><th rowspan="2">Measurement Requirements</th><th colspan="3">Dedicated Mission Requirements</th></tr>
<tr><th>Starshade</th><th>Instrument</th><th>Spacecraft & Mission</th></tr>
<tr><td rowspan="2">Planet contrast sensitivity ≤ 4E-11 (limΔmag ≥ 26)</td><td rowspan="2">Manufacturing and deployment requirements (see Section 6.4)
Thermal and structural deformation (see Section 6.4)
Sun angle: 28° to 83° off normal (Sections 6.4.6, 7.3.1)
Hole area < 1 cm^2 (Section 6.4.4)</td><td rowspan="2">Formation guide camera requirements (Appendix D)</td><td>Telescope S/C:
Pointing requirements: 30 mas (see Section 7.3.2)
Lateral position control: 1 m (Appendix D.4)</td></tr>
<tr><td>Starshade S/C:
Pointing requirement: 1° 3-σ (see Appendix D.6)
Spin rate: 1 rev per 3 min (Sections 6.4.2, 7.5)</td></tr>
<tr><td rowspan="2">Planet detection SNR: ≥ 5</td><td rowspan="2">Detector requirements (see Section 7.3)</td><td>Orbit: heliocentric Earth-leading, Earth drift-away (Section 4.5)</td></tr>
<tr><td></td></tr>
<tr><td>Spectral res (Earths or larger) ≥ R10
Spectral res (sub-Neptunes or larger): ≥ R50
Planet characterization SNR: ≥ 10</td><td></td><td>IFS requirements (see Section 7.3)</td><td></td></tr>
<tr><td>Total Bandpass = 400–1,000 nm</td><td rowspan="2">Bandpass: partial (Section 4.4.1)
Inner disk structure Dia. 16 m
Petal length 7 m, petal #22 (Sections 4.4 and 6.1)</td><td>Bandpass: 400–1000 nm (Section 4.3, Section 2.3)</td><td rowspan="2">Spacecraft separation distances: 30,000 to 50,000 km (Sections 4.4 and 6.1 and Appendix D)</td></tr>
<tr><td>IWA ≤ 100 mas</td><td></td></tr>
<tr><td>Spectral res (Giants): ≥ R70
Planet characterization SNR: ≥ 10</td><td rowspan="2"></td><td rowspan="2">IFS requirements
Pixel scale: 29 mas/pixel (see Section 7.3.2)</td><td rowspan="2">Min mission duration: > 2 years (Section 5.3.1)</td></tr>
<tr><td>Planet cross-track position ≤ 0.01 AU</td></tr>
<tr><td>FOV > 10 AU at 10 pc</td><td></td><td>IFS FOV > 3 asec (Section 7.3.2)</td><td></td></tr>
<tr><td>Measure polarization</td><td></td><td>Polarization: 0°, 45° (Section 7.3.3)</td><td></td></tr>
</table>

Table 7.2-1 shows the system mass estimate with a maximum expected launch mass of 2,903 kg, which includes a total contingency of 43%. The launch capacity is 3,570 kg leaving 19% of launch vehicle capacity (or 23% of launch mass) as margin.

The telescope spacecraft performs retargeting maneuvers using solar electric propulsion (SEP) and carries sufficient xenon gas for a 5-year mission. Total SEP ΔV capacity is 3.7 km/s, including 1.5 km/s to perform the 2-year initial survey detailed in Section 5. Subsequent observations focus on repeat visits, with longer observation times and targets spaced farther apart, such that ΔV is accumulated at a much slower rate.

The telescope spacecraft also performs formation control using chemical propulsion and also carries sufficient hydrazine fuel for a 5-year mission. Total chemical ΔV capacity is 100 m/s.

The starshade spacecraft performs pointing and spin-rate control using chemical propulsion and carries sufficient hydrazine fuel for a 5-year mission. Nominally, no ΔV is required, but contingency propellant is carried for 30 m/s of ΔV capacity.

An S-band radio frequency (RF) link is maintained between the two spacecraft for both communications and the measurement of separation distance, via 2-way ranging. This link is implemented with transponders and communication protocols developed for the GRAIL mission. Both spacecraft have direct-to-Earth (DTE) links with 34-m DSN ground stations. Nominally, Earth communications are provided via the telescope spacecraft, which relays commands and telemetry to the starshade. The telescope spacecraft can store science data for up to 5 days and generally downlinks science data at the end of an

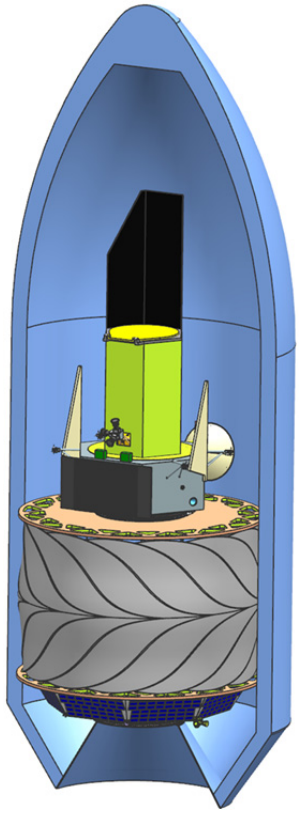

Figure 7.2-2. Starshade and telescope spacecraft in launch configuration.

Table 7.2-1. System mass budget (kg) shows ample launch mass margin.

Element	Current Best Estimate	Contin-gency (%)	Max Expected
Telescope S/C – Wet Mass	**1228**		**1,644**
System-level Contingency	**---**	**23**	**220**
Propellant	**246**	**—**	**246**
Xenon	222	—	222
Hydrazine	24	—	24
Telescope S/C – Dry Mass	**982**	**20**	**1,178**
Payload	**359**	**16**	**416**
Heritage Telescope	319	15	367
Sunshade	20	15	23
Instrument	20	30	26
Bus (including SEP & SAs)	**623**	**22**	**762**
Solar Electric Propulsion	108	11	120
Ultraflex Solar Array	34	30	44
Starshade S/C – Wet Mass	**918**		**1293**
System-level Contingency	**---**	**15**	**128**
Hydrazine Propellant	**49**	**—**	**49**
Starshade S/C – Dry Mass	**869**	**28**	**1,116**
Starshade Payload	**455**	**30**	**591**
ESPA-based Bus System	**415**	**26**	**525**
Total Launch Mass	**2146**		**2,937**
Launch Capacity	3,570		3,570
Margin	1424		633
Margin (% of Launch Mass)	**66**		**22**

observation via its high-gain antenna (HGA) at X-band.

7.3 Payload Overview

The complete payload for the Dedicated Mission is represented in the block diagram in **Figure 7.3-1**. The full payload spans both spacecraft and includes the hardware needed to conduct the direct imaging science, as well as that needed for formation flying. The starshade spacecraft carries the 22-petal, 30-m starshade, as well as an IR laser, LED array, and an S-band GRAIL-heritage transponder with four patch antennas—all needed for flying the two spacecraft in formation. The payload on the telescope spacecraft consists of a 1.1-m aperture diameter Next View-like telescope, its back-end imaging instrument and another S-band transponder with a helical antenna for the other half of the formation flying radio link. The imaging instrument contains three focal planes: the first is an optical CCD (e2v CCD-273 or equivalent) supporting planet direct imaging; the second is an identical optical CCD used for spectral characterization within an integral field spectrometer (IFS); and the third is an HgCdTe IR detector for fine guiding in support of the formation flying.

When formation flying, range between the two spacecraft is measured using the S-band RF link. Lateral position is measured optically using different beacons and different sensors according to the mode. In Transition mode, an LED beacon carried on the starshade is tracked using the telescope's star tracker camera. During the Acquisition phase as the starshade nears alignment, the starshade's LED beacon is turned off, the infrared laser beacon is turned on and the FGC camera within the imaging instrument becomes the sensor. After the observational formation is established, planet light is collected by the telescope and directed to either the planet imager or the IFS. A more detailed description of the formation flying

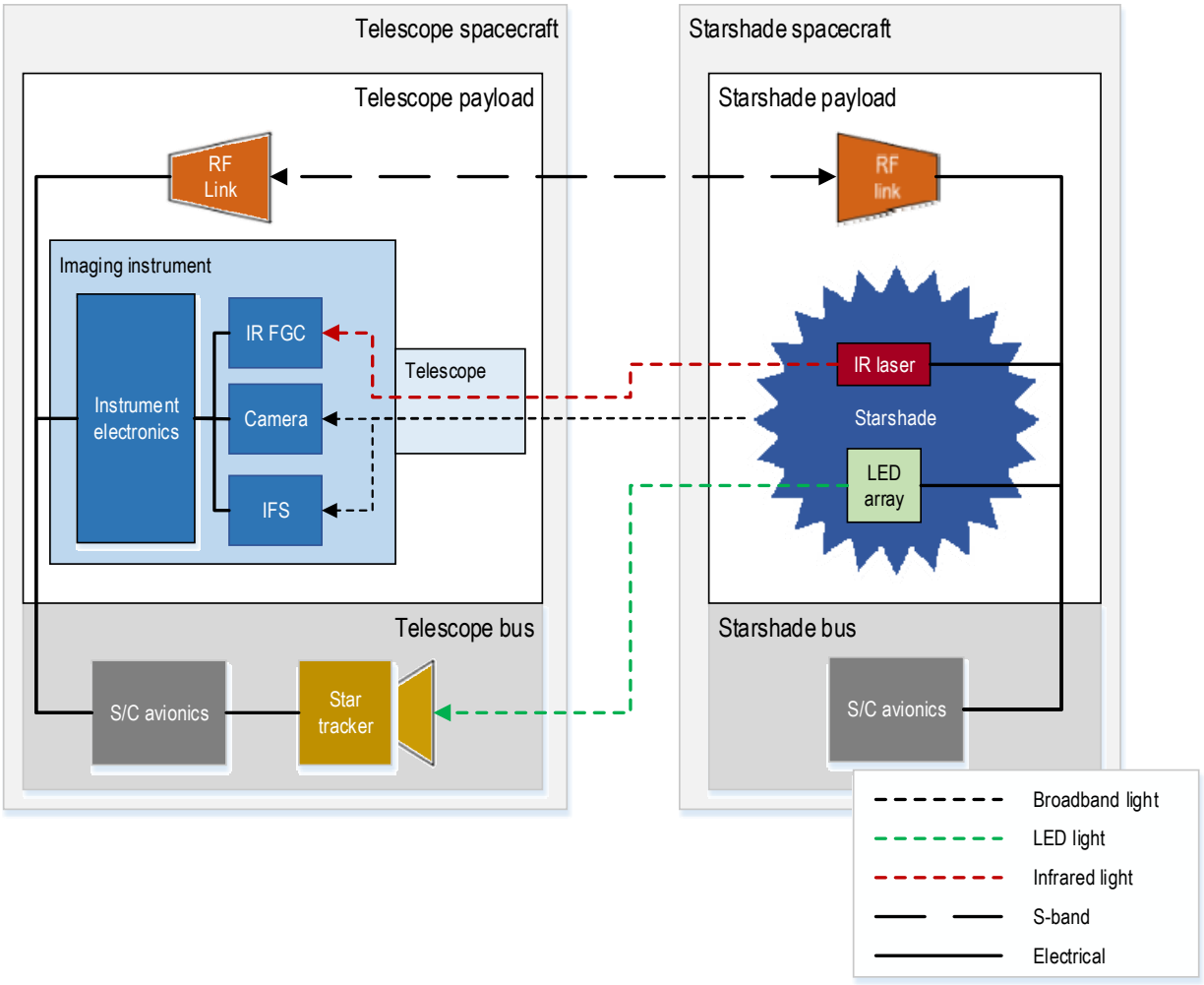

Figure 7.3-1. Dedicated Mission option payload block diagram.

architecture and approach is covered in Section 6.3.

Details on the starshade design and its key technologies are included in Sections 6.1, 6.2, and Section 9. The imaging instrument and telescope are discussed in Sections 7.3.2 and 7.3.1, respectively.

7.3.1 Telescope

The Starshade Dedicated Mission employs a 1.1-m NextView-like telescope, which was developed for commercial Earth imaging. Four are currently operational. The telescope has a 1.1-m diameter primary mirror with an on-axis secondary suspended by a conventional spider.

The standard telescope requires only two minor modifications to the mechanical system to operate for this exoplanet imaging mission. First, a sunshade is added to keep sunlight out of the telescope barrel when pointing as close as 28° from the Sun. The sunshade is a lightweight structure integrated into the existing cover door assembly and conforming to the shape of the existing hexagonal structure. It stays clear of the cover door as the door swings open and has sufficiently low mass to avoid modification of existing telescope structures. Second, the standard telescope utilizes a three-mirror optical system, which maximizes the field of view for Earth imaging. For the starshade, such a wide field of view is not required and the system will be converted to a Cassegrain format. This change greatly simplifies the optical instrument design

and improves optical throughput by reducing the number of reflections before light enters the optical instrument. To bring the focus to the desired point within the optical instrument, a new secondary mirror will be fabricated.

Figure 7.3-2 shows the main opto-mechanical parts of the NextView telescope. A mechanical bench structure resides behind the 1.1-m-diameter primary mirror (schematically depicted here, without any of the supporting structure), with the instrument package mounted behind the bench. The instrument's optical components are mounted inside a mechanical assembly containing two mechanisms and three cooled focal plane areas. Detector electronics are co-located with the assembly. Note that this self-contained instrument package measuring approximately 300×225×75 mm could readily be deployed on alternative space telescopes should other starshade mission opportunities arise.

7.3.2 Instrument Package

The instrument package has been simplified as much as possible, maximizing optical throughput, and has overall dimensions of about 30×27×10 cm. It supports all the science observations detailed in Sections 2 and 5 in three overlapping wavelength bands (called blue, green, and red). Each operating band provides the requisite starlight suppression at specific telescope-starshade separation distances. The science instrument supports spectroscopy at Nyquist resolution R_N = 70, whole band imaging, three types of polarization measurement, plus a 3-color image capability within the blue band.

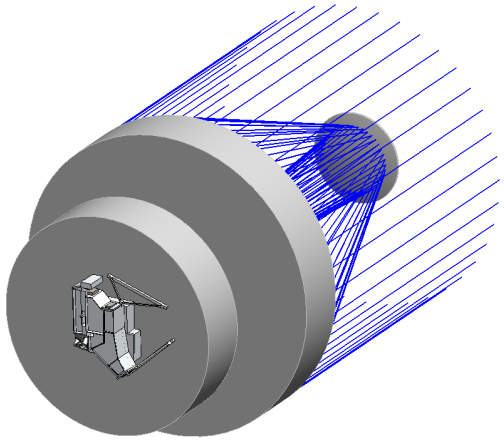

Figure 7.3-2. The compact optical instrument package mounted behind the telescope aft metering structure, which is in turn located behind the primary mirror.

Table 7.3-1 shows the three science bands with inner working angles and starshade ranges. To reduce thermal engineering complexity, the instrument's detectors are located in close proximity within the mechanical structure.

The instrument package (**Figure 7.3-3**) contains three cameras with the following functions:

1. A field camera (planet camera) for imaging the target planetary system, with a field of view of 1 arcmin
2. An IFS with sufficient field of view to cover a solar system equivalent at 10 pc distance
3. An FGC camera with a field of view of 2 arcmin, used both for navigation when the starshade and telescope are near the correct alignment and for maintaining fine spacecraft formation alignment during observations

Table 7.3-1. Spectral bands for science and guide cameras.

	Blue	Green	Red	Guide
Inner Working Angle	80 mas	102 mas	124 Mas	NA
Telescope Range	39 Mm	30 Mm	25 Mm	-
Field of View	1 arcmin	1 arcmin	1 arcmin	2 arcmin
Field of View (IFS)	3 arcsec	3 arcsec	3 arcsec	-
Wavelength Range	400–645 nm	510–825 nm	615–1000 nm	1400–1600 nm
	Coarse spectrum ('color') bands in the blue band			
Wavelengths	400–480 nm	480–564 nm	564–647 nm	-

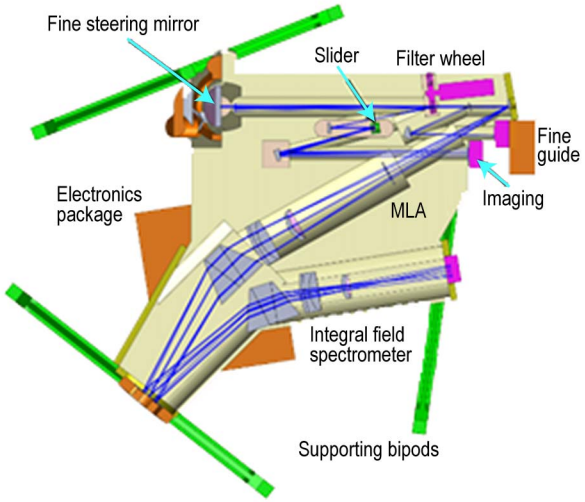

Figure 7.3-3. Detail view of the optical instrument.

Table 7.3-2. Detector specifications.

	Imaging Camera	IFS	Guide Channel
Array Type	e2v CCD 273	e2v CCD 273	Teledyne Hawaii H1RG
Format	2k×2k	2k×2k	1k×1k
Field of View	1 arcmin	3 arcsec	2 arcmin
Pixels/View	1k×1k	105×105	1k×1k
Resolution	60 mas	60 mas	120 mas
Optical Throughput	51%	42%	47%
Dark Current	0.00055 e^-/px/s	0.00055 e^-/px/s	<0.05 e^-/px/s
Read Noise (cds)	3 e- rms	3 e- rms	<30 e- rms
Pixel Size	12 µm	12 µm	15 µm
Operating Temperature	153K	153K	120K
Quantum Efficiency	>70% (425–950 nm)	>70% (425–950 nm)	>70% at 1500 nm

Optical performance specifications and detector array data for each camera are shown in **Table 7.3-2**. Each array has its own readout and digitizing electronics that sends data to the spacecraft computer interface. **Figure 7.3-3** shows the instrument layout. A fast-steering mirror (FSM) intercepts the beam from the telescope secondary mirror and performs static alignment and dynamic jitter control. A control loop for the FSM is closed around the FGC and contained entirely within the instrument package. Beam pointing is controlled relative to a designated point on the detector to within 75 mas (3-sigma) at frequencies below 1 Hz. The heritage spacecraft bus independently controls bore-sight pointing within 9 arcsec (3-sigma) and jitter within 30 mas (3-sigma) at higher frequencies; these specifications are consistent with the heritage bus design.

Following the FSM, dichroic optics mounted in a motorized wheel select the science wavelength band and either directs light to the field camera or to the spectrometer. Longer wavelength light (>1,000 nm) is transmitted for use in the FGC.

Imaging. 400 to 1000 nm light reflects off the first dichroic, reaching a slider containing optical components which enable different imaging modes. From the slider, the light is redirected and focused onto the field camera CCD focal plane.

Formation guidance. Long wavelength light is reflected off a second dichroic directing it to the FGC camera.

Spectroscopy. 400 to 1000 nm light passes through both dichroics to the IFS. A microlens array pixelates the field of view, and light is collimated, dispersed, and then refocused to the science CCD.

7.3.3 Cameras

The two science cameras provide for imaging and spectroscopy of the target exoplanet system. The field camera allows imaging in different modes including a coarse three color spectrum allowing a simple characterization of objects in the field. A polarization imaging capability is included to facilitate studies of dust disks.

7.3.3.1 Field Camera

The field camera utilizes half of an available 2048×4096 e2v CCD273 array, selected for its excellent read noise performance of 3 e- rms. Alternative commercial types are available with similar high performance, but the CCD273 is being qualified for flight on the European dark energy mission Euclid. Even more improved read noise will likely become available with other detectors already in development, but this

is not assumed in the observation times allotted in the Section 5 DRM, which are based upon this existing detector. The standard format is 4K×4K, but it can be cut down to a 2K×4K format, which still provides more than ample surface. The unused surface area will be masked off, resulting in a 2K×2K detector format. The detector is passively cooled to 153 K by means of a heat pipe connected to an external radiator. Light directed to the camera is magnified to produce a focal spot a few pixels wide. After some integration time, this enables accurate centroiding and discrimination of objects in the field.

7.3.3.2 Spectrometer Camera

The spectrometer camera utilizes the same CCD array type (CCD-273) as the field camera, also passively cooled to 153 K. Light is dispersed along rows of pixels. The magnification is set so that the spot size is approximately equal to the pixel size for the longest wavelengths. This concentration of light reduces the relative effects of readout noise and dark current on the science measurements by ensuring that only one pixel (or at most two) receives almost all the light of a given wavelength range $\Delta\lambda = \lambda/R$.

7.3.3.3 Formation Guidance Channel Camera

A high sensitivity, low noise Teledyne Hawaii H1RG with an HgCdTe detector array commonly used for astronomical observations is baselined for use as the fine guidance sensor. This array has flown on HST. It is passively cooled to an operating temperature of 120K by connection via heat pipe to an external radiator. To operate with the camera, the starshade will be equipped with a 1,550-nm laser beacon that will allow guiding and formation alignment functions. The camera magnification is chosen so that the starshade appears a few pixels wide. This enables accurate centroiding and also provides a field of view sufficient to track the starshade when it is within several thousand meters of the line of sight to the star.

The fine guidance camera has three functions:

- *Starshade tracking and formation acquisition*. The camera allows tracking of the starshade (using a laser beacon on the shade) as the formation nears alignment on the target star
- *Starshade fine alignment*. Once the starshade is positioned directly over the star, the camera senses any disturbance to the alignment.
- *Target tracking*. Feedback from the camera controls a FSM, maintaining the chosen star in a selected position on the focal plane.

Operating Modes

The instrument package may be operated in different science modes as shown in **Table 7.3-3**; this is achieved using two separate mechanisms. There are four basic science modes: spectroscopy on the IFS, direct imaging, 3-color imaging, and polarization imaging accomplished on the field camera. These latter functions are selected using a slider. There are three wavelength bands, corresponding to previously defined blue, green, and red bands (B, G, and R). These are selected using the dichroic wheel; three sets of two dichroics are provided to accommodate the working ranges. In imaging or polarization imaging modes, any of these bands can be used, enabling imaging of the exoplanetary system at all of the working ranges. For the blue band, a coarse spectral imaging capability is available via the dichroic stack.

Table 7.3-3. Science observing modes.

	Science Modes	Wave-length band	Slider	Resolution ($\lambda/\Delta\lambda$)
Spectroscopy	Fine spectrum	B, G or R	-	$R_N = 70$
Imaging	Direct image	B, G or R	Mirror	R = 1
	Coarse spectrum	Blue	Dichroic stack	R = 3
	Polarization 1	B, G or R	Polarizer 1	-
	Polarization 2	B, G or R	Polarizer 2	-

Spectral Observations

Light passing through a single element of the microlens array (MLA) is dispersed across the focal plane so that a spectrum appears along a pixel single row of the CCD. Adjacent rows may also contain some light from the same microlens element. The background spectrum (largely exozodiacal light) will appear in many of the rows and can subsequently be subtracted from the object spectrum in a post-acquisition process. Fixed dispersing prisms are employed yielding $\lambda/\Delta\lambda = 140$ between CCD pixels so that the Nyquist spectral resolution R_N is 70. When lower resolution is desired, 'on chip' binning (summing of adjacent pixels) of spectral data can be used to reduce resolution by factors of 2, 3, 4, or more, while keeping read noise to just one unit per spectral bin. Off-chip binning is of course also possible.

Imaging Observations

Direct image. A mirror reflects the science light to the CCD.

Course spectrum. The dichroic stack consists of two dichroic optics and a mirror selecting wavelengths in three equal spaced bands between 400 and 645 nm. The optics reflect light at slightly different angles producing three separate images of the exoplanetary system on the CCD. These images are limited in extent by a field stop located between the dichroic and the recollimating mirror so that they cannot overlap.

Polarization. A reflecting polarizing prism produces two separate images of the exoplanetary system on the CCD. Two of these prisms are provided (set at 0° and 45°) enabling construction of the Stokes vector components I, Q, and U. These allow determination of the polarization orientation and intensity of the light, together with the intensity of any rotating polarization.

7.3.4 Starshade Design

Details of the starshade payload optical and mechanical designs are given in Sections 6.1 and 6.2.

7.3.5 Formation Sensing and Control

The formation flying architecture is discussed in Section 6.3.

7.4 Telescope Bus

The telescope bus is based on Kepler, which has been proven capable of handling a telescope payload of similar size, requiring similar bus resource support. The primary modifications from this bus design are: the additions of gimbaled XIPS-25 SEP thrusters to enable repositioning the telescope between target fields; Ultraflex solar arrays to provide power to the SEP system; and a GRAIL-like S-band communications system to provide the formation flying ranging link between the two spacecraft. All bus hardware has been flown in space on prior missions.

The bus layout is shown in **Figure 7.4-1.** The Kepler heritage bus dimensions, construction, and general layout are preserved. The command and data handling (C&DH), power, and hydrazine propulsion subsystems are used as is.

The Kepler spacecraft is used in this baseline design as an existence-proof of busses capable of fulfilling this mission at an affordable cost. The actual spacecraft bus used for any eventual mission will be selected through a competitive process.

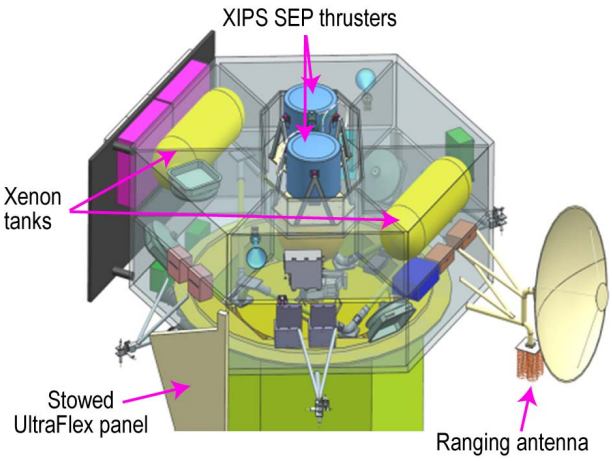

Figure 7.4-1. Telescope bus layout.

7.5 Starshade Bus

The starshade bus draws on the LCROSS structural architecture, which uses an EELV secondary payload adaptor (ESPA) ring as the base structure for the spacecraft. An ESPA ring is a cylindrical structure designed to provide an efficient load path from the launch vehicle to a primary spacecraft while carrying additional, smaller, secondary payloads. Like LCROSS, Exo-S uses the ring to carry the spacecraft bus subsystems (most subsystems draw heritage from the WISE spacecraft), while supporting the starshade payload and telescope spacecraft during launch.

An adapter ring on the telescope-facing side of the starshade interfaces the starshade spacecraft with the telescope spacecraft for launch. The interface ring is anodized black and is positioned in the starshade shadow during observations to prevent solar glint from scattering into the telescope. The diameter of the interface ring is the same as the diameters of the hub load-carrying cylinder and the ESPA ring so the launch loads are carried through each element efficiently.

Exo-S carries a fixed solar array with sufficient area to generate the estimated spacecraft power needs while spinning. The solar array is mounted to the starshade upper deck and is sized to provide 420 W of power at EOL.

Figures 7.5-1 and **7.5-2** show the starshade spacecraft and bus configurations after separation from the telescope spacecraft.

The starshade spacecraft is spin stabilized, which eliminates the need for reaction wheels. Pointing is loosely controlled to within 1–3 σ and a fraction of this allowable error is allocated to wobble, which results from imperfect mass properties. Spin stabilization requires thruster clusters mounted on both top and bottom decks of the starshade to apply balanced torques with no net ΔV. The spacecraft is repointed, by firing thrusters to apply balanced torques in a direction 90° from the rotation. Repointing consumes propellant in proportion to the spin rate. The baseline spin period is 3 minutes.

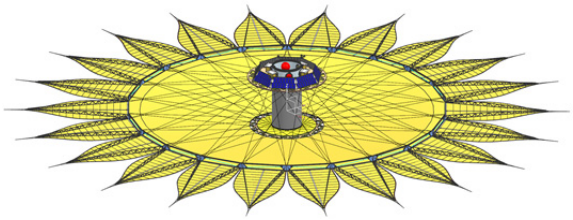

Figure 7.5-1. Starshade spacecraft with starshade deployed. Bus side shown.

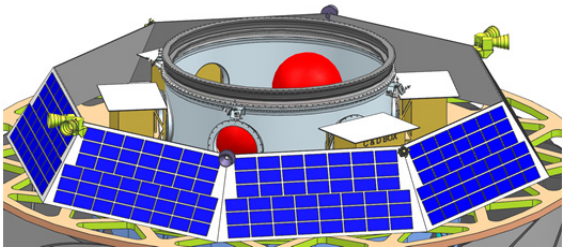

Figure 7.5-2. Starshade bus with fixed solar panels.

The C&DH is a simplified version of the telescope bus C&DH with no science data storage and few operational modes.

During typical operations, the telescope spacecraft acts as a relay between the starshade spacecraft and ground operations. Immediately after launch and during safe mode, the starshade uses an X-band low-gain antenna for a direct-to-Earth link. For the spacecraft-to-spacecraft link, the starshade uses the heritage GRAIL S-band system and maintains a near constant 100 bps link with the telescope spacecraft for ranging and health data.

7.6 Dedicated Mission Implementation

With the Dedicated Mission defined in the preceding sections, this section discusses what is needed to implement that design. A cost estimate and schedule are presented; the basis for both are also included.

7.6.1 System Integration

Many aspects of the Exo-S integration and test (I&T) activities **(Figure 7.6-1)** are like those found on other competed astrophysics missions. A commercial bus vendor is responsible for the bus integration, spacecraft

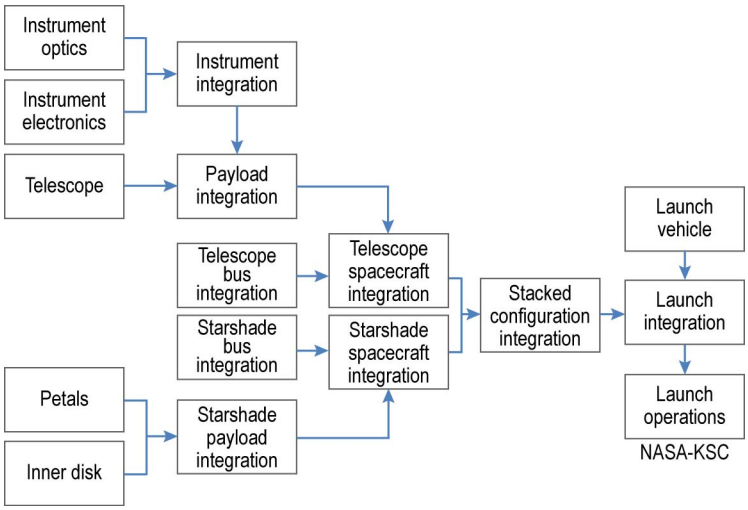

Figure 7.6-1. Exo-S integration flow chart.

integration and launch support. The telescope provider handles not only telescope testing but also end-to-end optical testing with the imaging instrument, leveraging established procedures, and existing test facilities and support equipment.

There are, however, several unique characteristics of the Exo-S concept that need to be addressed in the I&T planning. The first consideration is that not all requirements will be verifiable by test (such as end-to-end system functional performance); some will be handled by analyses, modeling, or simulations. While not ideal, this condition has been addressed successfully in a number of past situations (e.g., Mars atmospheric deceleration, primary mirror 0g relaxation, spacecraft docking, etc.). For Exo-S, formation flying cannot be tested in an 'as-you-fly' configuration on the ground since the spacecraft are separated by up to 50,000 km. FF ranging radios, beacons and thrusters can be tested in routine spacecraft subsystem tests. The primary FF challenges lie with sensing lateral performance errors using the FGC and modeling starshade optical behavior. These capabilities will be demonstrated in pre-Phase A. A breadboard FGC and instrument computer will be tested in the subscale starshade test facility in development at Princeton University.

The FF algorithms and software, leveraging proto-flight software developed and ground-demonstrated for StarLight, Terrestrial Planet Finder Interferometer (TPF-I), and PROBA-3 (PRoject for OnBoard Autonomy-3) (Scharf et al. 2010), will be fully exercised in a Control Analysis Simulation Testbed (CAST) and a flight software (FSW) testbed. All functionality and performance requirements are first verified in CAST, then reverified in the FSW testbed under flight-like operating conditions.

Another Exo-S I&T challenge lies with the integration and deployment testing of the starshade. At a 30-m diameter, most flight integration facilities cannot support the fully deployed starshade. The vendor performing starshade payload I&T must have the requisite test facility for deployment. Testing is analogous to large deployable antenna systems, requiring similar gravity compensation fixtures. Most vendors involved in the design of large deployable antennas have the required facilities.

By using a single spacecraft provider for both busses, Exo-S can take advantage of pooled hardware and resources, simplified communications within a single spacecraft-level I&T team, and early bus-to-bus interface testing.[1] The bus vendor will also handle the more typical payload integration and launch stack integration efforts.

7.6.2 Mission Operations

Exo-S will observe at least 38 targets in the first two years of operations. While the time on target and the time transiting to a target vary

[1] For the purposes of this concept study, the spacecraft busses and integration and test activities were assumed to be produced by a single vendor. For any eventual mission, bus and integration and test providers would all be decided through the standard procurement bid and proposal process, which could result in multiple providers.

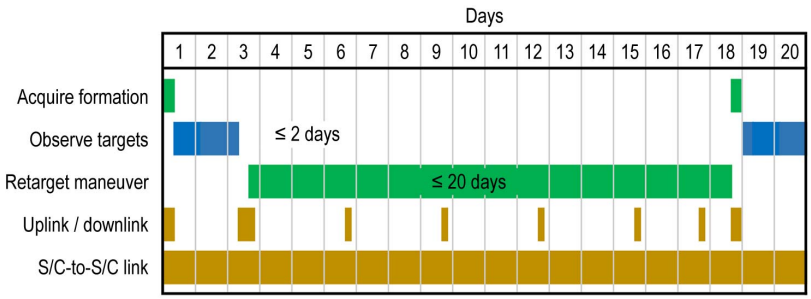

Figure 7.6-2. Notional observation cycle.

for each observation, each will follow a repetitive operational cycle approximately as illustrated in **Figure 7.6-2**. Science data is stored and downlinked at the end of each observation with the telescope spacecraft pointing its fixed antenna at the ground station. An operational sequence is then uplinked for the next target. Each sequence starts with a retargeting maneuver and formation acquisition.

Tracking and telecommunications are via the DSN using 34-m-diameter antennas. Engineering functions are transmitted on S-band and science data is downlinked on X-band. As noted earlier, the two spacecraft have a separate S-band link for communications and 2-way ranging. Both spacecraft can communicate with the mission operations center (MOC) via ground stations, but communications are primarily through the telescope spacecraft, which relays commands and telemetry to and from the starshade spacecraft. Navigational tracking requirements are typical of any single space telescope. Retargeting maneuvers and formation acquisition are performed in autonomous fashion without special DSN tracking or ground intervention. A link is maintained during acquisition for monitoring purposes only.

The Exo-S ground system follows the architecture developed for Kepler. The MOC is at an organization familiar with operating Earth-orbiting and near-Earth missions. The spacecraft bus contractor provides on-orbit subsystem technical support during the mission. DSN support is provided by JPL. Kepler ground system software is modified for the mission-specific two spacecraft architecture of Exo-S. Science data is archived at the mission's science data center (SDC) and made available to the science community within a yet to be determined time of collection.

As stated in Section 6.2, science observations are precluded during specific seasonal meteor showers. The starshade will be oriented with its edge onto the meteor flux. The telescope spacecraft may still perform retargeting maneuvers during these showers. Science planning will account for these events to minimize any loss in observing time.

7.6.3 Mission Cost

The current Exo-S Design Team estimate for the Dedicated Mission total project cost is $1.1B, slightly above the $1B target. Since the Interim Report, the Exo-S has received a cost estimate from JPL's Team X; at $1.25B it too is slightly over the target. Differences between these two estimates are entirely related to how each approached the estimates of the two required spacecraft. Exo-S relied on actual historic costs for Kepler and WISE spacecraft, taken from NASA CADRe (cost analysis data requirements) records with small upward adjustments for design differences, and Team X used JPL institutional models that reflect the cost of building the spacecraft at JPL. Since the Exo-S mission has been architected around the use of commercial spacecraft busses (by keeping the more complex aspects of the mission entirely within the payload), the level of spacecraft expertise and design sophistication found at JPL is not needed, and the commercial-based Exo-S estimate is the more realistic.

Lower cost approaches—such as those presented in the Interim Report—carry additional risks that made them less attractive

especially given the inescapable technology development risks required for this mission. Faced with the required technology development needed for Exo-S, the CATE team advised, and the STDT accepted, that all avoidable risks be eliminated in the concept even if this resulted in a cost above the target. A Rendezvous starshade mission that does meet the cap is described in Section 8. That option does require the availability of a future space telescope mission at Earth-Sun L2.

The Exo-S estimate is shown in Appendix E.

The largest contributors to the total mission costs are the payload (starshade, telescope, and imager/spectrometer instrument), two spacecraft, launch services, and reserves. Launch services costs were specified by the study guidelines. For the lowest cost intermediate-class launch vehicle, the cost was set at $110M based on a KSC-provided NASA launch vehicle cost tool. Reserves were calculated at 30% of the total project cost excluding launch services costs.

The starshade payload estimate is based on a cost model estimate developed by JPL's Cost and Pricing Office using a standard aerospace cost estimation tool, PRICE H. This tool is particularly useful in estimation of designs lacking good system-level historic analogues such as with the starshade.

The Design Team telescope and the imager/spectrometer costs were generated from two widely accepted statistical models, both utilizing only objective input parameters. The imager is modeled as an optical instrument using the NASA Instrument Cost Model (NICM), which is based on over 150 completed flight instruments. NICM is the primary NASA instrument cost estimation tool and has been in wide use for over 10 years. The telescope estimate is derived from aperture size and is calculated from statistical fits to historic actual costs given in "Update to Single-Variable Parametric Cost Models for Space Telescopes" (Stahl et al. 2013). The aperture-based model was chosen over the mass-driven model since, unlike mass, there is no uncertainty in the valuation of the telescope's aperture diameter.

The Exo-S telescope spacecraft bus design draws heavily from the bus of the highly successful Kepler telescope spacecraft. The primary difference is the addition of a SEP system to the Exo-S bus.

The starshade spacecraft bus cost is based on the WISE bus actual costs. There are no reaction wheels since the spacecraft is spin stabilized.

Assembly, test, and launch operations (ATLO) costs were also taken from the Kepler and WISE missions. These costs were simply added, ignoring any efficiencies possible in a joint ATLO operation.

Exo-S Dedicated Mission draws heavily from Kepler for its ground system design. Exo-S has a similar heliocentric orbit. Like Kepler, the MOC is assumed to be run by a non-NASA contractor. The SDC is the same as Kepler; only minor upgrades and setup costs are needed. Again, Kepler costs for ground system and operations are presented for comparison. Other WBS costs (management, systems engineering, and mission assurance) are based on Team X models and are consistent with past JPL Discovery and New Frontiers-class missions.

Technology development costs included in the Design Team estimate contain the costs needed to raise key concept elements requiring technology development from Technology Readiness Level (TRL) 5, at the start of FY17, to TRL 6. This work includes the development of a starshade system prototype and the development and test of algorithms for the spacecraft formation flying capability. The formation flying software development costs are derived from a similar JPL software development effort completed for PROBA-3 in 2010. The Exo-S technology development is discussed in detail in Section 9. These estimates are based on grassroots estimates of the work needed to retire (i.e., raise to TRL 5)

each of the Exo-S technical risks as described in the Exo-S technology development plan. The scope of the technology work required and the cost for completing that work have each been reviewed independently by internal JPL experts and managers.

7.6.4 Mission Schedule

The Exo-S schedule is shown in **Figure 7.6-3**. This schedule was developed from a combination of the Kepler schedule and the Deep Impact schedule including all technical delays and programmatically driven funding delays. Given that the basis for this schedule estimate is built from completed missions—with Kepler being the longest mission development of any Discovery or New Frontiers mission—this schedule is a very conservative estimate. The overall schedule (Phases A–E) is 130 months long and includes 94 months of spacecraft development (Phase A through launch), and 36 months of operations. Pre-Phase A technology development work on the starshade and formation flying systems precedes the start of the project. The scope of this work is not included in the $1B cost cap and is discussed elsewhere in Section 9. Phase A begins at the end of FY17. Formulation (Phases A and B) runs for 36 months and includes requirements definition, system and subsystem design, and the start of procurements for long-lead items. It also encompasses the work needed to move the technology development of the starshade and formation flying systems from TRL 5 to TRL 6. The flight system implementation (Phases C and D) takes 58 months and includes the fabrication, integration, and test of the two flight systems. Implementation ends with the launch and initial on-orbit checkout in August 2025. The schedule shows an overall margin of six months, which is in keeping with JPL margin practices for a schedule of this duration.

The Phase A through Phase D duration for Exo-S is 94 months compared to 71 months for the dual-spacecraft Deep Impact mission, and 91 months for the Kepler exoplanet mission. The New Frontiers–class planetary missions are around the $1B cost cap placed on these studies and their Phases A through D schedules ran from 56 months (New Horizons) to 81 months (Juno), with an average of 71 months including the planned schedule for Osiris Rex (Origins Spectral Interpretation Resource Identification Security Regolith Explorer).

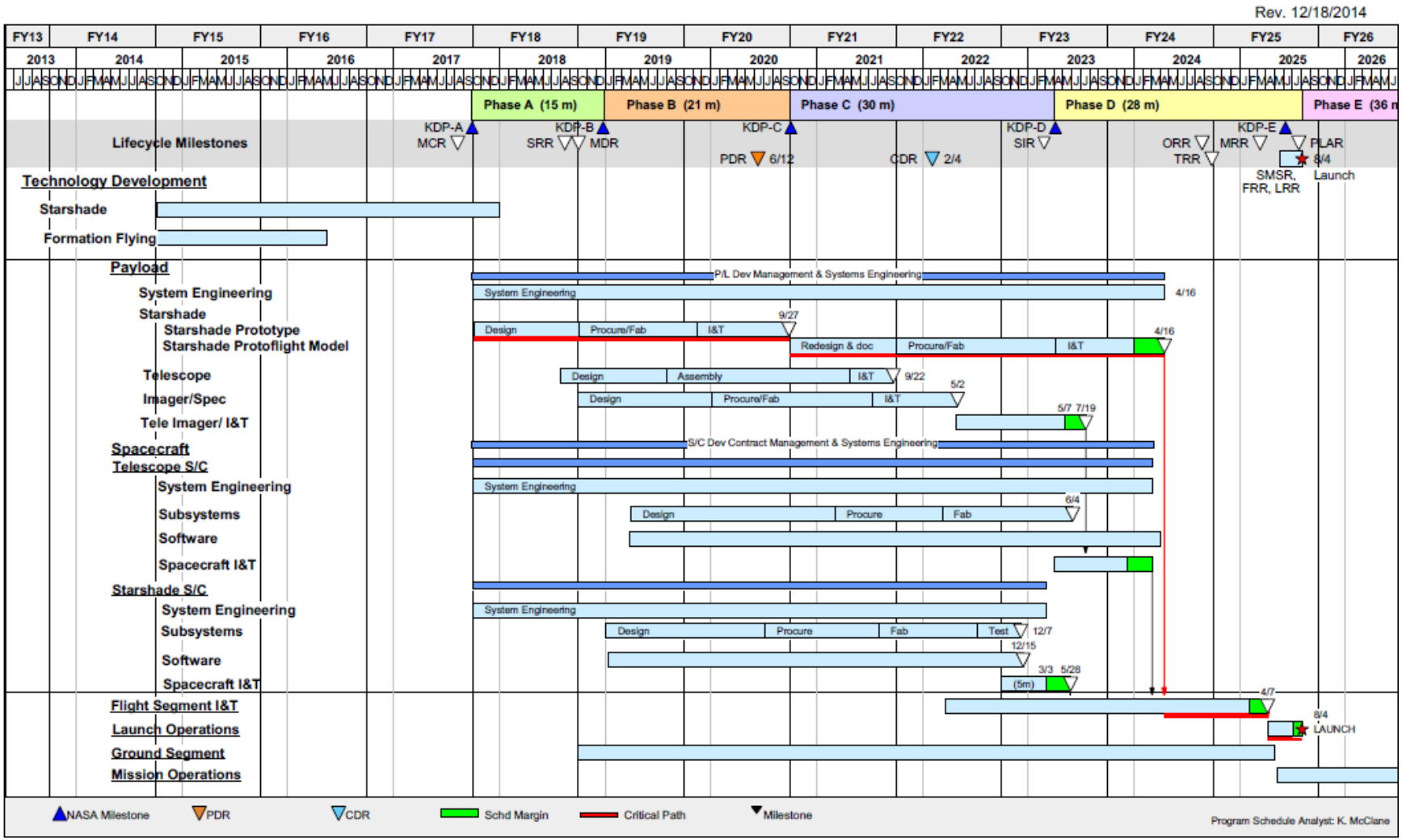

Figure 7.6-3. Dedicated Mission schedule.

8 STARSHADE RENDEZVOUS MISSION AND STARSHADE-READY PACKAGE FOR WFIRST/AFTA

The STDT has chosen to add design details for a starshade mission utilizing an already operational space telescope. This concept is termed the Rendezvous Mission since the starshade must meet up with the telescope spacecraft. For the purpose of developing the starshade follow-on mission, the WFIRST/AFTA is used as the telescope spacecraft example because it is a large astrophysics telescope capable of supporting direct imaging with a starshade, and the current timing of its development fits with a potential starshade development and launch. In addition, since WFIRST/AFTA is currently in development, the Exo-S study was able to access necessary telescope mission design details and expertise. Also for the purposes of developing this design point, WFIRST/AFTA was presumed to be in an L2 orbit rather than its present architecture's geostationary orbit. These assumptions are strictly for the purposes of developing the Rendezvous Mission and do not reflect an agreement with WFIRST/AFTA.

A starshade mission structured in this way offers several advantages. By leveraging the existing telescope asset, the starshade science can be easily achieved for less than the probe-class target of $1B, and at the same time allows use of a larger, more capable telescope than the Dedicated Mission. In addition, as a follow-on to a successful operational telescope spacecraft mission, the minimum mission science goals will have already been met.

In light of these advantages, the Rendezvous Mission was considered essential to this report.

8.1 Concept Overview and Key Performance Requirements

The Rendezvous Mission concept is designed as a Class C mission with a 3-year mission duration. It launches into an Earth-Sun L2 orbit. Telecommunications is handled by the Deep Space Network (DSN) as in the Dedicated Mission, but the Rendezvous Mission uses the telescope asset as a data relay with the DSN. The rendezvous starshade spacecraft does the repositioning from target to target, and not the telescope spacecraft as for the Dedicated Mission. The starshade uses the WISE-based spacecraft bus design as for the Dedicated Mission.

The mission's key performance requirements are organized into three main design elements: the starshade, the imaging instrument and the spacecraft/mission. (See the Rendezvous mission trace as shown in **Table 8.1-1** for the measurement requirements identified in Section 2.7.). Discussions on the basis for the Rendezvous requirements are included throughout the report with specific report sections identified in **Table 8.1-1**.

The overall system mass is shown in **Table 8.1-2.** Since there is minimal uncertainty on propellant mass and since propellant makes up most of the mass estimate, margin is better assessed as a percentage of dry mass. At 44% dry mass margin, the Rendezvous mission meets JPL design margins. It is important to realize that the large amount of propellant affords the concept added resiliency since mass above the margin is available by reducing the propellant. All major science goals can be achieved in the first two years of operation so some propellant for the third year could be sacrificed (with some reduction in the number of third year revisits) should mass be needed beyond the recommended margin.

8.2 Mission Design

Orbit selection choices for the Rendezvous Mission are limited by the direct imaging mission's need for a low gravity gradient environment and the need to meet up with an already on-orbit telescope spacecraft. The most accessible and stable orbital options that permit the required long period alignment needed for Exo-S, are heliocentric Earth-

Table 8.1-1. Dedicated Mission design requirements

	Rendezvous Mission Requirements		
Measurement Requirements	**Starshade**	**Instrument**	**Spacecraft & Mission**
Planet contrast sensitivity ≤ 4E-11 (limΔmag ≥ 26)	Manufacturing and deployment requirements (see Section 6.4) Thermal and structural deformation (see Section 6.4) Sun angle: 28° to 83° off normal (Section 6.4.6.3) Hole area < 1 cm^2 (Section 6.4.4)	Formation guide camera requirements (Appendix D)	**WFIRST/AFTA S/C:** Lateral position control: 1 m (Section 6.3.1, Appendix D.4) **Starshade S/C:** Pointing requirement: 1° 3-σ (see Appendix D.6) Spin rate: 1 rev per 3 min (Section 6.4.2)
		Detector requirements (see Section 8.4)	Orbit: L2 halo orbit (Section 4.6)
Planet detection SNR: ≥ 5			
Spectral res (Earths or larger) ≥ R10 Spectral res (sub-Neptunes or larger): ≥ R50 Planet characterization SNR: ≥ 10		IFS requirements (see Section 8.4)	
Total bandpass = 400–1,000 nm	Bandpass: partial (Section 4.4.1) Inner Disk Structure Dia. 20 m Petal Length 7 m Petal #28	Bandpass: 400–1000 nm (Section 4.3, 2.3)	Spacecraft separation distances: 30,000 to 50,000 km (Section 6.1 and Appendix D)
IWA ≤ 100 mas			
Spectral res (giants): ≥ R70 Planet characterization SNR: ≥ 10		IFS requirements Pixel scale: 10 mas/pixel (see Section 8.4)	Min mission duration: 2 years (Section 5.3.3)
Planet cross-track position ≤ 0.01 AU			
FOV > 10 AU at 10 pc		IFS FOV > 3 asec (Section 8.4.1)	
Measure polarization		0°, 45°	

leading, Earth drift-away and L2. Since the starshade could not catch up to a telescope launched into a drift-away orbit ahead of it, the only practical choice for the Rendezvous Mission is an orbit at L2.

Table 8.1-2. System mass estimate shows large propellant mass, which can be traded for launch mass margin.

Element	Current Best Estimate	Contin-gency (%)	Max Expected Value
Starshade S/C—Wet Mass	3,180		3,477
Hydrazine Propellant + Press.	2,021	-	2,021
Starshade S/C—Dry Mass	1,158	26	1,456
Starshade Payload	570	30	741
WISE-based Bus System	588	21	715
Total Launch Mass	3,180		3,477
Launch Capacity	3,695		3,695
Dry Launch Capacity	1,674		1,674
Margin	515		218
Margin (% of Launch Mass)	16%		6.3%
Margin (% of Dry Mass)	44%		15%

A low energy L2 trajectory was selected based on minimizing the propellant required to get the starshade into orbit (**Figure 8.2-1**). The transfer trajectory assumes a C3 of 0.5 km^2/sec^2. The estimated maximum launch mass is 3,700 kg and is based on a low cost intermediate class launch vehicle. Three trajectory correction maneuvers (TCMs) totaling 38.4 m/s are needed to adjust the starshade for rendezvous conditions.

Rendezvous with the telescope is possible over an extensive period of time (three to six weeks) depending on the phasing of the telescope orbit. For large halo orbits like the Exo-S Rendezvous concept's (780,000 km y-amplitude), there is no real rendezvous maneuver since the starshade quickly approaches the telescope to within 50,000 km without control. In some sense, the pointing

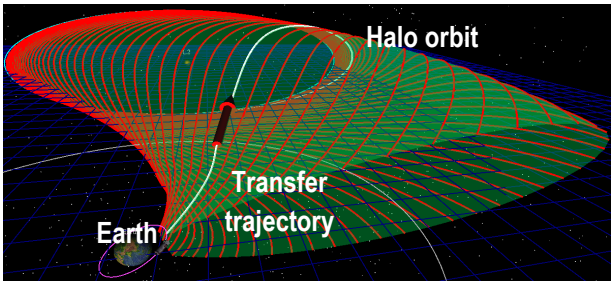

Figure 8.2-1. The family of low energy transfer orbits to the L2 halo orbit form a tube. The cyan trajectory with the closest approach to the Earth is selected for transfer to L2.

maneuver to align with the first star for observation with the telescope is the 'rendezvous maneuver'.

However, phasing with the telescope for rendezvous is critical, limiting the launch opportunities. At least four launch opportunities per year are expected; additional analysis may identify more launch opportunities. Each opportunity consists of a 20-day launch period; however, to avoid encounters with the Moon, the 20 days may not be continuous.

Table 8.2-1 provides the ΔV summary of the Rendezvous Mission. Once the starshade is on target to observe a star, the station keeping maneuvers (SKM) required are on average 1.2 cm/sec for the bang-bang controls to remain within a 1-m tube around the telescope to star line of sight, every 11.5 minutes. This amounts to 1.5 m/s per day for the SKMs. The retargeting ΔV includes the ΔV needed to execute the 55 target DRM (case 3 in Section 5) plus an additional 700 m/s for the third year. Both the retargeting and SKM ΔVs are computed using the Circular Restricted 3 Body Problem (CR3BP), which assumes a combined Earth-Moon mass at the barycenter. The controls are integrated and derived using differential correction with partial optimization. Retargeting maneuvers are described in Section 5.

8.3 Payload Overview

The complete payload for the Rendezvous Mission is shown in the block diagram provided in **Figure 8.3-1**. As in the Dedicated

Table 8.2-1. ΔV summary.

Occulter ΔV	CBE ΔV per (m/s)	Cont. (%)	MEV ΔV per (m/s)	MEV ΔV tot (m/s)
TCM 1	20	25%	25	25
TCM 2	2	25%	3	3
TCM 3	2	25%	3	3
Rendezvous	5	43%	7	7
Retargeting	23	25%	29	2013
SKM (per day on target)	1.5	10%	2	361
Dispose of the SC	10	43%	14	14
Total				**2426**

Mission, the Rendezvous Mission payload spans both spacecraft and includes the hardware needed to conduct the direct imaging science and formation flying. The starshade spacecraft carries the slightly larger 28-petal, 34-m starshade, as well as the formation flying laser, green-light LED array, and S-band transponder with four patch antennas. The other half of the direct imaging payload system is 'borrowed' from an existing large telescope mission. The only changes to the existing telescope mission are the addition of the other half of the S-band ranging and spacecraft-to-spacecraft communications link, and—presuming the mission includes a coronagraph—some minor changes to its imaging system to enable the formation sensing needed for formation flying.

Formation flying operations vary slightly from the Dedicated Mission in two ways: 1) the starshade repositions instead of the telescope, and 2) the Rendezvous imaging instrument does not include a formation guidance channel (FGC). Instead, final formation alignment sensing is performed by the imaging camera detector while the planetary science is captured on the integral field spectrograph (IFS).

As a consequence of these formation flying changes, the starshade's laser beacon must be in the visible, bandpass filters must be slightly adjusted, and starshade positional commanding and information must be transmitted across the spacecraft-to-spacecraft telecom link. A detailed description of the formation flying architecture and approach is provided in Section 6.3.

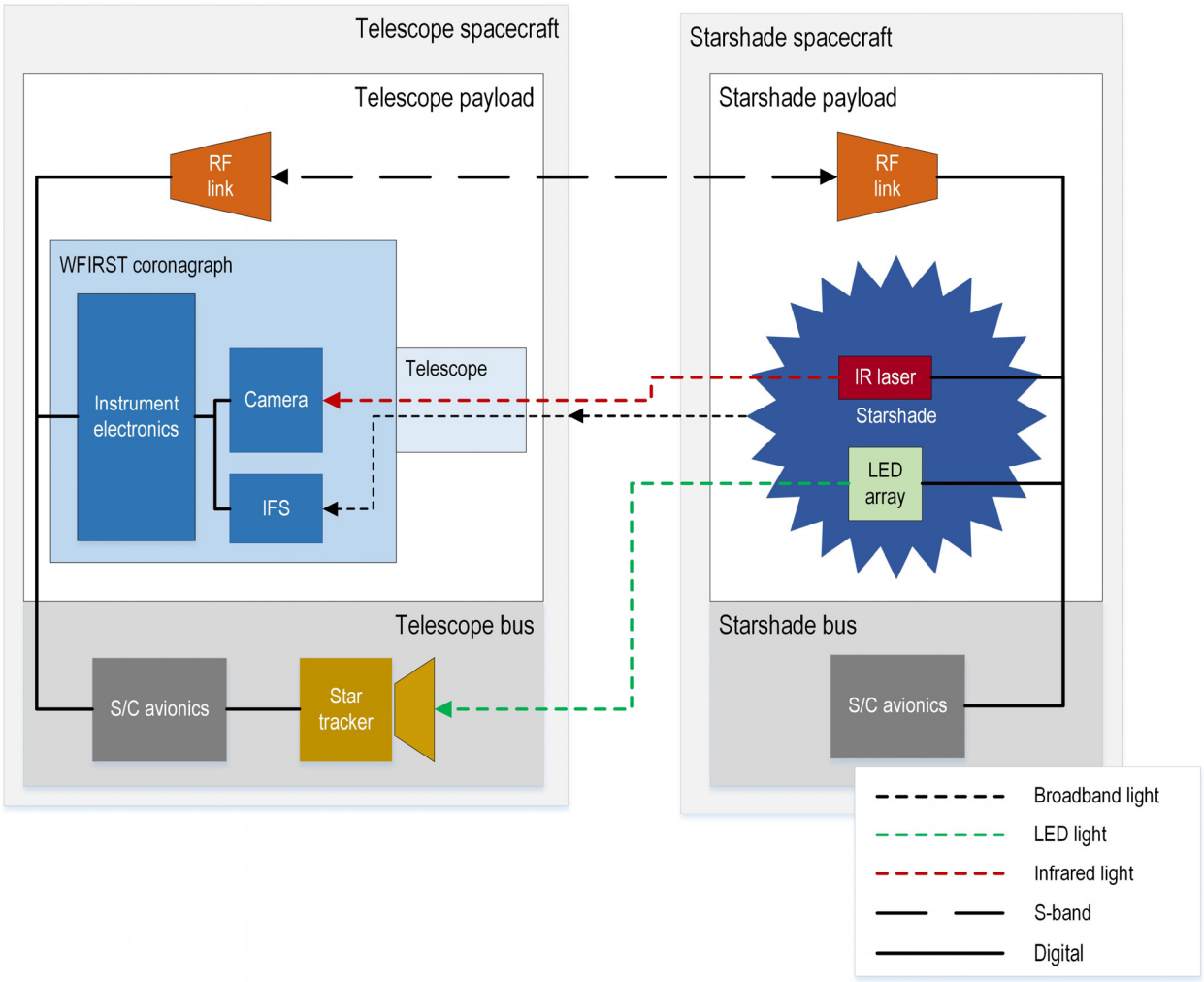

Figure 8.3-1. Starshade Rendezvous Mission payload block diagram.

Details on the starshade design and its key technologies are included in Sections 6.1, 6.2, and 9. The WFIRST/AFTA coronagraph and spacecraft modifications are discussed in Section 8.4.

8.4 Telescope and Spacecraft Starshade-Ready Package

Rendezvous starshade-specific requirements must be added into the existing telescope mission. The Rendezvous architecture has been selected based on minimizing these liens; however, several related to formation flying and the starshade direct imaging science cannot be avoided. Aside from the L2 orbital requirement previously discussed in Sections 4 and 8.2, the addition of the starshade requires some small imaging instrument changes and a formation flying ranging link added to the telescope mission. These modifications and their related trades are discussed in this section.

8.4.1 Instrument

The options for a starshade instrument operating on the WFIRST/AFTA telescope range from a minimal installation employing as much of the coronagraph instrument as possible to addition of a complete instrument, including a field camera, integral spectrometer, and FGC. The linear optical layout of the coronagraph permits a number of insertion points for a starshade instrument. Here, four options are discussed (shown in **Table 8.4-1**) before settling on one preferred option. The

increased aperture of the 2.4-m WFIRST/AFTA telescope potentially provides 23× faster integration times than a 1.1-m telescope. There are other significant considerations, such as increased spatial resolution requiring a larger instrument for the same field of view (FOV), which affect the choice.

Minimal. A scenario that minimizes engineering impact to the coronagraph, employs a modified coronagraph IFS as the science instrument and uses the coronagraph imaging camera for guidance. In this scenario, the FOV of the spectroscopy channel is narrowed to accommodate a larger spectral range, but there is otherwise no impact to the coronagraph instrument. The starshade instrument resides within the existing coronagraph beam train.

Preferred. In a preferred alternative low impact scenario, modifying the IFS to increase both its bandwidth and FOV improves starshade performance and also benefits the coronagraph instrument.

Both low-impact scenarios also allow the option to use the imaging camera for wide-field imaging by using the IFS channel camera as the guide camera after formation is acquired. Use of EMCCD (electron multiplying CCD) arrays for the coronagraph cameras allows read out at high rates with no read noise penalty. This option results in wide-field imaging of exoplanetary systems together with starlight suppression, a capability beyond that of the coronagraph alone.

High throughput. By contrast, because of the large number of optical surfaces in the coronagraph, optimal science performance would be achieved by inserting a separate starshade instrument as high up in the coronagraph beam train as possible; this is noted here as a secondary option. The simplest version of such an instrument entails the addition of a purpose-built starshade IFS (very similar to the coronagraph IFS but with extended FOV and spectral bandwidth) following the coronagraph's fast steering mirror (FSM). This option increases science performance by utilizing the increased photon flux available before the coronagraph beam train where the optical flux is ~67% higher, resulting in integration times that are 60% shorter. Only a single focal plane is added to the coronagraph instrument carrier. Formation guidance is done on the coronagraph's imaging camera. Wide-field imaging is also possible in the blue band by switching to use the coronagraph's IFS focal plane as the guidance camera.

Purpose built. For completeness, note that a purpose-built starshade instrument similar to that conceived for the Dedicated Mission would have additional science benefits. It would be located near the top of the beam train and contain an IFS, imaging channel and guide channel. Such a system would add more science capability such as additional polarization imaging options, faster imaging, imaging in a few color bands, a wider FOV and greater flexibility in the choice of starshade operating wavelength bands enabling greater instantaneous spectral coverage. The existing coronagraph volume is adequate to accommodate this option.

8.4.1.1 Options Summary

To summarize the options (referring to **Table 8.4-1**), use of the standard coronagraph IFS would cut the FOV and bandwidth significantly, resulting in only a 4-fold integration time improvement compared with the Dedicated Mission. Under the Minimal option, modifications to the IFS result in much faster integration times but reduce FOV even more. In the Preferred option, the FOV is doubled, but still significantly reduced. Thus, modifications for Minimal and Preferred scenarios yield improvements in FOV and speed; the last row

Table 8.4-1. Performance of instrument options for the Rendezvous Mission compared with Dedicated Mission parameters (46% bandwidth and 3 arcsec FOV).

Option	Bandwidth	Faster By	FOV
Coronagraph IFS	18%	4×	0.7 as
Minimal	34%	12×	0.5 as
Preferred	34%	12×	1.1 as
High Throughput	46%	19×	3 as

of **Table 8.4-1** indicates the potential of the High-throughput scenario comprising a powerful starshade-optimized IFS built into the top of the beam train, operating with its own 4k×4k focal plane. Such a setup would allow even faster integration, better spectral range, and a wider FOV comparable to that achieved on the Dedicated Mission.

The Preferred option is chosen for study because it yields good performance with minimal impact to the coronagraph system while taking some advantage of the starshade's potential for wide-field imaging. The Minimal option is discounted because it compromises the already small field of view of the IFS, leading to reduced performance for both starshade and coronagraph instruments. The High throughput option is discounted because it requires an additional focal plane, effectively incorporating a new channel into an already complex coronagraph instrument. For similar reasons, the Purpose-built option is also excluded at this time. The following descriptions of the starshade-ready parts of the coronagraph instrument therefore relates to the Preferred option.

8.4.1.2 Modifications to the Coronagraph Instrument

The WFIRST/AFTA coronagraph (**Figure 8.4-1**) takes an off-axis view through the telescope. A three-mirror anastigmat arrangement corrects much of the optical aberration introduced by this design. The collimated input beam strikes a FSM and then enters the coronagraph beam train, encountering approximately 25 optical surfaces on its path to the IFS focal plane. The resulting optical throughput is about 22%. The coronagraph path contains a number of pupil planes and focal planes where motorized masks and apertures are substituted for different coronagraph modes.

The starshade is operated in the pass-through mode with almost everything 'wide open'. Towards the end of the beam train, an existing filter wheel is reoriented (modification 4 in **Figure 8.4-1**) and a flip mirror mechanism removed (modification 3) to create a split between light directed to the IFS and light directed to the imaging camera. In coronagraph mode, either the IFS or the imaging camera is used, but in starshade mode, both systems are used simultaneously. Dichroic filters perform this function so that coronagraph mode operates as normal (modification 5).

The most significant modifications are to the IFS. The full operational bandwidth is extended from 600–1000 nm to 400–1000 nm, which is achieved by changing the dispersing prism glasses (modification 1). The instantaneous bandwidth is increased from 18% (coronagraph uses three 18% bands to

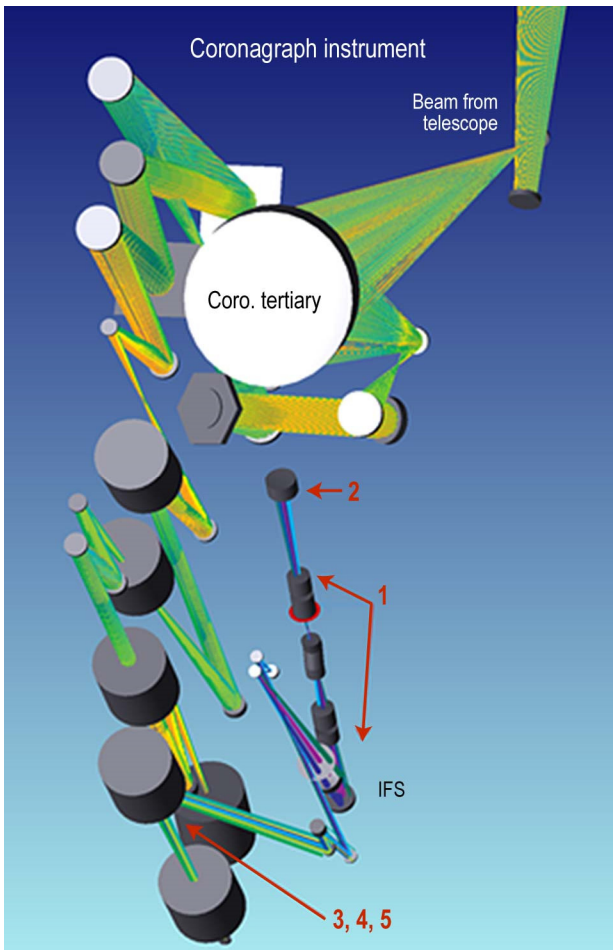

Figure 8.4-1. Modifications for starshade: 1: Larger bandpass, modified optics. 2: Replace 1k×1k detector with four 1k×1k detectors, also adding a pyramidal mirror. 3: Remove flip-mirror mechanism. 4: Reorient dichroic mirror mechanism to fold beam. 5: Add starshade-compatible dichroics.

cover the range 600–1000 nm) to 34% (starshade now uses three 34% bands to cover the range 400–1000 nm). To maintain the spectral resolution at $R_{(Nyquist)}$= 70, the length of the spectra on the detector focal plane must be increased. To enable this, the spacing of the microlens array at the entrance to the IFS is increased by 30%. The system of imaging lenses within the IFS is enlarged accordingly. These modifications correspond to the Minimal scenario.

The extra space needed by the longer spectra implies either a larger focal plane or a reduced FOV (0.5 arcsec radial). The coronagraph FOV is currently 0.71 arcsec radial, significantly less than the 1.8 arcsec capability of the coronagraph mask at 400 nm, so a modification to increase the radial FOV to 1.0 arcsec also improves coronagraph capability (Preferred scenario). The coronagraph requires an EMCCD detector, which has good immunity to charge trapping caused by radiation damage, and is available in a 1k×1k format. Currently the e2v CCD201-20 is at TRL 5, with advancement to TRL 6 by end of FY16. A larger 4k×4k version is being developed for ground-based observatories.

A larger focal plane of 2k×2k pixels is needed to accommodate the larger FOV. To achieve this, four 1k×1k detectors are placed together at the focus and the IFS optics and microlens array are modified to separate the focal plane image into four separate quadrants (**Figure 8.4-2**). This layout is based on the existing starshade IFS design outlined in Section 7, and would be implemented similarly as a modified coronagraph IFS, replacing the IFS shown in **Figure 8.4-1**. The modifications to the IFS consist of a prism array placed immediately behind the microlens array (MLA) and a near-flat, low pyramidal mirror half way along the IFS beam train. The prism array is based on standard blazed grating technology. Alternatively, the required beam-separating characteristic can be built directly into the MLA. The prism array and pyramidal mirror separate the single input beam to the IFS into four beamlets running along parallel paths to the four detectors.

8.4.1.3 Instrument Capability

Spectral Ranges

The instrument passbands have been narrowed from 46%, used on the Starshade Dedicated Telescope Mission, to 34% (**Table 8.4-2**). Outside these working bands, the starshade leaks a significant amount of light. Thus, for example, when operating in the green band, guiding becomes possible on the imaging camera using out-of-band light shorter than 600 nm or longer than 850 nm. When working in the blue or red passbands, the corresponding leaked longer or

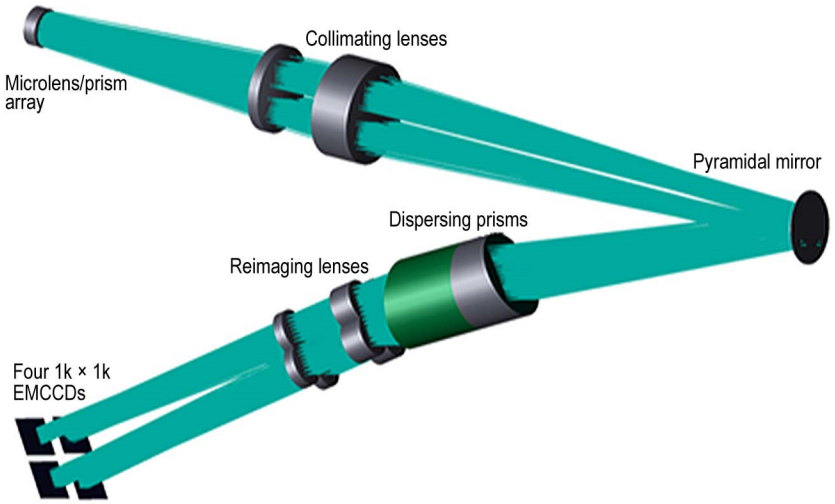

Figure 8.4-2. Modified starshade IFS enabling use of four 1kx1k EMCCDs to form a single 2k×2k focal plane.

Table 8.4-2. IWAs, working ranges, and spectral bands for science and guide channels.

	Blue	Green	Red	Imaging	Guide
Inner Working Angle	71 mas	100 mas	118 Mas	As for blue or red	NA
Telescope Range	50 Mm	35 Mm	30 Mm	Ditto	Any
Wavelength Range	425–600 nm	600–850 nm	706–1000 nm	Either blue or red	400–1000 nm minus science light

shorter wavelengths, respectively, are passed to the guide camera. In imaging mode, using the IFS channel as the guide camera, only the blue or red bands are available for imaging owing to the restricted instantaneous spectral operation ranges of the IFS.

Spectroscopy

The modified IFS supports spectroscopy at Nyquist resolution R_N = 70 in the three wavelength bands shown in **Table 8.4-2**. At 1.0 arcsec, the IFS has sufficient FOV to cover a solar system equivalent out to the orbit of Saturn at 10 pc distance.

Imaging

Light directed to the coronagraph imaging camera passes through a Wollaston polarizer, which creates two images on the focal plane. The pixel scale is the same as for the spectrometer and therefore, the FOV is ~10 arcsec. When used as the starshade guide camera, both or either of these images can be used for guiding.

8.4.1.4 Focal Planes

Both the imaging camera and the IFS utilize the 1K×1K EMCCD array CCD 201-20, operated at or below 163 K, selected for the coronagraph because of its near-zero read noise performance and good radiation immunity. The detectors are passively cooled. **Table 8.4-3** summarizes the principal detector parameters. In the IFS channel, the FOV is pixelated by the 102 lenslets across the MLA. In the guide channel, the two polarized images each occupy half the 1k width.

8.4.2 Communication

As with the Dedicated Mission, the Rendezvous S-band spacecraft-to-spacecraft link has two functions. First, it enables the telescope spacecraft to act as the relay between the starshade spacecraft and ground systems for routine command and telemetry. This arrangement is cost-efficient, since it greatly reduces the need for direct DSN support to the starshade spacecraft. The second and more important function of the S-band link is that it enables essential range measurements between the two spacecraft, which makes formation flying and starshade direct imaging possible. If a future space telescope asset is made to support starshade direct imaging, the telescope spacecraft must be able to support half of this S-band link. Therefore, inclusion of an S-band telecommunication system for spacecraft-to-spacecraft communications and formation flying range measurements is a required modification to the telescope spacecraft.

For the Rendezvous Mission, the S-band system must meet the following requirements:

- Knowledge of the range of the two spacecraft must be ±250 km or less
- The link must operate at up to 50,000 km separation
- The link data rate must be at least 100 bps
- The link must use frequencies allocated for spacecraft-to-spacecraft communications

Table 8.4-3. Detector specifications.

	IFS Channel	Guide Channel
Array Type	e2v CCD 201	Same
Format	4* 1k×1k	1kx1k
Field of View	1 arcsec (radial)	10 arcsec (diameter)
Pixels/View	102×102	500×500
Resolution	21 mas	Same
Optical Throughput	22%	28%
Dark Current	0.0005 e−/px/s	Same
Read Noise (effective)	0.03 e− rms	Same
EM Gain	500	Same
Pixel Size	13 µm	Same
Operating Temperature	≤163 K	Same
Quantum Efficiency	>70% (425–775 nm)	Same

As part of this study, two possible telecommunication systems were evaluated. The first option was the Gravity Recovery and Interior Laboratory (GRAIL) mission's S-band ranging system. It uses a time-transfer system (TTS) designed to provide highly accurate range measurements between two spacecraft. The TTS also provides a low-rate data link between the spacecraft. The second option was an S-band variation of the Electra radios in regular use on current Mars missions. Since it was not purpose-built for range measuring, the Electra radio requires significant development to meet the Exo-S role. In addition, it consumes more power than the selected GRAIL TTS design.

The telescope portion of the S-band link consists of a GRAIL transceiver, an amplifier, a diplexer, cabling, and a quad-helix antenna array. The characteristics of the telescope S band telecommunication system are listed in **Table 8.4-4**.

Table 8.4-4. Telescope S-band subsystem characteristics.

Range Accuracy	<3.5 m
Minimum Data Rate	100 bps
DC Power	29.5 W
Mass	5.3 kg
Frequency Bands	2025–2110 MHz, 2200–2290 MHz

8.4.3 Formation Sensing and Control

The WFIRST/AFTA hardware modifications needed for formation flying are entirely contained in the previously described modifications to the coronagraph and telecom systems. Some software modifications are also needed to implement the formation flying control algorithms. The formation flying design for the Rendezvous Mission is discussed in Section 6.3 and Appendix D.

8.5 Starshade Bus

The Rendezvous starshade bus is similar to the starshade bus in the Dedicated Mission. The architecture and WISE-heritage avionics are the same. The spacecraft remains spin-stabilized and carries the same attitude sensors. The X-band ground link is unchanged.

However, to allow the Rendezvous approach to work with the most possible telescope missions, the design liens and new requirements on the telescope spacecraft must be kept to a minimum. Major resizing of the telescope spacecraft's existing propulsion system moves away from this goal. As such, the Rendezvous approach assumes that the starshade is the repositioning spacecraft, resulting in several changes to the starshade spacecraft.

First, a large biprop propulsion system capable of moving the starshade from one target star to the next is needed. The massive amount of propellant required for this task and the propellant tanks are relocated to within the starshade hub's central cylinder to lower the spacecraft's center of gravity in launch configuration and better balance the spacecraft for spin stabilization. The Rendezvous Mission carries enough propellant for about three years of operation (at the DRM's observational cadence discussed in Section 5) and completely fills the hub cylinder's available space with tankage; a longer biprop mission would require a major starshade redesign with consideration for propellant storage as one of the driving design requirements.

Second, the Rendezvous Mission concept does not need to carry a telescope spacecraft during launch, and accordingly, does not need an ESPA ring bus structure. Less structure mass means more propellant and more science targets. For the Rendezvous Mission, the starshade's hub functions as the spacecraft's primary structure; bus subsystems are mounted directly to one of its flanges.

8.6 Starshade Rendezvous Mission Implementation

With the Rendezvous Mission defined in the preceding sections, this section discusses the design implementation. A cost estimate and

schedule are presented; the basis for both are also included.

8.6.1 Mission Operations

Operations for the Rendezvous Mission are largely the same as the Dedicated Mission. Due to the L2 location, tracking and telecommunications are still handled by the DSN. The starshade spacecraft still communicates primarily through the S-band spacecraft-to-spacecraft ranging link, but can communicate with the ground directly if needed. Retargeting and formation flying are still handled autonomously.

The primary differences between the Rendezvous Mission and Dedicated Mission are repositioning and communications. As stated earlier, when repositioning to the next target star, the starshade moves and not the telescope. The propulsion system has been changed from a SEP system to a biprop system due to difficulties with operating a continuous thrust system such as the SEP, on a spin-stabilized spacecraft. Additionally, the large, deployable solar arrays typically used with a SEP system could create thermal and mechanical distortion on the starshade; a technology development effort for a solar array integrated into the starshade optical shield would be needed to enable SEP usage on the starshade.

For communications, a ground station does not have to be constructed from scratch, but the existing ground station network for WFIRST/AFTA can be used. Exo-S will observe 55 targets in the first two years of operations. While the time on target and the time transiting to a target vary for each observation, each will follow a repetitive operational cycle similar to the Dedicated cycle shown in **Figure 7.6-2**. As with the Dedicated Mission, science data is stored and downlinked at the end of each observation with the telescope spacecraft pointing its antenna at the ground station. An operational sequence is then uplinked for the next target. In practice, uplink and downlink opportunities are determined by the WFIRST/AFTA mission but the estimated Exo-S data volume per day while observing (255 MBs) is expected to be small in comparison to WFIRST/AFTA's (less than 1% of the 1.3-m WFIRST concept's data volume, which was also downlinked from an L2 orbit) so existing storage and data handling capabilities should be sufficient to support the Exo-S mission.

Unlike the Dedicated Mission, the Rendezvous Mission represents one of several science programs on the WFIRST/AFTA mission, so the telescope can be used to address other science objectives while the starshade is repositioning. This arrangement offers a more efficient use of available assets and resources. For this reason, interleaving the Exo-S direct-imaging science with other mission science observations should be considered the preferred operational approach when using a starshade with any large astrophysics telescope.

8.6.2 Mission Cost

As part of the Rendezvous study, the Exo-S Design Team estimated the starshade portion of a follow-on direct imaging mission as costing about $610M. The cost estimate for the Rendezvous Mission includes: costs for the design, development, fabrication and test of a starshade spacecraft (payload and bus); ground system development for the starshade spacecraft; launch costs; project management, systems engineering, and mission assurance; operations costs for a three-year mission; starshade direct imaging science costs; and Phases A/B technology development costs for the starshade and formation flying system. No costs were assumed for the telescope spacecraft and its associated ground system development since these were expected to be existing assets available to the starshade mission. Starshade-required modifications to the telescope payload and spacecraft are expected to cost about $5M and are a lien against the telescope mission. Additionally,

and more specifically, no costs were assumed for the required changes to the current WFIRST/AFTA geostationary mission beyond the previously mentioned modification costs. This study presumes that a large telescope spacecraft is available at L2; as noted earlier, WFIRST/AFTA is used only as an example. The Exo-S Rendezvous estimate is shown in Appendix E. The mission was assumed to be reliability Class C (per NPR 8705.4). Reserves were calculated at 30% of the total project cost excluding launch services costs.

Most of the costs in the Rendezvous estimate were established from the same tools, databases, and assumptions used in the Dedicated estimate; consequently, the estimates share similar basis of estimate. As in the Dedicated Mission, the starshade payload estimate is based on a cost model estimate generated by JPL's Cost and Pricing Office. The model used for the estimate is PRICE H, a tool in wide use in aerospace, which is readily adaptable to complex designs lacking good system-level analogues such as the starshade. The Rendezvous starshade costs include resources for a slightly larger starshade (34 m vs. 30 m) and an integrated hub that also functions as the bus structure. The starshade bus cost was based on WISE actual costs with adjustments for the addition of a large biprop system. Science costs are based on WISE actual pre-launch science costs. Management, systems engineering, and mission assurance costs are also based on WISE actual costs; as such, they are consistent with a Class C mission. Technology development costs are about the same with both options.

While the Rendezvous Mission represents a significant cost reduction over the Dedicated Mission, there are additional design choices that could further reduce the total mission cost. Reducing the mission duration to two years could save around an additional $25–40M with some reduction in the overall science yield. This option was not examined in detail in this report due to the less favorable science yield, but might be considered in future studies if lower cost constraints are specified.

8.6.3 Mission Schedule

Since the Rendezvous Mission presumes the availability of an existing telescope, the development schedule is less complex than the Dedicated Mission, which must cover the development of two spacecraft. However, both schedules are approximately the same overall length since the critical path runs through the starshade development on each, and the starshade development duration is the same for both options. The Rendezvous schedule is based on the Dedicated schedule (**Figure 8.6-1**), with the telescope, telescope bus, and instrument development efforts removed. The flight system I&T was also shortened since this option will not need to prepare for a joint launch configuration. Support to the WFIRST/AFTA coronagraph was added to account for the development and starshade-based requirements and interface definition. All other durations were taken from the Dedicated schedule.

The Exo-S schedules were developed from a combination of Kepler and WISE schedules. The starshade schedule is based on a grassroots estimate from starshade development engineers drawing from experience with large deployable antenna developments for communications satellites. The launch is presented in the schedule as approximately one year after the launch of WFIRST/AFTA. This date is fairly flexible; Exo-S could launch as early as the planned WFIRST/AFTA launch date or it could launch several years later. For the purposes of this study, a delay between the two launches was viewed as advantageous both due to programmatic considerations (non-coincident spacecraft development) and due to the benefit of early WFIRST/AFTA coronagraph results in Exo-S final target adjustments. The overall schedule (Phases A–E) is 130 months long and includes 94 months of spacecraft development (Phase A through

launch and initial checkout), and 36 months of operations. Launch will be in August 2025.

Pre-Phase A work consists of starshade and formation flying technology development work, and systems engineering support to WFIRST/AFTA. Phase A begins in FY18 and spacecraft design begins in FY19. Formulation (Phases A and B) runs for 36 months and includes requirements definition, system and subsystem design, and the start of procurement for long-lead items. The flight system implementation (Phases C and D) takes 58 months and includes the fabrication, integration, and test of the starshade flight system. The schedule shows an overall margin of six months, which is in keeping with JPL margin practices for a schedule of this duration.

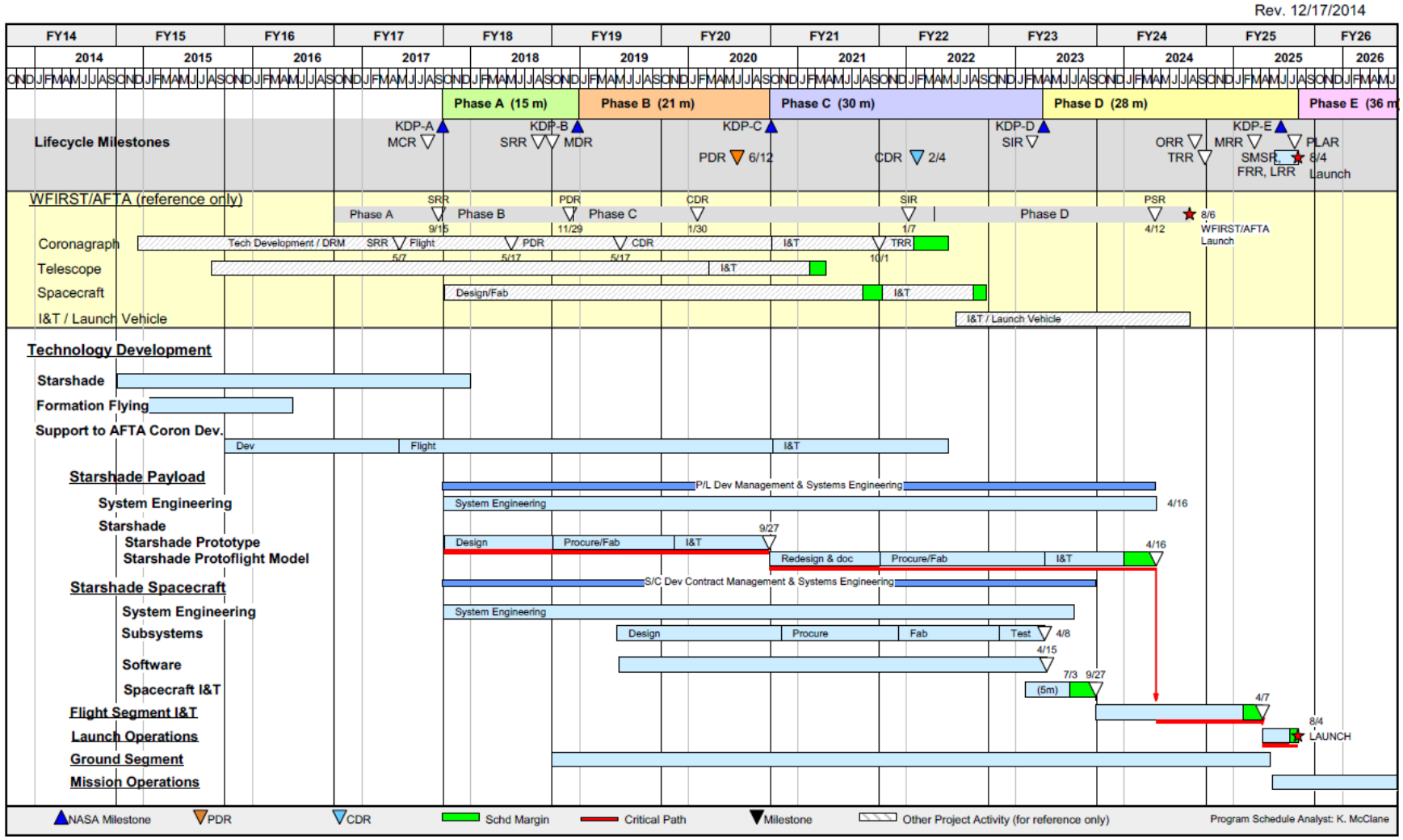

Figure 8.6-1. Starshade Rendezvous Mission schedule.

9 STARSHADE TECHNOLOGY READINESS

This section describes the key technology gaps, summarizes the completed efforts to resolve critical technology issues, and presents plans to resolve the current open technology issues.

Starshade performance is tied to five key requirements: stray light control; optical model validation; formation flying (FF); petal and truss precision deployment; and petal and truss shape control.

All technology efforts are focused on the starshade and, to a lesser extent, formation flying. While the starshade has not flown before, extensive heritage from large deployable antennas makes the starshade development manageable. FF control is straightforward, owing to a very benign disturbance environment. The remaining challenge is long-distance formation flying, which is achieved through integration of a fine formation guidance channel (FGC) with the science instrument.

Optical design drives the technology development for the starshade. The error budgets (described in Section 6.4) push the state of the art in analytical and manufacturing technologies. Fortunately, bridging these gaps to Technology Readiness Level (TRL) 5 at the start of Phase A in 2017 primarily requires demonstrations of existing technologies to tighter tolerances.

Table 9-1 summarizes the current open issues:

- Control edge-scattered sunlight
- Demonstrate contrast and diffraction performance and validate optical models
- Demonstrate lateral formation sensing accuracy
- Demonstrate flight-like petal fabrication and deployment
- Mature perimeter truss technology readiness including the optical shield

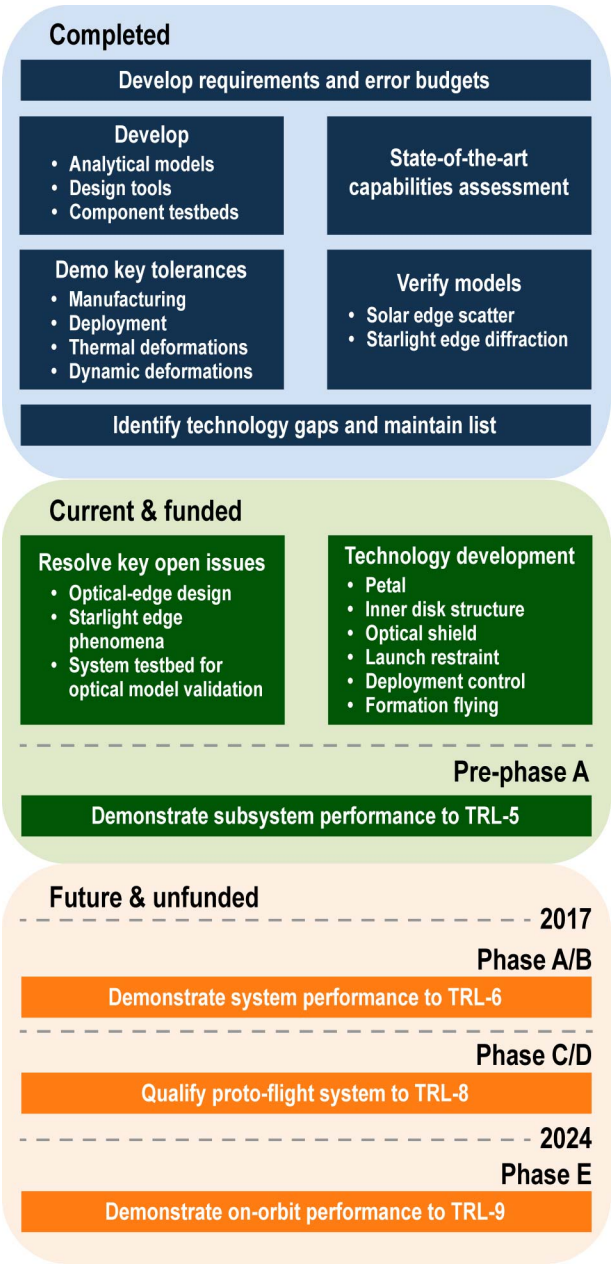

Figure 9-1. Technology development plan on-track to be ready for a new start in 2017.

9.1 Solar Glint

Exo-S observes target stars when the Sun-starshade-star angle is between 28° and 83°. Then, sunlight is incident on the starshade at 28° to 83° from surface normal and always on the side opposite to the telescope. A small fraction of incident sunlight reflects and diffracts from the starshade optical edge into the telescope to appear as solar glint and

Table 9-1. Starshade technology gaps.

ID	Title	Description	Current	Required
S-1	Control edge-scattered sunlight	Limit edge-scattered sunlight with optical edges that also handle stowed bending strain	Graphite edges meet all specs. except sharpness, with edge radius ≥ 10 µm	Edge radius ≤ 1 µm, Reflectivity ≤ 12%, Stowed radius ≥ 1.5 m
S-2	Demonstrate contrast and suppression performance and validate optical models	Demonstrate flight contrast and suppression, and validate starshade diffraction model in testbed that scales to flight design	Achieved contrast of 3×10^{-10}, except near petal edges, and suppression OF ~1e-6, in testbed at Fresnel # ≈ 500, at 632 nm wavelength	Contrast ≤ 1×10^{-10}, over all space from IWA to OWA, suppression < 10^{-9} in testbed at Fresnel # ≤ 25, over 250 nm bandpass in visible/NIR.
S-3	Demonstrate lateral formation-sensing accuracy	Demonstrate lateral formation-sensing accuracy consistent with keeping telescope in dark shadow created by starshade	Centroid accuracy ≥ 1% of a pixel is common, benefit from long integration times	Lateral sensing error ≤ 20 cm, estimate centroid positions to ≤ 0.3% of optical resolution
S-4	Demonstrate flight-like petal fabrication and deployment	Establish petal at TRL 5	Demonstrated manufacturing tolerances with early prototype, including: flat optical edges, no blankets, no interface to launch restraint, and deployment control system	Demonstrate manufacturing tolerances with flight-like petal, including: sharp optical edges, optical shield, interfaces to launch restraint and deployment control system
S-5	Demonstrate inner disk deployment with optical shield	Establish perimeter truss at TRL 5	Demonstrated deployment tolerance with 12-m Astromesh antenna, no blankets, no outrigger struts, no launch restraint	Demonstrate deployment tolerances with 20-m perimeter truss, optical shield, outrigger struts, launch restraint

contributes to instrument background noise. Specular reflection and solar diffraction is limited to portions of the edge that are oriented normal to the Sun–starshade–telescope plane, as shown in **Figure 9.1-1**. Diffuse reflections may originate from any illuminated part of the starshade edge, but tend to be stronger where the specularly reflected light originates.

This section details the modeling of solar glint, the flight design approach, the optical edge mechanical design status, and the technology development plan. A TDEM-12 activity to make headway in this plan is in progress and led by Suzanne Casement of Northrop Grumman Aerospace Systems (NGAS).

9.1.1 Glint Modeling Predictions and Measurements

A starshade system model was developed to predict solar glint fluxes as a function of solar incidence angle. The model was validated by testing a variety of representative edges in a scatterometer testbed, developed for this purpose (Martin et al. 2013).

Figure 9.1-2 compares model predictions to measurements of a commercial stainless steel razor blade. The model is in excellent agreement with measurements over solar incidence angles between about 50° and 80°. Diffracted sunlight is the dominant term and the sum of all reflected sunlight is at least 1 visual magnitude dimmer than diffracted light (**Figure 9.1-2**).

The tested razor blade is representative of a physical limit and is not intended as a flight solution since its geometry is not ideal. It accurately represents the diffraction, which is independent of edge radius of curvature (RoC) and reflectivity (R). The reflected flux for other edge designs can be scaled in proportion to the product of RoC and R (i.e., edge surface area). The tested razor blade had a 0.2-µm RoC and was highly specular with 60% reflectivity. Any similarly specular edge with a RoC × R product of 12 will reflect the same solar flux into the telescope.

Solar glint affects image plane background illumination at 60° solar incidence (**Figure 9.1-3**). A high performance specular edge like the razor blade is assumed. The rectangular area

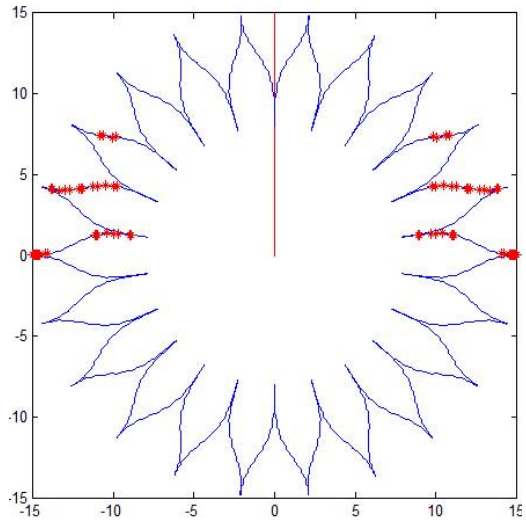

Figure 9.1-1. Lit-up edge regions. Red symbols indicate where specularly reflected and diffracted sunlight originates. The Sun is 30° into paper at top of figure (60° solar incidence). Units are meters.

corresponds to a region of the sky around the star, shown as a 60 m × 60 m area at the starshade plane. The outer circle represents the extreme extent of the starshade (the location of the tips). The general background produced by exozodiacal light (blue color on figure) is amended by the glint, which is seen as two lobes arising from the edge locations where diffraction and specular reflection occur (see **Figure 9.1-1**). For Exo-S, diffraction limited imaging results in smoothing and blurring

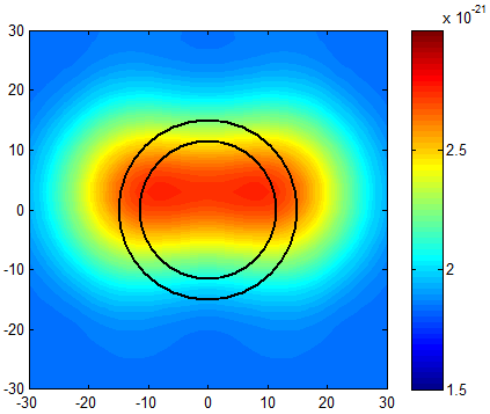

Figure 9.1-3. Solar glint contribution to instrument contrast (pre-calibration). Lobes correspond to lit-up edge regions. It can be seen that the shade makes only a small contribution to the overall illumination which is mainly exozodiacal light. Axis units are meters, and the circles are the minimum and maximum extent of the petals.

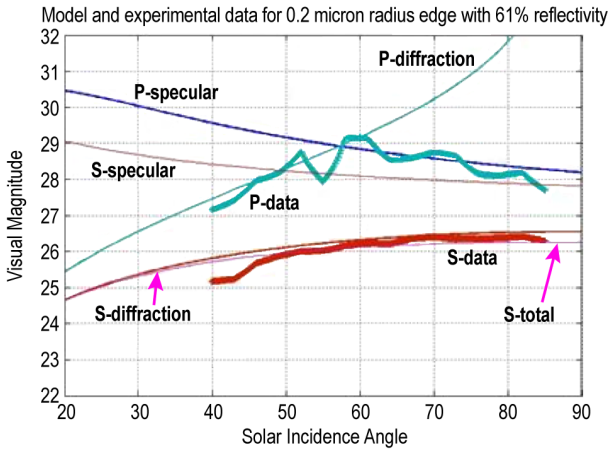

Figure 9.1-2. Model predictions compared to stainless steel razor blade measurements (not baseline design), for total light diffracted and specularly reflected by the starshade edge.

together of the two glinting areas producing the dog-bone shape of the region shown in yellow. The lobe brightness is equivalent to a point source at 27 visual magnitudes and increases to 26 visual magnitudes at 40° solar incidence. Overall, the starshade edges contribute a small amount of light to the background.

9.1.2 Flight Design Approach

The flight design approach is twofold. First, reflected solar glint is limited to 1 visual magnitude dimmer than diffracted solar glint. As in the test case, this corresponds to a RoC × R product ≤12. The current design goal is RoC ≤ 1 μm and $R \leq 10\%$.

Second, solar glint is calibrated to 1% of predicted flux, so that the systematic noise floor is limited to 1/5th as bright as the faintest exo-Earth in the Design Reference Mission (DRM; Section 5). Solar glint is highly stable and can be calibrated as a function of solar incidence angle during long retargeting coast periods when the starshade and telescope can point at each other. A target star is not necessary for these calibrations.

9.1.3 Optical Edge Development

The mechanical design of the optical edge needs to provide the requisite RoC and reflectivity, while also accommodating the bending strain associated with petal stowing

and any thermal strain associated with any CTE (coefficient of thermal expansion) mismatch with the petal structure to which it is bonded. Graphite-reinforced materials were initial choices, as they can match the petal structure CTE and have high strain capacity. However, experimentation with a variety of graphite types and machining techniques show that the required edge RoC cannot be met. A material that provides a sharper edge is required.

Several material options are currently under study including both metal and ceramic types. The plan is to produce an edge segment prototype (~1 m in length) and subject it to a full battery of tests, including: RoC measurement, light-scattering properties, bending strain, and thermal strain. In addition, the prototype edge segment will be installed on an existing petal prototype to demonstrate the requisite installation precision and compliance with TRL 5. The edges will be subjected to a number of environmental tests as well as furling and unfurling in conjunction with deployment tests.

9.2 Starlight Contrast, Suppression, and Diffraction Verification

Starshade optical performance will not be demonstrated by ground-based testing of any full-scale unit. The requisite distances are prohibitive. Rather, it will be demonstrated in a two-step process. First, subscale tests will demonstrate contrast (image plane) and suppression (pupil plane) performance consistent with imaging exo-Earths and will validate the optical models, upon which full-scale shape tolerance allocations are based. The scaling approach is to match the flight design in terms of the number of Fresnel zones to within a factor of ~2 and to also match the number of resolution elements across the starshade, so that the diffraction equations defining the dark shadow are representative of the mission.

Second, shape tolerance allocations will be verified on the fully deployed flight unit. Key capabilities are already demonstrated via early prototypes. The status and plans toward the first step are detailed here.

9.2.1 Previous Test Results and Issues

Several experiments over the last decade have made progress toward demonstrating the viability of creating a dark shadow with a starshade, including: the University of Colorado (Schindhelm et al. 2007; Leviton et al. 2007); Northrop-Grumman (Samuel et al. 2009); Princeton University (Cady et al. 2009; Sirbu et al. 2013); and larger scale tests in a dry lake bed (Glassman et al. 2013). Each of these experiments is limited in contrast and suppression performance to some extent by one or more of the following test environment issues:

- Wavefront errors due to collimating optics
- Diffraction effects due to the finite extent of the optical enclosure
- Diffraction off starshade support struts
- Dust in open air testing, both airborne and contaminating the starshade edge
- Size limitations resulting in large Fresnel number and overresolved images

9.2.2 Current Test Results and Issues

The current starshade optical testbed at Princeton University addresses the first three limitations identified above. An expanding beam is used to eliminate collimating optics and accounts for the corresponding contribution to Fresnel number. It also helps to limit testbed length to a manageable level. Diffraction effects from the optical enclosure and support struts are mitigated with an innovative mounting scheme whereby the starshade is supported by an outer ring with an apodization profile optimized in similar fashion to the starshade profile. This introduces a non-flight outer working angle (OWA) limit at the tip of the outer ring. Dust

effects are limited by testing in an indoor facility within an optical enclosure.

Figure 9.2-1 shows a diagram of the current starshade test article, which is etched into a 4″ silicon wafer. The starshade has 16 petals with tips at an IWA of 400 mas. The optical edges are about 50 µm thick without sharp corners as compared to the 1 µm RoC specified for flight optical edges (see Section 9.1.1). The red circles are placed approximately at the IWA of 400 mas and OWA of 638 mas. The annular region between the IWA and OWA is the discovery space, the region of high contrast. Again, the OWA is unique to the test article and is not a feature of the flight starshade design. Because of limitations in testbed size and in the original design, the theoretical suppression of this mask is only 10^{-7}. However, because of the large Fresnel number the mask is highly resolved, resulting in a contrast of almost 10^{-14}.

The starshade testbed at Princeton University is currently operating in a 40′ long optical enclosure. A monochromatic laser operating at 632 nm simulates starlight. The geometry creates 590 Fresnel zones across the starshade, whereas the baseline flight design operates with 12 zones.

The bright banding along all edges was not initially expected and limited the experimental contrast several orders of magnitude away from the theoretical prediction (**Figure 9.2-2**). Further modeling shows that the pattern could be well predicted by the limitations in the manufacturing process. The initial production of this mask used feature sizes in the etching process of over 2 µm. Modeling shows that better than 0.5 µm is necessary. When combined with estimates of the random manufacturing error, models of the input beam profile, mask tilt, and environmental conditions, the models were able to match the measured suppression and contrast extremely closely. For instance, the model predicts a suppression of $10^{-4.85}$ while the measured suppression in the pupil is $10^{-4.82}$.

To obtain a quantitative measurement of the contrast achieved in the dark hole away from the bright edges, an azimuthal median was taken. A set of geometrical wedge constraints were imposed to minimize the effect of the bright edges (**Figure 9.2-3**). The azimuthal median measurements were compared to the diffraction theory predictions

Figure 9.2-1. Starshade test article supported by a diffraction controlling outer ring. Red circles indicate the inner and outer working angles.

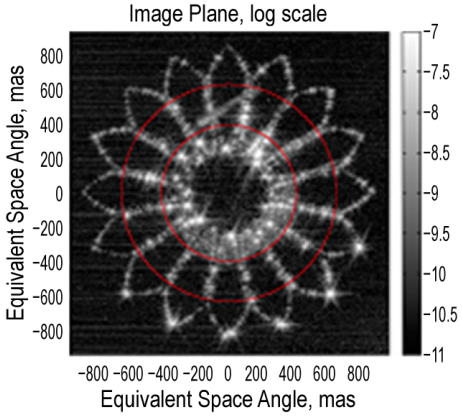

Figure 9.2-2. Measured contrast in image plane. Bright edges reflect manufacturing limitations of this mask.

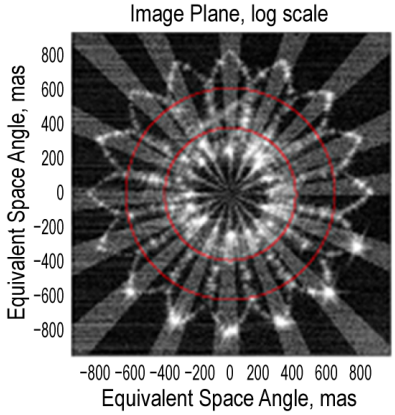

Figure 9.2-3. Wedge regions define azimuthal median contrast away from bright edges.

and error modeling (**Figure 9.2-4**). The median contrast across all 16 wedges at the IWA is about 1.0×10^{-10} and improves to about 2.5×10^{-11} at the OWA. The model reproduces the peaks, which dominate the suppression performance, with excellent agreement although the contrast in the dark annular regions is about a half an order of magnitude worse than modeled. This final discrepancy can be attributed to some of the brighter points across the struts, which may be due to localized defects. More recent preliminary experiments using a new mask with 0.5-μm feature sizes show background limited contrast better than 10^{-10}.

Not detailed here, for the sake of brevity, is the precursor testing of a circular-shaped control mask with the same outer ring configuration. This was used successfully to validate the calibration methodology and provide a reference point to compare the benefit of the optimized apodization profile.

While the 50-mm class starshades opened the door to testing and showed that the starshade will operate in principle, testing of larger starshades was clearly a high priority.

Cash (2011) predicted that a meter-class starshade could be tested through kilometers of air. A TDEM-12 activity, led by Tiffany Glassman of NGAS, is nearing completion and is demonstrating performance sufficient to allow model validation of contrast predictions at the 10^{-8} level. A very bright source is placed on a flat dry lake bed. A kilometer away, a starshade sits on a tripod and another kilometer further away is a small telescope viewing the starshade.

A typical result is shown in **Figure 9.2-5**—light from the source is seen scattering at grazing incidence off the ground. The tripod is seen in shadow, and a halo, caused by forward scattering of dust in the air, is seen around the starshade, with a ring of diffracted points at the base of the petals. Shown on the left of **Figure 9.2-5** is a test planet created by placing a weak light source to the left of the bright source.

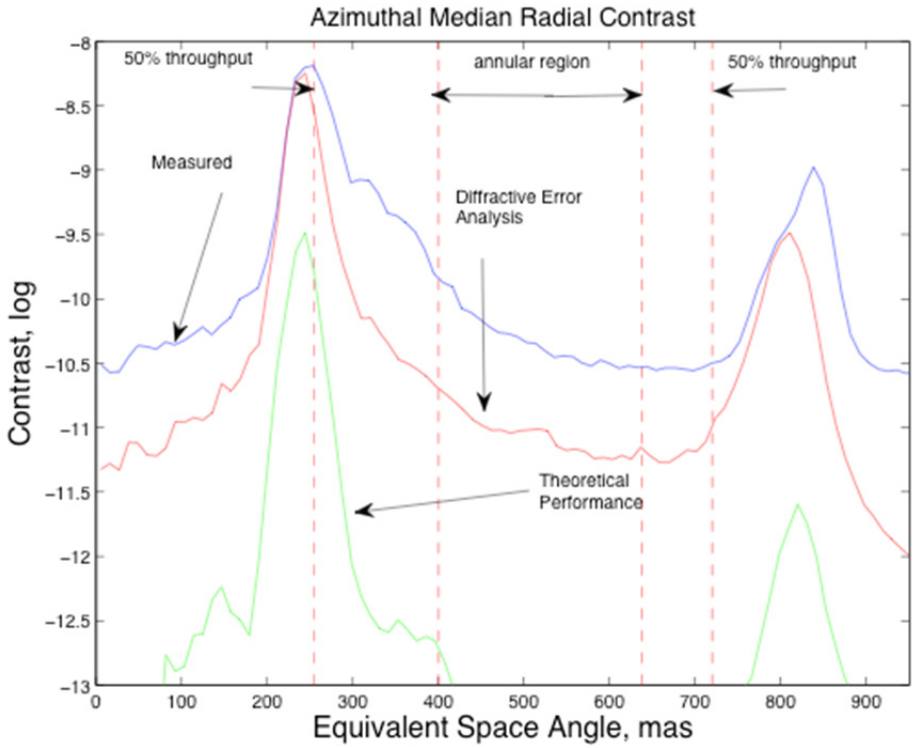

Figure 9.2-4. Azimuthal median comparison for the optimized starshade. The theoretical diffraction and error modeled simulations are shown and compared to the laboratory measurement. The peaks, which dominate the suppression performance, are well modeled.

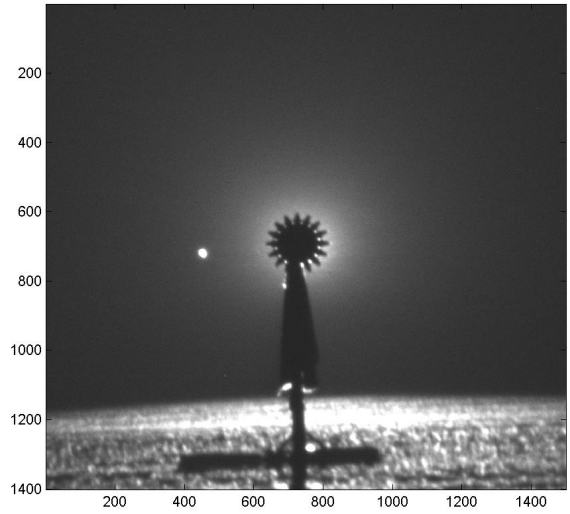

Figure 9.2-5. Starshade outdoor ground testing. (Photo courtesy of Northrop Grumman Corporation.)

The dust, unintentionally, provides a demonstration of scattering of starlight by exozodiacal dust. The brightness peaks sharply toward the center and, near the starshade, provides the effect limit on contrast. Test objectives include characterizing sensitivity to lateral control errors and the benefit of spinning the starshade.

9.2.3 Future Plans

A new TDEM activity (TDEM-12) led by Professor N. Jeremy Kasdin of Princeton University is underway to address optical performance verification and model validation. The development and testing of an improved subscale starshade with more precise edge shape and optical edge RoC ≤ 1 μm is the first priority. A completely new and much improved optical testbed is planned with length greater than 70 m. The goal is to achieve a Fresnel number within a factor of 2 of the baseline flight design. The starlight simulator will also be capable of producing broadband light.

A separate TDEM-12 activity led by Tiffany Glassman of NGAS is also underway to improve upon the open air testing (**Figure 9.2-5**) of larger starshades, on the order of 1 m in diameter. The test objectives include characterizing and modeling sensitivity to lateral control errors and the benefit of spinning the starshade.

Another new TDEM-13 activity led by Professor Webster Cash of the University of Colorado, Boulder features meter-class starshades for further testing on dry lake beds and in the 500 m XRCF vacuum beamline facility at the Marshall Space Flight Center.

9.3 Formation Flying

The starshade is designed to produce a dark shadow that extends radially 1 m beyond the telescope aperture. Contrast degrades rapidly beyond the 1-m specification (**Figure 9.3-1**). Formation control is required to keep the starshade center positioned laterally within ±1 m of the telescope boresight. This requires sensing the lateral position error to within about 30 cm (3 σ). The technology plans for demonstrating this capability are detailed in this section. The axial separation distance between starshade and telescope is loosely controlled to within ±250 km.

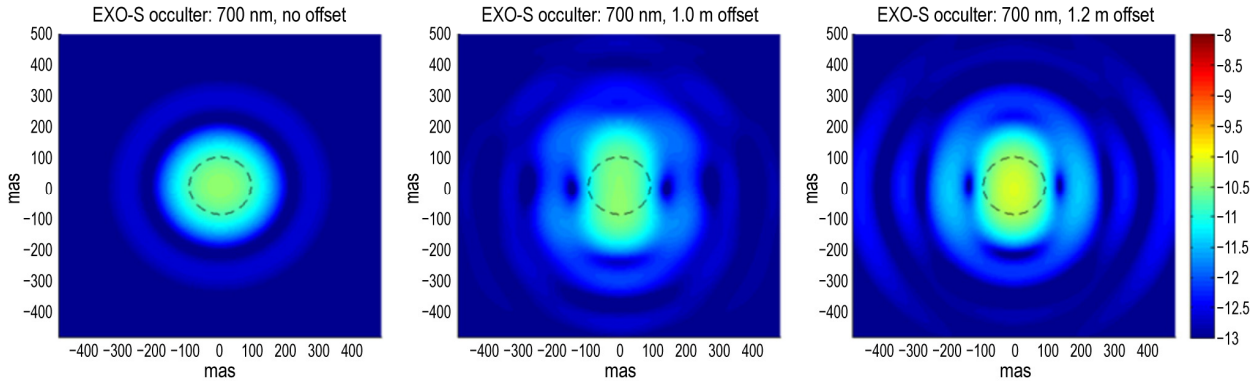

Figure 9.3-1. Image plane contrast in orders of magnitude at 700 nm with no lateral error (left), 1 m error (center), and 1.2 m error (right). The dashed circle indicates the inner working angle.

9.3.1 Current Test Results and Issues

Keeping the telescope within the dark-shadow created by the starshade (±1 m control tolerance), at separation distances approaching 50,000 km, may seem like a daunting challenge. Precision-bearing sensing for formation flying and its integration with the overall formation flying system are challenging engineering problems that will be studied in the forthcoming TDEM-13s.

Two factors make the formation sensing challenge tractable. First, the formation sensor utilizes the science telescope. This provides good angular resolution and collects a large number of photons, both essential requirements for high accuracy sensing. The telescope simultaneously images both the starshade laser beacon and long wavelength light from the target star that diffracts into the shadow. Models show that centroiding on the leakage starlight is aided by a multiplying effect that increases the apparent motion of the shade (when within ~1 m of center) by as much as 20-fold. Onboard image processing algorithms can then estimate centroid positions with 3 σ accuracy better than 0.3% of optical resolution. Built into these algorithms is a model of starshade diffraction at long wavelengths.

Second, the environment is very benign in heliocentric Earth-leading, Earth drift-away orbit. Solar pressure is the dominant disturbance and permits a very low control bandwidth. This contributes to improving formation-sensing accuracy by allowing long sensor integration times.

9.3.2 Future Plans

Requisite formation sensing capability will be demonstrated through a new TDEM activity (TDEM-13, led by Professor N. Jeremy Kasdin). A breadboard formation sensing and control instrument, including FGC and image processing algorithms, will be built and then integrated into the Princeton starshade optical testbed, as discussed in Section 9.2.3. The detector will be mounted on a 2-axis stage to simulate lateral position errors.

The TDEM activity will develop the system design for formation flying and prototype algorithms for formation sensing in addition to trajectory estimation and formation control algorithms. Simulations will be used to estimate performance and explore optimal formation control and acquisition strategies. After integration of the instrument breadboard into the Princeton starshade optical testbed, the control loop will be demonstrated with detector position stages simulating thrusters. One outcome of this work is expected to be a validation of formation flying to flight-like levels using real hardware in the loop.

Another TDEM activity (TDEM-13) led by Professor Webster Cash has been awarded to demonstrate two wavefront sensors that will advance long-distance formation flying sensing to TRL 6. The proposed experiments will demonstrate medium- and fine-level alignment sensors that have been previously identified as potential formation flying sensors for external occulters. The medium-level sensor is an astrometric telescope located on the starshade that guides the starshade as it slews between stars and up to the onset of the shadow onto the science telescope. Once in the shadow, a wavefront sensor on the science telescope uses long wavelength starlight diffracted around the starshade (a phenomenon known as the spot of Arago) to map the distribution of light at the aperture and to guide to the center of the shadow. Recovered intensity from behind the starshade of >1% at wavelengths outside of the science bandpass will be measured, and the measured wavefronts at different wavelengths and starshade configurations used to validate model predictions. This will be the first demonstration of starshades at wavelengths >1 μm and will provide a new wavelength regime in which to investigate the starshade's performance and validate the state-of-the-art diffraction codes.

Professor Cash's TDEM-13, noted above, will feature meter-class starshades on motion control devices. It will test both the Janus and the Spot of Arago formation flying alignment protocols both in air and in the 500-m vacuum line at Marshall Space Flight Center.

9.4 Petal Shape Fabrication

The petal width profile must be manufactured to within a tolerance of ±100 µm. Compliance was demonstrated by test through a TDEM activity (TDEM-09) led by Professor N. Jeremy Kasdin of Princeton University.

9.4.1 Previous Test Results and Issues

The TDEM-09 petal prototype is 6 m long of graphite construction (**Figure 9.4-1,** 1-m tip section not shown). By comparison, the baseline Exo-S starshade petal is 7-m long. Optical edge segments of matching graphite construction are precisely positioned and bonded in place to define the petal width profile.

The petal structure was assembled in a multistep process. It was populated with metrology targets and precisely measured using a *large off-site* coordinate measuring machine (CMM) with ±5 µm accuracy over the full petal length. This knowledge was used to precisely position optical edge segments relative to local metrology targets on the structure, using a *small on-site* CMM with ±10 µm accuracy over a few centimeters. After bonding all 10 optical edge segments in place, the petal was measured a final time with the large CMM.

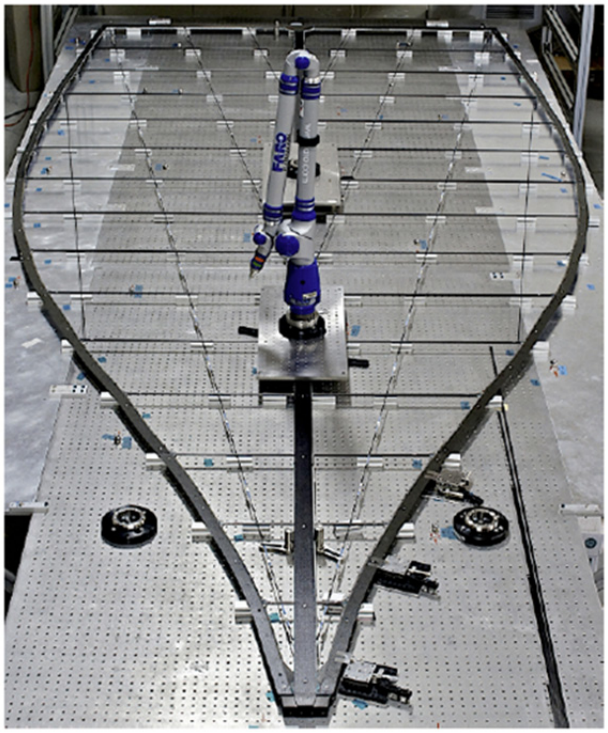

Figure 9.4-1. TDEM-09 petal prototype used to demonstrate manufacturing tolerance on petal width profile. Micrometer stages for positioning edge segments shown at bottom right.

Figure 9.4-2 shows resultant edge position errors relative to a best-fit nominal shape. The edge profile is within tolerance over 99% of edge length. Optical performance was simulated, in terms of image plane contrast, by randomizing these single petal results over a full complement of petals (**Figure 9.4-3**), with results expressed as a contrast probability distribution with a peak at the allocation of 2×10^{-11}.

TDEM-09 results fully demonstrate the achievability of the allocated manufacturing tolerances on petal width profile. The flight build will benefit from investment in an *in-situ metrology tool*. This tool will be mated to the assembly table (i.e., optical bench) and used for petal assembly, edge installation, and final shape measurement without moving the petal. Further improvement in the accuracy of the petal is also available in the optical edge machining accuracy, relative to the conventional CNC router used for this TDEM.

One simplification for this TDEM is the use of square-cut optical edge segments. The

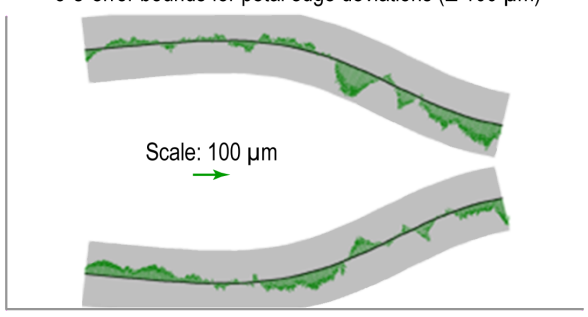

Figure 9.4-2. Measured petal shape error (green arrows) vs. 100 µm tolerance for 1×10^{-10} imaging (gray band) shows full compliance with the allocated tolerance.

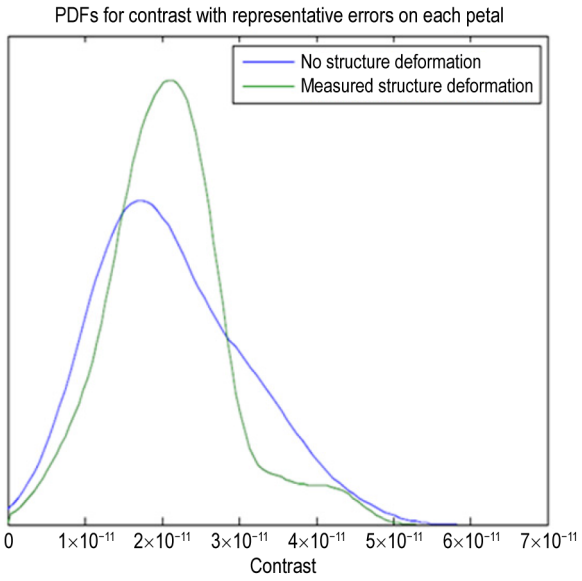

Figure 9.4-3. Contrast power density distribution per Monte Carlo simulation of randomized errors on all petals.

flight unit requires a sharp bevel cut edge to limit scattered sunlight. This may change the type of metrology sensor head, but does not invalidate the results.

9.4.2 Future Plans

A current TDEM activity (TDEM-12) led by Professor N. Jeremy Kasdin is underway to retire the petal manufacturability risk by building a petal at full-scale with flight-like materials with sharp bevel cut edges. Flight-like materials are equivalent to flight materials without the expensive material certifications. This petal will demonstrate deployment from stow to full deployment position with measurements that show compliance with the allocated tolerance. Other tests to demonstrate the petal robustness in thermal and launch vibration environments are currently being evaluated.

9.5 Perimeter Truss Deployment

Truss positional accuracy is critical to the starshade achieving its overall deployed shape requirement. Each petal attaches to the truss at two hinge points and the deployed position of these hinge points contribute to the petal positional accuracy, so their deployed location must be precisely controlled. The diameter of the best-fit circle through all petal hinge points represents the achieved inner disk diameter and the allocated tolerance (i.e., mean radial bias error) is ±0.25 mm. The allocated random tolerance is ±0.5 mm in each of radial and tangential directions. There is by definition no tangential mean position bias because this is nearly identical to a rigid body rotation of the starshade. Compliance was demonstrated by test as a TDEM activity (TDEM-10) led by Professor N. Jeremy Kasdin. New starshade deployment testbed (SDT) was completed in September 2014 that integrated starshade truss upgrades to the first-generation truss design, and tests are ongoing to demonstrate improvements in performance.

9.5.1 Current Test Results and Issues

The subscale partial system prototype developed for TDEM-10 (**Figure 9.5-1**) consists of: 1) 3-m diameter central hub of aluminum construction; 2) an existing antenna-based prototype truss with a 12-m diameter; and 3) four petals 4.25-m long of mixed aluminum and composite construction. The existing antenna truss was modified to add petal attachment fixtures and replace antenna webbing with spokes. The petals were sized to match the existing inner disk structure. Integration and test was performed at the NGAS Astromesh production facility in Goleta, California. Existing gravity compensation fixtures were used for the inner disk (see fan-shaped rails in **Figure 9.5-1**). Additional rails were added for the petals. Numerous optical targets were distributed around the prototype, but the final measurements were largely based upon targets closest to the hinge points. After each deployment, target positions were measured with both photogrammetry and a laser tracker.

After 10 initial deployment/metrology cycles, mechanical shims were installed to reduce the mean radial bias error. Additional shim cycles were not considered due to constraints on facility access. An additional 15

Figure 9.5-1. Deployed position tolerance demonstration. Petal root positions are measured after each of 20 deployments.

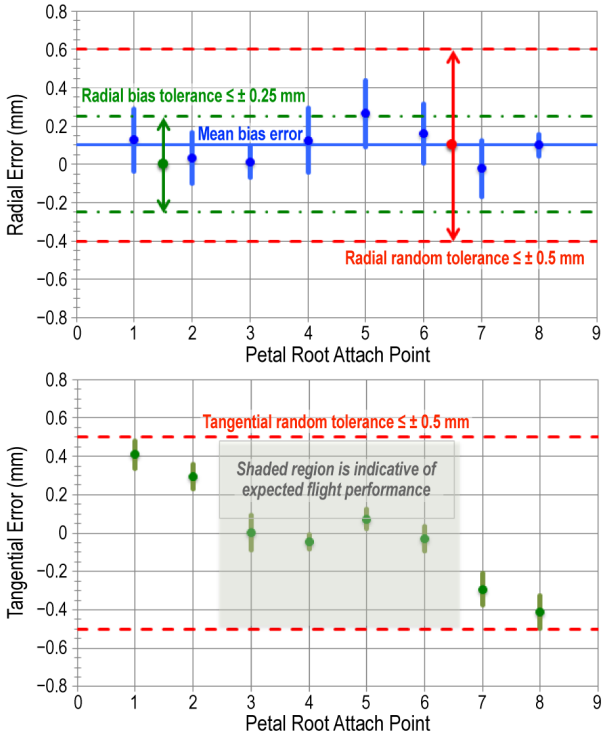

Figure 9.5-2. Measured deployment errors (3 σ with 90% confidence) are all within tolerance allocations.

deployment/metrology cycles formed the final data set. The results, expressed as 90% confidence intervals, are shown in **Figure 9.5-2**. Small number statistics yield intervals that were effectively at the 4 σ level. All intervals are contained within the allocated tolerance.

Radial errors show a residual bias that could be reduced with additional shimming. Tangential errors are minimal for the two inner petals and larger, but still within the tolerance limit, for the two outer petals. This behavior is an expected manifestation of the preexisting hardware. The petals need to be registered to truss node points at the junction between bays and where all forces are nominally nulled. These are points on the truss with precise deployment repeatability.

The existing antenna truss provides no registration features to precisely locate the nodal positions. A retrofitted registration feature was possible for the primary nodes, but not the alternating slave nodes. A registration tool was installed to the primary node between petals 2 and 3 (*attach points 4 and 5*). A precision tool was used to locate attach points 3 and 6. Attach points on petals 1 and 2 (*attach points 1, 2, 7, and 8*) were positioned with further extrapolation and the errors started compounding.

9.5.2 Future Plans

The existing truss design is optimized as a reflector antenna. The inventor of the antenna truss led its redesign and evolution to the starshade application. Section 6.2.1.5 describes the adaptation of the antenna truss design to the starshade. The new starshade inner disk structure includes the necessary registration features at every node and provides additional torsional stiffness, sufficient to avoid the need for complex outrigger struts to register the petal in plane.

This starshade optimized perimeter truss design was fabricated at ½ scale and completed in September 2014 (**Figure 9.5-3**). It currently serves as the SDT used for demonstrating other starshade technologies such as the optical shields for the inner disk structure.

Figure 9.5-3. Starshade deployment testbed at JPL is used to demonstrate starshade technologies such as the optical shields for the inner disk structure.

9.6 Lower Priority Technology Gaps

A number of smaller technology development areas feed into some of the five primary technology development efforts in a cross-cutting manner. These gaps will be closed in the process of closing the five main technology development efforts. These lesser technology development efforts are identified below.

9.6.1 Optical Shield Development

Both the petal and truss technology maturation plans require the development of their respective optical shields (OS)—the starlight blocking covering that makes the starshade shape opaque. Work has begun on the OS; materials have been selected, an architecture has been defined, and prototype OS panels have been constructed. Fabrication and testing of the petal and truss OS systems still remains to be completed. Details of the OS requirements, architecture, design, work completed, and the remaining development plan can be found in Appendix B.

9.6.2 Thermal Deformations

Early contrast error budget estimates identified starshade thermal deformation as a potentially significant contributor. Subsequent analyses have shown that through careful material selection the expected thermal deformations can be easily kept within budgeted tolerances. As such, thermal deformation management is viewed as a routine engineering development effort and not technology development. These thermal analyses are described in Section 6.2.7.3. Margins are deemed sufficiently large to defer any test-based verification until Phase B.

9.6.3 Holes and Opacity

Since the starshade covers significant area and is largely constructed of the thin, lightweight OS, it is susceptible to holes created by micrometeoroids. A cumulative pinhole area of 1 cm^2 introduces a contrast contribution of 1×10^{-12}. Modeling of this current OS design and known micrometeoroid fluxes show the design to be conservative. Details of the OS design and the pinhole error contribution modeling are covered in Appendix B and Section 6.4, respectively.

A formal request will be made to leverage relevant knowledge from the James Webb Space Telescope development team for micrometeoroid protection. Tests to demonstrate robustness against micrometeoroid impact are being evaluated.

9.7 Summary

The Exo-S technology development plan (Appendix C) lays out clear paths to close the key technology gaps in time to start Phase A by 2017. The five paths can be summarized as:

- **Solar glint.** Initial scatterometry testing of razor edges has validated starshade system

models and has set a critical edge design parameter: RoC (μm) × R (%) ≤12. Early materials testing has eliminated graphite as a possible edge material but other materials are under evaluation. A recent TDEM (TDEM-12, S. Casement et. al.) will evaluate materials for use as edges with a goal of demonstrating optic edge radius ≤ 1 μm and reflectivity ≤ 10%. Glint reducing edges will reach TRL 5 after integration on a prototype petal and successfully meeting environmental and deployment test requirements in 2016/2017.

- **Starshade optical performance modeling**. The starshade optical performance must rely on subscale testing and validation by modeling. Experiments over nearly a decade have shown that the subscale starshades are able to create deep shadows at the observing telescope, though none has yet to achieve the required 1×10^{-10} contrast uniformly outside of the IWA. Improved indoor (TDEM-13, Kasdin et al.) and outdoor (TDEM-12, Glassman et al.) starshade testbeds have been funded with a goal of improving the measured contrast and suppression as well as the agreement between measured and modeled contrast.
- **Formation flying**. While formation flying is not new to space missions, the sensing aspects of Exo-S require technology development. An initial FF design and error budget analysis have been established. Two new TDEMs (TDEM-13, Cash et al., and TDEM-13, Kasdin et. al.) will carry out initial testing of the sensing methods and control algorithms. The demonstration of closed loop control will raise the FF design to TRL 5 and close this gap.
- **Petal maturation.** A great deal has been done toward closing the gap on the petal design. Manufacturing and deployment requirements have been established. A baseline design is in place, and thermal and mechanical performance has been modeled. TDEM-09 has demonstrated a manufactured petal width profile tolerance ≤ 100 μm, meeting exo-Earth detection requirements. Additional activities are proposed to mature technology readiness to TRL 5 by the end of calendar year 2017. This includes a TDEM-12 led by Kasdin to construct and test a full-scale, flight-like petal prototype, including flight-like materials with optical edges and an optical shield on a full-scale starshade petal.
- **Truss maturation.** There has also been much progress toward closing the truss technology gap. Deployment requirements have been established and have been demonstrated on an early prototype. A second generation ½-scale prototype has been constructed and will be used as a testbed to develop the full starshade system design. Remaining work includes developing the starshade deployment system and OS development and testing. The truss will reach TRL 5 after successfully repeating deployment tests and demonstrating compliance to required deployment tolerances.

Finally, a full-scale starshade prototype will be developed and subjected to environmental and performance testing to raise the starshade to TRL 6 following the start of Phase A. This path to flight is identical for both the Rendezvous and the Dedicated missions.

10 REFERENCES

Executive Summary

National Research Council 2010, New Worlds, New Horizons in Astronomy and Astrophysics (Washington, DC: The National Academies Press).

Section 1

Bastien, F.A. et al. 2014, AJ, 147, 29.
Batalha, N.M. et al. 2011, ApJ, 729, 27.
Casertano, S. et al. 2008, A&A, 482, 699.
Cash, W. 2006, Nature, 442, 51.
Cash, W. et al. 2009, in UV/Optical/IR Space Telescopes: Innovative Technologies and Concepts IV, ed. H.A. MacEwen et al., Proc. SPIE, 7436, 743606.
Cassan, A. et al. 2012, Nature, 481, 167.
Copi, C.J. & Starkman, G.D. 2000, ApJ, 532, 581.
Deming, D. et al. 2013, ApJ, 774, 95.
Domagal-Goldman, S.D. et al. 2011, AsBio, 11, 5.
Doyle, L.R. et al. 2011, Sci, 333, 6049.
Fressin, F. et al. 2013, ApJ, 766, 81.
Guyon, O. & Martinache, F. 2013, BAAS, 221, 419.05.
Howard, A.W. & Fulton, B.J. 2014, Doppler Limits Report, http://exep.jpl.nasa.gov/reportsAndDocuments/completenessStudy/rv_limits_report.pdf.
Howard, A.W. 2013, Sci, 340, 572.
Kaltenegger, L. & Traub, W.A. 2009, ApJ, 698, 519.
Kasdin, N.J., Cady, E. J., Dumont, P. J., et al. 2009, Occulter design for theia, in Society of Photo-Optical Instrumentation Engineers (SPIE) Conference Series, 7440.
Kolemen, E. & Kasdin, N. J. 2007, Optimal configuration of a planet-finding mission consisting of a telescope and a constellation of occulters, in Proceedings of the AAS Space Flight Mechanics Meeting (Sedona, AZ: AAS), 07-202.
Konopacky, Q. et al. 2013, Sci, 339, 1398.
Kopparapu, R.K. et al. 2013, ApJ, 765, 131.
Kreidberg, L. et al. 2014, Nature, 505, 69.
Lawson, P. 2013, Exoplanet Exploration Program Technology Plan, Appendix: 2012, http://exep.jpl.nasa.gov/files/exep/2012AppendixFall.pdf.
Lissauer, J. et al. 2014, ApJ, 784, 44.
Madhusudhan, N. et al. 2011, Nature, 469, 7328.
Madhusudhan, N. et al. 2014, in Protostars and Planets VI, ed. H. Beuther et al. (Tucson, AZ: University of Arizona Press), submitted.
Marchal, C. 1985, A&A, 12, 193.
Marley, M.S. et al., 2007, ApJ, 655, 541.
Marois, C. et al. 2010, Nature, 468, 1080.
Martin-Fleitas, J.M., Sahlmann, J., Mora, A., et al. 2014, Enabling Gaia observations of naked-eye stars, in Proceedings of SPIE 9143, 91430Y.
Oppenheimer, B. & Hinkley, S. 2009, ARAA, 47, 253.
Oppenheimer, B.R. et al. 2013, ApJ, 768, 1.
Perrin, M. et al. 2015, ApJ, 799, 182.
Petigura, E.A. et al. 2013, Measuring Areas of Curves, in PNAS 110, ed. I.M. Verma (Washington, DC), 19273.
Postman, M., Brown, T., Sembach, K., et al. 2012, OptEn, 51, 011007.
Rauer, H. et al. 2013, ExA, submitted (arXiv1310.0696).
Rein, H. 2012, MNRAS, 427L, 21.
Ricker, G.R. et al. 2015. SPIE JATIS, 1, 1.
Rogers, L.A. & Seager, S. 2010, ApJ, 716, 1208.
Rowe, J.F. et al. 2014, ApJ, 784, 44.
Schultz, A.B. et al. 2003, High-Contrast Imaging for Exo-Planet Detection, in Proc. SPIE 4860, ed. A.B. Schultz & R.G. Lyon (Bellingham, WA: SPIE), 54.
Seager, S. 2013, Sci, 340, 577.
Seager, S., and Bains, W. 2015, Science Advances, 1, 2, e1500047.

Seager, S. and Deming, D. 2010, ARAA, 48, 631.
Seager, S. et al. 2013, ApJ, 777, 95.
Seager, S. et al. 2015, The High Definition Space Telescope: Unveiling the High-Definition Universe: From Cosmic Birth to Living Earths, AURA, in preparation.
Simmons, W.L. 2005, A pinspeck camera for exo-planet spectroscopy, Technical report, M.S. Thesis, Department of Mechanical and Aerospace Engineering, Princeton University.
Simmons, W.L. et al. 2004, Optical, Infrared, and Millimeter Space Telescopes, in Proc. SPIE 5487, ed. A. Stohr, D. Jager, and S. Iezekiel (Bellingham, WA: SPIE), 1634.
Smith, M.W. et al. 2010, Space Telescopes and Instrumentation 2010: Optical, Infrared, and Millimeter Wave, in Proc. SPIE 7731, ed. J.M. Oschmann Jr. et al. (Bellingham, WA: SPIE), 773127.
Snellen, I. A. G. et al. 2010, Nature, 465, 1049.
Snellen, I. A. G. et al. 2013, ApJ, 764, 182.
Soummer, R. et al. 2010, Space Telescopes and Instrumentation 2010: Optical, Infrared, and Millimeter Wave, in Proc. SPIE 7731, ed. J.M. Oschmann et al. (San Diego, California: SPIE), 77312I.
Spitzer, L. 1962, AmSci, 50, 473.
Stapelfeldt, K. 2006, Proceedings of IAU Symposium, 232, 149.
Sumi, T. et al. 2010, ApJ, 710, 1641.
Vanderbei, R.J. et al. 2003, ApJ, 599, 686.
Vanderbei, R.J. et al. 2007, ApJ, 665, 794.
Wakeford, H.R. et al. 2013, MNRAS, 435, 3481.
Woodcock, G.R. 1974, Concept analysis and discussion: observations of extrasolar planets with an LST, NAS9-14323, D180-18501-2, in Future Space Transportation Systems Analysis.
Zsom, A. et al. 2013, ApJ, 778, 109.

Section 2

Backman, D. et al. 2009, ApJ, 690, 1522.
Barnes, R. & Greenberg, R. 2006, ApJ, 647, 163.
Brown, R.A. 2005, ApJ, 624, 1010.
Buchhave, L.A. et al. 2012, Nature, 486, 375.
Burke, C.J. et al. 2013, ApJS, 210, 19.
Cahoy, K.L. et al. 2010, ApJ, 724, 189.
Chen, C.H., Mittal, T., Kuchner, M., et al. 2014, ApJS, 211, 25.
Chiang, E., et al. 2009, ApJ, 693, 734.
Dawson, R.I., Murray-Clay, R.A., and Fabrycky, D.C. 2011, ApJ, 743, L17.
di Folco, E., et al. 2007, A&A, 475, 243.
Domagal-Goldman, S.D. et al. 2014, ApJ, 792, 90.
Greaves, J.S., et al. 2004, MNRAS, 351, L54.
Hillenbrand, L.A. et al. 2008, ApJ, 677, 630.
Howard, A. W. et al. 2010, Sci, 330, 653.
Hu, Renyu. Personal communication.
Karkoschka, E. 1994, Icarus, 111, 174.
Karkoschka, E. 1998, Icarus, 133, 134.
Kopparapu, R. et al. 2013, ApJ, 765, 131.
Kuchner, M.J. & Stark, C.C. 2010, AJ, 140, 1007.
Nesvorny, D. et al. 2010, ApJ, 713, 816.
Petigura, E.A. et al. 2013, Measuring Areas of Curves, in Proc. PNAS 110, ed. I.M. Verma (Washington, DC: PNAS), 19273.
Pierrehumbert, R. & Gaidos, E. 2011, ApJ, 734, 13.
Robinson, T.D. et al. 2011, AsBio, 11, 393.
Seager, S., Whitney, B.A., & Sasselov, D.D. 2000, ApJ, 540, 504.
Stark, C.C. & Kuchner, M.J. 2008, ApJ, 686, 637.
Stark, C.C. et al. 2014, ApJ, 789, 58.
Torrey, P. et al. 2014, MNRAS, submitted.
Traub, W. 2003, The Colors of Extrasolar Planets, in Scientific Frontiers in Research on Extrasolar Planets, ed. D. Deming and S. Seager, ASP Conference Series, 294, 595.
Turnbull, M.C. et al. 2012, PASP, 124, 418.
Vogelsberger, M. et al. 2014, Nature, 509, 177.

Section 3

Abt, H.A. 1983, ARA&A, 21, 343.
Binney, J. & Merrifield, M. 1998, Galactic Astronomy (Princeton University Press).
CANDELS.http://candels.ucolick.org/data_access/GOODS-S.html.
Coe, D. et al. 2006, AJ, 132, 926.
Cuntz, M., 2014, ApJ 780, 14.
Doyle, L.R. et al. 2011, Sci, 333, 6049.
Dumusque, X. et al. 2012, Nature, 491, 207.
Duquennoy, A. & Mayor, M. 1991, A&A, 248, 485.
Eggl, S., Pilat-Lohinger, E., Funk, B., Georgakarakos, N., Haghighipour, N. 2013, 428, 3104.
Ford, E.B., Seager, S., Turner E.L. 2001, Nature, 412, 885.
Guo, Y., Ferguson, H.C., Giavalisco, M. et al. 2013, ApJS, 207, 24.
Haghighipour, N. 2006, ApJ, 644, 543.
Hinz, P. 2013, AAS, 221, 403.06.
Holman, M.J. & Wiegert, P.A. 1999, AJ, 117, 621.
Howard, A.W. & Fulton, B.J. 2014, http://exep.jpl.nasa.gov/reportsAndDocuments/completenessStudy/HST Calibration Database. http://www.stsci.edu/hst/observatory/crds/astronomical_catalogs.html.
Illingworth, G.D. et al. 2013, ApJS, 209, 6.
Jaime, L., Aguilar, L., & Pichardo, B. 2014, MNRAS, 443, 260.
Koekemoer, A.M. et al. 2013, ApJ, 622, 319.
Konacki, M. et al. 2009, ApJ, 704, 513.
Kuhn, J.R. & Hawley, S.L., 1999, PASP, 111, 601.
Mathieu, R.D. 1994, ARA&A, 32, 465.
Miller, J.S., Robinson, L.B., & Goodrich, R.W. 1987, A CCD Spectropolarimeter for the Lick Observatory 3-Meter Telescope, Instrumentation for Ground-Based Optical Astronomy Santa Cruz Summer Workshops in Astronomy and Astrophysics.
Noecker, C. Personal communication.
Pallé, E., Ford, E.B., Seager, S., et al. 2008, ApJ, 676, 1319.
Pirzkal, N. et al. 2005, ApJ, 622, 319.
Raghavan, D. et al. 2010, arXiv:1007.0414.
Roberge, A. et al. 2012, PASP, 124, 799.
Robin, AC, Reylé, C., Derrière S. & Picaud, S. 2003, A&A, 409, 523.
Robinson, T. D. et al. 2011, AsBio, 11, 393.
Schwieterman, E. et al. 2015, in prep.
Spyak, P.R. & W.L. Wolfe 1992, OptEn, 31, 1775.
Windhorst, R.A. et al. 2011, ApJS, 193, 27.

Section 4

Cash, W. et al. 2009, in UV/Optical/IR Space Telescopes: Innovative Technologies and Concepts IV, ed. H.A. MacEwen et al., Proc. SPIE, 7436, 743606.

Section 5

Brown, R.A. 2015, ApJ, submitted.
Burrows, C.J., Brown, R.A., & Sabatke, E.M. 2006, Aberrational delta magnitude, in Final report of an Instrument Concept Study for a Wide-Field Camera for TPF-C, ed. R.A. Brown, 133.
Endicott, J. et al. 2012, High Energy, Optical, and Infrared Detectors for Astronomy V, in Proc. SPIE 8453, ed. A.D. Holland and J.W. Beletic (Bellingham, WA: SPIE), 845304.
Glassman, T. et al. 2011, Creating Optimal Observing Schedules for a Starshade Planet-Finding Mission (Redondo Beach, CA: IEEE), 1724.
Hunyadi, S., Lo, A., & Shaklan, S. 2007, in Proc. SPIE 6693, ed. D. Coulter (San Diego, CA) 669303.
Kasdin, N.J. & Braems, I. 2006, ApJ, 646, 1260.
Kasdin, N.J. & Braems, I. 2008, ApJ, 672, 734.
Linder, D. 2007, TPF-O Design Reference Mission, in Proc. SPIE 6687, ed. H.A. MacEwen & J. Breckinridge, 668714.
Savransky, D., Kasdin, N.J., & Cady, E. 2010, PASP, 122, 401.

Section 6

Arenberg, J. et al. 2007, Techniques and Instrumentation for Detection of Exoplanets III, in Proc. SPIE 6693, ed. D.R. Coulter (Bellingham, WA: SPIE), 669302.

Cady, E. 2012, OpEx, 20, 15196.

Cash, W. 2006, Nature, 442, 51.

Copi, C.J. & G.D. Starkman 2000, ApJ, 532, 581.

Dubra, A. & Ferrari, J. 1999, AmJPh, 67, 87.

Glassman, T. et al. 2010, Space Telescopes and Instrumentation 2010: Optical, Infrared, and Millimeter Wave, in Proc. SPIE 7731, ed. J.M. Oschmann, Jr., M.C. Clampin, & H.A. MacEwen (Bellingham, WA: SPIE), 773150.

Kasdin, N.J. et al. 2011, Techniques and Instrumentation for Detection of Exoplanets V, in Proc. SPIE 8151, ed. S. Shaklan (Bellingham, WA: SPIE), 81510J.

Kasdin, N.J. et al. 2012, Space Telescopes and Instrumentation 2012: Optical, Infrared, and Millimeter Wave, in Proc. SPIE 8442, ed. M. Clampin, G. Fazio, H. MacEwen, & J. Oschmann (Bellingham, WA: SPIE), 88420A.

Palle, E. et al. 2003, JGRD, 108, 4710.

Regehr, M., & Shaklan, S. 2014, Reflection of Light from a Starshade, JPL internal memo.

Shaklan, S. et al. 2010, Space Telescopes and Instrumentation 2010: Optical, Infrared, and Millimeter Wave, in Proc. SPIE 7731, ed. J.M. Oschmann, Jr., M.C. Clampin, H.A. MacEwen (Bellingham, WA: SPIE), 77312G.

Shaklan, S. et al. 2011, Techniques and Instrumentation for Detection of Exoplanets V, in Proc. SPIE 8151, ed. S. Shaklan (Bellingham, WA: SPIE), 815113.

Vanderbei, R.J. et al. 2007, ApJ, 665, 794.

Section 7

Scharf, D. et al. 2010, IEEE Systems Journal, 4(1), 84, Parts 1 and 2.

Stahl, H.P. et al. 2013, OptEn, 52, 091805.

Section 8

(none)

Section 9

Cady, E. et al. 2009, Techniques and Instrumentation for Detection of Exoplanets IV, in Proc. SPIE 7440, ed. S.B. Shaklan (Bellingham, WA: SPIE), 744006.

Cash, W. 2011, ApJ, 738, 76.

Glassman, T. et al. 2013, Techniques and Instrumentation for Detection of Exoplanets VI, in Proc. SPIE 8864, ed. S.B. Shaklan (Bellingham, WA: SPIE), 886418.

Leviton, D. et al. 2007, UV/Optical/IR Space Telescopes: Innovative Technologies and Concepts III, in Proc. SPIE 6687, ed. H.A. MacEwen and J.B. Breckinridge (Bellingham, WA: SPIE), 66871B.

Martin, S.R. et al. 2013, Techniques and Instrumentation for Detection of Exoplanets VI, in Proc. SPIE 8864, ed. S.B. Shaklan (Bellingham, WA: SPIE), 88641A.

Samuele, R. et al. 2009. Starlight suppression from the starshade testbed at NGAS, in Proc. SPIE 7440, 744004.

Schindhelm E. et al. 2007, Techniques and Instrumentation for Detection of Exoplanets III, Proc. SPIE 6693, ed. D.R. Coulter (Bellingham, WA: SPIE), 669305.

Sirbu, D. et al. 2013, OpEx, 21, 32234.

11 ACRONYMS

A&A	Astronomy & Astrophysics Journal
ACS	Advanced Camera for Surveys
AFTA	Astrophysics Focused Telescope Asset
AJ	Astronomical Journal
ALMA	Atacama Large Millimeter/ submillimeter Array
ApJ	Astrophysical Journal
ApJS	Astrophysical Journal Supplement
ASMCS	Astrophysics Strategic Mission Concept Study
ATLO	assembly, test, and launch operations
AU	astronomical unit
BOE	basis of estimate
BOSS	Big Occulting Steerable Satellite
BRDF	bidirectional reflectance distribution function
BVR	blue, visual, red
C&DH	command and data handling
C/O	carbon to oxygen
CADRe	Cost Analysis Data Requirements
CANDELS	Cosmic Assembly Near-infrared Deep Extragalactic Legacy Survey
CAOM	Common Archive Observation Model
CAST	Control Analysis Simulation Testbed
CATE	Cost Appraisal and Technical Evaluation
CCD	charge coupled device
CDR	Critical Design Review
CG	center-of-gravity
CMM	coordinate measuring machine
CoRoT	COnvection ROtation et Transits
COTS	commercial, off-the-shelf
CPS	California Planet Survey
CR3BP	Circular Restricted 3 Body Problem
CTE	coefficient of thermal expansion
DC	direct current
DOF	degree of freedom
DRM	Design Reference Mission
DSMS	Deep Space Mission System
DSN	Deep Space Network
DTE	direct to Earth
E-ELT	European Extremely Large Telescope
EELV	evolved expendable launch vehicle
EGS	Extended Groth Strip
EKF	extended Kalman filter
ELT	Extremely Large Telescope
EM	electron-multiplying
EMC	electromagnetic compatibility
EMCCD	electron multiplying CCD
EMI	electromagnetic interference
EOL	end of life
ESA	European Space Agency
ESPA	EELV Secondary Payload Adapter
ESPRESSO	Echelle SPectrograph for Rocky Exoplanet and Stable Spectroscopic Observations
ExEP	Exoplanet Exploration Program
Exo-C	Exo-Coronagraph
Exo-S	Exo-Starshade
FBS	fine-bearing sensor
FEM	Finite Element Method
FF	formation flying
FGC	formation guidance channel
FGS	fine guidance sensor
FOV	field of view
FRR	Flight Readiness Review
FS	flight system
FSM	fast-steering mirror
FSW	flight software

FWHM	full width at half maximum
FY	fiscal year
GMT	Giant Magellan Telescope
GN&C	guidance, navigation, and control
GOODS-N	Great Observatories Origins Deep Survey—North
GOODS-S	Great Observatories Origins Deep Survey—South
GPI	Gemini Planet Imager
GRAIL	Gravity Recovery and Interior Laboratory
GSI	Global Science Institute
Gyr	gigayear
HGA	high-gain antenna
HIP	Hipparcos Catalog
HOSTS	Hunt for Observable Signatures of Terrestrial planetary Systems
HST	Hubble Space Telescope
HUDF	Hubble Ultra-Deep Field
HZ	habitable zone
I&T	integration and test
IDS	inner disk structure
IFS	integral field spectrometer
IFU	integral field unit
IR	infrared
ISS	International Space Station
IWA	inner working angle
JPL	Jet Propulsion Laboratory
JWST	James Webb Space Telescope
KDP	Key Decision Point
L	stellar luminosity
LBTI	Large Binocular Telescope Interferometer
LCROSS	Lunar Crater Observation and Sensing Satellite
LED	light-emitting diode
LEO	low Earth orbit
limΔmag	planet contrast at the threshold of detectability
LRR	Launch Readiness Review
LV	launch vehicle
MAST	Mikulski Archive for Space Telescopes
MCR	Mission Concept Review
MDR	Mission Definition Review
MER	Mars Exploration Rover
MIT	Massachusetts Institute of Technology
MLA	microlens array
MNRAS	Monthly Notices of the Royal Astronomical Society
MOC	Mission Operations Center
MPC	model predictive control
MRR	Mission Readiness Review
MSL	Mars Science Laboratory
NASA	National Aeronautics and Space Administration
NGAS	Northrop Grumman Aerospace Systems
NGC	Northrop Grumman Corporation
NICM	NASA Instrument Cost Model
NICMOS	Near Infrared Camera and Multi-Object Spectrometer
NIR	near-infrared
NIRCam	Near Infrared Camera
NPR	NASA Procedural Requirements
NRC	National Research Council
NRO	National Reconnaissance Office
NSV	New Catalogue of Suspected Variable Stars
NuSTAR	Nuclear Spectroscopic Telescope Array
NUV	near ultraviolet
O^3	Occulting Ozone Observatory
OPALS	Optical PAyload for Lasercomm Science
OpEx	Optics Express
ORR	Operational Readiness Review
OS	optical shield
Osiris Rex	Origins Spectral Interpretation Resource Identification Security Regolith Explorer
OWA	outer working angle

PASP	Publications of the Astronomical Society of the Pacific
PDR	Preliminary Design Review
PLAR	Post Launch Assessment Review
PLATO	PLAnetary Transits and Oscillations of stars
POSS	Palomar Observatory Sky Survey
PRISMA	Hyperspectral Precursor and Application Mission
PROBA	PRoject for OnBoard Autonomy
PSF	point spread function
QE	quantum efficiency
R	reflectivity
R	spectral resolution
RCS	reaction control subsystem
RF	radio frequency
RoC	radius of curvature
ROSES	Research Opportunities in Space and Earth Sciences
RV	radial velocity
S/C	spacecraft
S/N	signal to noise
SA	solar array
SCExAO	Subaru Coronagraphic Extreme Adaptive Optics
SDC	Science Data Center
SDR	software-defined radio
SDT	starshade deployment testbed
SEP	solar electric propulsion
SKM	station keeping maneuvers
SMSR	Safety and Mission Success Review
SNR	signal-to-noise ratio
SOC	Science Operations Center
SPHERE	Spectro-Polarimetric High-contrast Exoplanet Research
SPIE	The International Society for Optics and Photonics
SRP	Starshade Ready Package
SRR	System Requirements Review
SSCM10	Small Satellite Cost Model 2010
STDT	Science and Technology Definition Team
STIS	Space Telescope Imaging Spectrograph
STSci	Space Telescope Science Institute
TCMs	Trajectory Correction Maneuvers
TD	time delay
TDEM	Technology Development for Exoplanet Missions
TESS	Transiting Exoplanet Survey Satellite
THEIA	Telescope for Habitable Exoplanets and Interstellar/ Intergalactic Astronomy
TMT	Thirty Meter Telescope
TOF	time of flight
TPF-I	Terrestrial Planet Finder Interferometer
TRL	Technology Readiness Level
TRR	Test Readiness Review
TTS	time-transfer system
UDS	Ultra Deep Survey
UHF	ultra high frequency
UKST	UK Schmidt Telescope
UMBRAS	Umbral Missions Blocking Radiating Astronomical Sources
UV	ultraviolet
VLP	Virtual Planet Laboratory
VLT	Very Large Telescope
WBS	Work Breakdown Structure
WDS	Washington Double Star (catalog)
WFC3	Wide Field Camera 3
WFIRST	Wide-Field Infrared Survey Telescope
WFP3	Wide Field Camera 3
WFPC2	Wide-Field Planetary Camera 2
WISE	Wide-field Infrared Survey Explorer
XDF	eXtreme Deep Field
XIPS-25	Xenon Ion Propulsion System (25 cm)

Appendices

A TARGET STAR LISTS

A.1 Target Star Lists for DRM Inputs

Table A.1-1. Binary/multiple systems excluded from the Exo-S input list.

HIP	Common	Sep(“)	dM (mag)	d (pc)	Spec Type
12706	gam Ceti	2.3	2.6	24.4	A2V+F4V
35550	del Gam	5.6	4.6	18.5	F2VkF0mF0
36850	Castor	5.0	1.0	15.6	A1V+A2V
42913	d Vel	0.4	3.6	24.7	A1Va(n)+
44248	10 UMa	0.5	2.3	16.0	F5IV-V
46651	psi Vel	0.9	1.2	18.8	F3V
55642	iota Leo	2.1	2.7	23.6	F5IV
61941	gam Vir	1.9	0.1	11.6	F2V
65447	__	1	3.9	25.0	A6Vn
71681	a Cen B	5	1.1	1.3	K2V
71683	a Cen A	5	1.1	1.3	G2V
81693	zeta Her	1.3	2.5	10.7	F9IV
84379	delta Her	0.1	1.3	23.0	A1IV
86032	a Oph	0.6	2.9	14.9	A5III
89937	chi Dra	0.1	2.1	8.1	F7Vvar
104887	tau Cyg	0.9	2.7	20.3	F2V+

Table A.1-2. Case 1 input target star list.

	HIP	Common	Spectra Type	dpc	V	RAICRS	DEICRS	Completeness
Earth Candidates	1599	-	G0V	8.59	4.2	5.007976	-64.8776	0.39
	3821	eta Cassiopei A	G3V	5.94	3.5	12.27125	57.81655	0.49
	8102	tau Ceti	G8.5V	3.65	3.5	26.02136	-15.9396	0.49
	12777	-	F7V	11.1	4.1	41.0487	49.22867	0.28
	14632	-	G0V	10.5	4.1	47.26201	49.6135	0.30
	15510	82 Eridani	G8.0V	6.04	4.3	49.97177	-43.0715	0.41
	19849	omicron 2 Eridani	K0.5V	4.98	4.4	63.82349	-7.64456	0.37
	22449	1 Ori	F6V	8.07	3.2	72.45891	6.961247	0.28
	27072	-	F7V	8.93	3.6	86.11656	-22.4475	0.33
	61317	beta CVn	G0V	8.44	4.2	188.4379	41.35677	0.39
	64394	-	G0V	9.13	4.2	197.9705	27.87604	0.39
	72659	ksi Bootis A	G7.0V	6.78	4.7	222.847	19.10063	0.44
	86974	-	G5IV	8.31	3.4	266.6155	27.7225	0.31
	88601	70 Ophiuchi A	K0V	5.1	4	271.3634	2.502439	0.46
	96100	sigma Draconis	G9.0V	5.75	4.7	293.0858	69.6654	0.43
	99240	delta Pavonis	G8.0IV	6.11	3.5	302.1744	-66.1793	0.49
	105858	-	F7V	9.26	4.2	321.6104	-65.3681	0.39
	108870	epsilon Indi A	K4V	3.62	4.7	330.8227	-56.7798	0.38
	5336	-	G5Vp	7.55	5.2	17.05384	54.92423	0.27
	7981	-	K1V	7.53	5.2	25.62479	20.27015	0.28
	15457	-	G5V	9.14	4.8	49.83975	3.369971	0.37
	17378	-	K0IV	9.04	3.5	55.81232	-9.7652	0.24
	57443	-	G3/5V	9.22	4.9	176.6344	-40.5013	0.36
	64924	-	G5V	8.56	4.7	199.6041	-18.3086	0.41
	73184	-	K4.0V	5.86	5.7	224.364	-21.4113	0.29
	78072	-	F6V	11.3	3.9	239.1125	15.66473	0.22
	99461	-	K2.5V	6.01	5.3	302.7984	-36.0974	0.26
	104214	61 Cygni A	K5.0V	3.5	5.2	316.7118	38.74149	0.43
	104217	61 Cygni B	K7.0V	3.5	5.9	316.7175	38.73441	0.36
Sub-Neptune Candidates	2021	beta Hyi	G1IV	7.46	2.8	6.413342	-77.255	0.44
	3093	-	K0V	11.1	5.9	9.842061	21.25137	0.28
	3765	-	K1V	7.45	5.7	12.09389	5.283389	0.44
	7751	-	K0/4	7.82	5.7	24.94685	-56.1964	0.43
	8362	-	K0V	10.1	5.6	26.9336	63.8531	0.31
	10138	-	K1V	10.8	6.1	32.60001	-50.8253	0.29
	10644	-	G0V	10.8	4.9	34.26007	34.22483	0.29
	12114	-	K3V	7.18	5.8	39.01597	6.883364	0.45
	13402	-	K1V	10.4	6	43.13288	-12.7693	0.30
	29271	-	G6V	10.2	5.1	92.55918	-74.7525	0.30
	32349	Sirius A	A1.0V	2.63	-1	101.2885	-16.7131	0.51
	37279	Procyon A	F5IV-V	3.51	0.4	114.8272	5.227508	0.51
	47080	-	G8IV-V	11.4	5.4	143.9168	35.81077	0.26
	56452	-	K0V	9.56	6	173.6248	-32.8333	0.34
	56997	-	G8Vvar	9.61	5.3	175.2626	34.20256	0.34
	57632	-	A3Vvar	11	2.1	177.2662	14.57234	0.28
	57757	-	F9V	10.9	3.6	177.672	1.765377	0.28
	67927	-	G0IV	11.4	2.7	208.6713	18.39859	0.26
	72848	-	K2V	11.5	6	223.3502	19.15227	0.25
	81300	-	K1V	9.75	5.8	249.0883	-2.32384	0.33
	84720	-	M0V	8.8	5.5	259.7623	-46.6365	0.37
	91262	Vega	A0Vvar	7.68	0	279.2341	38.78299	0.43
	97649	Altair	A7IV-V	5.12	0.8	297.6945	8.867385	0.49
	113368	Fomalhaut	A3V	7.7	1.2	344.4118	-29.6218	0.43

Table A.1-2. Case 1 input target star list.

	HIP	Common	Spectra Type	dpc	V	RAICRS	DEICRS	Completeness
	114622	-	K3.0V	6.54	5.6	348.3114	57.16764	0.47
Jupiter Candidates	746	-	F2III-IV	16.8	2.3	2.29204	59.15022	0.36
	910	-	F5V	18.7	4.9	2.816284	-15.4673	0.33
	950	-	F3/5V	21.3	5.2	2.932867	-35.1334	0.28
	3583	-	G1V	15.2	5.8	11.43931	-47.5522	0.40
	3909	-	F7V	15.8	5.2	12.53218	-10.6438	0.39
	4151	-	F8V	18.7	4.8	13.26783	61.12356	0.33
	5862	-	G0V	15.1	5	18.79403	-45.5321	0.40
	7918	-	G2V	12.7	5	25.44382	42.61381	0.47
	8497	-	F0V	23.2	4.7	27.39663	-10.6862	0.25
	8796	-	F6IV	19.4	3.4	28.27042	29.5794	0.31
	8903	-	A5V...	18	2.6	28.65979	20.8083	0.34
	9007	-	G8IIIBCNIV	17.9	3.7	28.9868	-51.6096	0.34
	9236	-	F0V	22	2.9	29.69113	-61.5699	0.27
	9884	alf Arietis	K2III	20.2	2	31.79286	23.46278	0.30
	12444	-	F7V	21.8	5.8	40.0521	-9.45268	0.28
	12653	-	G0V	17.2	5.4	40.63816	-50.8008	0.35
	12843	-	F5/6V	14.2	4.5	41.27492	-18.5727	0.42
	14879	-	F8V	14.2	3.8	48.01783	-28.9891	0.42
	14954	-	G0V	22.6	5.1	48.19302	-1.19593	0.26
	15330	-	G3/5V	12	5.5	49.43529	-62.5769	0.49
	15371	-	G2V	12	5.2	49.5464	-62.5079	0.49
	16245	-	F3IV/V	21.7	4.7	52.34244	-62.9384	0.28
	16852	-	F8V	14	4.3	54.21883	0.402833	0.42
	17651	-	F3/5V	17.6	4.2	56.71245	-23.2484	0.35
	18859	-	F7/8V	18.8	5.4	60.65274	-0.26831	0.33
	19076	-	G5V	16.9	5.9	61.33396	22.00922	0.35
	19335	-	F7V	21	5.5	62.15206	38.04023	0.29
	19893	-	F0V	20.5	4.2	64.00621	-51.4871	0.29
	19921	-	K1/2III	18.2	4.4	64.12118	-59.3017	0.34
	21770	-	F1V	20.2	4.4	70.14093	-41.8636	0.30
	22263	-	G3V	13.3	5.5	71.90088	-16.9349	0.45
	23693	-	F6/7V	11.6	4.7	76.37788	-57.473	0.50
	24813	-	G0V	12.6	4.7	79.78366	40.10067	0.47
	25110	-	F6V	20.9	5.1	80.64074	79.23076	0.29
	25278	-	F8VSB	14.4	5	81.10546	17.38355	0.42
	27288	-	A2VANN	21.6	3.6	86.73896	-14.8219	0.28
	27321	-	A5V	19.4	3.9	86.82118	-51.0667	0.31
	28103	-	F1V	14.9	3.7	89.10133	-14.168	0.41
	29650	-	F6V	20.8	5.2	93.71223	19.15689	0.29
	29800	-	F5IV-V	19.2	5	94.11071	12.27171	0.32
	29860	-	G0.5Vb	19.2	5.7	94.3177	5.099696	0.32
	32362	-	F5IV	18	3.3	101.3226	12.89606	0.34
	32439	-	F8V	17.9	5.4	101.5603	79.56628	0.34
	32480	-	G0V	16.7	5.2	101.6847	43.57702	0.36
	33277	-	G0V	17.2	5.7	103.8279	25.37564	0.35
	34065	-	G3V	16.5	5.6	105.9892	-43.609	0.36
	34834	-	F0IV	21.4	4.5	108.1406	-46.7596	0.28
	35136	-	G0V	16.9	5.5	108.9588	47.24042	0.36
	35550	-	F0IV...	18.5	3.5	110.0308	21.98234	0.33
	36366	-	F0V...	18	4.2	112.2775	31.78408	0.34
	36439	-	F6V	20.2	5.4	112.4827	49.67266	0.30
	38908	-	G0V	16.2	5.6	119.4429	-60.3034	0.38

Table A.1-2. Case 1 input target star list.

	HIP	Common	Spectra Type	dpc	V	RAICRS	DEICRS	Completeness
	39757	-	F2MF5IIP	19.5	2.8	121.8863	-24.3044	0.30
	39780	-	G2IV	23.3	5.3	121.941	21.58198	0.25
	39903	-	F5V	20	4.7	122.2536	-61.3017	0.30
	40035	-	F7V	22.4	5.5	122.6666	-13.7993	0.26
	40702	-	F5V	19.6	4	124.6303	-76.92	0.30
	40843	-	F6V	18.3	5.1	125.0161	27.21862	0.34
	42438	-	G1.5Vb	14.4	5.6	129.7989	65.02069	0.42
	44075	-	F7/8IV/V	21	5.8	134.6824	-16.1332	0.29
	44127	-	A7IV	14.5	3.1	134.8035	48.04235	0.42
	45333	-	F9V	19.6	5.2	138.5856	61.4234	0.30
	46509	-	F5V	17.3	4.6	142.2868	-2.76896	0.35
	46853	-	F6IV	13.5	3.2	143.218	51.6786	0.43
	47592	-	G0V	15	4.9	145.5611	-23.9162	0.41
	48113	-	G2V	18.4	5.1	147.1466	46.02123	0.33
	49081	-	G1V	15	5.4	150.2543	31.92471	0.41
	50384	-	F8Vw	22.8	5.8	154.3117	23.10646	0.25
	50564	-	F6IV	21.4	4.8	154.9346	19.47144	0.28
	50954	-	F2/3IV/V	16.2	4	156.0989	-74.0315	0.38
	51459	-	F8V	12.8	4.8	157.6574	55.98062	0.47
	51502	-	F2V	21.5	5.3	157.7709	82.55854	0.28
	51523	-	F5V	21.8	4.9	157.8426	-53.716	0.28
	54872	-	A4V	17.9	2.6	168.5267	20.52403	0.34
	58576	-	G8IV	12.8	5.5	180.1849	-10.4448	0.47
	59072	-	F0IV	19.8	4.1	181.7202	-64.6136	0.30
	59199	-	F0IV/V	14.9	4	182.1031	-24.7288	0.41
	61174	-	F2V	18.3	4.3	188.0187	-16.1959	0.34
	64408	-	G3V	20.7	4.8	198.0144	-37.8031	0.29
	64583	-	F5V	18.2	4.9	198.5643	-59.1029	0.34
	64792	-	G0Vs	17.6	5.2	199.1946	9.423693	0.35
	65109	-	A2V	18	2.7	200.1503	-36.7121	0.34
	65721	-	G5V	18	5	202.1081	13.78019	0.34
	66249	-	A0/1IV	22.7	3.4	203.674	-0.59594	0.26
	67153	-	F3V	19.4	4.2	206.4232	-33.0434	0.31
	67275	-	F7V	15.6	4.5	206.8168	17.45677	0.39
	68933	-	K0IIIB	18	2.1	211.6722	-36.3687	0.34
	69701	-	F6III	22.2	4.1	214.0037	-5.99953	0.27
	69965	-	F7(W)F3V	18	5.9	214.7547	-25.8163	0.34
	70497	-	F7V	14.5	4	216.3001	51.85171	0.41
	71284	-	F3Vwvar	15.8	4.5	218.6695	29.74481	0.39
	71908	-	APSREU(CR)	16.6	3.2	220.6279	-64.9746	0.36
	71957	-	F2V	18.3	3.9	220.7648	-5.65743	0.34
	72567	-	G2V	18.2	5.9	222.5655	23.91177	0.34
	72603	-	F3V	23	5.1	222.6719	-15.9971	0.25
	72622	-	A3III/V	23.2	2.8	222.7199	-16.0416	0.25
	73996	-	F5V	19.6	4.9	226.8248	24.86959	0.30
	75181	-	G3/5V	14.8	5.7	230.4566	-48.317	0.41
	76267	-	A0V	23	2.2	233.6716	26.71491	0.25
	76829	-	F3/5V	17.4	4.6	235.298	-44.6606	0.35
	77052	-	G3V	14.7	5.9	236.0077	2.515525	0.41
	77070	-	K2III	22.7	2.6	236.0666	6.42552	0.26
	77257	-	G0Vvar	12.1	4.4	236.6114	7.35324	0.49
	77622	-	Am(kA2hA5mA7V)	21.6	3.7	237.7037	4.47758	0.28
	77760	-	F9V	15.9	4.6	238.1675	42.44999	0.39

Table A.1-2. Case 1 input target star list.

	HIP	Common	Spectra Type	dpc	V	RAICRS	DEICRS	Completeness
	77952	-	F0III/IV	12.4	2.8	238.7867	-63.4297	0.48
	78459	-	G2V	17.2	5.4	240.2617	33.30539	0.35
	78527	-	F8IV-V	21	4	240.4738	58.56444	0.29
	79607	-	F8V	21.1	5.6	243.671	33.85882	0.29
	79672	-	G5V	13.9	5.5	243.9047	-8.36824	0.42
	80686	-	G0V	12.1	4.9	247.1158	-70.0847	0.49
	82396	-	K2IIIB	19.5	2.3	252.5427	-34.2926	0.30
	84143	-	F2V	22.5	3.3	258.0382	-43.2385	0.26
	84862	-	G0V	14.3	5.4	260.1645	32.47027	0.42
	86486	-	F2V	21.5	4.8	265.0989	-49.4152	0.28
	89042	-	G1V	17.6	5.5	272.6094	-62.0028	0.35
	89962	-	K0III-IV	18.5	3.2	275.3288	-2.89712	0.33
	92043	-	F6V	19.2	4.2	281.4155	20.54712	0.32
	95447	-	G8IVvar	15.2	5.2	291.2407	11.94285	0.40
	95501	-	F2IV	15.5	3.4	291.374	3.114579	0.40
	96441	-	F4V	18.3	4.5	294.1106	50.22046	0.34
	96895	-	G2V	21.1	5.9	295.4545	50.52545	0.29
	97295	-	F5	21.2	5	296.6066	33.72869	0.28
	97675	-	F8V	19.2	5.1	297.7563	10.41605	0.32
	98036	-	G8IVvar	13.7	3.7	298.8282	6.407933	0.43
	98470	-	F7V	21.2	5.7	300.084	-33.7027	0.28
	98819	-	G1V	17.8	5.8	301.0269	17.07116	0.34
	100017	-	G3V	17.6	5.9	304.3776	66.85297	0.35
	102422	-	K0IV	14.3	3.4	311.322	61.83679	0.42
	102485	-	F5V	14.7	4.1	311.524	-25.2705	0.41
	102488	-	K0III	22.3	2.5	311.5518	33.96945	0.27
	103389	-	F7V	22	5.7	314.197	-26.2962	0.27
	105199	-	A7IV-V	15	2.4	319.6441	62.58546	0.41
	107089	-	K0III	21.2	3.7	325.3686	-77.3895	0.28
	107556	-	A5mF2 (IV)	11.9	2.8	326.7595	-16.1266	0.49
	107649	-	G0V	16	5.6	327.065	-47.3029	0.38
	109176	-	F5V	11.7	3.8	331.752	25.34505	0.50
	109422	-	F6V	18.3	4.9	332.5353	-32.5484	0.34
	110649	-	G3IV	20.6	5.3	336.2341	-57.7966	0.29
	111449	-	F7V	22.7	5.2	338.6729	-20.7079	0.26
	112447	-	F7V	16.3	4.2	341.6727	12.17408	0.37
	113357	-	G5V	15.6	5.5	344.366	20.76868	0.39
	114924	-	F7V	20.5	5.6	349.1758	53.21405	0.29
	114948	-	F8V	20.5	5.6	349.2395	-62.0011	0.29
	114996	-	F3IV/V	23.1	4	349.3576	-58.2359	0.25
	116771	-	F7V	13.7	4.1	354.9868	5.627354	0.43
Known Giant Planets	7513	-	F8V	13.5	4.1	24.1999	41.40638	
	7978	-	F8V	17.4	5.5	25.62146	-53.7406	
	10626	-		44.2	7.6	34.2	43.773	
	16537	epsilon Eridani	K2.0V	3.21	3.7	53.23509	-9.45831	
	22336	-	G5V	26.4	5.8	72.15084	-5.67344	
	22627	-	M4	12.3	12	73.02351	6.477293	
	24205	-	G1/2V	28.4	7	77.9431	4.403873	
	26394	-	G1V	18.3	5.7	84.28664	-80.4717	
	27253	-		39.3	6	86.64	1.169	
	31592	-	K1III(+M)	19.8	4	99.17083	-19.2557	
	33212	-	F8	29.9	6.8	103.6785	24.24579	
	37826	Pollux	K0IIIvar	10.4	1.2	116.3307	28.02631	

Table A.1-2. Case 1 input target star list.

	HIP	Common	Spectra Type	dpc	V	RAICRS	DEICRS	Completeness
	40952	-	G8/K1(III+F/G)	28.1	7.2	125.3679	-39.706	
	49699	-	K0	18.2	7.6	152.1799	34.24241	
	50473	-		32.4	7	154.59	12.621	
	53721	-	G0V	14.1	5	164.8676	40.43012	
	65808	-		33.1	7.3	202.33	-35.57	
	71395	-	K0	16.5	7.5	219.0018	9.747125	
	74500	-	G5V	26.2	6.5	228.3705	-25.3092	
	79242	-		34.3	7.7	242.56	-84.232	
	79248	-	K0V	17.6	6.6	242.6009	43.81837	
	80337	-	G3/5V	12.8	5.4	246.0051	-39.193	
	83043	-	M2	10.3	9.7	254.5372	25.74539	
	83389	-	G8V	18.6	6.8	255.6512	47.0798	
	85647	-	M0	16.5	9.6	262.5477	-51.6365	
	86796	-	G3IV/V	15.5	5.1	266.0363	-51.8336	
	90485	-		36.6	5.9	276.96	-26.817	
	95467	-	K2IV/V	26.8	8.4	291.2913	-66.4694	
	96901	-	G5V	21.2	6.2	295.4671	50.51792	
	98767	-	G6IV+...	15.9	5.7	300.9039	29.89808	
	99825	-	K3V	8.91	5.7	303.8191	-27.0325	
	106440	-	M1.5V	4.95	8.7	323.3917	-49.007	
	109388	-	M3	9.1	10	332.4153	-4.64068	
	113137	-	G2/3IV	26.7	6	343.6648	-70.0739	
	113421	-	G8IV/V	19.9	6.2	344.5648	-2.39535	
	116616	-		49.1	7.1	354.49	48.997	
	116727	-	K1IV	14.1	3.2	354.8374	77.63197	

Table A.1-3. Case 2 input target star list.

	HIP	Common	Spectra Type	dpc	V	RAICRS	DEICRS
Super Six	2021	beta Hyi	G1IV	7.46	2.8	6.4133	-77.26
	8102	tau Ceti	G8.5V	3.65	3.5	26.021	-15.94
	17378	-	K0IV	9.04	3.5	55.812	-9.765
	22449	1 Ori	F6V	8.07	3.2	72.459	6.9612
	27072	-	F7V	8.93	3.6	86.117	-22.45
	99240	delta Pavonis	G8.0IV	6.11	3.5	302.17	-66.18
Priority 1	746	-	F2III-IV	16.8	2.3	2.292	59.15
	3821	eta Cassiopei A	G3V	5.94	3.5	12.271	57.817
	14879	-	F8V	14.2	3.8	48.018	-28.99
	28103	-	F1V	14.9	3.7	89.101	-14.17
	32349	Sirius A	A1.0V	2.63	-1.4	101.29	-16.71
	37279	Procyon A	F5IV-V	3.51	0.4	114.83	5.2275
	44127	-	A7IV	14.5	3.1	134.8	48.042
	46853	-	F6IV	13.5	3.2	143.22	51.679
	50954	-	F2/3IV/V	16.2	4	156.1	-74.03
	57632	-	A3Vvar	11	2.1	177.27	14.572
	57757	-	F9V	10.9	3.6	177.67	1.7654
	67927	-	G0IV	11.4	2.7	208.67	18.399
	71908	-	APSREU(CR)	16.6	3.2	220.63	-64.97
	77952	-	F0III/IV	12.4	2.8	238.79	-63.43
	78072	-	F6V	11.3	3.9	239.11	15.665
	86974	-	G5IV	8.31	3.4	266.62	27.722
	91262	Vega	A0Vvar	7.68	0	279.23	38.783
	95501	-	F2IV	15.5	3.4	291.37	3.1146
	97649	Altair	A7IV-V	5.12	0.8	297.69	8.8674
	98036	-	G8IVvar	13.7	3.7	298.83	6.4079
	102422	-	K0IV	14.3	3.4	311.32	61.837
	105199	-	A7IV-V	15	2.4	319.64	62.585
	107556	-	A5mF2 (IV)	11.9	2.8	326.76	-16.13
	109176	-	F5V	11.7	3.8	331.75	25.345
	113368	Fomalhaut	A3V	7.7	1.2	344.41	-29.62
Priority 2	2072	-	A6VN	23.8	3.9	6.5505	-43.68
	8796	-	F6IV	19.4	3.4	28.27	29.579
	8903	-	A5V...	18	2.6	28.66	20.808
	9007	-	G8IIIBCNIV	17.9	3.7	28.987	-51.61
	9236	-	F0V	22	2.9	29.691	-61.57
	9884	alf Arietis	K2III	20.2	2	31.793	23.463
	27288	-	A2VANN	21.6	3.6	86.739	-14.82
	27321	-	A5V	19.4	3.9	86.821	-51.07
	32362	-	F5IV	18	3.3	101.32	12.896
	39757	-	F2MF5IIP	19.5	2.8	121.89	-24.3
	46733	-	F0IV	23.8	3.6	142.88	63.062
	53910	-	A1V	24.4	2.3	165.46	56.382
	54872	-	A4V	17.9	2.6	168.53	20.524
	59774	-	A3Vvar	24.7	3.3	183.86	57.033
	65109	-	A2V	18	2.7	200.15	-36.71
	66249	-	A0/1IV	22.7	3.4	203.67	-0.596
	68933	-	K0IIIB	18	2.1	211.67	-36.37
	71957	-	F2V	18.3	3.9	220.76	-5.657
	72622	-	A3III/V	23.2	2.8	222.72	-16.04
	76267	-	A0V	23	2.2	233.67	26.715
	77070	-	K2III	22.7	2.6	236.07	6.4255
	77622	-	Am(kA2hA5mA7V)	21.6	3.7	237.7	4.4776

Table A.1-3. Case 2 input target star list.

	HIP	Common	Spectra Type	dpc	V	RAICRS	DEICRS
	78527	-	F8IV-V	21	4	240.47	58.564
	82396	-	K2IIIB	19.5	2.3	252.54	-34.29
	84143	-	F2V	22.5	3.3	258.04	-43.24
	86742	-	K2III	25.1	2.7	265.87	4.5669
	89962	-	K0III-IV	18.5	3.2	275.33	-2.897
	90496	-	K1IIIB	24	2.8	276.99	-25.42
	93747	-	A0Vn	25.5	3	286.35	13.864
	102488	-	K0III	22.3	2.5	311.55	33.969
	107089	-	K0III	21.2	3.7	325.37	-77.39
	114996	-	F3IV/V	23.1	4	349.36	-58.24
Known Gas Giants	7513	-	F8V	13.5	4.1	24.2	41.406
	7978	-	F8V	17.4	5.5	25.621	-53.74
	10626	-		44.2	7.6	34.2	43.773
	16537	epsilon Eridani	K2.0V	3.21	3.7	53.235	-9.458
	22336	-	G5V	26.4	5.8	72.151	-5.673
	22627	-	M4	12.3	12	73.024	6.4773
	24205	-	G1/2V	28.4	7	77.943	4.4039
	26394	-	G1V	18.3	5.7	84.287	-80.47
	27253	-		39.3	6	86.64	1.169
	37826	Pollux	K0IIIvar	10.4	1.2	116.33	28.026
	40952	-	G8/K1(III+F/G)	28.1	7.2	125.37	-39.71
	49699	-	K0	18.2	7.6	152.18	34.242
	50473	-		32.4	7	154.59	12.621
	53721	-	G0V	14.1	5	164.87	40.43
	65808	-		33.1	7.3	202.33	-35.57
	71395	-	K0	16.5	7.5	219	9.7471
	74500	-	G5V	26.2	6.5	228.37	-25.31
	79242	-		34.3	7.7	242.56	-84.23
	79248	-	K0V	17.6	6.6	242.6	43.818
	80337	-	G3/5V	12.8	5.4	246.01	-39.19
	83043	-	M2	10.3	9.7	254.54	25.745
	83389	-	G8V	18.6	6.8	255.65	47.08
	85647	-	M0	16.5	9.6	262.55	-51.64
	86796	-	G3IV/V	15.5	5.1	266.04	-51.83
	90485	-		36.6	5.9	276.96	-26.82
	95467	-	K2IV/V	26.8	8.4	291.29	-66.47
	96901	-	G5V	21.2	6.2	295.47	50.518
	98767	-	G6IV+...	15.9	5.7	300.9	29.898
	99825	-	K3V	8.91	5.7	303.82	-27.03
	106440	-	M1.5V	4.95	8.7	323.39	-49.01
	109388	-	M3	9.1	10	332.42	-4.641
	113137	-	G2/3IV	26.7	6	343.66	-70.07
	113421	-	G8IV/V	19.9	6.2	344.56	-2.395
	116616	-		49.1	7.1	354.49	48.997
	116727	-	K1IV	14.1	3.2	354.84	77.632
	31592	-	K1III(+M)	19.8	4	99.171	-19.26

Table A.1-4. Case 3 input target star list.

	HIP	Common	Spectra Type	dpc	V	RAICRS	DEICRS	Completeness
Earth Candidates	1599	-	G0V	8.59	4.23	5.008	-64.88	0.40
	3821	eta Cassiopei A	G3V	5.94	3.45	12.271	57.817	0.49
	8102	tau Ceti	G8.5V	3.65	3.49	26.021	-15.94	0.49
	12777	-	F7V	11.1	4.1	41.049	49.229	0.29
	14632	-	G0V	10.5	4.05	47.262	49.614	0.31
	15510	82 Eridani	G8.0V	6.04	4.26	49.972	-43.07	0.42
	19849	omicron 2 Eridani	K0.5V	4.98	4.43	63.823	-7.645	0.39
	22449	1 Ori	F6V	8.07	3.17	72.459	6.9612	0.29
	27072	-	F7V	8.93	3.59	86.117	-22.45	0.33
	61317	beta CVn	G0V	8.44	4.24	188.44	41.357	0.40
	64394	-	G0V	9.13	4.24	197.97	27.876	0.40
	64924	-	G5V	8.56	4.74	199.6	-18.31	0.43
	72659	ksi Bootis A	G7.0V	6.78	4.67	222.85	19.101	0.45
	86974	-	G5IV	8.31	3.41	266.62	27.722	0.31
	88601	70 Ophiuchi A	K0V	5.1	4.03	271.36	2.5024	0.46
	96100	sigma Draconis	G9.0V	5.75	4.67	293.09	69.665	0.44
	99240	delta Pavonis	G8.0IV	6.11	3.53	302.17	-66.18	0.49
	104214	61 Cygni A	K5.0V	3.5	5.2	316.71	38.741	0.45
	105858	-	F7V	9.26	4.22	321.61	-65.37	0.40
	108870	epsilon Indi A	K4V	3.62	4.69	330.82	-56.78	0.39
	5336	-	G5Vp	7.55	5.17	17.054	54.924	0.30
	5862	-	G0V	15.1	4.96	18.794	-45.53	0.27
	7918	-	G2V	12.7	4.96	25.444	42.614	0.35
	7981	-	K1V	7.53	5.24	25.625	20.27	0.31
	10644	-	G0V	10.8	4.86	34.26	34.225	0.40
	12843	-	F5/6V	14.2	4.47	41.275	-18.57	0.26
	15371	-	G2V	12	5.24	49.546	-62.51	0.26
	15457	-	G5V	9.14	4.84	49.84	3.37	0.40
	17378	-	K0IV	9.04	3.52	55.812	-9.765	0.24
	23693	-	F6/7V	11.6	4.71	76.378	-57.47	0.42
	24813	-	G0V	12.6	4.69	79.784	40.101	0.37
	25278	-	F8VSB	14.4	5	81.105	17.384	0.29
	29271	-	G6V	10.2	5.08	92.559	-74.75	0.33
	47592	-	G0V	15	4.92	145.56	-23.92	0.28
	51459	-	F8V	12.8	4.82	157.66	55.981	0.38
	56997	-	G8Vvar	9.61	5.31	175.26	34.203	0.25
	57443	-	G3/5V	9.22	4.89	176.63	-40.5	0.39
	73184	-	K4.0V	5.86	5.72	224.36	-21.41	0.32
	77257	-	G0Vvar	12.1	4.41	236.61	7.3532	0.35
	78072	-	F6V	11.3	3.85	239.11	15.665	0.23
	80686	-	G0V	12.1	4.9	247.12	-70.08	0.37
	95447	-	G8IVvar	15.2	5.16	291.24	11.943	0.26
	99461	-	K2.5V	6.01	5.32	302.8	-36.1	0.29
	104217	61 Cygni B	K7.0V	3.5	5.95	316.72	38.734	0.40
	105090	AX Microscopii	K9.0V	3.95	6.69	319.32	-38.86	0.25
	114622	-	K3.0V	6.54	5.57	348.31	57.168	0.26
Sub-Neptune Candidates	2021	beta Hyi	G1IV	7.46	2.82	6.4133	-77.26	0.45
	3093	-	K0V	11.1	5.88	9.8421	21.251	0.29
	3765	-	K1V	7.45	5.74	12.094	5.2834	0.45
	7751	-	K0/4	7.82	5.68	24.947	-56.2	0.43
	8362	-	K0V	10.1	5.63	26.934	63.853	0.33
	10138	-	K1V	10.8	6.12	32.6	-50.83	0.29
	12114	-	K3V	7.18	5.82	39.016	6.8834	0.45

Table A.1-4. Case 3 input target star list.

	HIP	Common	Spectra Type	dpc	V	RAICRS	DEICRS	Completeness
	13402	-	K1V	10.4	6.05	43.133	-12.77	0.30
	23311	-	K4III	8.71	6.23	75.203	-5.751	0.39
	32349	Sirius A	A1.0V	2.63	-1.44	101.29	-16.71	0.51
	32984	-	K3V	8.71	6.58	103.08	-5.174	0.39
	37279	Procyon A	F5IV-V	3.51	0.4	114.83	5.2275	0.51
	42808	-	K2V	11.1	6.58	130.83	-38.88	0.28
	47080	-	G8IV-V	11.4	5.39	143.92	35.811	0.27
	49908	-	K7.0V	4.87	6.6	152.85	49.455	0.49
	54035	Lalande 21185	M2.0V	2.54	7.49	165.84	35.981	0.51
	56452	-	K0V	9.56	5.96	173.62	-32.83	0.35
	57632	-	A3Vvar	11	2.14	177.27	14.572	0.29
	57757	-	F9V	10.9	3.59	177.67	1.7654	0.29
	57939	-	G8Vp	9.09	6.42	178.23	37.733	0.36
	58345	-	K4V	10.2	6.99	179.49	-27.71	0.32
	64797	-	K2V	11.1	6.56	199.21	17.018	0.28
	67927	-	G0IV	11.4	2.68	208.67	18.399	0.27
	68184	-	K3V	10.1	6.49	209.38	61.492	0.33
	72848	-	K2V	11.5	6	223.35	19.152	0.27
	81300	-	K1V	9.75	5.76	249.09	-2.324	0.34
	84478	36 Ophiuchi C	K5.0V	5.95	6.33	259.06	-26.54	0.48
	84720	-	M0V	8.8	5.52	259.76	-46.64	0.38
	85295	-	M1V	7.7	7.49	261.44	2.1143	0.44
	86400	-	K2V	11	6.53	264.82	3.5555	0.29
	88972	-	K2V	11	6.38	272.41	38.459	0.29
	91262	Vega	A0Vvar	7.68	0.03	279.23	38.783	0.44
	97649	Altair	A7IV-V	5.12	0.76	297.69	8.8674	0.49
	109176	-	F5V	11.7	3.77	331.75	25.345	0.26
	113283	-	K4VP	7.61	6.48	344.1	-31.57	0.44
	113368	Fomalhaut	A3V	7.7	1.23	344.41	-29.62	0.44
	114046	Lacaille 9352	M1.0V	3.28	7.35	346.45	-35.86	0.51
	116745	-	K4V	11.4	7.09	354.9	-72.72	0.27
Jupiter Candidates	544	-	K0V	13.7	6.06	1.6522	29.022	0.43
	746	-	F2III-IV	16.8	2.26	2.292	59.15	0.36
	910	-	F5V	18.7	4.89	2.8163	-15.47	0.33
	950	-	F3/5V	21.3	5.24	2.9329	-35.13	0.29
	1031	-	K0V	20.2	7.22	3.2099	-57.91	0.30
	1292	-	G6V	17.5	6.59	4.0468	-79.85	0.35
	1349	-	G2V	22.6	6.85	4.2233	-52.65	0.27
	1392	-	F5	15.2	7.05	4.3521	8.8763	0.41
	1499	-	G5V	23.2	6.45	4.6734	-8.053	0.26
	1803	-	G3V	20.9	6.39	5.7148	-12.21	0.29
	2072	-	A6VN	23.8	3.93	6.5505	-43.68	0.25
	3497	-	G5V	22.1	6.55	11.163	-65.65	0.28
	3583	-	G1V	15.2	5.8	11.439	-47.55	0.41
	3810	-	F8V...	23.5	5.06	12.245	16.941	0.25
	3850	-	G8/K0V	18.7	7.16	12.36	-23.21	0.34
	3909	-	F7V	15.8	5.16	12.532	-10.64	0.40
	3979	-	G5V	21.5	6.96	12.795	-5.039	0.29
	4148	-	K2V	14.2	7.15	13.253	-30.36	0.42
	4151	-	F8V	18.7	4.8	13.268	61.124	0.33
	5842	-	K2V	21.6	7.24	18.751	-68.82	0.28
	5944	-	G0	23.2	6.59	19.122	42.939	0.26
	6379	-	K0	16.8	7.17	20.497	76.71	0.36

Table A.1-4. Case 3 input target star list.

	HIP	Common	Spectra Type	dpc	V	RAICRS	DEICRS	Completeness
	7235	-	K0V	19.1	6.96	23.315	-24.18	0.33
	7339	-	G6V	20.7	6.52	23.641	68.948	0.30
	7372	-	K1V	21.6	7.1	23.754	-29.91	0.28
	7734	-	G5IV	21.4	6.61	24.899	45.878	0.29
	8486	-	G0	22.6	6.75	27.348	-10.7	0.27
	8497	-	F0V	23.2	4.65	27.397	-10.69	0.26
	8796	-	F6IV	19.4	3.42	28.27	29.579	0.32
	8903	-	A5V...	18	2.63	28.66	20.808	0.35
	9007	-	G8IIIBCNIV	17.9	3.69	28.987	-51.61	0.35
	9236	-	F0V	22	2.86	29.691	-61.57	0.28
	9829	-	G2V	22.8	6.89	31.626	24.334	0.27
	9884	alf Arietis	K2III	20.2	2.01	31.793	23.463	0.30
	10531	-	K2V	18.6	7.2	33.924	67.673	0.34
	10798	-	G8V	12.7	6.33	34.744	-25.95	0.48
	12444	-	F7V	21.8	5.79	40.052	-9.453	0.28
	12653	-	G0V	17.2	5.4	40.638	-50.8	0.36
	14150	-	G8V	20.6	6.62	45.608	26.61	0.30
	14879	-	F8V	14.2	3.8	48.018	-28.99	0.42
	14954	-	G0V	22.6	5.07	48.193	-1.196	0.27
	15330	-	G3/5V	12	5.53	49.435	-62.58	0.50
	16245	-	F3IV/V	21.7	4.7	52.342	-62.94	0.28
	16852	-	F8V	14	4.29	54.219	0.4028	0.43
	17420	-	K2V	13.9	7.1	55.98	-19.11	0.43
	17439	-	K1V	16	7	56.038	-38.28	0.39
	17651	-	F3/5V	17.6	4.22	56.712	-23.25	0.35
	18859	-	F7/8V	18.8	5.38	60.653	-0.268	0.33
	19076	-	G5V	16.9	5.9	61.334	22.009	0.36
	19255	-	G5	20.4	7.13	61.893	38.075	0.30
	19335	-	F7V	21	5.51	62.152	38.04	0.29
	19855	-	G5IV	21.1	6.94	63.858	6.1999	0.29
	19859	-	G0IV...	21.3	6.32	63.87	6.1871	0.29
	19893	-	F0V	20.5	4.25	64.006	-51.49	0.30
	19921	-	K1/2III	18.2	4.44	64.121	-59.3	0.34
	21770	-	F1V	20.2	4.44	70.141	-41.86	0.30
	22263	-	G3V	13.3	5.49	71.901	-16.93	0.46
	23437	-	G0V	22.5	7.02	75.571	-56.08	0.27
	25110	-	F6V	20.9	5.08	80.641	79.231	0.29
	25544	-	G6/8V	19.2	6.98	81.915	-60.42	0.33
	26779	-	K1V	12.3	6.2	85.335	53.482	0.49
	27288	-	A2VANN	21.6	3.55	86.739	-14.82	0.29
	27321	-	A5V	19.4	3.85	86.821	-51.07	0.32
	27435	-	G3V	15.2	5.97	87.145	-4.094	0.41
	27887	-	K3V	13	7.17	88.518	-60.02	0.47
	28103	-	F1V	14.9	3.71	89.101	-14.17	0.41
	28267	-	F7V	23.6	6.99	89.59	-4.65	0.25
	28954	-	K0	15.3	6.75	91.669	15.542	0.41
	29432	-	G4V	23.5	6.86	93.002	6.7837	0.25
	29525	-	G8V	18	6.42	93.302	10.628	0.35
	29568	-	G5V	16.7	6.37	93.439	-23.86	0.37
	29650	-	F6V	20.8	5.2	93.712	19.157	0.29
	29800	-	F5IV-V	19.2	5.03	94.111	12.272	0.33
	29860	-	G0.5Vb	19.2	5.7	94.318	5.0997	0.33
	30314	-	G1V	23.8	6.53	95.629	-60.22	0.25

Table A.1-4. Case 3 input target star list.

	HIP	Common	Spectra Type	dpc	V	RAICRS	DEICRS	Completeness
	30503	-	G2V	21.9	6.37	96.183	-28.78	0.28
	31156	-	G8	17.9	6.91	98.074	17.78	0.35
	31592	-	K1III(+M)	19.8	3.95	99.171	-19.26	0.31
	32362	-	F5IV	18	3.32	101.32	12.896	0.35
	32439	-	F8V	17.9	5.43	101.56	79.566	0.35
	32480	-	G0V	16.7	5.25	101.68	43.577	0.37
	33277	-	G0V	17.2	5.75	103.83	25.376	0.36
	33690	-	K1V	18.3	6.8	105	-61.34	0.34
	33817	-	K1V	14.6	6.69	105.31	-25.95	0.42
	34017	-	G4V	19.1	5.94	105.88	29.339	0.33
	34065	-	G3V	16.5	5.56	105.99	-43.61	0.38
	34069	-	K0V	20.8	6.85	106	-43.61	0.29
	34834	-	F0IV	21.4	4.49	108.14	-46.76	0.29
	35136	-	G0V	16.9	5.54	108.96	47.24	0.36
	35296	-	K3V	14.6	6.7	109.37	-46.98	0.42
	35550	-	F0IV...	18.5	3.5	110.03	21.982	0.34
	36210	-	G5V	22.7	6.71	111.86	-51.4	0.27
	36366	-	F0V...	18	4.16	112.28	31.784	0.35
	36439	-	F6V	20.2	5.36	112.48	49.673	0.30
	36515	-	G3V	21.8	6.64	112.68	-37.34	0.28
	37349	-	K0/2V	14.2	7.17	115	-3.597	0.42
	38228	-	G5IV	22	6.9	117.48	27.363	0.28
	38784	-	G8V	17.2	6.55	119.08	80.265	0.36
	38908	-	G0V	16.2	5.58	119.44	-60.3	0.39
	39157	-	G8V	16.8	6.98	120.13	29.215	0.36
	39342	-	K1V	17.3	7.18	120.63	-66.02	0.35
	39757	-	F2MF5IIP	19.5	2.79	121.89	-24.3	0.32
	39780	-	G2IV	23.3	5.3	121.94	21.582	0.25
	39903	-	F5V	20	4.74	122.25	-61.3	0.30
	40035	-	F7V	22.4	5.53	122.67	-13.8	0.27
	40693	-	K0V	12.5	5.94	124.6	-12.63	0.48
	40702	-	F5V	19.6	4.05	124.63	-76.92	0.32
	40843	-	F6V	18.3	5.13	125.02	27.219	0.34
	41484	-	G5V	22.3	6.32	126.9	45.654	0.28
	41926	-	K0V	12.2	6.37	128.22	-31.5	0.49
	42438	-	G1.5Vb	14.4	5.63	129.8	65.021	0.42
	43726	-	G3/5V	17.4	5.99	133.58	-5.435	0.35
	44075	-	F7/8IV/V	21	5.81	134.68	-16.13	0.29
	44127	-	A7IV	14.5	3.1	134.8	48.042	0.42
	44897	-	F9V	19.2	5.93	137.21	33.882	0.33
	45170	-	G9V	20.4	6.48	138.07	14.995	0.30
	45333	-	F9V	19.6	5.19	138.59	61.423	0.32
	45617	-	K3V	17.3	7.21	139.47	28.562	0.36
	46509	-	F5V	17.3	4.59	142.29	-2.769	0.35
	46580	-	K3V	12.9	7.2	142.48	5.6549	0.47
	46733	-	F0IV	23.8	3.64	142.88	63.062	0.25
	46843	-	K0	17.8	7.05	143.18	26.989	0.35
	46853	-	F6IV	13.5	3.16	143.22	51.679	0.45
	48113	-	G2V	18.4	5.07	147.15	46.021	0.34
	49081	-	G1V	15	5.37	150.25	31.925	0.41
	50075	-	G0V	22.8	6.36	153.35	-33.03	0.26
	50384	-	F8Vw	22.8	5.81	154.31	23.106	0.26
	50505	-	G5	20.2	6.65	154.72	44.049	0.30

Table A.1-4. Case 3 input target star list.

	HIP	Common	Spectra Type	dpc	V	RAICRS	DEICRS	Completeness
	50564	-	F6IV	21.4	4.78	154.93	19.471	0.29
	50921	-	G5V	22.4	6.92	155.98	-29.65	0.27
	50954	-	F2/3IV/V	16.2	3.98	156.1	-74.03	0.39
	51502	-	F2V	21.5	5.25	157.77	82.559	0.29
	51523	-	F5V	21.8	4.89	157.84	-53.72	0.28
	54704	-	G8/K0V	22.1	7.05	168	-26.14	0.28
	54745	-	G0V	21.9	6.41	168.14	35.814	0.28
	54872	-	A4V	17.9	2.56	168.53	20.524	0.35
	55210	-	G8V	21.6	7.23	169.59	-5.067	0.29
	55846	-	G6/8III/IV	17.7	6.49	171.69	3.0127	0.35
	56242	-	G0V	23.3	6.27	172.94	14.365	0.25
	56809	-	G0V	23.3	6.47	174.69	45.108	0.26
	57507	-	G5V	17.5	6.48	176.82	-30.29	0.35
	58576	-	G8IV	12.8	5.53	180.18	-10.44	0.48
	59072	-	F0IV	19.8	4.14	181.72	-64.61	0.31
	59199	-	F0IV/V	14.9	4.02	182.1	-24.73	0.41
	59272	-	G0...	22.2	6.81	182.37	-11.86	0.28
	59750	-	F6V	22.4	6.11	183.79	-10.31	0.27
	61053	-	F9V	21.8	6.2	187.71	53.076	0.28
	61174	-	F2V	18.3	4.3	188.02	-16.2	0.34
	61291	-	K1V	16.2	7.14	188.38	-68.76	0.39
	62145	-	K3V	14.9	7.01	191.06	51.76	0.41
	62207	-	G0V	17.4	5.95	191.25	39.279	0.35
	62523	-	G7V	16.9	6.29	192.2	24.84	0.36
	64408	-	G3V	20.7	4.84	198.01	-37.8	0.30
	64583	-	F5V	18.2	4.91	198.56	-59.1	0.34
	64792	-	G0Vs	17.6	5.18	199.19	9.4237	0.35
	65109	-	A2V	18	2.72	200.15	-36.71	0.35
	65352	-	G8/K0V	15.4	7.06	200.91	2.7228	0.40
	65515	-	G9IV-V	21.6	7.29	201.44	56.97	0.29
	65530	-	G6V	21.2	6.5	201.5	63.261	0.29
	65721	-	G5V	18	4.96	202.11	13.78	0.35
	66249	-	A0/1IV	22.7	3.38	203.67	-0.596	0.27
	66765	-	K1V	15.7	6.91	205.27	-34.46	0.40
	67153	-	F3V	19.4	4.23	206.42	-33.04	0.32
	67275	-	F7V	15.6	4.48	206.82	17.457	0.40
	67422	-	K2	13.4	7.05	207.27	26.98	0.45
	68682	-	G8V	17	6.27	210.88	10.788	0.36
	68933	-	K0IIIB	18	2.06	211.67	-36.37	0.35
	69414	-	G8/K0V	22.1	7.05	213.19	-3.319	0.28
	69671	-	G1V	21.2	6.31	213.91	-45	0.29
	69701	-	F6III	22.2	4.07	214	-6	0.28
	69965	-	F7(W)F3V	18	5.88	214.75	-25.82	0.35
	69972	-	K3V	11.8	6.66	214.77	-59.38	0.50
	70319	-	G5V	17.2	6.25	215.81	1.2427	0.36
	70497	-	F7V	14.5	4.04	216.3	51.852	0.42
	70857	-	G5	19.9	6.89	217.34	80.81	0.30
	70873	-	G5V	23.7	6.36	217.4	41.796	0.25
	71181	-	K3V	13.2	7.24	218.37	52.908	0.46
	71284	-	F3Vwvar	15.8	4.47	218.67	29.745	0.40
	71743	-	G6V	23.7	7.24	220.13	-16.21	0.25
	71855	-	G5V	20	6.73	220.47	-75.14	0.30
	71908	-	APSREU(CR)	16.6	3.16	220.63	-64.97	0.37

Table A.1-4. Case 3 input target star list.

	HIP	Common	Spectra Type	dpc	V	RAICRS	DEICRS	Completeness
	71957	-	F2V	18.3	3.86	220.76	-5.657	0.34
	72567	-	G2V	18.2	5.86	222.57	23.912	0.34
	72603	-	F3V	23	5.15	222.67	-16	0.26
	72622	-	A3III/V	23.2	2.75	222.72	-16.04	0.26
	73996	-	F5V	19.6	4.93	226.82	24.87	0.32
	74537	-	G8/K0V	17.7	6.58	228.47	-1.35	0.35
	74702	-	K0V	15.8	6.93	229	0.7967	0.40
	75181	-	G3/5V	14.8	5.65	230.46	-48.32	0.41
	75277	-	K0	19.6	7.12	230.7	18.919	0.32
	75718	-	A1V	20.6	6.88	232.04	-9.347	0.30
	75809	-	G8IV-V+...	21.8	6.57	232.3	80.448	0.28
	76267	-	A0V	23	2.21	233.67	26.715	0.26
	76382	-	K2V	22.3	6.8	234.01	39.802	0.27
	76829	-	F3/5V	17.4	4.63	235.3	-44.66	0.35
	77052	-	G3V	14.7	5.86	236.01	2.5155	0.42
	77070	-	K2III	22.7	2.61	236.07	6.4255	0.27
	77358	-	G6IV	15.4	6.01	236.87	-37.92	0.41
	77622	-	Am(kA2hA5mA7V)	21.6	3.71	237.7	4.4776	0.29
	77760	-	F9V	15.9	4.6	238.17	42.45	0.39
	77801	-	G0IV	17.3	6.08	238.3	13.198	0.35
	77952	-	F0III/IV	12.4	2.81	238.79	-63.43	0.49
	78459	-	G2V	17.2	5.4	240.26	33.305	0.36
	78527	-	F8IV-V	21	3.99	240.47	58.564	0.29
	78709	-	G8V	22.2	7.1	241.02	25.253	0.28
	78775	-	G8V	14.5	6.66	241.24	39.156	0.42
	79190	-	K1/2V	14.7	7.11	242.43	-56.45	0.42
	79492	-	G8V	23.6	6.68	243.33	13.528	0.25
	79578	-	G1V	21.6	6.55	243.55	-31.66	0.29
	79607	-	F8V	21.1	5.55	243.67	33.859	0.29
	79672	-	G5V	13.9	5.5	243.9	-8.368	0.43
	81375	-	K0V	20.3	7.07	249.28	0.2542	0.30
	81520	-	G3V	22.5	7.02	249.77	-58.26	0.27
	82396	-	K2IIIB	19.5	2.26	252.54	-34.29	0.32
	82588	-	K1V	17.3	6.65	253.25	-0.023	0.36
	83541	-	K1V	17.8	6.58	256.12	-28.58	0.35
	83601	-	F8V	20.7	5.99	256.32	0.7034	0.30
	84143	-	F2V	22.5	3.31	258.04	-43.24	0.27
	84862	-	G0V	14.3	5.38	260.16	32.47	0.42
	85042	-	G5V	19.5	6.28	260.71	-2.388	0.32
	85653	-	G5	22.3	7.22	262.57	47.402	0.28
	86486	-	F2V	21.5	4.75	265.1	-49.42	0.29
	88175	-	F2IV	23.6	4.62	270.12	-3.69	0.25
	88348	-	K0V	22.1	7.01	270.63	26.314	0.28
	88694	-	G3V	17.6	5.94	271.6	-36.02	0.35
	89042	-	G1V	17.6	5.47	272.61	-62	0.35
	89474	-	G2V	22.8	6.3	273.89	45.21	0.26
	89805	-	G0/1V	23	6.17	274.92	-63.89	0.26
	89962	-	K0III-IV	18.5	3.23	275.33	-2.897	0.34
	90790	-	K1V	13.3	6.81	277.83	-18.91	0.46
	92043	-	F6V	19.2	4.19	281.42	20.547	0.33
	93858	-	G8V	17	6.15	286.72	-37.81	0.36
	93966	-	G5V	21.4	6.07	286.99	16.854	0.29
	94346	-	G8V	20	7.04	288.05	57.671	0.30

Table A.1-4. Case 3 input target star list.

	HIP	Common	Spectra Type	dpc	V	RAICRS	DEICRS	Completeness
	95149	-	G1/2V	18.8	6.48	290.37	-34.98	0.33
	95319	-	G8V	15.8	6.37	290.89	33.222	0.40
	95501	-	F2IV	15.5	3.36	291.37	3.1146	0.40
	95995	-	K1V	17	6.6	292.79	58.587	0.36
	96183	-	G5V	20.6	6.86	293.36	21.841	0.30
	96441	-	F4V	18.3	4.49	294.11	50.22	0.34
	96895	-	G2V	21.1	5.92	295.45	50.525	0.29
	97295	-	F5	21.2	5	296.61	33.729	0.29
	97675	-	F8V	19.2	5.12	297.76	10.416	0.33
	97944	-	K3/4V	14	6.21	298.57	-23.94	0.43
	98036	-	G8IVvar	13.7	3.71	298.83	6.4079	0.43
	98470	-	F7V	21.2	5.65	300.08	-33.7	0.29
	98677	-	G7V	19	7.15	300.64	15.593	0.33
	98792	-	K1V	15.8	7.27	300.97	23.343	0.40
	98819	-	G1V	17.8	5.79	301.03	17.071	0.35
	98921	-	G5IV	18.8	6.18	301.29	38.478	0.33
	98959	-	G3V	17.7	6.07	301.38	-67.32	0.35
	99137	-	F8/G0V	23.4	6.25	301.9	-55.02	0.25
	100017	-	G3V	17.6	5.92	304.38	66.853	0.35
	100925	-	G6/8V	19.5	6.61	306.93	-30.87	0.32
	101382	-	G9V	22.1	7.08	308.22	41.897	0.28
	101997	-	G8/K0V	14.4	6.36	310.05	-23.77	0.42
	102040	-	G5V	20.9	6.43	310.19	19.935	0.29
	102264	-	G3/5V	22.3	6.95	310.82	-29.42	0.27
	102422	-	K0IV	14.3	3.41	311.32	61.837	0.42
	102485	-	F5V	14.7	4.13	311.52	-25.27	0.42
	102488	-	K0III	22.3	2.45	311.55	33.969	0.28
	103389	-	F7V	22	5.69	314.2	-26.3	0.28
	103458	-	G0V	22.1	6.52	314.42	-44.13	0.28
	104239	-	K1V	17.6	7.19	316.79	-13.92	0.35
	105199	-	A7IV-V	15	2.43	319.64	62.585	0.41
	105712	-	G5V	20.4	6.98	321.17	-68.23	0.30
	106696	-	K2V	14.6	7.14	324.17	-50.84	0.42
	107022	-	G8V	22	7.07	325.13	-74.07	0.28
	107089	-	K0III	21.2	3.73	325.37	-77.39	0.29
	107350	-	G0V	17.9	5.95	326.13	14.772	0.35
	107556	-	A5mF2 (IV)	11.9	2.85	326.76	-16.13	0.50
	107649	-	G0V	16	5.57	327.07	-47.3	0.39
	109378	-	G8/K0V	21.6	6.53	332.37	-7.548	0.29
	109422	-	F6V	18.3	4.93	332.54	-32.55	0.34
	109527	-	K0	22.9	7.22	332.8	36.257	0.26
	109821	-	G5V	22.1	6.23	333.66	-41.38	0.28
	110649	-	G3IV	20.6	5.31	336.23	-57.8	0.30
	110712	-	G3V	23	6.12	336.46	-75.02	0.26
	111449	-	F7V	22.7	5.2	338.67	-20.71	0.27
	112117	-	G0V	23.6	5.99	340.65	-47.21	0.25
	112447	-	F7V	16.3	4.2	341.67	12.174	0.38
	113357	-	G5V	15.6	5.45	344.37	20.769	0.40
	114924	-	F7V	20.5	5.58	349.18	53.214	0.30
	114948	-	F8V	20.5	5.65	349.24	-62	0.30
	114996	-	F3IV/V	23.1	3.99	349.36	-58.24	0.26
	116085	-	K2V	16.9	6.75	352.84	59.165	0.36
	116613	-	G5	23.3	6.58	354.49	46.199	0.25

Table A.1-4. Case 3 input target star list.

	HIP	Common	Spectra Type	dpc	V	RAICRS	DEICRS	Completeness
	116763	-	K1V	18.6	7.19	354.96	-32.74	0.34
	116771	-	F7V	13.7	4.13	354.99	5.6274	0.43
Known Giant Planets	7513	-	F8V	13.5	4.09	24.2	41.406	
	7978	-	F8V	17.4	5.52	25.621	-53.74	
	10626	-		44.2	7.61	34.2	43.773	
	16537	epsilon Eridani	K2.0V	3.21	3.71	53.235	-9.458	
	22336	-	G5V	26.4	5.76	72.151	-5.673	
	22627	-	M4	12.3	12	73.024	6.4773	
	24205	-	G1/2V	28.4	6.98	77.943	4.4039	
	26394	-	G1V	18.3	5.65	84.287	-80.47	
	27253	-		39.3	5.95	86.64	1.169	
	37826	Pollux	K0IIIvar	10.4	1.16	116.33	28.026	
	40952	-	G8/K1(III+F/G)	28.1	7.16	125.37	-39.71	
	42030	-		49.8	7.46	128.52	-1.568	
	43587	-	G8V	12.3	5.96	133.15	28.331	
	43790	-	M1	19.8	9.99	133.78	1.549	
	49699	-	K0	18.2	7.55	152.18	34.242	
	50473	-		32.4	7.02	154.59	12.621	
	53721	-	G0V	14.1	5.03	164.87	40.43	
	65808	-		33.1	7.26	202.33	-35.57	
	71395	-	K0	16.5	7.49	219	9.7471	
	74500	-	G5V	26.2	6.46	228.37	-25.31	
	79242	-		34.3	7.7	242.56	-84.23	
	79248	-	K0V	17.6	6.61	242.6	43.818	
	80337	-	G3/5V	12.8	5.37	246.01	-39.19	
	83043	-	M2	10.3	9.66	254.54	25.745	
	83389	-	G8V	18.6	6.76	255.65	47.08	
	85647	-	M0	16.5	9.59	262.55	-51.64	
	86796	-	G3IV/V	15.5	5.12	266.04	-51.83	
	90485	-		36.6	5.9	276.96	-26.82	
	95467	-	K2IV/V	26.8	8.39	291.29	-66.47	
	96901	-	G5V	21.2	6.16	295.47	50.518	
	97336	-		48.3	7.83	296.75	34.42	
	98767	-	G6IV+...	15.9	5.73	300.9	29.898	
	99825	-	K3V	8.91	5.72	303.82	-27.03	
	106353	-	K1/2V	26.9	8.45	323.1	-20.96	
	106440	-	M1.5V	4.95	8.67	323.39	-49.01	
	109388	-	M3	9.1	10.4	332.42	-4.641	
	113137	-	G2/3IV	26.7	6.04	343.66	-70.07	
	113421	-	G8IV/V	19.9	6.16	344.56	-2.395	
	115697	-		50.9	7.06	351.61	8.644	
	116616	-		49.1	7.12	354.49	48.997	
	116727	-	K1IV	14.1	3.21	354.84	77.632	

A.2 Notes on the Brightest Stars in the Sky

The brightest exoplanets in the sky for a given diameter should orbit the five systems brighter than V = 2: Sirius (2.6 pc), Procyon A (3.5 pc), Altair (5 pc), Vega (7.7 pc), and Fomalhaut (also 7.7 pc). All except Procyon are A-type stars, and much younger than the Sun (<2 Gyr). If the concept of a 'habitable zone' applies in these environments, then the nominal HZ falls entirely within Exo-S' field of view for all of these stars. Vega and Fomalhaut are well-known debris disks, one of which appears to host a dust-enshrouded planet or collisional aftermath far from the star. Procyon A is the least luminous and the only F star (F5VI-V). Procyon is significantly older than Vega and Fomalhaut (~2 Gyr), perhaps offering the best chance at imaging planetary bodies and exozodiacal structures within and exterior to the nominal habitable zone. In many cases, such planets would be 'hot Earths' or potential Venus analogs, located interior to the habitable zone. Sirius and Procyon harbor a white dwarf secondary and offer the potential for exploring planet survival and/or formation after significant stellar mass loss.

A.3 DRMS for Cases 1, 2, and 3

Table A.3-1. DRM for Case 1: Dedicated Mission, maximize Earth twins in HZ.

#	HIP	Common Name	Glat	SR	Observation Time (hrs)	Delta Mag	Slew Time (days)	ΔV (m/s)	On Target Time (days)	Sun Angle (deg)	Weight-ing
1	7513	-	-20.7	7	20.71	19.3	0.00	0.00	0.68	32.6	4
2	31592	-	-11.8	70	0.39	20.3	20.03	88.13	0.68	67.2	4
3	37826	Pollux	23.4	70	0.01	19.5	15.28	70.18	0.67	54.4	4
4	36366	-	21.3	7	1.22	22.5	5.89	13.85	0.72	44.4	3
5	53721	-	63.4	70	0.78	19.4	18.99	32.19	0.70	68	4
6	61317	beta CVn	75.3	7	331.32	25.8	11.82	22.50	14.47	75.2	1
7	64394	-	85.4	7	445.95	25.9	10.99	21.28	19.25	66.6	1
8	72659	ksi Bootis A	61.4	7	181.09	25.0	14.64	34.17	8.21	63.6	1
9	78072	-	45.7	7	276.84	26.0	13.25	27.70	12.20	62.6	1
10	86974	-	25.6	7	140.70	26.0	14.78	28.34	6.53	72.6	1
11	88601	70 Ophiuchi A	11.4	7	68.30	25.1	13.36	29.63	3.51	53.2	1
12	99825	-	-29.4	70	0.28	18.4	18.17	34.69	0.68	55.6	4
13	106440	-	-46.4	70	224.33	20.7	11.32	49.83	10.01	58.8	4
14	7978	-	-61.8	70	2.52	19.7	13.38	60.17	0.77	80	4
15	1599	-	-51.9	7	359.50	25.8	14.44	14.17	15.65	61.8	1
16	108870	epsilon Indi A	-48.0	7	22.62	23.9	9.86	33.57	1.61	42.4	1
17	110649	-	-50.0	7	8.14	22.5	4.08	13.76	1.01	45.2	3
18	114996	-	-54.8	7	0.94	22.5	6.33	18.86	0.71	49	3
19	116727	-	15.3	70	0.19	20.5	26.78	62.68	0.67	77.8	4
20	96100	sigma Draconis	21.9	7	80.05	24.6	11.44	43.49	4.00	81.4	1
21	3821	eta Cassiopei A	-5.1	7	103.44	25.8	14.97	49.27	4.98	47.8	1
22	5336	-	-7.9	7	207.56	24.7	11.32	21.93	9.31	43.4	1
23	27072	-	-24.3	7	185.51	26.0	22.83	79.02	8.40	46.2	1
24	47080	-	47.8	7	92.37	24.0	20.32	63.08	4.52	34	2
25	56997	-	73.3	7	79.73	24.0	12.61	32.84	3.99	46.2	2
26	57632	-	70.8	7	0.68	24.0	11.03	29.14	0.69	35.4	2
27	57757	-	60.8	7	4.80	24.0	9.06	22.72	0.87	29.4	2
28	67927	-	73.0	7	1.34	24.0	14.44	38.93	0.72	44.8	2
29	85647	-	-9.5	70	181.67	19.5	22.17	55.90	8.24	80.6	4
30	86796	-	-11.5	70	2.12	20.3	3.34	12.35	0.76	72.8	4
31	83389	-	37.7	70	129.66	20.9	20.38	96.84	6.07	71	4
32	84862	-	32.3	7	9.23	22.5	12.48	16.88	1.05	57.6	3
33	83043	-	35.3	70	80.52	19.1	7.80	16.36	4.02	48.2	4
34	98767	-	-0.7	70	65.10	21.6	14.08	57.11	3.38	65	4
35	91262	Vega	19.2	7	0.07	24.0	12.01	25.31	0.67	62	2
36	8102	tau Ceti	-73.4	7	17.33	24.8	32.21	41.39	1.39	69.8	1
37	8497	-	-68.6	7	2.70	22.5	7.37	10.41	0.78	64.4	3
38	17378	-	-46.0	7	166.52	26.0	12.86	35.99	7.61	80	1
39	19849	omicron 2 Eridani	-38.0	7	51.08	24.6	8.33	14.43	2.80	74.4	1
40	16537	epsilon Eridani	-48.0	70	0.13	19.5	8.90	18.13	0.67	54.2	4
41	22449	1 Ori	-23.1	7	99.56	26.0	14.64	25.02	4.81	58.6	1
42	14632	-	-7.4	7	379.81	26	18.29	38.88	16.49	37	1

Table A.3-2. DRM for Case 2, Dedicated Mission, maximize planet harvest.

#	HIP	Common Name	Glat	SR	Observation Time (hrs)	Delta Mag	Slew Time (days)	ΔV (m/s)	On Target Time (days)	Sun Angle (deg)	Weight -ing
1	7513	-	-20.7	70	42.09	19.3	0.00	0.00	0.68	32.6	4
2	31592	-	-11.8	70	0.39	20.3	20.03	88.13	0.68	67.2	4
3	37826	Pollux	23.4	70	0.01	19.5	15.28	70.18	0.67	54.4	4
4	53721	-	63.4	70	0.78	19.4	25.60	21.07	0.70	68	4
5	46853	-	45.7	7	146.15	26.0	10.94	27.44	6.76	45.2	1
6	44127	-	40.8	7	133.55	26.0	8.09	11.42	6.23	31.6	1
7	57632	-	70.8	7	32.92	26.0	15.97	52.98	2.04	40.2	1
8	67927	-	73.0	7	70.66	26.0	13.08	39.68	3.61	56.6	1
9	78072	-	45.7	0	447.59	26.0	12.92	38.33	19.32	72.6	1
10	86974	-	25.6	7	215.96	26.0	13.10	35.12	9.66	77	1
11	91262	Vega	19.2	7	2.80	26.0	10.32	22.95	0.78	80.4	1
12	99825	-	-29.4	70	0.28	18.4	28.35	31.69	0.68	55.6	4
13	106440	-	-46.4	70	224.33	20.7	11.32	49.83	10.01	58.8	4
14	7978	-	-61.8	70	2.52	19.7	13.38	60.17	0.77	80	4
15	2021	beta Hyi	-39.8	7	86.98	26.0	13.48	27.55	4.29	65	0
16	8102	tau Ceti	-73.4	7	247.56	26.0	17.72	61.26	10.98	65.2	0
17	746	-	-3.3	7	38.54	26.0	20.09	62.37	2.27	65.8	1
18	116727	-	15.3	70	0.19	20.5	11.62	24.55	0.67	77.8	4
19	22449	1 Ori	-23.1	7	148.12	26.0	19.61	71.18	6.84	53.8	0
20	17378	-	-46.0	7	259.21	26.0	12.85	28.26	11.47	30.8	0
21	27072	-	-24.3	7	291.28	26.0	14.90	32.50	12.80	49	0
22	28103	-	-18.5	7	354.74	26.0	7.08	21.21	15.45	37.8	1
23	32349	Sirius A	-8.9	7	0.66	26.0	14.09	11.29	0.69	40.6	1
24	39757	-	4.4	7	83.09	26.0	11.01	31.58	4.13	43.6	2
25	65109	-	25.8	7	75.21	26.0	17.84	68.40	3.80	68.6	2
26	68933	-	24.1	7	29.55	26.0	7.17	22.61	1.90	66.4	2
27	85647	-	-9.5	70	181.67	19.5	26.02	19.22	8.24	80.6	4
28	86796	-	-11.5	70	2.12	20.3	3.34	12.35	0.76	72.8	4
29	83389	-	37.7	70	129.66	20.9	20.38	96.84	6.07	71	4
30	83043	-	35.3	70	80.52	19.1	21.32	12.94	4.02	48.2	4
31	98767	-	-0.7	70	65.10	21.6	14.08	57.11	3.38	65	4
32	97649	Altair	-8.9	7	6.09	26.0	11.32	30.95	0.92	37.6	1
33	109176	-	-24.3	7	391.78	26.0	14.10	44.39	16.99	59.8	1
34	105199	-	9.2	7	49.02	26.0	16.61	34.39	2.71	76	1
35	9884	alf Arietis	-36.2	7	27.64	26.0	17.04	67.24	1.82	53.8	2
36	16537	epsilon Eridani	-48.0	70	0.13	19.5	13.41	64.86	0.67	54.2	4
37	3821	eta Cassiopei A	-5.1	7	232.90	26.0	20.85	54.82	10.37	50	1
38	102422	-	11.6	7	217.10	26.0	16.08	26.60	9.71	76.6	1

Table A.3-3. DRM for Case 3, Rendezvous Mission, maximize Earth twins in HZ.

#	HIP	Common Name	Glat	SR	Observation Time (hrs)	Delta Mag	Slew Time (days)	ΔV (m/s)	On Target Time (days)	Sun Angle (deg)	Weight-ing
1	16537	epsilon Eridani	-48.05	70	24.00	19.9	0.00	0.00	1.00	80	4
2	17420	-	-49.74	9	21.75	22.5	10.40	19.28	0.91	72.25	3
3	17651	-	-50.32	9	0.18	22.5	4.58	17.24	0.01	69	3
4	14879	-	-59.03	9	0.10	22.5	3.64	15.32	0.00	59.75	3
5	17378	-	-46.00	9	17.02	26.0	21.11	18.23	0.71	48	1
6	19849	omicron 2 Eridani	-38.04	9	5.52	24.6	2.12	12.73	0.23	52.75	1
7	22449	1 Ori	-23.07	9	10.04	26.0	6.73	31.05	0.42	53	1
8	25278	-	-10.29	9	196.22	26.0	5.29	29.86	8.18	55.5	1
9	37279	Procyon A	13.02	9	0.01	24.0	6.74	26.22	0.00	75.5	2
10	37826	Pollux	23.41	70	24.00	19.0	17.85	25.57	1.00	55	4
11	47080	-	47.80	9	10.12	24.0	8.78	26.70	0.42	67.75	2
12	56997	-	73.32	9	56.86	25.0	11.63	18.28	2.37	82	1
13	61317	beta CVn	75.32	9	34.76	25.8	6.45	27.90	1.45	81	1
14	53721	-	63.37	70	24.00	20.2	3.82	37.87	1.00	60	4
15	24813	-	1.54	9	115.27	26.0	24.89	30.85	4.80	41.5	1
16	14632	-	-7.38	9	39.51	26.0	7.10	31.30	1.65	75.25	1
17	12777	-	-9.61	9	42.71	26.0	0.41	37.03	1.78	81	1
18	51459	-	51.70	9	143.90	26.0	13.54	18.73	6.00	44.5	1
19	49908	-	52.15	9	86.64	24.0	5.91	20.75	3.61	42.75	2
20	83389	-	37.66	70	24.00	20.8	19.88	26.34	1.00	79	4
21	86974	-	25.63	9	14.32	26.0	9.18	29.23	0.60	78.25	1
22	88601	70 Ophiuchi A	11.37	9	7.23	25.1	11.26	34.21	0.30	68.25	1
23	106440	-	-46.35	70	24.00	19.9	22.27	39.28	1.00	82	4
24	105858	-	-40.29	9	49.70	26.0	8.11	27.97	2.07	71	1
25	98959	-	-31.99	9	3.54	22.5	1.97	13.69	0.15	60.75	3
26	99240	delta Pavonis	-32.41	9	12.29	25.8	1.09	16.64	0.51	60	1
27	108870	epsilon Indi A	-48.04	9	2.51	23.9	3.55	17.22	0.10	70	1
28	1599	-	-51.92	9	37.68	25.8	9.05	27.44	1.57	77.75	1
29	2021	beta Hyi	-39.78	9	0.18	24.0	7.13	15.79	0.01	70	2
30	107089	-	-35.19	9	0.09	22.5	8.97	15.76	0.00	59.25	3
31	7978	-	-61.77	70	24.00	19.8	2.58	8.73	1.00	82	4
32	98767	-	-0.67	70	55.30	20.3	48.78	33.20	2.30	50	4
33	5336	-	-7.87	9	22.44	24.7	4.51	20.88	0.93	75.25	1
34	3821	eta Cassiopei A	-5.05	9	10.59	25.8	3.97	17.45	0.44	72.5	1
35	114622	-	-3.20	9	20.35	24.2	6.67	18.89	0.85	63.75	1
36	91262	Vega	19.24	9	0.01	24.0	6.24	18.38	0.00	78.5	2
37	116727	-	15.32	70	24.00	19.5	8.87	8.95	1.00	78	4
38	104217	61 Cygni B	-5.82	9	10.92	23.5	9.07	21.81	0.46	58.5	1
39	104214	61 Cygni A	-5.82	9	2.97	23.5	3.92	9.09	0.12	60.25	1
40	96100	sigma Draconis	21.88	9	8.65	24.6	51.72	28.82	0.36	82.5	1
41	100017	-	16.92	9	2.70	22.5	6.74	10.45	0.11	82.25	3
42	83043	-	35.34	70	24.00	18.7	100.68	7.10	1.00	82	4
43	85647	-	-9.54	70	24.00	19.4	14.38	71.46	1.00	80	4
44	79248	-	46.95	70	24.00	20.5	31.39	38.11	1.00	63	4
45	64394	-	85.41	9	46.68	25.9	13.29	34.56	1.95	55.5	1
46	72659	ksi Bootis A	61.36	9	19.37	25.0	5.25	12.75	0.81	41.5	1
47	77257	-	44.10	9	72.07	26.0	25.86	28.09	3.00	41.5	1
48	109388	-	-45.40	70	46.99	19.5	9.57	35.15	1.96	55	4
49	8102	tau Ceti	-73.44	9	1.84	24.8	17.82	34.13	0.08	81.25	1

Table A.3-3. DRM for Case 3, Rendezvous Mission, maximize Earth-twins in HZ.

#	HIP	Common Name	Glat	SR	Observation Time (hrs)	Delta Mag	Slew Time (days)	ΔV (m/s)	On Target Time (days)	Sun Angle (deg)	Weight-ing
50	7235	-	-80.13	9	17.01	22.5	7.21	19.24	0.71	70.25	3
51	12843	-	-62.53	9	79.27	26.0	6.36	13.44	3.30	82	1
52	15510	82 Eridani	-56.08	9	10.81	25.1	13.05	30.08	0.45	74	1
53	7751	-	-59.66	9	16.93	24.0	9.32	8.67	0.71	59.25	2
54	12653	-	-58.32	9	1.12	22.5	4.07	10.63	0.05	64	3
55	10138	-	-61.96	9	36.67	24.0	2.82	17.79	1.53	59	2

B OPTICAL SHIELD

B.1 Introduction

This appendix provides more details on the optical shield (OS) element of the starshade mechanical design, including OS requirements, design descriptions, and development plans.

B.2 Requirements

The optical shield is a flexible covering for the starshade that allows it both to operate as a large starlight occulter and to stow in limited launch-fairing volume. As such, the OS has both optical and mechanical functions; accordingly, the OS has corresponding optical and mechanical functional requirements (**Table B.2-1**). Aside from the usual space environmental requirements and the ubiquitous need to minimize mass, the OS must:

- Prevent starlight from passing through the starshade to the telescope
- Minimize reflectance off the starshade and into the telescope
- Minimize the optical impact of micrometeoroid-created holes
- Provide complete coverage of the starshade shape upon deployment
- Allow the starshade to be stowed within a portion of the 5-m launch fairing
- Prevent OS mechanical loads from distorting the starshade shape on orbit

The first two requirements—opacity and reflectance—have already been addressed through material sample optical tests as part of the surface material selection process. Black Kapton has been selected.

The OS is not micrometeoroid 'proof': It cannot stop micrometeoroid intrusions. Instead the OS is designed to minimize the optical impact of micrometeoroid-generated holes. This requirement is addressed through design and verified by material and optical testing at the sample level.

The last three requirements—all related to the stowing and deployment of the OS, and its impact on the overall starshade shape—are the most challenging of the set. Careful consideration for folding patterns, attachment methods, and interface optical coverage has gone into the design. Verification requires system-level deployment tests, which in turn require the construction of a deployment testbed facility.

Table B.2-1. Remaining optical shield tests.

	Requirement	Verification
Micrometeoroid	<1 cm^2 cumulative pinhole area over entire OS	Optical and material testing on samples
Optical Coverage	Complete coverage of the starshade shape is required on deployment	System-level deployment tests
Stowing within Fairing	Must fit within a 5-m fairing	
Deployment Shape Accuracy	Starshade must meet shape tolerances with the OS in flight configuration (Section 6.4.3)	

B.3 Design Description

The OS is made up of two main elements: the OS that covers the inner disk and the OS that covers the petals. The fully deployed OS is shown in **Figure B.3-1**. A grid-like pattern is visible on the OS in the figure. This pattern represents the panels that make up the OS. This section presents the current designs for both elements and discusses their operational characteristics.

B.3.1 OS Material and Basic Panel

Before the discussion of the OS main elements, a short description of the basic panels that make up the disk and petal OS is needed. The panels represent a solution to the OS's issue with micrometeoroid damage. A pinhole in a thin-sheet occulter creates a direct path for starlight to get into the observing telescope. If the occulter were thicker, a micrometeoroid would create a 'tunnel' through the material rather than a simple hole. The alignment of such tunnels would be random, so only a small subset of all tunnels would allow light to pass in the direction of the

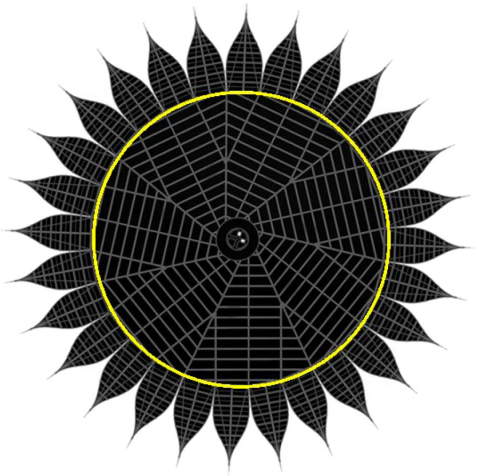

Figure B.3-1. Deployed optical shield. Inner disk OS is inside the yellow circle, petal OSs are on the petals outside the circle.

telescope. Mass considerations drive the design to two layers of opaque black Kapton sandwiching a urethane foam core (**Figure B.3-2**). Being primarily urethane foam, the panels are lightweight and flexible. Folding and manufacturing needs result in the blankets of interconnected panels shown in **Figure C.3-1**. Each panel is shaped and sized for a predetermined folding pattern.

B.3.2 Inner Disk OS

When deployed, the inner disk OS expands to an outer diameter of up to 20 m (20 m for the Rendezvous, 16 m for the Dedicated). The OS inner diameter is 1.6 m and terminates at the central cylinder of the starshade's hub. In this deployed state, the inner disk OS is slightly conical—with a cone angle of 6 degrees from the truss plane. When stowed, the inner disk OS fits into the starshade's hub structure, in an annular cylindrical space (**Figure B.3-3**) with an inner diameter of 1.6 m, outer diameter of 2.9 m and a height of 2.3 m.

For the inner disk OS, the OS is segmented into smaller, individual panels with flexible fold lines between each panel, forming an origami pattern known as a 'flasher.' The flasher design allows for a determinate folding pattern that can be engineered to accommodate the thickness of the folded material and thus is required to fold only at the determined hinge lines. The flasher design results in the foldability of many rigid panels without compression of the panels. **Figure B.3-4** depicts the deployment of a prototype flasher juxtaposed with the folding pattern of the inner disk OS.

Fold line 'hinges' are created by bonding an additional layer of Kapton across adjoining individual panels. This creates a lightweight and flexible hinge design that is tolerant of perturbing loads. A conventional pinned hinge design would be less forgiving and could bind. Additionally, the panels themselves can also flex, allowing for even more compliance during deployment.

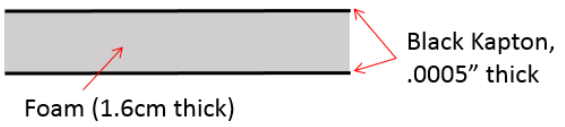

Figure B.3-2. OS Flex-panel Cross-section.

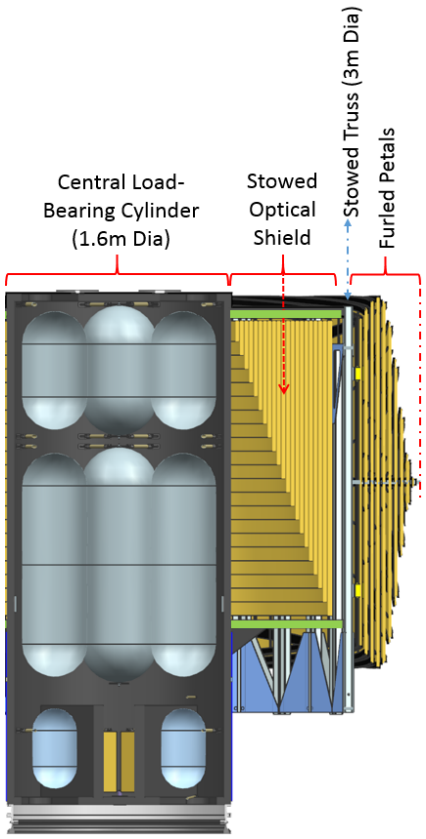

Figure B.3-3. Starshade in stowed configuration showing optical shield stow volume

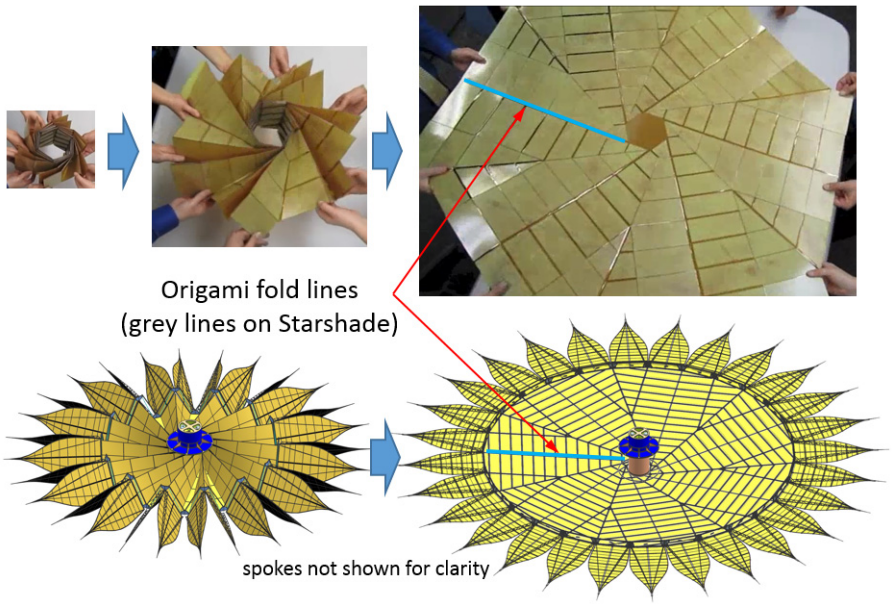

Figure B.3-4. Origami-based deployment of the OS. Top: deployment of a representative tabletop prototype. Bottom: depiction of full-scale starshade deployment.

Another design consideration for the inner disk OS is the need to minimize OS stresses imparted to the inner disk truss. The OS is designed to be mechanically decoupled from the truss structure. It is firmly attached to the starshade's center hub, and loosely connected to the truss. OS panels will have 'closeouts'—carbon-fiber edge coverings that will overlap with the truss structure to form a continuous light barrier without mechanically attaching to the truss (**Figure B.3-5**).

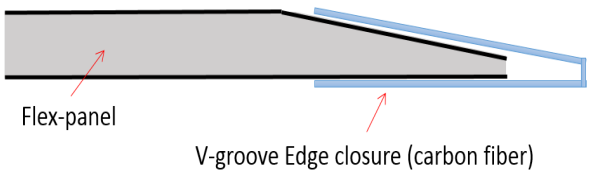

Figure B.3-5. Edge closeout design for the optical shield.

B.3.3 Petal OS

Since the petals simply wrap around the hub when stowed, no elaborate folding and packing scheme is required. Of greater concern with the petal OS is its effect on the shape of the overall petal. Petal OS–induced stresses into the petal structure must be minimized. To achieve this, the petal OS is made up of many separate flexible panels that are individually and pseudo-kinematically attached, or 'shingled,' to the graphite composite petal lattice structure (**Figure B.3-6)**. Each flex-panel will be fixed at the corner closest to the petal root and center spine. Additional nonfixed attachment points along the petal center spine and petal battens allow for radial expansion of each flex-panel away from the fixed attachment point, mechanically decoupling each OS panel from the petal structure. Mounting the OS panels in this way (**Figure B.3-7**) prevents thermally induced mechanical deformations into the petal lattice structure.

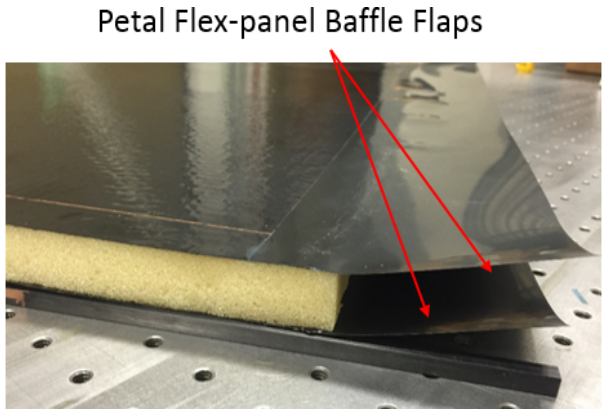

Figure B.3-6. Overlapping 'shingles' that prevent light leaks between panels.

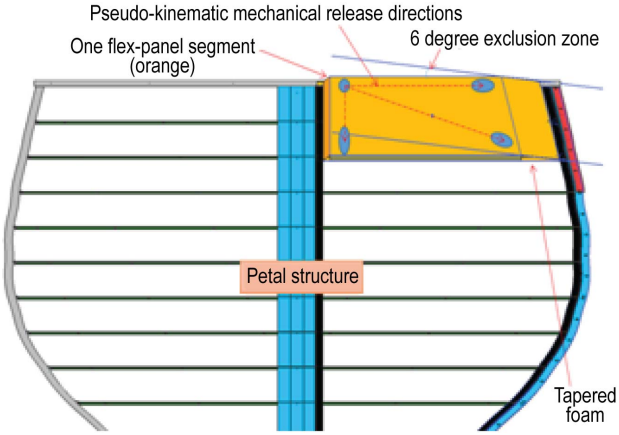

Figure B.3-7. Petal showing flex panel layout and kinematic release directions.

To prevent light from leaking between flex-panels, each flex-panel has thin Kapton flaps (**Figure B.3-6**) that overlap adjoining panels and prevent light leaking between the panels. These flaps are not mechanically connected, allowing each panel to expand and contract separately.

The petal OS panels do not deploy relative to the petals on which they are attached, but remain restrained to the lattice structure as the petals are wrapped around the hub. When in stowed configuration, the petal OSs are lightly compressed, a measure that provides the additional benefit of damping petal vibrations during launch. Preliminary analyses indicate that the baseline foam selection will substantially increase the first few vibration modes of the entire starshade during launch.

Lastly, the petal OS panel-to-petal edge transitions are covered with an overlapping closeout (**Figure B.3-5**) that covers any gaps between the panels and the petal structure without mechanically connecting the two.

B.4 OS Design Development

The optical shield development plan is in place, and progress is being made toward reaching TRL 5 by FY17 (**Figure B.4-1**). The work to reach this goal breaks down into four

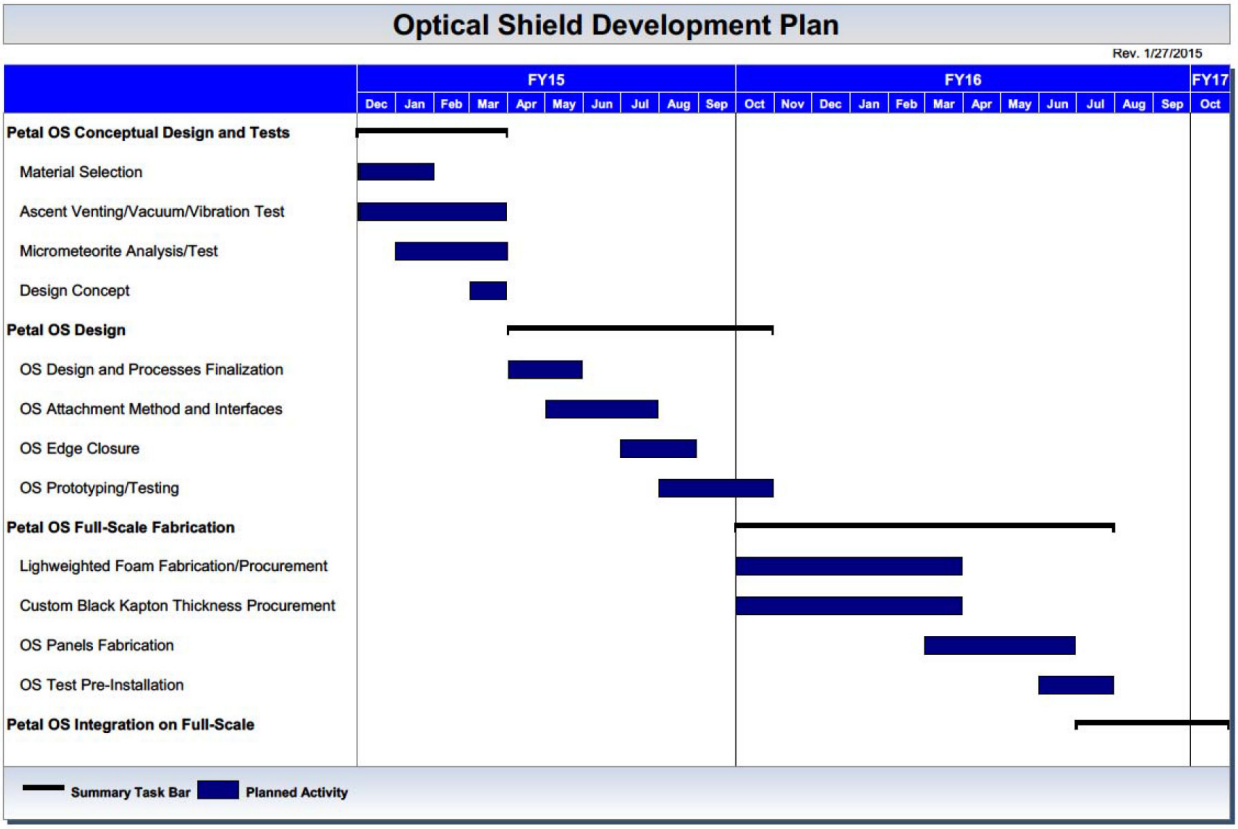

Figure B.4-1. OS development schedule.

areas: panel development, petal OS development, inner disk OS development, and system-level testing.

B.4.1 Panel Development

Panel development work has made significant progress. Panel materials testing and selection have been completed. Based on reflectivity and opacity testing, and known suitability for space applications, a black Kapton (**Figure B.4-2**) has been selected as the panel light-blocking surface material. The film includes a 'scrim' grid of tear-resistant material, providing protection against tear propagation. Urethane foam has been chosen as the panel separation layer. The current design uses a lightweight, 1.6-cm-thick sheet. The materials are bonded together with 3M Fastbond® 49 adhesive.

A fabrication process for the panels has also been established. Panels will be fabricated in large, roughly meter-square segments. Prior to bonding, the foam sheet will be lightweighted with material cutouts (**Figure B.4-3**). One layer of Kapton will be bonded to the foam sheet at a time. The Kapton is placed on a granite block with the scrim side up; adhesive is then applied to the scrim side of the Kapton. To minimize the mass of the adhesive, a 'screeding' technique, similar to a screen-printing process, is used (**Figure B.4-4**). The foam is then placed on the adhesive and allowed to set. The process is repeated for the other side.

The foam-sandwich flex-panels introduce a need to address air exhaust during spacecraft ascent. The panels have been designed to withstand the pressure differential during launch until the escaping gas from the foam

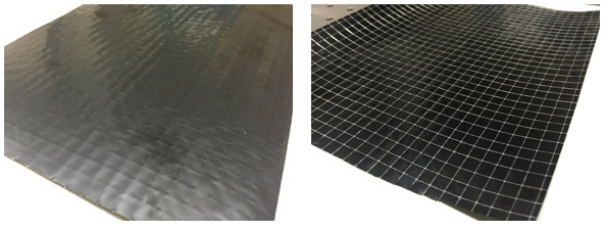

Figure B.4-2. 25.4-micron black 100XC Kapton® with ripstop.

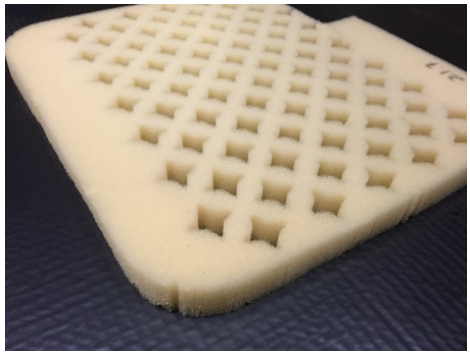

Figure B.4-3. Urethane open-cell foam, dye-cut for light-weighting.

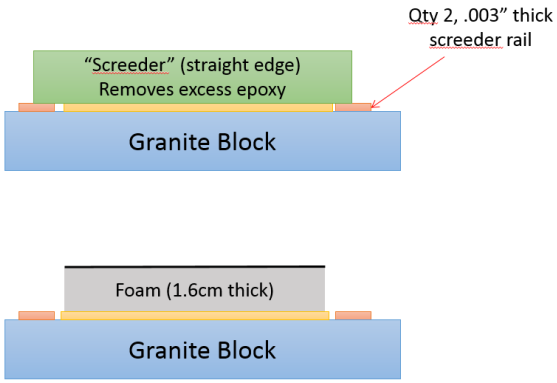

Figure B.4-4. Diagram of screeding process. Process uses a 48" straight-edge and 0.003" thick feeler gauges to apply a thin and even adhesive layer.

eliminates the difference. Testing has demonstrated five times the needed strength margin, accommodating pressure change rates of up to 5 psi per second (35 kPa/s). No further outgassing tests are needed before system-level vacuum tests.

The panels will need to undergo micrometeoroid testing. Prior to subjecting the test panel to micrometeoroid bombardment, the panel's opacity will be measured. Particles similar in size and mass to micrometeoroids will be accelerated to 5–10 km/s and fired at the panel. The angle of bombardment must be varied to simulate the more random directional bombardment expected in space. The mass flux of the bombardment will be in line with micrometeoroid modeled fluxes for a 3-year mission. Following bombardment, the opacity of the panel will again be measured to compare against requirements. Lastly, the panel will be visually inspected to assess the size and

density of pinholes, and to identify any unexpected damage.

Throughout the early portion of the OS development, a series of system-level mechanical and thermal analyses will be performed to feed-forward results of these models into the panel (as well as the inner disk and petal OS) development. Additionally, tests on panel mechanical and thermal properties will help update these models and enable better assessment of the entire OS system.

B.4.2 Inner Disk OS

Work will continue on the inner disk OS in parallel with the petal OS. An initial folding scheme exists and will be refined this year. The final folding pattern for the inner disk OS requires several iterations of CAD modeling and prototyping.

The following will be completed this fiscal year: a panel-to-panel hinge prototype will be developed and tested for mechanical properties; pseudo-kinematic mounting hardware will be designed and prototype parts fabricated; edge closeout designs will be finalized and fabrication methods settled.

This prototype build up will lead to a ½-scale inner disk OS, which will be integrated into a ½-scale inner disk truss structure. This ½-scale prototype will be used to debug inner disk OS fabrication and assembly problems, and complete limited inner disk testing and adjustments ahead of the full ½-scale starshade system tests.

B.4.3 Petal OS

A conceptual design for the petal OS now exists and early mechanical modeling has begun. A prototype interpanel flap, to light tight the spaces between panels, has been designed and fabricated (**Figure B.3-6**). Petal OS attachment methods will be evaluated and prototype hardware will be constructed in the spring and early summer of this year. The edge closeout method and materials have been settled. Prototype closeout design and fabrication will be carried out this summer.

All of this prototype hardware development is working toward the construction of a ½-scale prototype petal OS. An existing ½-scale petal structure will be used for this development. This scale model of a petal will be used to debug the petal OS design, as well as fabrication and assembly methods. In addition, this model will be used to conduct early thermal tests to verify the petal OS mounting method.

In FY16, a full scale (7-m) petal prototype development will begin. This prototype and its associated tests will bring the petal design to TRL 5 by FY17. To support this prototype, a full-scale petal OS will be built. A series of thermal tests to verify the petal shape (and the lack of petal OS-induced stresses into the petal structure) are planned.

B.4.4 System Level Testing

To complete the TRL 5 validation of the starshade OS system, a number of system level analyses, simulations and tests will be needed. Mechanical and thermal modeling of the OS has already begun and the results are being used in early OS panel design decisions. This modeling work will continue into the TRL 5 system tests with model fidelity being improved by incorporating test-measured performances into the models. Development of a working tabletop model to simulate the actual starshade deployment steps is now under way and will demonstrate concept feasibility. But the most difficult and important validation work ahead is the system-level deployment tests on the ½-scale starshade model that will be used to elevate the starshade (and OS) design to TRL 5.

Unlike most of the other validation work discussed so far, the deployment tests require significant up-front effort to develop a deployment test facility. This facility must have sufficient room to conduct the tests and it must have a gravity compensation capability to simulate space-like conditions when the starshade is deployed.

The design of this gravity off-loading system (**Figure B.4-5**) requires careful consideration of a number of factors related to the OS. OS panels require additional support lines along the inner disk OS, in addition to the support lines for the hub and the truss. Panel construction and fold lines allow for tether points for proper weight transfer. The inner disk OS unfolds in a spiral motion, resulting in the preferred tether points following a path different than the radial paths of the deploying truss nodes. To accommodate their path, a second, OS gravity off-loading system hub is located above the starshade truss off-loading hub and deploys in a controlled fashion, matched to the rotation of the starshade hub. Support lines are always above a radial fold peak in the inner disk OS origami crease pattern.

These deployment tests, including stowage verification, proper unassisted deployment, petal positional and shape tolerances, will be the TRL 5 validation for the OS design.

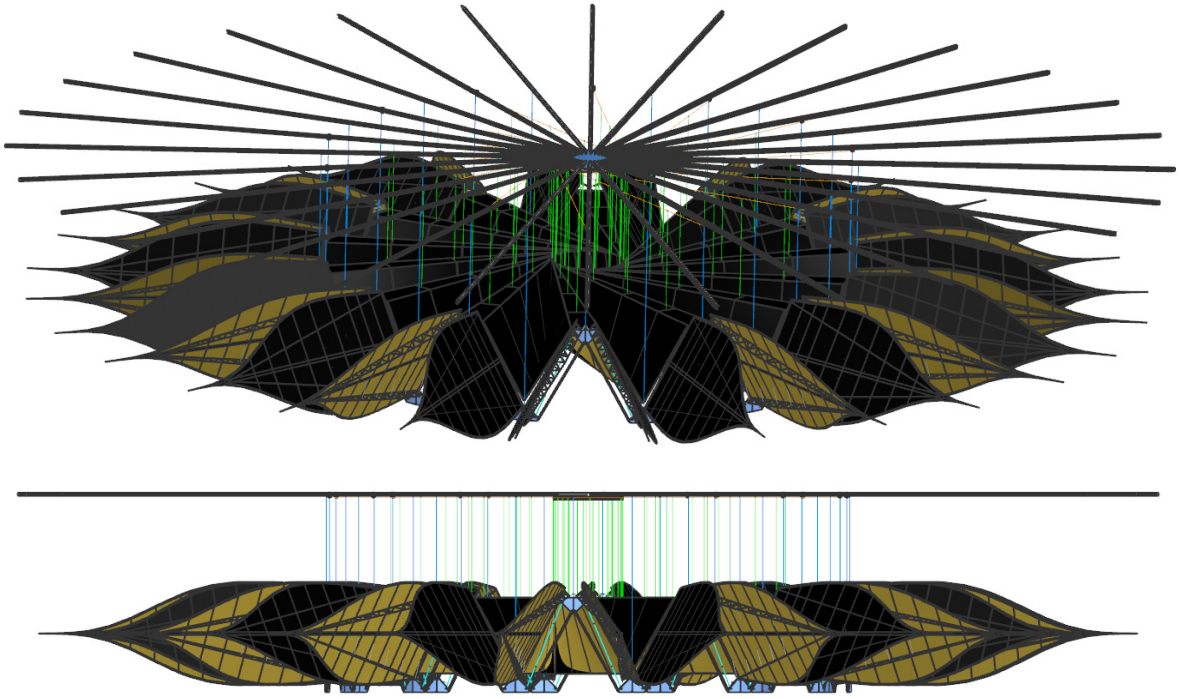

Figure B.4-5. Gravity compensation rails, support lines, and starshade. Note that all the support lines are vertical.

C TECHNOLOGY PLAN

The Exo-S technology gaps and their retirement flow plans are shown in **Figures C-1** through **C-4**. The costs of the major activities needed to complete the technology development are included in **Table C-1**. A discussion of the technology work (both completed and what lies ahead) is included in Section 9. **Figures C-1** through **C-4**, **Table C-1**, and the discussion in Section 9 define the technology plan needed to develop the starshade missions described in the Exo-S study.

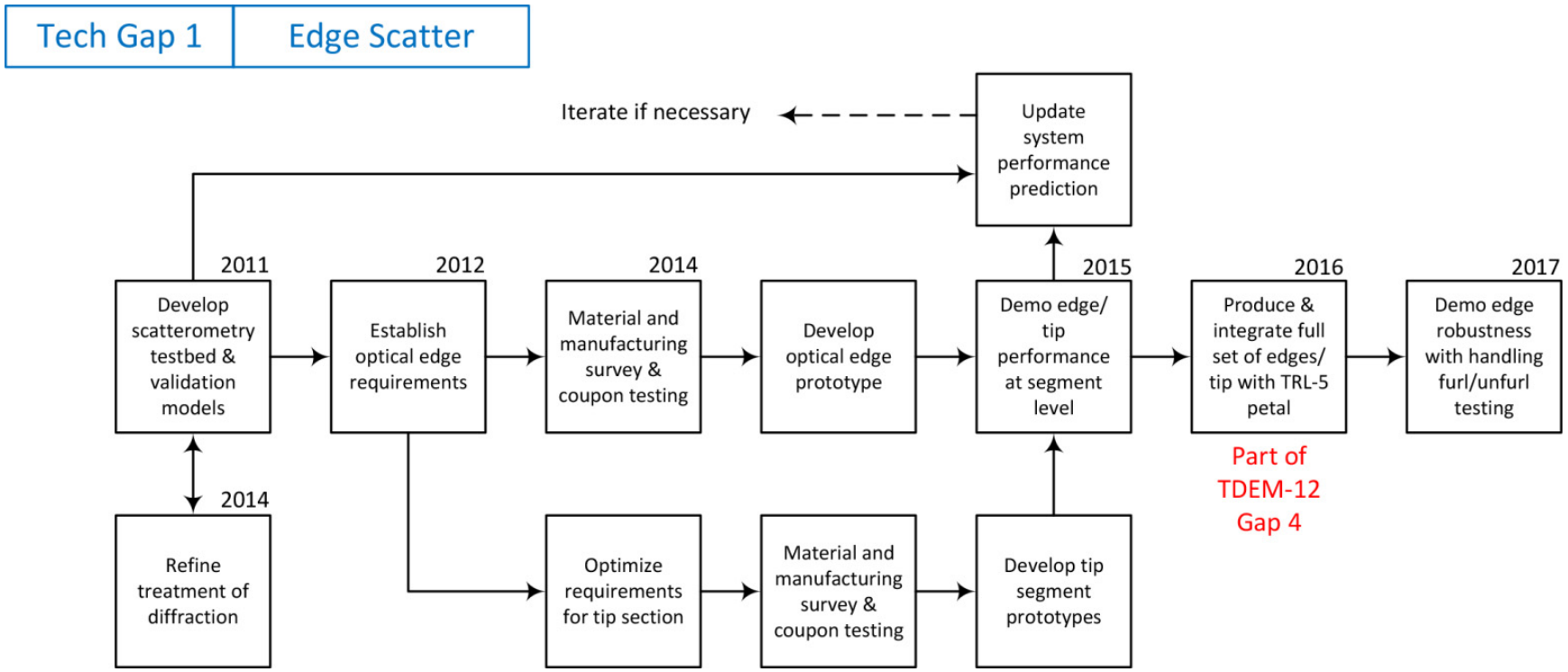

Figure C-1. Starshade edge scatter technology gap retirement flow plan.

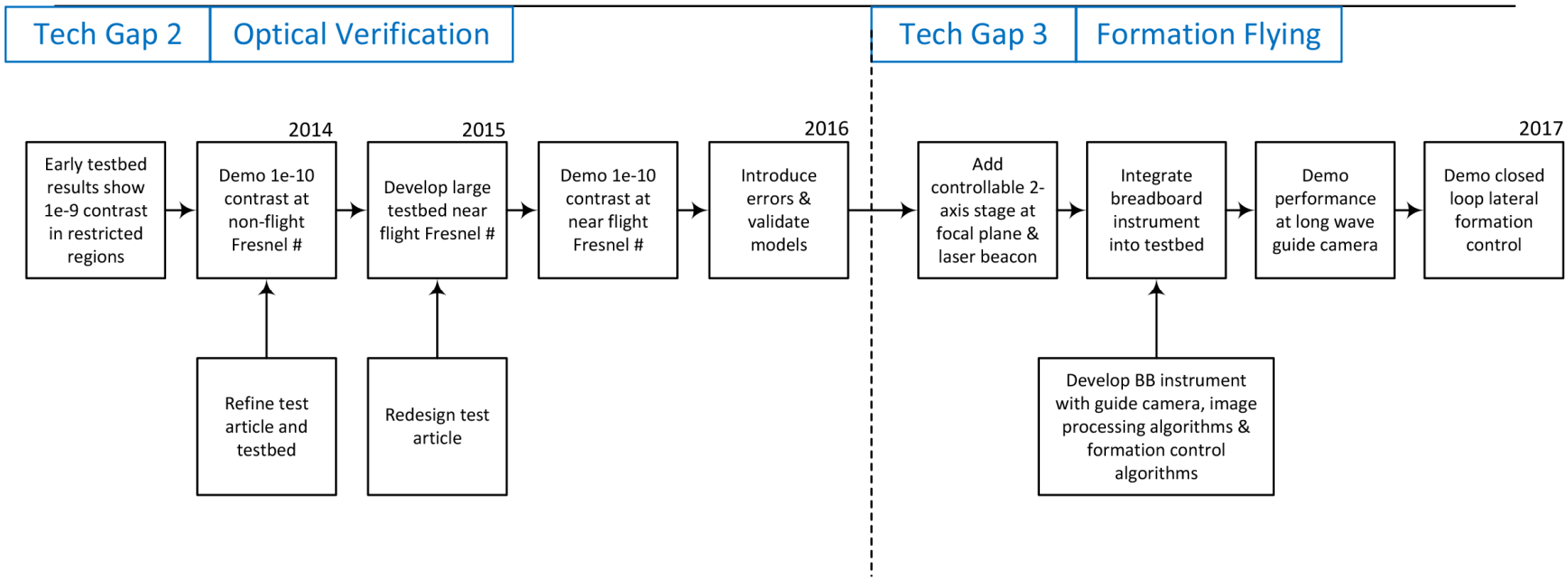

Figure C-2. Starshade optical verification and formation flying technology gaps retirement flow plan.

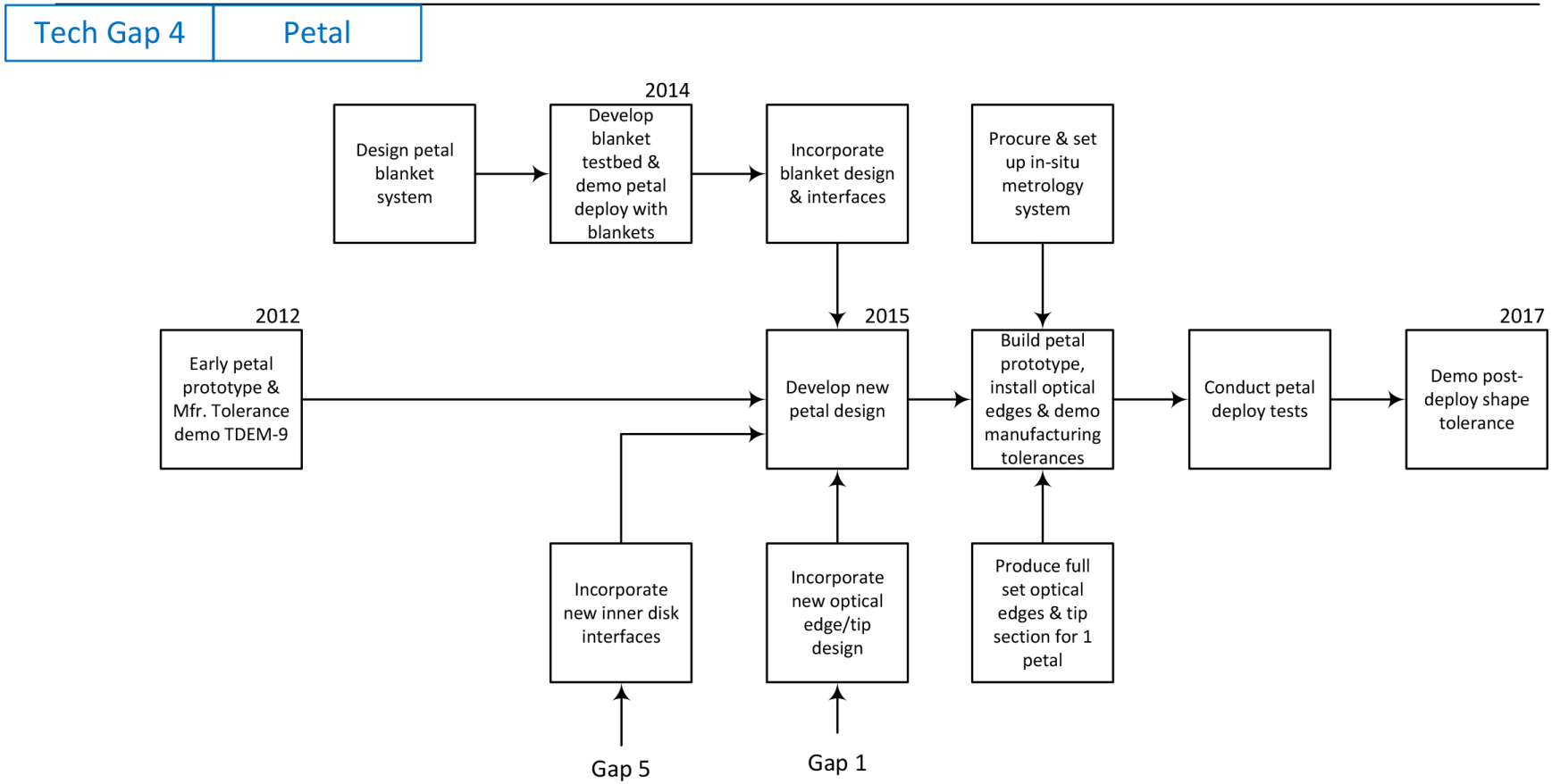

Figure C-3. Starshade petal development technology gap retirement flow plan.

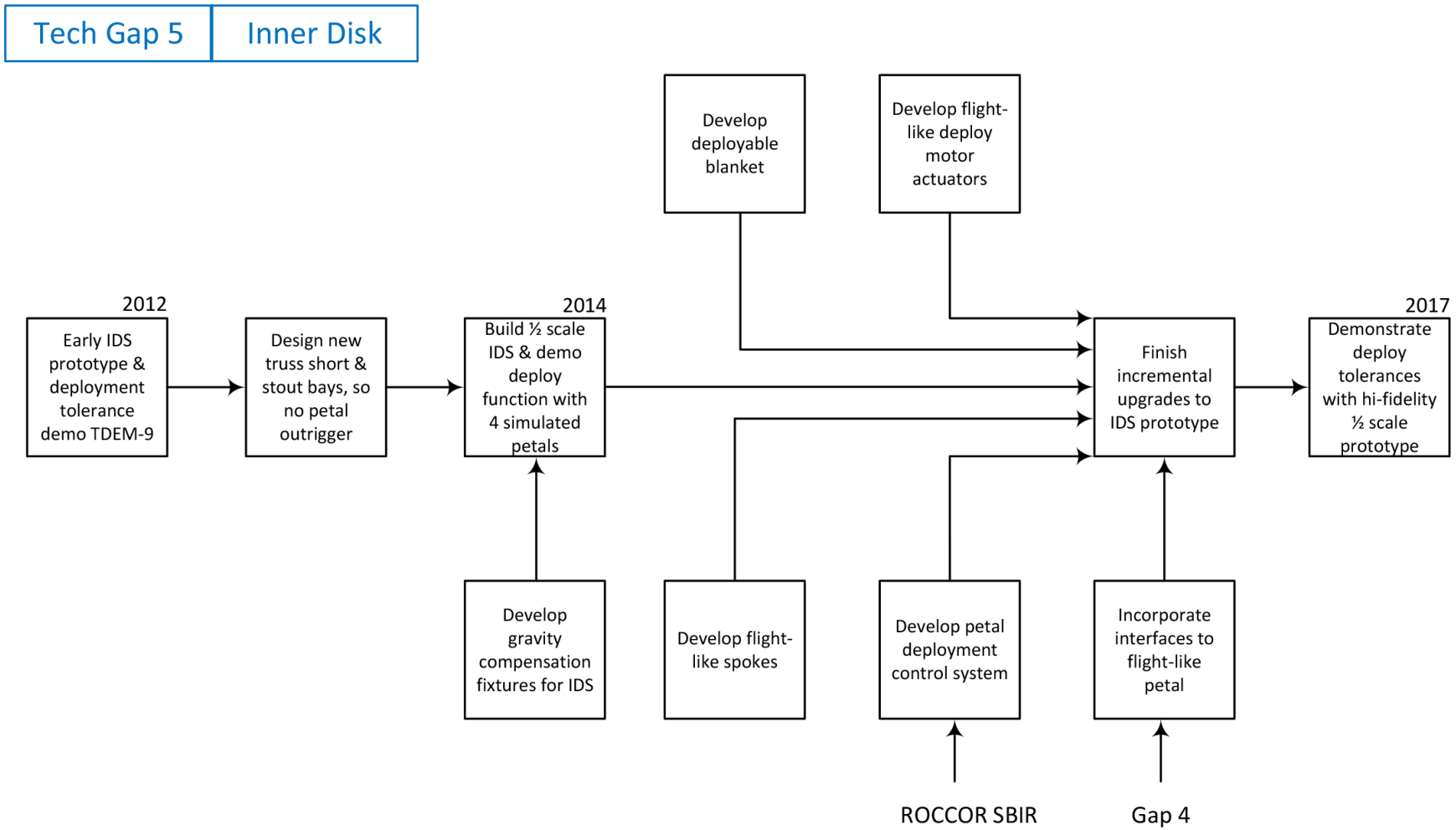

Figure C-4. Starshade inner disk structure development technology gap retirement flow plan.

Table C-1. Starshade technology development task cost estimates.

ID #	Title	Tasks to Resolve	Cost Estimate
S-1	Control edge-scattered sunlight	a) Upgrade testbed and operate	$1.7M
		b) Verify specification and develop design solution	
		b') Modeling support to NGAS	
		c) Develop & test edge prototype + tip section	
		d) Develop & operated edge segment testbed: strain test, radius profile, in-plane profile	
S-2	Demonstrate contrast and suppression performance and validate optical models	a) Provide test article with sharp edges	$0.8M
		b) Develop lab testbed	
		b') Model edge phenomenon	
		c) Characterize sensitivities in field	
		c') Modeling support to NGAS	
S-3	Demonstrate lateral formation-sensing accuracy	a) Develop image processing and control system algorithms, develop FGS breadboard, demo perf. in Princeton optical testbed	$2.2M
S-4	Demonstration of flight-like petal fabrication and deployment	a) Develop petal blanket testbed & POC blanket	$10.2M
		a') Develop prototype petal blanket	
		b) Petal and system designs	
		d) Procure petal level metrology system & operate	
		e) Produce full-set of optical edges and tip section	
		f) Procure petal materials/parts (long-lead composites)	
		g) Assemble petal, integrate blanket/edges/tip, deploy test & demo manufacturing tolerance	
S-5	Demonstration of inner disk deployment with optical shield	a) Develop POC truss at 1/2 scale (no blanket) and demo functionality	$8.8M
		b) Develop gravity compensation fixture in bldg 299	
		c) Design blanket and produce bench size mockup	
		d) Produce prototype blanket, integrate w/ POC truss, demo deploy tolerances	
		e) Produce full set of simulated petals	
		f) Petal unfurl control system	
		g) Integrate unfurl control system & simulated petals and demo contiguous unfurl/deploy*	
			Total: **$23.7M**